ANALYSIS AND CLASSIFICATION OF B-MODE LIVER ULTRASOUND IMAGES
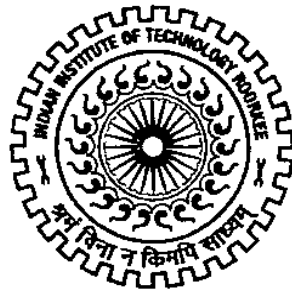
Ph.D. THESIS

by

JITENDRA VIRMANI

DEPARTMENT OF ELECTRICAL ENGINEERING
INDIAN INSTITUTE OF TECHNOLOGY ROORKEE
ROORKEE – 247 667 (INDIA)
DECEMBER, 2013

ANALYSIS AND CLASSIFICATION OF B-MODE LIVER ULTRASOUND IMAGES

A THESIS

*Submitted in partial fulfilment of the
requirements for the award of the degree
of*

DOCTOR OF PHILOSOPHY
in
ELECTRICAL ENGINEERING

by

JITENDRA VIRMANI

DEPARTMENT OF ELECTRICAL ENGINEERING
INDIAN INSTITUTE OF TECHNOLOGY ROORKEE
ROORKEE – 247 667 (INDIA)
DECEMBER, 2013

INSTITUTE ETHICS COMMITTEE

POSTGRADUATE INSTITUTE OF MEDICAL EDUCATION AND RESEARCH, CHANDIGARH

No. 11/7048.
Dated 06/06/2011

Prof. N.K.Ganguly, MD
Chairman
Institute Ethics Committee

Prof. A. Chakrabarti, MD
Convener
Institute Ethics Committee

Dr. Naveen Kalra
Addl. Professor
Department of Radiodiagnosis and Imaging
PGIMER, Chandigarh

Ref : Analysis and classification of Liver Ultrasound images (NK 8/976)

Sub : Ethics Committee approval

Dear Dr. Naveen Kalra,

Vide your letter No. RDG/2011/862 dated 17-05-2011 we received from you 5 copies of the following documents in reference to the above mentioned study to be conducted at Postgraduate Institute of Medical Education & Research, Chandigarh.

"Analysis and classification of Liver Ultrasound images"

At this Institute Ethics Committee meeting held on 23-05-2011, the above mentioned documents were examined & discussed. After consideration, the committee approved the project.

It is understood that the study will be conducted under your direction. A report of the study should be sent to the Ethics Committee yearly. Any adverse reaction or condition appeared during the study period should be reported to the Ethics Committee immediately.

The members who attended the meeting held on <u>23-05-2011</u> at which your proposal was discussed are as follows :

1. Dr.N.K.Ganguly (Chairman)

2. Justice P.K.Palli

3. Dr. (Mrs) S. Bambah

4. Dr. Girish Varshney

5. Dr. Kusum Joshi

6. Dr. S.Prabhakar

7. Dr. L.K.Dhaliwal

8. Dr. Sanjay Jain

9. Dr.Sunil Arora

10. Dr. A.Chakrabarti (Convener)

It is hereby confirmed that neither you or any of the study team members have participated in the voting decision making procedures of the committee.

Yours sincerely,

(A.Chakrabarti)
Convener,
Institute Ethics Committe

Copy to : Prof.-in-charge, Medical Education Cell, PGIMER

INDIAN INSTITUTE OF TECHNOLOGY ROORKEE
ROORKEE

CANDIDATE'S DECLARATION

I hereby certify that the work which is being presented in this thesis entitled **"ANALYSIS AND CLASSIFICATION OF B-MODE LIVER ULTRASOUND IMAGES"** in partial fulfilment of the requirements for the award of *the Degree of Doctor of Philosophy* and submitted in the Department of Electrical Engineering of Indian Institute of Technology Roorkee, Roorkee is an authentic record of my own work carried out during a period from July, 2009 to December, 2013 under the supervision of Dr. Vinod Kumar, Professor, Department of Electrical Engineering, Indian Institute of Technology Roorkee, Roorkee and Dr. Naveen Kalra, Additional Professor, Department of Radiodiagnosis and Imaging, Post Graduate Institute of Medical Education and Research, Chandigarh.

The matter presented in this thesis has not been submitted by me for the award of any other degree of this or any other Institution.

(JITENDRA VIRMANI)

This is to certify that the above statement made by the candidate is correct to the best of our knowledge.

(Naveen Kalra)   (Vinod Kumar)
Supervisor   Supervisor

Date:

The Ph.D. Viva-Voce Examination of *Mr. Jitendra Virmani*, Research Scholar, has been held on…………….

Supervisors   Chairman, SRC   External Examiner

Head of the Department/Chairman, ODC

Acknowledgements

List of Abbreviations

ABNOR   Abnormal

AC   Autocorrelation

ANN   Artificial Neural Network

ANN   Artificial Neural Network

ASM   Angular Second Moment

B-Dist   Bhattacharya Distance

B-Mode   Brightness Mode

BNN   Binary Neural Network

BPNN   Back Propagation Neural Network

CAD   Computer-aided Diagnosis

CFS   Correlation Based Feature Selection

CM   Confusion Matrix

CT   Computed Tomography

Div   Divergence

DWT   Discrete Wavelet Transform

E5   Edge Detector Filter of Length 5

E7   Edge Detector Filter of Length 7

E9   Edge Detector Filter of Length 9

FD   Fractal Dimension

FDR   Fisher Discriminant Ratio

FDWT   Fast Discrete Wavelet Transform

FLL   Focal Liver Lesion

FOS	First Order Statistics
FPS	Fourier Power Spectrum
FS	Feature Set
FVL	Feature Vector Length
GA	Genetic Algorithm
GA–SVM	Genetic Algorithm–Support Vector Machine
GB	Giga Byte
GLCM	Gray Level Co-occurrence Matrix
GLDS	Gray Level Difference Statistics
GLHS	Gray Level Histogram Statistics
GLRLM	Gray Level Run Length Matrix
GRBF	Gaussian Radial Basis Function
GUI	Graphic User Interface
GWT	Gabor Wavelet Transform
HCAD	Hierarchical Computer-aided Diagnostic System
HCC	Hepatocellular Carcinoma
HEM	Hemangioma
HVS	Human Visual System
Hy-HCAD	Hybrid-Hierarchical Computer-aided Diagnostic System
ICA	Individual Class Accuracy
IDM	Inverse Difference Moment
IRB	Institutional Review Board
IROIs	Inside Regions of Interest
k-NN	k-Nearest Neighbor
Kurt	Kurtosis

L5	Level Detector Filter of Length 5
L7	Level Detector Filter of Length 7
L9	Level Detector Filter of Length 9
LHCC	Large Hepatocellular Carcinoma
LHCCI	Large Hepatocellular Carcinoma Image
LOO	Leave-One-Out
LSI	Liver State Index
MET	Metastatic Carcinoma
ML	Malignant Lesion
M-Mode	Motion Mode
MoU	Memorandum of Understanding
MPNN	Modified Probabilistic Neural Network
MRI	Magnetic Resonance Imaging
MRS	Multiresolution Scheme
NGTDM	Neighborhood Gray Tone Dependence Matrix
NN	Neural Network
NNE	Neural Network Ensemble
NOR	Normal
NSW	Non-separable Wavelet Transform
OAO	One-Against-One
OCA	Overall Classification Accuracy
OL	Other Lesion
PC	Principal Component
PCA	Principal Component Analysis
PET	Positron Emission Tomography

PGIMER	Post Graduate Institute of Medical Education and Research
PML	Primary Malignant Lesion
PNN	Probabilistic Neural Network
R5	Ripple Detector Filter of Length 5
R7	Ripple Detector Filter of Length 7
R9	Ripple Detector Filter of Length 9
RAM	Random Access Memory
RBF	Radial Basis Function
RCL	Representative Coarseness Level
RFVL	Reduced Feature Vector Length
ROC	Region of Convergence
ROIs	Regions of Interest
S5	Spot Detection Filter of Length 5
S7	Spot Detection Filter of Length 7
S9	Spot Detection Filter of Length 9
SBS	Sequential Backward Search
SFM	Statistical Feature Matrix
SFS	Sequential Forward Search
SGLDM	Spatial Gray Level Dependence Matrix
SHCC	Small Hepatocellular Carcinoma
SHCCI	Small Hepatocellular Carcinoma Image
Skew	Skewness
SML	Secondary Malignant Lesion
S_p	Spread Parameter
SROIs	Surrounding Regions of Interest

Std	Standard Deviation
SVD	Singular Value Decomposition
SVM	Support Vector Machine
TDs	Texture Descriptors
TEI	Texture Energy Image
TEM	Texture Energy Measure
TFV	Texture Feature Vector
TGC	Time Gain Compensation
US	Ultrasound
W5	Wave Detection Filter of Length 5
W9	Wave Detection Filter of Length 9
WPT	Wavelet Packet Transform

List of Figures

xvi

List of Tables

Abstract

The present research work has been carried out with an aim to enhance the diagnostic potential of conventional B-Mode ultrasound (US) imaging modality for diagnosis of liver diseases. To achieve this objective, the design and implementation of an interactive system for diagnosis of liver diseases using B-Mode liver US images is proposed in the present study. The research objectives for the present work were formulated keeping in view the needs of the radiologists, based on the practical difficulties faced by them in routine clinical practice.

The study was conducted by collecting a comprehensive image database of 124 B-Mode liver US images with representative cases from each image class, acquired from the patients who underwent US examination at the Department of Radiodiagnosis and Imaging, PGIMER, Chandigarh, India during a period from March 2010 to March 2012.

The image database comprises of 21 Normal (NOR), 16 Cirrhotic, 12 Cyst, 15 Hemangioma (HEM), 28 Hepatocellular Carcinoma (HCC) and 32 Metastatic Carcinoma (MET) liver images. Further bifurcation of Cyst, HEM and MET images into typical and atypical cases, and HCC cases into small HCC (SHCC) and large HCC (LHCC) cases is shown in Fig. 1.
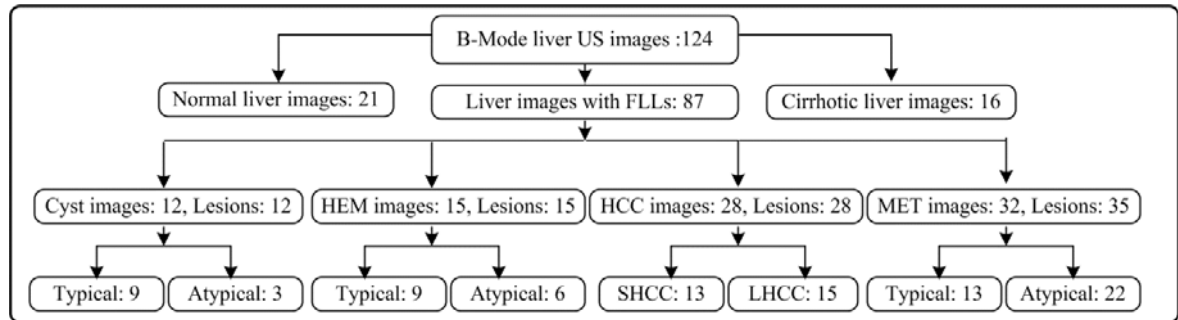
Fig. 1 The description of image database used in the present research work.
Note: FLLs: Focal liver lesions; HEM: Hemangioma; HCC: Hepatocellular carcinoma; MET: Metastatic carcinoma or metastasis; SHCC: Small HCC; LHCC: Large HCC.

The proposed interactive system for diagnosis of liver diseases using B-Mode US images consists of two modules as shown in Fig. 2. *Module* 1 is designed to assist or provide second opinion to the radiologist if there is confusion within Normal, Cirrhosis, HCC or MET liver image classes.
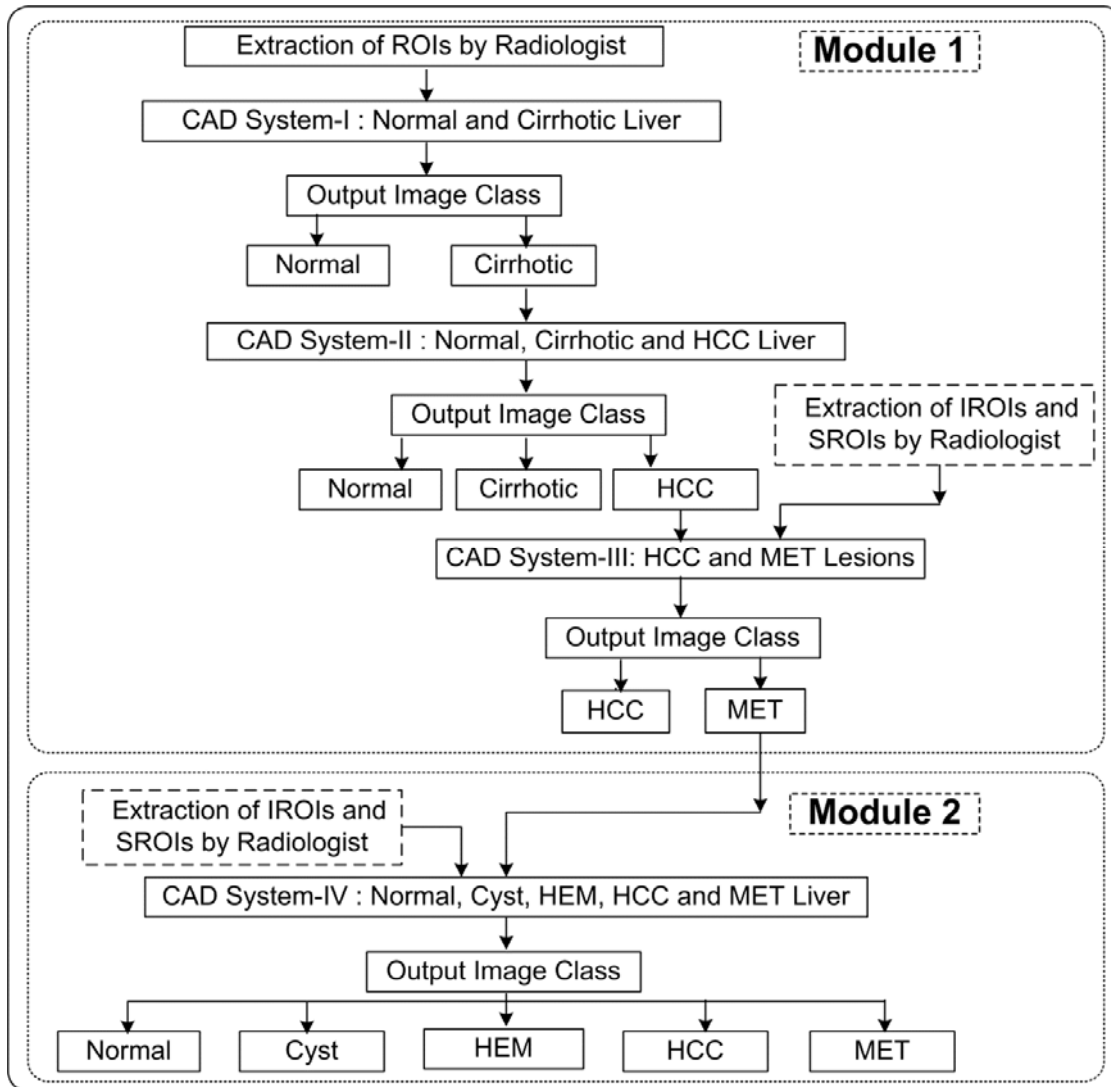
Fig. 2 Block diagram of the proposed interactive system for diagnosis of liver diseases.
Note: IROIs: Inside lesion regions of interest; SROIs: Surrounding lesion regions of interest.

Early diagnosis of liver cirrhosis using texture descriptors computed from regions of interest (ROI) extracted from conventional B-Mode liver US images is clinically significant as most of the cirrhotic patients are asymptomatic, and the biochemical tests like elevated liver enzyme detect cirrhosis at an advanced stage.

It is worth mentioning that the patients with liver cirrhosis are at high risk of developing hepatocellular carcinoma (HCC, a primary malignant focal liver lesion), and cirrhosis is also the leading cause of portal hypertension.

Since fibrosis is an essential stage leading to liver cirrhosis, it is important to know whether the fibrotic changes in liver parenchyma correspond to liver cirrhosis so that medication can be administered timely and the associated complications can be prevented.

Furthermore, since liver cirrhosis is considered as a pre-cursor to development of HCC and it is considerably difficult to diagnose small HCCs developed on already nodular cirrhotic liver parenchyma, the diagnosis as to whether the textural changes in the liver parenchyma are cirrhotic changes or they indicate the development of HCC is absolutely necessary.

It is worth mentioning that there is a considerable overlap between the sonographic appearances of HCC and MET lesions, at the same time the differential diagnosis between HCC and MET lesions is essential for effective treatment of liver malignancies.

Accordingly, the *Module* 1 of the proposed interactive system for diagnosis of liver diseases incorporates three different CAD systems: (*i*) CAD System-I for binary classification between normal and cirrhotic liver tissue, (*ii*) CAD System-II for classification between normal, cirrhotic and HCC liver, and (*iii*) CAD system-III for binary classification between HCC and MET liver malignancies.

The region of interest (ROI) extracted by the radiologist, is fed to CAD system-I, for characterization between normal and cirrhotic liver tissue. Although the design of the proposed CAD system-I yields 100 % accuracy for characterization between normal and cirrhotic liver tissue, but due to severely limited sensitivity of US for detection of small HCCs developed on cirrhotic liver, it is quite possible that the region of interest (ROI) belonging to cirrhotic liver may actually represent a HCC. Therefore, the ROI which is predicted as cirrhotic by the CAD system-I is passed through CAD System-II for characterization between normal, cirrhotic and HCC liver tissue. If the prediction of the CAD System-II for an ROI is cirrhosis, it gives greater confidence to the radiologist that the liver tissue is cirrhotic. However, if for a particular ROI the decision of the CAD System-II is HCC, it is advised to investigate whether the ROI belongs to a HCC lesion or a MET lesion because of their significant overlapping sonographic appearances. Although, both HCC and MET lesions represent malignant liver lesions, differential diagnosis between HCC and MET lesion is absolutely necessary for better management of the disease and adequate scheduling of treatment options. Therefore, the ROI, if predicted as HCC by CAD System-II, is passed through CAD System-III for binary classification between HCC and MET liver tissue. If it is predicted as HCC, it gives greater confidence to the radiologist that the ROI represents HCC, or else if the ROI is predicted as

MET, it is recommended to pass the ROI to the CAD System-IV of *Module* 2 of the proposed interactive system for diagnosis of liver diseases for its differential diagnosis with other FLLs.

Exhaustive experimentation was carried out for the design of efficient classifiers for CAD System-I, CAD System-II, CAD System-III and CAD System-IV. The radiologists observe the texture patterns of the IROIs (inside lesion regions of interest, i.e., regions of interest extracted from region well inside the lesion boundary) as well as the texture patterns of the SROIs (surrounding lesion regions of interest, i.e., regions of interest extracted from liver parenchyma surrounding the lesion and approximately at the same depth as that of the centre of the lesion) for making differential diagnosis between HCC and MET lesions using B-Mode US images. Accordingly, texture feature extraction from IROIs and SROIs were carried out for design of CAD System-III for classification between HCC and MET lesion. Therefore, if the prediction of CAD system-II for a ROI is HCC, the radiologist is required to mark an additional SROI for the classification task. The results obtained from exhaustive experiments carried out in the present work indicate that the texture feature extraction from both IROIs and SROIs enhances the efficiency of the CAD System-III for classification between HCC and MET lesions.

The classification performance obtained by CAD System-I, CAD-System-II and CAD System-III designs implemented for the design of *Module* 1 of the proposed interactive system for diagnosis of liver diseases using B-Mode US images is depicted in Table 1.

Table 1 *Classification performance CAD System-I, CAD System-II and CAD System III of Module 1*

CAD System Design	OCA (%)
CAD System-I: (Normal and cirrhotic Liver): Design based on first four singular value mean features derived by singular value decomposition of gray level co-occurrence matrix and SVM classifier [RFVL:4]	100
CAD System-II: (Normal, cirrhotic and HCC Liver): Design based on 2D-WPT multiresolution texture descriptors [RFVL: 10]	88.8
CAD System-III: (HCC and MET): Design based on texture features computed from IROIs and texture ratio features computed from IROIs and corresponding SROI. [RFVL: 9]	91.6

Note: MRS: Multiresolution scheme, RFVL: Reduced feature vector length, OCA: Overall classification accuracy, IROIs: Inside lesion regions of interest, SROIs: Surrounding lesion regions of interest.

The CAD System-IV of *Module* 2 is designed to assist or provide second opinion to the radiologist for making differential diagnosis between FLLs using B-Mode US images.

The radiologists diagnose typical focal liver lesions (FLLs) easily by their classic sonographic appearances; however, the differential diagnosis between atypical FLLs from B-Mode ultrasound (US) is quite a challenging task faced in routine clinical practice, mainly due to existence of overlapping sonographic appearances even within individual classes of FLLs. Even then, B-Mode US is considered as preferred examination for characterization of FLLs, mainly due to its noninvasive, nonradioactive, inexpensive nature and real-time imaging capabilities. Therefore, a CAD system for classification of FLLs from B-Mode US images is highly desired. At the same time, it is worth mentioning that there are certain disadvantages associated with the use of B-Mode US for characterization of FLLs: (*a*) limited sensitivity for detection of small FLLs (< 2 cm) developed on cirrhotic liver which is already nodular and coarse-textured, (*b*) sonographic appearance of HCC and MET lesions are highly overlapping, (*c*) sonographic appearances of cystic metastasis and atypical cyst are often overlapping, (*d*) sonographic appearances of atypical HEM, sometimes mimic with atypical MET or HCC, and (*e*) difficulty to characterize isoechoic lesions with very slim difference in contrast between region inside the lesion and the surrounding liver parenchyma in some cases.

Therefore, it is important to address these issues and design an efficient CAD system for FLLs using a comprehensive and representative image database with (*a*) typical and atypical cases of Cyst, hemangioma (HEM) and metastasis (MET), (*b*) small as well as large hepatocellular carcinoma (HCC), and (*c*) normal (NOR) liver tissue.

As it is well known fact that US imaging has limited sensitivity for detection of SHCCs less than 2 cm in size, therefore in order to design a robust classification system, it is ensured that the constituent HCC images in the dataset offered a high degree of variability in terms of size and sonographic features.

To ensure generality, the training data for designing the classifier was chosen carefully in consultation with experienced participating radiologists, so as to include all the typical and atypical image classes for Cyst, HCC, HEM and MET lesions as well as small and large HCC lesions for designing a robust classifier with representative cases for all image subclasses. Two sets of images were created for each image class, ROIs from one set of images were used for training and ROIs from the other set were used for testing to avoid any biasing.

The *Module* 2 incorporates a CAD System-IV for classification between Normal, Cyst, HEM, HCC and MET liver image classes. In the present work, rigorous experiments were carried out for designing an efficient CAD system for characterization of FLLs. Radiologists

visualize the texture patterns of the regions inside and outside of the lesion for differential diagnosis between FLLs using B-Mode US images. Accordingly, texture feature extraction from IROIs as well as SROIs was considered for the design of the proposed CAD system. Thus, IROIs (extracted from the region inside the lesion) and a corresponding SROI (extracted from the surrounding of each lesion) are inputted to *Module* 2 for classification between NOR, Cyst, HEM, HCC or MET liver image classes.

The CAD system designs implemented in the present research work for characterization of FLLs using B-Mode US images, include designs (*a*) using PCA-kNN, PCA-PNN, PCA-NN and PCA-SVM based multiclass classifiers, (*b*) using hierarchical framework of PCA-kNN, PCA-PNN, PCA-NN and PCA-SVM based binary classifiers, and (*c*) using an ensemble of neural network classifiers.

A brief comparision of classification performance obtained by different CAD System-IV designs implemented for the design of *Module* 2 of the proposed interactive system for diagnosis of liver diseases using B-Mode US images is depicted in Table 2.

Table 2 Comparison of c*lassification performance: CAD System-IV designs for Module 2*

Experiment No.	CAD System-IV Design	OCA (%)
1	PCA-SVM based CAD system	87.2
2	PCA-NN based CAD system	87.7
3	PCA-PNN based CAD system	86.1
4	PCA-kNN based CAD system	85.0
5	PCA-SVM based Hierarchical CAD system	90.5
6	PCA-NN based Hierarchical CAD system	88.3
7	PCA-PNN based Hierarchical CAD system	91.6
8	PCA-kNN based Hierarchical CAD system	90.5
9	Hybrid Hierarchical CAD system	92.7
10	Neural Network Ensemble based CAD system	95.0

Note: OCA: Overall classification accuracy, NN: Neural network, PNN: Probabilistic neural network, kNN: *k*-nearest neighbour classifier.

From Table 2, it can be observed that the neural network ensemble based CAD system yields the best performance for characterization of FLLs using B-Mode US images. Therefore, the NNE based CAD system should be used for the design of *Module* 2 of the proposed interactive system for diagnosis of liver diseases using B-Mode US images.

Contents

Chapter 8

Hybrid Hierarchical CAD System for Focal Liver Lesions

Chapter 9

Neural Network Ensemble based CAD System for Focal Liver Lesions

Chapter 10

Conclusions

Chapter 1

Introduction

1.1 Motivation

Liver is the most vital and largest organ of the human body. It performs many important functions like production and excretion of bile (a digestive fluid), synthesis of cholesterol, production of triglycerides (fats), metabolism of proteins, fats and carbohydrates, storage of vitamins and minerals, synthesis of plasma proteins, breakdown of insulin and other hormones, blood pressure management, blood detoxification, etc. Liver is a metabolically active organ necessary for survival. The working cells of the lever (called *hepatocytes*) have unique capability to reproduce whenever the liver is injured. Thus, liver regeneration can occur after surgical removal of a portion of the liver or after an injury that destroys a part of the liver. However, there is absolutely no way to compensate for long-term liver dysfunction, because of the diversity of functions it handles.

As liver is the largest solid organ of the human body, it becomes an easy target for many diseases. Liver diseases are widely recognized as an emerging public health crisis particularly in South Asian countries [214]. In clinical diagnosis, liver diseases are always taken seriously as it is a vital organ, which performs very important functions required for sound operation of human body. Liver diseases are classified in two broad categories, i.e., *diffuse liver diseases* and *focal liver diseases*.

1.1.1 Diffuse Liver Diseases

In diffuse liver diseases, the abnormality is distributed throughout the liver tissue. It has been verified by histological and pathological investigations that the severity of diffuse liver diseases is closely related to hepatic fibrosis progression [208]. In diffuse liver disease, higher than normal amount of collagen fibre is deposited in the extra-cellular spaces of the hepatocytes, due to which these hepatocytes lose blood thereby leading to liver fibrosis. According to different fibrosis stages, diffuse liver diseases can be sorted into three classes, namely, *hepatitis*, *fatty liver* and *cirrhosis*.

Among diffuse liver diseases, the liver cirrhosis (characterized as irreversible hepatic fibrosis) is considered more serious as it represents the end stage of chronic diffuse liver disease.

The viral hepatitis, such as hepatitis B or C is one of the causes of liver cirrhosis; the virus can induce chronic inflammation in the liver causing fibrotic changes. The extent of fibrosis in liver tissue can range from fibrous expansion in the portal area to cirrhosis [208].

In liver cirrhosis, strong association with fibrosis results in regenerative nodule formation which leads to alterations in normal hepatic structure such as (*i*) decrease in homogeneity, (*ii*) modification in hepatic vessels, (*iii*) modification in shape and contour, and (*iv*) increase in liver volume (toxic cirrhosis) or decrease in liver volume (viral cirrhosis). [109]

Since fibrosis is a necessary stage that leads to cirrhosis which is an irreversible process, therefore, it is critical to detect the fibrosis status at an early stage so that proper medication is administered to avoid cirrhosis. [26]

For many years, diffuse liver diseases are the leading cause of mortality. Therefore, an early diagnosis of diffuse liver diseases is important during regular checkups [101]. US is usually performed as a screening step for evaluation of diffuse liver disease. But as the sonographic diagnosis is subjective based on clinical observation, biopsy (an invasive procedure) is considered a gold standard for arriving at the final diagnosis. Furthermore, the needle biopsy of the liver parenchyma may lead to biased results due to sampling error. Moreover this procedure being invasive may result in severe complications leading in morbidity and even mortality [213].

The pathological changes in diffuse liver diseases alter certain physical and micro architectural properties like density, elasticity, homogeneity of the tissue. However, these alterations are difficult to be observed even though they certainly affect the propagation of ultrasound (US) during sonographic examination. Hence, the computerized, statistical analysis of US image texture has become necessary. [109]

1.1.2 Focal Liver Diseases

In focal liver diseases, the abnormality is concentrated in a small localized region of the liver parenchyma which is often referred to as *focal liver lesion* (FLL). Liver Cysts, Hemangioma (HEM, i.e., a primary benign FLL), Hepatocellular carcinoma (HCC, i.e., a primary malignant FLL) and Metastatic carcinoma (MET, i.e., a secondary malignant FLL), are some of the commonly occurring focal liver diseases.

1.1.2.1   Liver Cyst

Liver Cysts are most common FLLs, and are frequently observed on US. Cysts represent the fluid filled cavities in the liver. Liver Cysts can be congenital or acquired from trauma or any previous infection. Usually, cysts are asymptomatic unless they are large enough to cause *mass effect* (i.e., compression and displacement of adjacent structures). Mostly, liver cysts are incidental findings during the US scan. *Typical cysts* appear with anechoic echotexture, well defined smooth thin lined capsule and posterior acoustic enhancement. On the other hand, *atypical cysts* contain low level fine echoes which occur as a result of hemorrhage or infection and are outlined by thick irregular wall. These atypical cysts are usually asymptomatic; however, the symptomatic ones are regularly monitored on US and treated with percutaneous aspiration under US guidance or laparoscopic unroofing. Typical cysts can be easily diagnosed from their characteristic appearance on B-Mode US, but atypical cysts can be easily confused with *cystic metastasis*. Atypical cysts always appear with internal echoes and thickened irregular walls. Differential diagnosis of cystic metastasis and atypical cyst using conventional gray scale B-Mode US can be quite challenging.

1.1.2.2   Hemangioma (*HEM*)

The hemangioma (HEM) is the most common primary benign FLL. It is a highly vascular benign FLL which is composed of tiny blood vessels. HEMs usually appear as a solitary lesion, but may also be multiple in 10 % of cases. In most of the cases, HEMs are small (< 3 cm) and are found incidentally. In very rare cases, these lesions are symptomatic; but it is sometimes difficult to diagnose these lesions as they can be indistinguishable from MET lesions [184]. They appear in all age-groups but are more frequent in adult females. Once HEMs are detected in adult, they are stable in size, any further change in size and appearance is uncommon. HEMs found in children tend to be large and symptomatic. Many of these HEMs found in children regress with time, while others may have to be emoblized with coils under radiological guidance.

The sonographic appearance of HEMs varies considerably. In 70 % of cases, HEMs encountered in routine clinical practice are *typical HEMs*. These typical HEMs have a characteristic sonographic appearance; it appears as a round, homogeneous, hyperechoic, well defined lesion. These typical HEMs may sometimes exhibit posterior acoustic enhancement due to blood filled capillaries [140]. *Atypical HEMs* are a great mimic and a definite diagnosis with conventional gray scale B-Mode US is difficult. Atypical HEMs can be isoechoic or even hypoechoic mimicking the sonographic appearance of certain atypical MET and HCC lesions

[29]. These atypical HEMs generally cause diagnostic problems as they may appear as hypoechoic lesions or as lesions with mixed echogenicity. Large HEMs (> 3 cm) are often heterogeneous and demonstrate spectrum of reflectivity based on the composition and central areas of degeneration. These large HEMs frequently exhibit slightly increased through-transmission with posterior acoustic enhancement. In case of atypical HEMs, where the diagnosis is not certain and a malignancy is suspected, administration of an ultrasound contrast agent and further imaging like MRI scanning helps to characterize the lesion confidently.

1.1.2.3 *Hepatocellular Carcinoma* (*HCC*)

The *hepatocellular carcinoma* (HCC), also called as malignant hepatoma (liver cancer), is primary malignant FLL [111-113,153]. HCC accounts for 80 to 90 % of all the malignant FLLs, amongst various primary FLLs [38]. The US imaging modality is used world-wide for screening of HCCs. This occurrence of HCC is most common in adult population. It is the fifth most common cancer worldwide and the third leading cause of cancer related deaths [56, 105, 207]. Worldwide, HCCs are detected with an estimated occurrence of 100000 - 300000 new cases per year [18]. The occurrence of HCC is not uniform throughout, with highest occurrence rates in Sub-Saharan Africa and the Southeast Asia. The areas of low occurrence include North America and Northern Europe. Males have higher occurrence of HCC than females.

The risk factors which give rise to development of HCC are (*i*) cirrhosis, (*ii*) chronic infection with the hepatitis B and hepatitis C virus, and (*iii*) metabolic diseases. The symptoms of liver cancer vary among individuals. Many patients with primary liver cancer reveal no symptoms until the cancer develops to an advanced stage [158]. In some cases, jaundice, general feeling of poor health, loss of appetite, weight loss, nausea, fever, fatigue, bloating, itching, swelling of legs, or weakness may be present. In certain cases abdominal pain or discomfort may also occur. It is worth mentioning that these symptoms can be vague and very similar to other diseases and conditions.

In 85 % cases, HCC occurs in patients with cirrhosis. The appearance of HCC on B-Mode US depends mostly on whether or not there is underlying cirrhosis. In fact, in radiology practice, cirrhosis is seen as precursor to development of HCC as the occurrence of HCCs on normal liver is very rare. Detecting *small HCCs* (SHCCs) developed on coarse and nodular cirrhotic liver parenchyma presents a daunting challenge for experienced radiologists. On the other hand, in rare cases when the HCC develops on normal liver parenchyma it can be easily diagnosed from its sonographic appearance, as it appears as a well differentiated HCC or as fibro lamellar HCC (which commonly appears with calcified areas).

The sonographic appearance of a *large HCC* (LHCC) is often inhomogeneous, whereas SHCCs can be hypoechoic and homogeneous [209]. Experienced participating radiologists opined that *no sonographic appearance can be considered typical for HCC as there is a wide variability of sonographic appearances even within SHCCs and LHCCs*. The sonographic appearances of SHCC vary from hypoechoic to hyperechoic. LHCC appear frequently with mixed echogenicity [62, 73, 189, 191].

1.1.2.4 *Metastasis* (*MET*)

The *Metastatic carcinoma* or Metastasis (MET) is the most common secondary malignant FLL. MET is caused by the cancerous cells that spread from the primary cancerous tumors of the other parts of the body. As the liver is the largest solid organ of the human body, it becomes an easy target for occurence of metastatic tumors [11]. Also, since one of the main functions of the liver is to filter blood, cancer cells from other parts of the body may enter the liver and become tumors. MET lesion may be hyper-vascular or hypo-vascular, and small or large, depending upon the site of the primary cancer. Hypo-vascular MET lesions can present central necrotic areas [64]. METs are the most common secondary malignant neoplasms which can originate from many different types of cancer. In the initial stages, MET lesion may be asymptomatic or it may produce symptoms that may not be specific to the disease. For example, symptoms like loss of weight and appetite, fever may be present which is not specific to liver cancer only. It is very difficult to diagnose MET lesion at an early stage. So most of the time, the disease is detected only at an advanced stage. Depending upon the site of the primary tumor, 30 to 70 % patients who die of cancer, have liver metastasis.

Metastatic tumors are common during the late stages of cancer. MET may occur singly or as multiple deposits of varying sizes. The internal texture pattern of MET lesion is often inhomogeneous although the sonographic appearance is variable [209].

The typical characteristic of MET lesion is liquefactive necrosis, producing a fluid centre with an inhomogeneous internal texture pattern. Thus, sonographic appearance of *typical* MET lesion is the *target* or *bull's-eye* appearance (i.e., hypoechoic centre surrounded by a hyperechoic rim).

Atypical MET lesions can appear with extremely variable sonographic appearances ranging from anechoic, hypoechoic, isoechoic, hyperechoic and even with mixed echogenicity. Differentiating atypical MET lesions from certain HEM and HCC lesions is considerably difficult [179].

1.1.2.5 *Malignant Liver Neoplasms*

Among all the malignant FLLs, HCC and MET are considered as most severe malignant liver neoplasms and are responsible for the third most common cause of cancer related deaths worldwide. HCC alone accounts for 1.25 million deaths world-wide because of the presence of large population with hepatitis C virus infection [206, 212]. The diagnosis of these malignant neoplasms can be delayed or completely missed, as most of these present no symptoms until the tumor has progressed to an advanced stage. Additionally, the symptoms, if present, can be extremely vague and similar to other diseases, conditions or disorders. If a patient has symptoms of the liver disease, a medical practitioner performs one or more procedures like physical examination, blood tests, diagnostic imaging, surgical biopsy or laparoscopy [29]. Early detection and accurate staging of liver cancer is an important issue in histopathology and practical radiology.

1.1.3 Ultrasound Imaging

The field of medical imaging and image analysis has evolved due to collective efforts from many disciplines like medicine, engineering and basic sciences. In current medical practice, imaging procedures are one of the major bases for diagnosis apart from other procedures like pathological examinations and biopsy. The overall objective of the medical imaging system is to acquire useful information about the physiological processes of the organs of the human body. The choice of the best imaging technique for any particular clinical application is based on several factors including resolution, speed, convenience, acceptability and safety. As an example, the US imaging modality is ideally suited for imaging the soft tissues, over other techniques accounting for all these factors [3, 4, 93, 119, 194]. The other imaging modalities used for diagnosis of liver diseases include computed tomography (CT) and magnetic resonance imaging (MRI) [54, 71]. The US, CT and MRI are all non-invasive imaging modalities. However, CT uses ionizing radiations, which are otherwise harmful for human body. On the other hand, US don't produce any known harmful effects on any of the tissues examined during clinical practice. The clinical relevance of the US imaging modality is high worldwide due to its versatility, wide spread availability, portability and ease of operation in comparision to CT and MRI.

The US is particularly useful for differentiating between *cystic* and *solid FLLs*, whereas CT and MRI are particularly sensitive for differential diagnosis between solid FLLs [54]. For differential diagnosis between solid FLLs, the radiologists don't rely on US examinations only, because of varying overlapping sonographic appearances between them. Therefore, for

confirming their diagnosis the radiologists resort to administration of contrast agents, or additional imaging procedures (CT and MRI) which are costlier and time consuming, or invasive procedures such as biopsy. Furthermore, the diagnostic information extracted from the US examination is highly operator dependent; but this limitation can be overcome by proper training of the observer. In addition, obese patients can be difficult to scan with US and thus obtaining good quality diagnostic US images for these patients can be considerably difficult. Despite the disadvantages associated with US imaging modality, it is the most preferred option for screening of the liver, especially in the developing countries like India where most of the patients generally come from rural environment who cannot afford the financial burden of radiological procedures which are relatively costlier.

The aim of the present research work is to do value addition in the diagnostic performance obtained by most commonly available conventional gray scale B-Mode US imaging modality for diagnosis of liver diseases.

1.2 Sonographic Appearances of Different Liver Image Classes used in the Present Research Work

The brief details of the sonographic appearances of liver image classes used in the present research work are depicted below:

1.2.1 Sonographic Appearance of Normal Liver

The sample of the Normal liver image from the image database is given in Fig. 1.1.
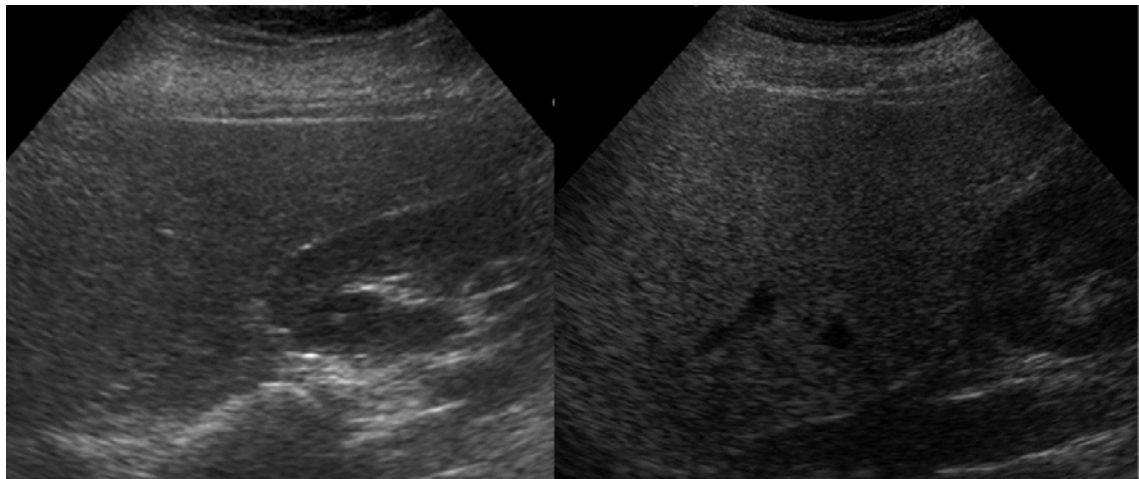
Fig. 1.1 Conventional gray scale ultrasound liver images with appearance of normal liver.
Note: Normal liver exhibits homogeneous echotexture with medium echogenicity.

The sonographic appearance of normal (NOR) liver is homogeneous with slightly increased echogenicity as compared to the right kidney [108, 183 - 187, 191]. The NOR liver appears as a mid gray organ with smooth outlining and homogeneous echotexture because of its uniform acoustic impedance on ultrasound. The smooth liver parenchyma is interrupted by anechoic structures such as vessels (i.e., the hepatic veins, portal veins, hepatic arteries, etc. The capsule of the liver appears hyperechoic especially at its border with the diaphragm. The diaphragm appears as a curvilinear bright reflector. It is difficult to quantify the size of the liver as there are large variations in shape within normal subjects. The size of the liver is therefore assessed subjectively. All the NOR cases are considered as typical as there is no atypical appearance for normal liver tissue.

1.2.2 Sonographic Appearance of Cirrhotic Liver

The sample images of the cirrhotic liver from the image database is given in Fig. 1.2.
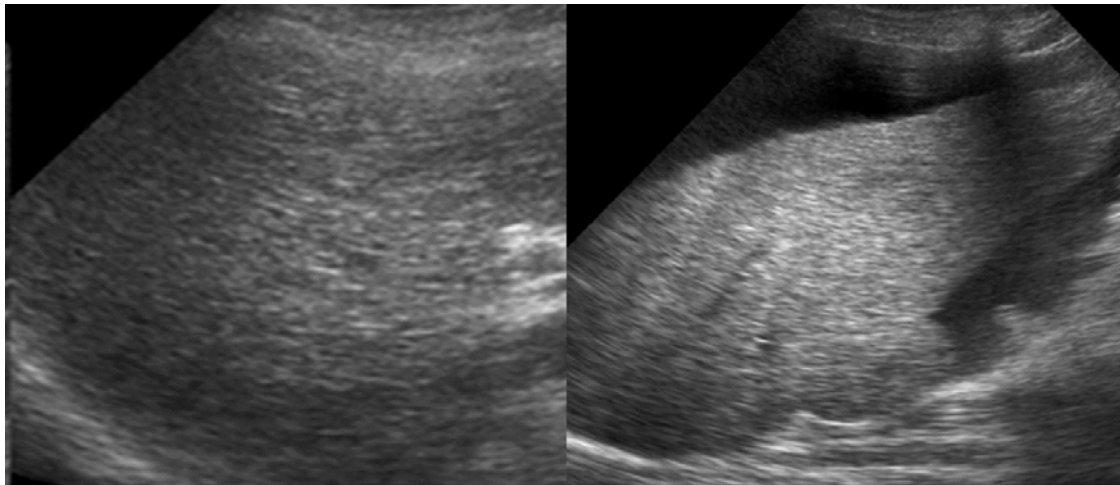
Fig. 1.2 Conventional gray scale B-Mode liver ultrasound images with appearance of cirrhotic liver
Note: Cirrhotic liver exhibits coarse echotexture with diffused uneven nodularity.

The cirrhotic liver exhibits coarse echotexture with diffused uneven nodularity [71, 75, 172]. Variation in size and shape of liver is observed depending upon severity of the liver cirrhosis.

The right lobe is mostly affected by cirrhosis [172]. Cirrhotic liver has relatively large speckles; so the coarseness with respect to normal tissue will be different [213]. It is clinically believed that changes in the process of normal liver progressing towards cirrhosis can be related to echotextural changes in the liver parenchyma [213].

1.2.3 Sonographic Appearance of Typical FLLs

The sample images of typical case of Cyst, HEM and MET lesions from the image database are shown in Fig. 1.3.
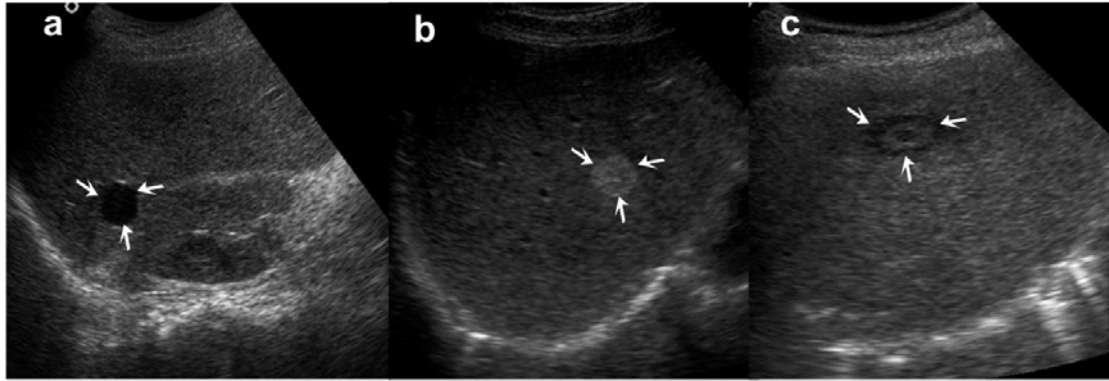
Fig. 1.3 Conventional gray scale ultrasound liver images with appearance of: **(a)** Typical cyst (thin walled anechoic lesion with posterior acoustic enhancement); **(b)** Typical HEM (well circumscribed uniformly hyperechoic appearance); **(c)** Typical MET (*target* or *bull's-eye* appearance i.e. hypoechoic centre surrounded by a hyperechoic rim).

Typical cyst appears as round, anechoic lesion with posterior acoustic enhancement and well defined thin imperceptible wall. Typical HEM always appears as a well circumscribed uniformly hyperechoic lesion. The typical sonographic appearance of MET lesion is the *target* or *bull's-eye* appearance (i.e., hypoechoic centre surrounded by a hyperechoic rim) [188, 190].

1.2.4 Sonographic Appearance of Atypical FLLs

The sample images for atypical case of Cyst, HEM and MET lesion are shown in Fig. 1.4.
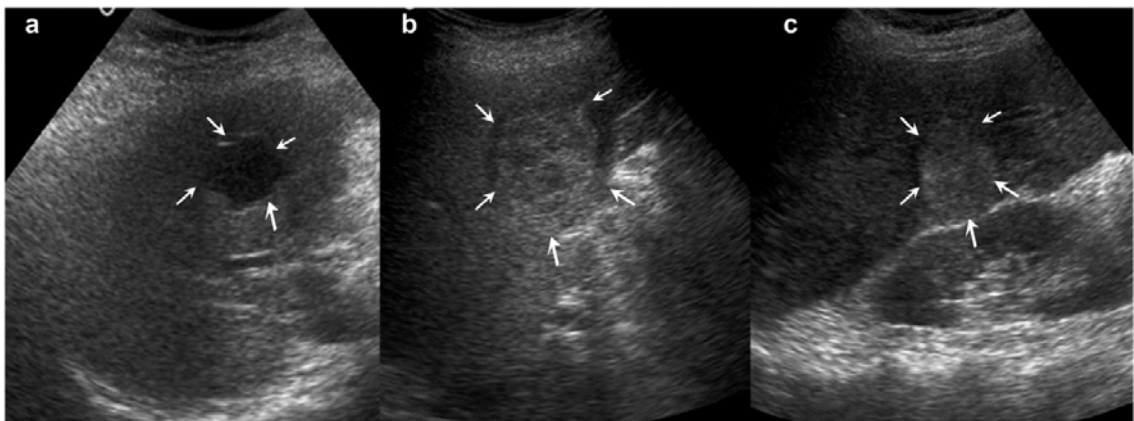
Fig. 1.4 Sample image variants of with appearance of : **(a)** Atypical cyst with internal echoes and irregular walls; **(b)** Atypical HEM with heterogeneous echotexture; **(c)** Hyperechoic atypical MET with heterogeneous echotexture.

Atypical cysts always appear with internal echoes and thickened irregular walls. Differential diagnosis of cystic metastasis and atypical cyst from conventional gray scale B-

Mode US can be quite challenging. Atypical HEMs are a great mimic and definite diagnosis with conventional gray scale B-Mode US is difficult [104]. Atypical HEMs can be isoechoic or even hypoechoic mimicking the sonographic appearance of certain atypical MET and HCC lesions. Atypical MET lesions can appear with extremely variable sonographic appearances ranging from anechoic, hypoechoic, isoechoic, hyperechoic and even with mixed echogenicity. Differentiating atypical MET lesions from certain HEM and HCC lesions is considerably difficult [188, 190]. Sonographic Appearance of Small and Large HCCs

1.2.5 Sonographic Appearance of Small and Large HCCs

The sample images of SHCC and LHCC cases from the image database are shown in Fig. 1.5.
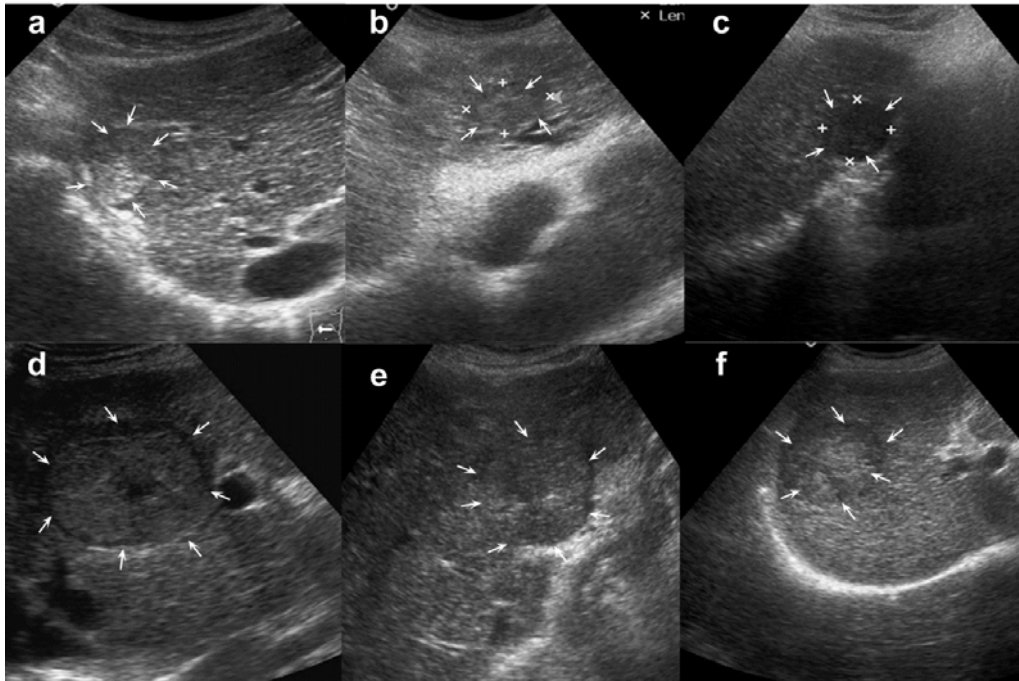
Fig. 1.5 Sample images of SHCC and LHCC variants from the image database: **(a)** Variant of SHCC with mixed echogenicity (coexistence of hyper-echoic and iso-echoic areas); **(b)** Isoechoic SHCC; **(c)** Hypoechoic SHCC; **(d-f)** Heterogeneous echotexture represents complex and chaotic structure exhibited by LHCC due to coexistence of areas of necrosis, fibrosis and active growth areas.
Note: Hypoechoic halo formation is visible in **(d)**, Necrotic area is visible at centre of LHHC in **(d)**.

The sonographic appearances of Small HCC (SHCC) vary from hypoechoic to hyperechoic. Large HCC (LHCC) appears frequently with mixed echogenicity [62, 73, 188 - 191]. Experienced participating radiologists opined that *no sonographic appearance can be considered typical for HCC* as there is wide variability of sonographic appearances even within small HCCs (SHCCs) and large HCCs (LHCCs).

1.3 Need For CAD Systems for Liver Diseases using B-Mode Ultrasound Images

The evolution of computer technology, medical image processing algorithms and artificial intelligence techniques have given ample opportunity to researchers to investigate the potential of computer-aided diagnostic systems for tissue characterization [54, 146, 176, 192]. Tissue characterization refers to quantitative analysis of tissue imaging features resulting in accurate distinction between normal and abnormal tissues. Thus, the result of tissue characterization is interpreted using numerical values. The overall aim of developing a computerized tissue characterization system is to provide additional diagnostic information about the underlying tissue which cannot be captured by visual inspection of B-Mode US images [210].

Ultrasonographic tissue characterization methods based on physical tissue models have been shown to be useful for improving the diagnostic accuracy of sonograms [2, 78]. Unfortunately, no physical model based diagnostic system have been developed for characterization of FLLs probably because these systems have been developed assuming single, homogeneous tissue model, whereas in case of FLLs the variability in sonographic appearances within different lesions is quite large and quite often large HCCs and MET lesions are inhomogeneous [209].

For viable and useful sonographic characterization of FLLs, radiologists need to extract subtle sonographic information which may be difficult to extract visually, consistently and objectively [209]. It is, therefore, expected that sophisticated computerized analysis of the texture patters of FLLs can yield objective characterization of lesions [209].

1.4 Objectives of the Present Study

The main objective of the research work presented in this thesis is to enhance the diagnostic potential of conventional gray scale B-Mode ultrasound for diagnosis of liver diseases by developing efficient CAD system designs using a comprehensive and representative image database. To achieve this, various research objectives were formulated according to the needs of the radiologists, based on the practical difficulties faced by them in routine clinical practice. These research objectives are described below:

(*i*)   *The collection of a comprehensive and representative image database*: In order to develop efficient and robust classifier designs, it is necessary to train the classifiers with a comprehensive image database with representative images from each subclass. Thus, collection of a comprehensive image database with representative cases from each class,

including (*a*) normal liver, (*b*) cirrhotic liver, (*c*) typical and atypical cases of cyst, HEM and MET lesions and (*e*) small as well as large HHC cases is taken up as the first objective of the present research work.

(*ii*) *The design, development and implementation of an efficient CAD system for normal and cirrhotic liver using B-Mode US images*: Liver cirrhosis, characterized irreversible hepatic fibrosis is the end stage of chronic diffuse liver disease which is considered as precursor to development of hepatocellular carcinoma (HCC), a primary malignant FLL. Therefore, it is understood that liver cirrhosis can be fatal if not diagnosed early, and it is believed that a CAD system for prediction of liver cirrhosis can support radiologist in better management of disease and adequate scheduling of treatment options. Therefore, design of a CAD system for classification between normal and cirrhotic liver is taken up as the next objective of the present research work.

(*iii*) *The design, development and implementation of an efficient CAD system for normal, cirrhotic and HCC liver using B-Mode US images*: In radiological practice, it is always considered difficult to diagnose, small FLLs (< 2 cm) developed on already nodular and coarse textured cirrhotic liver parenchyma. Experienced participating radiologists opined that in very rare cases, when HCC develops on normal liver parenchyma it can be easily diagnosed, but diagnosis of SHCC on cirrhotic liver parenchyma is considerably difficult. Thus, in order to monitor the progress of the disease from cirrhosis towards HCC, it is necessary to know whether the textural changes in the liver parenchyma are cirrhotic changes or indicate development of HCC. Therefore, the design of an efficient CAD system for characterization of normal, cirrhotic and HCC liver by using a comprehensive and representative image database consisting of (*a*) normal (*b*) cirrhotic and (*c*) SHCC and LHCC cases developed on cirrhotic liver, is taken up as the third objective of the present research work.

(*iv*) *The design, development and implementation of an efficient CAD system for primary and secondary malignant liver lesions using B-Mode US images*: The sonographic characterization of hepatocellular carcinomas (HCCs) and metastatic carcinomas (METs) presents a daunting challenge for radiologists, due to their highly overlapping sonographic appearances. As the characterization of malignant liver lesions as HCC or MET lesion is clinically significant for effective treatment and management of liver malignancies, the design of an efficient CAD system for binary classification between HCC and MET lesions by using a comprehensive and representative image database

consisting of (*a*) SHCC and LHCC cases and (*b*) typical and atypical MET cases, is taken up as the fourth objective of the present research work.

(*v*) *The design, development and implementation of an efficient CAD system for focal liver lesions using B-Mode US images*: Radiologists easily diagnose typical FLLs by their classic sonographic appearances; however, the differential diagnosis between atypical FLLs from B-Mode US images is quite challenging task faced by radiologist in routine practice, mainly due to the existence of overlapping sonographic appearances even within individual classes of atypical FLLs. Even then, B-Mode US is considered as preferred examination for characterization of FLLs, mainly due to its noninvasive, nonradioactive, inexpensive nature and real-time imaging capabilities. Therefore, a CAD system for classification of FLLs from B-Mode US images is highly desired. At the same time, it is worth mentioning that there are certain disadvantages associated with the use of conventional gray scale US for characterization of FLLs, namely, (*a*) limited sensitivity for detection of small FLLs (< 2 cm) developed on cirrhotic liver which is already nodular and coarse-textured [16, 20, 62, 73, 191], (*b*) sonographic appearance of HCC and MET lesions which are highly overlapping [16, 20, 62, 73, 152, 189], (*c*) sonographic appearances of cystic metastasis and atypical cyst which is often overlapping [16, 62], (d) sonographic appearances of atypical HEM, sometimes mimic with atypical MET and HCC, [21, 73, 179, 114, 209], and (*e*) difficulty to characterize isoechoic lesions with very slim difference in contrast between region inside the lesion and the surrounding liver parenchyma in some cases [114, 189].

Thus, the design of an efficient CAD system for FLLs using a comprehensive and representative image database consisting of (*a*) typical and atypical cases of Cyst, HEM and MET lesions, (*b*) SHCC as well as LHCC cases, and (*c*) NOR liver cases, is taken up as the fifth objective of the present research work.

(*vi*) *The design, development and implementation of an efficient hierarchical CAD system for focal liver lesions using B-Mode US images*: The CAD system designs with hierarchically placed classifiers provide the possibility to go stepwise from the general classification problem, normal versus abnormal liver tissue to the more particular classification problem, which is the identification of exact liver abnormality. Such a hierarchical design of CAD system is analogous to biological system where sequentially placed layers of physiological neurons are arranged in a hierarchical manner in order to solve complex problems in a stepwise manner.

13

The design of hierarchical classifier is based on the idea of splitting the original problem of classifying the liver tissue in five classes into four sub-problems (*i*) diagnosis between normal healthy liver tissue and abnormal liver tissue, (*ii*) diagnosis of abnormal liver tissue into Cyst and other lesion (OL) classes, (*iii*) diagnosis of liver tissue belonging to OL class as HEM (PBL) or malignant lesion (ML), and (*iv*) diagnosis of malignant lesion as HCC (PML) or MET (SML) classes. To develop an efficient hierarchical CAD system with texture features computed from regions inside and outside the lesions for diagnosis of FLLs using B-Mode liver ultrasound images is taken up as the sixth objective of the present research work.

(*viii*) *The design, development and implementation of a neural network ensemble (NNE) based CAD system for FLLs using B-Mode US images*: In human society, many experts each specializing in a particular task, meet to overcome a complicated problem in order to reach at a decision in a collective manner which is expected to be a better solution than can be given by an individual expert. Therefore, in the area of medical decision making as well, CAD system frameworks using ensemble of classifiers are expected to yield better results in comparision to the CAD system frameworks build upon single multi-class classifier designs. Thus, the design of an efficient CAD framework based on ensemble of classifiers for FLLs using B-Mode liver US images is taken up as the seventh objective of the present research work.

1.5 Organization of Thesis

This thesis report is organized into ten chapters, as described below.

(*i*) *Chapter* 1 lays the foundation as to why 'Analysis and Classification of B-Mode Liver Ultrasound Images' is clinically significant. It begins with documenting facts like why liver diseases are considered seriously? What types of liver diseases are most common? How these diseases affect the sonographic appearance of the liver tissue? Why B-Mode ultrasound examination is considered as primary choice for diagnosis of liver diseases? What are the problems faced by the radiologists for diagnosis of liver diseases using B-Mode ultrasound which are encountered in clinical practice? Why there is a need to develop efficient CAD systems for diagnosis of liver diseases using B-Mode US images? What are the objectives of the present research work? How these objectives were formulated? To conclude, the content documented in this chapter provides the basic

motivation regarding the fact that computer vision for liver US images can enhance the diagnostic potential of B-Mode US imaging modality.

(*ii*) *Chapter* 2 presents a brief literature review of the other related studies for diagnosis of liver diseases using B-Mode ultrasound images.

(*iii*) *Chapter* 3 lays the foundation of research methodology followed for undertaking this research work. The importance of medical ethics, while working with clinical human data is highlighted. The Chapter introduces the readers, to various set of protocols followed for undertaking this research work, i.e., the protocols followed for collection of comprehensive and representative image database, for assessment of images, for selection of ROIs, for selection of ROI size, for bifurcation of dataset into training dataset and testing dataset. Thus, the complete description of dataset used in the present research work is described in this Chapter.

(*iv*) *Chapter* 4 gives a detailed description of exhaustive experimentation carried out for design of an efficient CAD system for characterization of normal and cirrhotic liver tissue.

(*v*) *Chapter* 5 provides description of the proposed CAD system for characterization of normal, cirrhotic and HCC liver tissue.

(*vi*) *Chapter* 6 describes the details of the proposed CAD system for characterization of primary and secondary malignant liver lesion.

(*vii*) *Chapter* 7 gives detailed description of exhaustive experimentation carried out in the present work in order to design an efficient CAD system for focal liver lesions using single multi-class classifier design.

(*viii*) *Chapter* 8 reports the experimentation carried out to design an efficient hybrid hierarchical CAD (HCAD) system for focal liver lesions using hierarchically placed classifiers.

(*ix*) *Chapter* 9 gives the detailed description of design of the proposed neural network ensemble (NNE) based CAD system for focal liver lesions using B-Mode US images.

(*x*) *Chapter* 10 summarizes the conclusions drawn from the exhaustive experimentation carried out in the present research work on "Analysis and Classification of B-Mode Liver US Images". The future directions in which the work can be extended are also reported in this Chapter.

Literature Review

2.1 Introduction

Medical imaging provide effective mapping of the anatomy of human body. The analysis of the patterns exhibited by the biological tissues through their images have been in routine clinical use for diagnostic purposes, as different tissue pathological conditions produce different image patterns. With the rapid development and proliferation of medical imaging technologies, the role of medical imaging has expanded beyond the simple visualization and inspection of anatomical structure. Computer assistance in medicine is widely used for analysis and classification of biomedical signal and images for diagnostic purposes [19, 22, 24, 30, 45, 72, 80, 81, 86, 87, 125, 131, 132, 139, 143, 156, 157, 176, 198, 212]. The medical image analysis community has become preoccupied with the challenging problem of extracting clinically useful information of anatomic structures from images obtained through X-ray, CT, MRI, positron emission tomography (PET), ultrasound and other modalities [16, 20, 33, 62, 73, 121, 122, ,126, 134, 159, 162, 181, 211, 212]. These imaging modalities provide exceptional views of internal anatomy and the experienced radiologists quantify and analyze the embedded structures. However, manual analysis, i.e., visualization of medical images by trained radiologists is often time consuming process besides being susceptible to human errors depending upon one's expertise. To overcome the bottlenecks associated with manual analysis, the need for computer-assisted approaches to analyze these images has been visualized by the medical professionals and this has resulted in increased application of computer–assisted medical imaging in the clinical diagnosis and research [203].

The medical imaging modalities depend heavily on computer technology for creation and display of images. Using the computer, multidimensional digital images of physiological structures can be processed and manipulated to visualize hidden characteristic diagnostic features that are difficult to observe. Further, these features of interest can be quantified and analyzed using sophisticated computer programs and models to understand their behavior to help in diagnosis or to evaluate treatment protocols. In many critical radiological applications, the visualization and quantitative analysis of physiological structures provide unprecedented clinical information that is extremely valuable for diagnosis and treatment. The computerized processing and analysis of medical images provides a powerful tool to help physicians in this regard. The ability to improve diagnostic information from medical images can be further enhanced by designing computer- processing algorithms intelligently.

Thus, evolution of medical image processing and artificial intelligence techniques have given ample opportunity to researchers to investigate the potential of computer-aided diagnostic systems for characterization of tissues [54, 71].

Tissue characterization refers to quantitative analysis of tissue imaging features resulting in accurate distinction between normal and abnormal tissues. Thus, the result of tissue characterization is interpreted using numerical values. The overall aim of developing a computerized tissue characterization system is to provide additional diagnostic information about the underlying tissue which cannot be captured by visual inspection of images [210].

This chapter presents a review of published literature on CAD systems for: (*i*) prediction of liver cirrhosis, (*ii*) for characterization of normal, cirrhotic and HCC Liver and, (*iii*) for characterization of FLLs using B-Mode US images.

2.2 CAD Systems for Prediction of Liver Cirrhosis

As cirrhosis increases the risk for development of HCC, which is the leading cause of mortality by the disease, there is a significant interest among researchers to develop CAD systems for classification between normal and cirrhotic liver tissue [100]. Imaging modalities like US, CT and MRI can be used for diagnosis of cirrhotic liver. MRI has more diagnostic potential than CT and US for accurate characterization of liver cirrhosis. However, US is always considered as a first line examination for evaluation of liver tissue because of its undisputed advantages over CT and MRI. Thus, CAD system designs for binary classification between normal and cirrhotic liver by using B-Mode liver US images have been proposed in few studies in the literature [67, 101, 118, 183, 184, 185, 192, 213] whereas, other related studies have proposed a CAD system for classification between normal healthy liver tissue and different grades of cirrhotic liver using B-Mode liver US images [26, 75, 168]. Mojsilovic *et al*. [118] experimented classification between normal and cirrhotic liver tissue by using various sets of texture descriptors and an Euclidean distance classifier. They considered energy, entropy, inertia and cluster shade amongst the GLCM (Gray-level co-occurrence matrix) texture features for different values of inter-pixel distance $d = [2,…,12]$ and angle values [$\theta =$ 0°, 45°, 90°, 135°] and reported the classification accuracy of 75 % with Euclidean distance classifier. For Laws' TEM (texture energy measures) method the first order, second order and higher order statistics evaluated from texture energy images obtained by convolution with 12 Laws' masks the classification accuracy of 70 % is reported by using Euclidian distance classifier. By using statistics calculated from pyramidal wavelet image decomposition and a

18

Euclidean distance classifier the classification accuracy of 85 % is reported. By using statistics derived from tree-structured wavelet image decomposition and a Euclidean distance classifier the classification accuracy of 92 % is reported. However, their study reports the classification accuracy of 92 % by using statistics derived from their proposed 2N×1-DWT image decomposition and a Euclidean distance classifier. Their study highlighted the disadvantages of using standard wavelet decomposition schemes and reported that their proposed 2N×1-DWT decomposition is better for texture characterization. However, the classification accuracy of 92 % was obtained with both, tree structured wavelet transform and their proposed 2N×1-D wavelet transform, but it has been highlighted that in their study that 2N×1-DWT is more computationally efficient algorithm. Huang *et al*. [67] firstly preprocessed the normal and cirrhotic liver US images by wavelet denoising and wavelet packet denoising methods before feature extraction and classification. Their study reported the use of four GLCM texture descriptors, i.e., four directions mean statistic of angular second moment (ASM), contrast, entropy and inverse difference moment (IDM) features extracted from preprocessed images along with a probabilistic neural network (PNN) classifier for achieving binary classification between normal and cirrhotic liver. For comparision they also experimented classification by using Gray level difference histogram statistics (GDHS) extracted from preprocessed images along with PNN classifier. For GLCM statistics derived from images preprocessed by wavelet denoising method their study reports correct classification rate of 82.5 % for both normal and cirrhotic image classes. For GLCM statistics derived from images preprocessed by wavelet packet denoising method, their study reports classification accuracy of 85 % and 87.5 % for normal and cirrhotic images, respectively. For GDHS features derived from images preprocessed by wavelet denoising method their study reports classification accuracy of 77.5 % and 72.5 % for normal and cirrhotic image classes. For GDHS features derived from images preprocessed by wavelet packet denoising method their study reports correct classification rates of 80 % and 75 % for normal and cirrhotic images, respectively. They concluded that higher classification accuracy can be achieved by preprocessing the images using wavelet packet denoising and using GLCM statistics along with PNN classifier for achieving binary classification between normal and cirrhotic liver.

Lu *et al*. [101] designed a CAD system for classification between normal and cirrhotic liver by capturing the variations of echotexture in normal and cirrhotic liver with respect to the echo texture of accompanying spleen. Their study reports, exhaustive experiments carried out with features derived from liver, features derived from liver and accompanying spleen and the effect of including fractal dimension feature on classification between normal and cirrhotic

liver. They reported the classification accuracy of 94.7 % by using combined feature set consisting of features extracted from liver regions only and features derived from liver and accompanying spleen (i.e., the ratio features, value of feature derived from liver region / value of feature derived from spleen region) as well as fractal dimension feature with feature space dimensionality reduction by using principal component analysis (PCA) and classification by using classification trees.

Wan and Zhou, [192] attempted to classify normal and cirrhotic liver by using mean and energy texture features estimated from ten sub-band images obtained as a result of third level decomposition of the region of interest (ROI) by 2D-DWT with db4 wavelet filter resulting in a feature set of length 20. Their study also reports the use of mean and energy texture features derived from 16 sub-band images obtained as a result of second level decomposition of ROI by 2D-WPT with db4 wavelet filter resulting in a feature set of length 32, for the binary classification task. The study reports the use of various feature ranking methods, like hypothesis test, fisher discriminant ratio (FDR) and ROC curves and various feature subset selection methods based on class seperability criteria, such as divergence, Bhattacharya distance and scatter matrix related criterion, for feature selection. The study reports the use of selected 2D-DWT and 2D-WPT features along with support vector machine (SVM) classifier for achieving binary classification between normal and cirrhotic liver. Their study concluded that 2D-WPT features can better discriminate normal and cirrhotic liver in comparision with 2D-DWT features with the classification accuracy of 85.7 % and 77.6 %, respectively as obtained with support vector machine classifier using Leave one out (LOO) cross validation procedure.

Virmani *et al.* [185] reported the use of GLCM-Mean and GLCM-Range texture features computed for inter pixel distance $d = [1, 2, 3\ 4]$ individually along with a neural network (NN) classifier for classification between normal and cirrhotic liver tissue. The study reports the highest classification accuracy of 95.8 % with four directional GLCM-Mean texture features computed for $d = 2$. Among the GLCM-Range texture features the highest classification accuracy of 94.2 % has been observed for with GLCM-Range features computed for $d = 4$. Further, experiments carried out in the study indicate that all the four directional GLCM-Mean features computed for $d = 2$ yielding the highest classification accuracy of 95.8 % are not significant for the classification task. The correlation based feature selection (CFS) method yield that only seven GLCM-Mean features, i.e., angular second moment (ASM), contrast, variance, sum average, entropy, difference entropy and information measures of correlation-1

are least correlated to each other and most correlated to the class variable. These seven GLCM-Mean selected features yielded the classification accuracy of 95 % using a NN classifier. Further, experiments were carried out by singular value decomposition (SVD) of four directions GLCMs obtained for $d = 2$. The mean of the first two singular values obtained after SVD of GLCMs corresponding to normal and cirrhotic ROIs were used as features for classification with NN classifier. It was observed that the mean of the first two characteristic singular values yielded the classification accuracy of 95 % for characterization of normal and cirrhotic liver. The study reports that features computed by SVD of GLCM yield a computationally efficient system for characterization of normal and cirrhotic liver tissue.

Virmani *et al*. [183] attempted binary classification between normal and cirrhotic liver by features derived from Laws' masks analysis. The study reports the use of CFS technique for determining the features which are least correlated to each other and most correlated to the class variable. The SVM and NN classifiers have been used for the classification task. Mean standard deviation, skewness, kurtosis and energy statistics were initially computed from 15 rotation invariant texture energy images, resulting in a feature set of seventy five texture features for each ROI. CFS method yielded an optimal subset of eight discriminatory Laws' texture features which were inputted to the NN and SVM classifiers. The study reports the classification accuracy of 91.7 % and 92.5 % with NN and SVM classifiers. The results of the study demonstrate that only eight Laws' texture features are adequate to account for textural variations exhibited by normal and cirrhotic ROIs.

Virmani *et al*. [184] reports the use of first order statistics (FOS), i.e., average gray level, standard deviation, smoothness, skewness, entropy and uniformity texture features along with NN classifier for classification between normal and cirrhotic ROIs. The study reports the classification accuracy of 93.3 % with six FOS features and a NN classifier. The CFS method yielded three discriminatory FOS features, i.e., average gray level, standard deviation, and uniformity which were found to be least correlated with each other and most correlated with the class variable. The classification accuracy of 92.5 % is reported by using these FOS features along with NN classifier. The study proposed a liver state index (LSI) which was obtained by the three FOS features selected by CFS method. It was demonstrated that if the value of the LSI statistic is more than three the ROI belongs to normal class, otherwise and if the LSI statistic is less than or equal to the threshold value of three the ROI is labeled as belonging to cirrhotic class. It is documented that LSI statistic can be used for rapid prediction of cirrhosis as it can

be computed on the fly as soon as the radiologist marks the ROI. Therefore the LSI statistic can be used as a second opinion tool for prediction of cirrhosis in a clinical environment.

Zhou *et al*. [213] used features extracted from M-Mode and B-Mode ultrasound images along with fusion of selected features using sequential forward search (SFS) method and classification using fisher linear decision rule to develop a CAD system for binary classification between normal and cirrhotic liver. The study reports the use of texture features including first order statistics (i.e., mean, variance, skewness and kurtosis), gray level run length statistics (run percentage), gray level difference statistics (mean of adjacent pixels gray level difference statistics) derived from B-Mode US images of normal and cirrhotic liver. The study also reports the use of features derived from motion curve (i.e., amplitude and standard deviation of the motion curve) obtained from M-Mode ultrasound images of normal and cirrhotic liver. To obtain a subset of discriminatory features the sensitivity analysis of each feature was carried out by SFS technique and most sensitive features were fused for use with fisher linear discriminant classifier. Their study demonstrates that 100 % classification accuracy can be achieved by using a combined feature subset of 20 selected features. However, their experiments have been carried out on a limited and unbalanced dataset, i.e., total 43 ROIs (13 cirrhotic and 30 normal) and their methodology requires both the M-Mode and B-Mode image of the patient to be acquired.

Jeong *et al*. [75] attempted classification between normal and cirrhotic liver by calculating the representative coarseness level (RCL) parameter which is computed from texture features computed from the liver region and texture feature computed from the spleen region. The RCL parameters use in this study includes texture features such as edge density, GLCM features, run length matrix features, statistical feature matrix (SFM) features, and difference histogram variation based features. The linear combination of these computed RCL parameters were used to define a classifier for predicting the degree of severity of liver cirrhosis. For determining the coefficients the use of simple Levenberg-Marquardt minimization as training step is reported. The study demonstrates good quantitative correlation of classifier performance with the clinical diagnosis for normal and cirrhotic liver classes.

Sun *et al*. [168] experimented, classification between normal liver tissue and different grades of cirrhosis including type-1 cirrhosis (i.e., cirrhosis with grade 1), type-2 cirrhosis (i.e., cirrhosis with grade 2) and type-3 cirrhosis (i.e., most serious case). The study reports the preprocessing the US images by fast discrete wavelet transform (FDWT) to cut down the size of patterns fed to the three layer NN based on the back-propagation method. The study

demonstrates the use of information located in LL band indicating that after sub-band decomposition of the US image, nearly seventy five percent of the energy is concentrated in the LL band and only little energy exists in LH band and practically no features lie in HL and HH bands. However, the study reports the drawback of conventional multilayer NN classifier, highlighting that data carried by the last hidden layer doesn't utilize the information carried by the input data fully. The study reports improvement in results by first preprocessing the B-Scan patterns with wavelet transform and then feeding the compressed data into a pyramid neural network to diagnose the severity of cirrhosis. The results of the study indicate that the proposed CAD system using pyramid neural network results in better diagnosis especially for diagnosis between normal liver tissue and type-1 cirrhosis in comparision with the CAD design using traditional multilayer NN classifier.

Cao *et al*. [26] experimented classification between normal healthy liver tissue and fibrosis (fibrosis is a precursor for development of cirrhosis), since fibrosis is reversible, so it is clinically significant to detect fibrosis at an early stage. The study reports the effect of varying scanning parameters (US machine settings) on classification results. The images of the normal subjects and patients with liver fibrosis were acquired under different imaging conditions such as, by varying emission frequency as 2.5, 3.5, 4.5 and 7 MHz, and by gain from 95 to 170 in addition different TGC settings were also taken into account. The study experimented classification using linear fisher classifier and SVM classifier using the joint feature set consisting of fractal dimension (FD) and entropies of texture edge co-occurrence matrix. The results of the study indicate that while FD changes significantly with change in US machine settings, the entropy values are not sensitive to change in US machine settings. The classification accuracy obtained by using entropy features is much more satisfactory in comparision with classification accuracy obtained using FD features.

Yeh *et al*. [208] experimented, classification between normal liver tissue and different grades of fibrosis by using features derived from GLCM and non-separable wavelet (NSW) transform along with SVM classifier. Their study reports fibrosis grading into six classes, i.e., from 0 to 5, 0 being normal liver tissue and 5 being severe cirrhosis. The labels of the classes were determined by histological examination. The study experimented classification by dividing the dataset into two, three, four, five and six classes, respectively. The classification accuracy values obtained for two classes, three classes, four classes, and five classes with SVM classifier are 91 %, 85 %, 81 % and 72 %, respectively. Thus their study indicates that the performance of their proposed CAD system decreases as the number of classes increases.

Mitrea *et al.* [109] proposed a CAD system for classification between normal, hepatitis and cirrhosis liver US image classes based on GLCM and fractal dimension features and *k*-nearest neighbor classifier.

Wu *et al.* [202] experimented, the design of a CAD system for distinction between six grades of cirrhosis from B-Mode liver US images based on evolutionary feature construction and automatic ROI selection. The work reports the use self organization properties of genetic algorithm (GA) for automatic selection of ROIs and evolutionary optimization properties of GA for building the feature set. The images are first filtered by Gaussian filter so that the speckle noise is removed without destroying the speckle pattern of the ROI. In the feature extraction module, the GLCM and fractal dimension features are computed from ROIs and SVM is used as classifier. The study highlights the use of GA to optimize the selection of ROIs and to obtain stable parameters for the SVM classifier. The study reports improved classification results in comparison with other related studies including [26, 109, 208].

2.3 CAD Systems for Characterization of Normal, Cirrhotic and HCC Liver

Differentiating the texture patterns exhibited by hepatocellular carcinoma (HCC) developed on cirrhotic liver from its preceding stage of cirrhosis presents a daunting challenge for radiologists, as high variability exists in terms of echo patterns, i.e., texture, even within small HCCs (SHCCs). These SHCCs frequently appear as hypoechoic nodule, (i.e., solid tumor nodule without necrosis) or as hyperechoic nodule (i.e., solid tumor likely containing fat). In very few cases, SHCCs can also be isoechoic (i.e., same echogenicity as that of surrounding liver parenchyma). The HCC lesion may also exhibit hyperechoic echotexture with a hypoechoic halo (i.e., rim like structure surrounding HCC lesion) or alternatively hypoechoic echotexture with hyperechoic halo sign. Thus, the visual appearance of HCCs on ultrasonography examination offers a high degree of variability and therefore the subjective diagnosis of SHCC during screening is a difficult task even for experienced radiologists. The study in [34] reported, 64 % sensitivity for detecting SHCCs using B-Mode US images. Large HCCs (LHCCs) appear much more complex and heterogeneous with mixed echogenicity (i.e., coarse irregular internal echoes) as a result of areas of necrosis, fibrosis as well as active growth areas.

In study [62], it has been reported that US has limited sensitivity for detection of lesions in cirrhotic liver, though contrast enhance ultrasonography (CEUS) improves the sensitivity to 85 % for HCC lesions greater than 1 cm.

Given the fact that there is high variability between sonographic appearances of HCC lesions and especially the fact that the SHCC lesions are quite difficult to diagnose in already nodular cirrhotic liver parenchyma there has been a significant zeal in the research community to design a CAD system for characterization of normal, cirrhotic and HCC liver image classes. Brief details of CAD systems proposed in literature for characterization of normal, cirrhotic and HCC liver from B-Mode US images are given in Table 2.1.

Table 2.1 *Brief details of CAD systems proposed in literature for characterization of normal, cirrhotic and HCC liver*

	Dataset Description				*Classification Performance: SVM*			
Author's	*Patients*	*Images per class*	*No. of ROIs*	*ROI Size*	ICA_{NOR}(%)	ICA_{CIRR}(%)	ICA_{HCC}(%)	*OCA*(%)
Wu *et al.* [200]	45	15	90	32×32	86.6	100	83.3	90.0
Wu *et al.* [199]	-	-	90	30×30	80.0	90.0	93.3	87.8
Le *et al.* [97]	-	-	150	64×64	92.0	100	96.0	96.0
Le *et al.* [95]	-	-	432	64×64	100	91.5	94.5	95.3

Note: ICA: Individual class accuracy, OCA: Overall classification accuracy.

Wu *et al.* [200] compared the performance of traditional feature extraction methods like spatial gray level dependence matrix (SGLDM), Fourier power spectrum (FPS), gray level difference statistics (GLDS), Laws' texture energy measures (TEM) along with bayes classifier for classification of liver tissue as normal, cirrhotic or HCC. The experiments carried out in this study indicate that these traditional texture feature extraction methods reports low classification accuracy. The study highlights the use of multiresolution texture descriptors, i.e., fractal dimension (roughness) and lacunarity (granularity) of sub-images obtained at various resolution levels for characterization of normal, cirrhosis and HCC liver [200]. The study reports exhaustive experimentation using various combinations of multiresolution texture descriptors along with traditional texture feature extraction methods for the classification task. The results of the study indicate that 90 % classification accuracy can be achieved by using the combination of roughness and granularity texture descriptors computed at various resolutions along with FPS based features by using bayes classifier.

Wu and Chen [199] proposed multi-threshold dimension feature vector along with k-NN classifier for characterization between normal, cirrhotic and HCC liver. The features used in this study are reported to be invariant to geometric transformation and linear gray level transformation and yield the classification of 88 % for distinction between normal, cirrhotic and HCC liver. The study also reports the comparision of the results obtained with multi-threshold dimension feature vector with the feature vector consisting of 12 SGLDM features along with kNN classifier. It was observed that SGLDM features yield lower classification accuracy of 78.9 % for the classification task.

Lee *et al*. [97] used multiresolution fractal feature vector based on M-band wavelet transform instead of fractal feature vector based on standard pyramidal wavelet transform as used in study [200]. The study reports the use of two statistical classifiers (i.e., bayes classifier and k-nearest neighbor classifier) and there different artificial neural networks (i.e., back propagation neural network, probabilistic neural network and modified probabilistic neural network) for the classification of liver tissue into normal, cirrhotic and HCC classes. The exhaustive experiments carried out in their study, indicates that by using statistical classifiers the classification accuracy of 90.7 % and by using artificial neural networks the classification accuracy of at least 92 % is obtained for the classification task. The study reports the design of CAD system using fractal feature vector based on M-Band wavelet transform along with artificial neural network as an attractive alternative for the classification task.

Lee *et al*. [96] used the same multiresolution fractal feature vector based on M-band wavelet transform for design of hierarchical CAD using bayes classifier for classification of normal, cirrhotic and HCC liver. The first binary classifier yields classification accuracy of 92.2 % for distinction between normal and abnormal liver (i.e., by considering cirrhotic and HCC liver as abnormal liver class). The second binary classifier which provides classification of abnormal class as cirrhotic or HCC liver yielded the classification accuracy of 93.6 % for the classification task.

Lee *et al*. [94] used the same multiresolution fractal feature vector based on M band wavelet transform as used in [96, 97], but important modification was in the method of determining the fractal dimension. The study reports the drawback of box counting algorithm for determining the fractal dimension and highlights that the estimation errors in computing the fractal dimension due to presence of speckle noise inherent in ultrasound images can be overcome by their proposed modified box counting method. The results of the study indicate, that the classification accuracy for characterization of liver tissue as normal, cirrhotic and HCC

is enhanced to 95 % by their robust and efficient approach to compute fractal dimension instead of the standard box counting method along with the use of bayes classifier.

The study in [95] reported the use of same fractal feature vector obtained by computing the fractal dimension at various resolutions using M-band wavelet transform as used in the previous researches [94, 96, 97]   along with fusion of four classifiers, i.e., bayes classifier, fuzzy kNN classifier, back-propagation neural network classifier (BPNN) and modified probabilistic neural network classifier (MPNN) by using five different fusion schemes, i.e., majority rule, Borda count, averaging, weighted averaging and fuzzy integral fusion for characterization of liver tissue as normal, cirrhotic and HCC liver. It is reported that the fuzzy integral fusion of the four classifiers yield the maximum correct classification rate of 100 % , 91.5 %, and 94.5 % and for normal, cirrhosis and HCC classes, respectively.

In yet another related research reported in [111], the authors have attempted to obtain textural models for detection of hepatocellular carcinoma in early and advances stages. Their study reports investigations made on finding relevant texture features for separating the binary classes which eventually leads to the development of hepatocellular carcinoma, like cirrhosis without HCC and cirrhotic parenchyma around HCC, cirrhotic parenchyma around HCC and incipient HCC, cirrhotic parenchyma around HCC and advanced HCC, incipient HCC and advanced HCC, incipient HCC and normal liver as well as advanced HCC and normal liver.

The study in [112] defined incipient HCC as tumor of size varying between 1.5 to 2 cm and advanced HCC of size greater than 2cms. In their study, binary classifications like hyper-echogenic HCC vs. surrounding parenchyma around HCC and hypo-echogenic HCC vs. surrounding parenchyma around HCC is investigated.

2.4 CAD Systems for Characterization of Focal Liver Lesions

The differential diagnosis between focal liver lesions (FLLs) from B-Mode ultrasound (US) images is broad due to existence of wide variety of sonographic appearances even within individual classes of FLLs [16, 20, 62, 73, 126, 162]. Even then, B-Mode US is considered as a primary choice for characterization of FLLs mainly due to its nonionising, noninvasive, inexpensive nature and real time imaging capabilities [20, 162]. Therefore an efficient computer-aided diagnostic (CAD) system for classification of FLLs based on conventional gray scale B-Mode US images is highly desired. There are very few studies reported in literature for characterization of FLLs using B-Mode US images, the brief detail of these studies [114, 167, 138, 189, 209] is depicted in Table 2.2.

Table 2.2 *Brief details of studies for classification of FLLs using B-Mode US*

Authors (year)	Image Class	Dataset Description			
		Patients	Images per class	No. of ROIs	ROI size
Sujana *et al.* [167] (1996)	NOR, HEM, Malignant	-	-	113	10×10pixels
	Classifier used	*Distribution of ROIs for classifier design*			
	Neural Network, LDA	*Training data*		*Testing Data*	
		NOR(40)		NOR(13)	
		HEM(15)		HEM(5)	
		Malignant (30)		Malignant(10)	
	Features used:	FOS, GLCM and GLRLM features			
Yoshida *et al.* (2003) [209]	HEM , Malignant (HCC+MET)	44	HEM(17) HCC(11) MET(16)	193	64×64pixels
	Classifier used	*Cross validation procedure*			
	Neural Network	HEM(50), HCC(87) and MET(56)			
	Features used:	Wavelet packet texture features			
Poonguzhali *et al.* (2008) [138]	NOR, Cyst, HEM and Malignant	-	-	120	10×10pixels
	Classifier used	*Cross validation procedure*			
	Neural Network	NOR(30)			
		Cyst(30)			
		HEM(30)			
		Malignant (30)			
	Features used:	AC, Edge frequency, GLCM and Laws' TEM features			
Mittal, *et al.* [114] (2011)	NOR, Cyst, HEM,HCC and MET	88	NOR(16), Cyst (17) HEM18) HCC(15) and MET(45)	800	25×25pixels
	Classifier used	*Training data*	*Validation data*	*Testing data*	
	Neural Network	NOR(50)	NOR(10)	NOR(172)	
		Cyst (50)	Cyst(10)	Cyst (6)	
		HEM(50)	HEM(10)	HEM(30)	
		HCC(50)	HCC(10)	HCC(167)	
		MET(50)	MET(10)	MET(125)	
	Features used:	FOS, GLCM, GLRLM, GWT and Laws' TEM features			
Jeon, *et al.* [74] (2013)	Cyst, HEM, and Malignant	102	Cyst(50), HEM(50), Malignant(50)	150	variable ROI sizes
	Classifier used	*Cross Validation Procedure*			
	SVM	Cyst(50)			
		HEM(50)			
		Malignant(50)			
	Features used:	FOS, GLCM, AMI, GWT, AC and Laws' TEM features			

Note: AC: Autocorrelation, AMI: Algebraic moment invariant features.

The study in [114] used statistical features based on first order statistics (FOS), second order statistics, i.e., gray level co-occurrence matrix (GLCM), higher order statistics, i.e. gray level run length matrix (GLRLM), spectral features, i.e., Gabor wavelet transform (GWT) based features and spatial filtering based features, i.e., Laws' texture features along with two stage neural network classification module for characterization of liver tissue as NOR, Cyst, HEM, HCC and MET liver.

The study in [167] reported classification between NOR, benign and malignant liver classes by using FOS and GLRLM statistical features with linear discriminant analysis and a neural network (NN) classifier.

The study in [148] used GLCM, autocorrelation, Laws' and edge frequency based texture features and a NN classifier for classification of NOR, Cyst, HEM and malignant liver classes. In researches [148, 167] malignant lesions are considered as a single class; however, the diagnosis of malignant lesion as HCC or MET is clinically significant for effective treatment and management of liver malignancies [20, 162].

In another related study [209], multiscale wavelet packet texture descriptors are used with NN classifier for binary classification tasks, i.e., HEM vs. HCC, HEM vs. MET and HCC vs. MET. Their study reports, preprocessing the images by 5×5 median filter for speckle noise removal and by second order polynomial fitting technique based on least square method for background trend correction. The preprocessing was carried out to reduce the dependence sonographic appearances of the lesions on time-gain settings of the scanners and patients attenuation [209].

The multiscale texture features obtained from the sub-band images obtained from wavelet packet decomposition of the ROI images were fed to the NN classifier at each level of decomposition. The features extracted from sub-band images were included in the feature set if they yielded higher classification accuracy. Thus, repeated classification experiments using the extracted multiresolution features and a NN classifier were used to decide whether further decomposition is required or not. At last, the feature set of multiresolution features yielding the maximum classification accuracy was subjected to backward elimination method in which one by one the feature is eliminated from the feature set until the classification accuracy starts to decrease. The subset of features obtained after applying backward elimination is considered to be optimal feature set for the considered binary classification task. The study reports good results for binary classification between HEM and HCC, HEM and MET lesions in comparison with the classification performance obtained for HCC and MET liver image classes. The results

of the study indicate that multiresolution texture features and a NN classifier can be used for distinction between benign and malignant FFLs [209].

As per the best of the author's knowledge, only one study reported in literature, experimented classification between five liver image classes, i.e., Cyst, HEM, HCC,MET and NOR liver [114] by using a large feature vector consisting of 208 texture features extracted by using FOS, GLCM, GLRLM, GWT and Laws' feature extraction methods. Their proposed CAD system design, consisted of two stage classification system with total 11 NNs (i.e., a single five class NN in the first stage and 10 binary NNs in the second stage). However, the study reports good classification accuracy of 86.4 % with US images enhanced with modified anisotropic diffusion method [114]. One of the limitations of the proposed CAD in [114] is that their design doesn't use any feature selection or feature dimensionality reduction methodology to get rid of superfluous and redundant features in a large feature set consisting of 208 texture features. In the present work, in order to design efficient CAD systems feature space dimensionality reduction is carried out by using principal component analysis (PCA). Also, the study in [114] considered the HCC cases as typical and atypical HCCs, given the fact that there are large variations in sonographic appearances within SHCCs and even within LHCCs, many other studies opined that HCC doesn't have any typical appearance, accordingly these studies have considered bifurcation of HCC class into small and large HCCs classes to represent the variability present in HCC class [188-191]. From studies related to classification of FLLs [114, 148, 167, 209], it is understood that statistical, spectral and spatial filtering based Laws' texture features are important for characterization of FLLs using B-Mode US images.

Another concern while designing a CAD system is the choice of size for region of interest (ROI), in [167] the ROI size of 10×10 pixels is considered, however in [114, 148] the ROI size of 25×25 pixels has been used for computing texture features. It is worth mentioning that the use of 10×10 pixels and even 25×25 pixels as ROI size yields smaller number of pixels in comparison to minimum 800 pixels required to estimate reliable statistics [14, 50 ,76, 191]. The study in [209] reports the use of 64×64 pixels as ROI size, possibly because they used high-resolution scanned images instead of real US images. It is otherwise difficult to select such a large ROI size keeping in view the size of small lesions and resolution of images obtained from US machines. In the present work ROI size of 32×32 pixels is considered which gives a sample size of 1024 pixels, adequate for computing reliable estimates for texture parameters.

2.5 Concluding Remarks

The conclusions drawn from the literature survey of the related studies are depicted below:

(*i*)   The brief summary of the literature review available on the problem of characterizing normal, cirrhosis and HCC liver images indicate that there has been much focus on using fractal dimension information with multiresolution analysis to tackle the characterization problem, as it has been mentioned that the normal liver tissue has smooth texture, cirrhotic liver has rough texture in comparison to normal liver and roughness of HCC is even higher than that of cirrhotic tissue. At the same time, it is worth mentioning that this cannot always be guaranteed and will heavily depend upon the database used for the classifier design. In actuality, HCCs exhibit high variability in terms of their sonographic appearances, for example, when a SHCC appears as homogeneously hyperechoic lesion the roughness of the HCC ROI is usually lesser than that of cirrhotic ROI. Thus, it is very important to design the classifier with a comprehensive and representative image database consisting of a variety of SHCC and LHCC lesions.

(*ii*)   From, the studies related to classification of FLLs [114, 138, 167, 189, 209], it can also be concluded that statistical, spectral and spatial filtering based Laws' texture features are important for characterization of FLLs using B-Mode US images. It is worth mentioning, that these studies have used texture samples from regions inside the lesion for differential diagnosis between FLLs. Also, only a single study [114] has considered five-class classification of FLLs using B-Mode US images, Other studies have either not considered MET image class or considered HCC and MET image as single malignant class. It is worth mentioning that diagnosis as to whether the ROI is HCC or MET is clinically significant, for proper management of liver malignancies. Also, it is important to consider, HCC and MET as separate image classes due to overlapping sonographic appearances between HCCs and atypical MET lesions due to which the subjective differential diagnosis is difficult.

(*iii*)   It is understood that differential diagnosis between HCC and MET lesion is clinically significant as it can help the physician to follow the right treatment protocol and thereby aid in proper management of liver malignancies, but still a CAD system for binary classification between HCC and MET lesions using B-Mode US images has not been experimented yet.

(*iv*)   The advantage with the hierarchical CAD designs for characterization of FLLs is that these designs provide the possibility to go stepwise from the general classification

problem, i.e., normal versus abnormal liver tissue, to the more particular classification problem which is the identification of exact liver abnormality with hierarchically placed classifiers. It is worth mentioning that the design of a hierarchical CAD system for characterization of FLLs using B-Mode US images have not been experimented yet, while the research study [54] experimented a hierarchical CAD for FLLs using liver CT images. The hierarchical CAD system design in [54] used FOS and GLCM texture features with 3 binary NN classifiers arranged in a hierarchical framework for stepwise classification between NOR or abnormal (ABNOR), cyst or other lesion (OL) and HEM or HCC image classes.

(*v*)   The selection of ROI size plays important role as texture measurements are sensitive to ROI size. In other studies, it has been demonstrated that ROI size must be at least 800 pixels to provide good sampling distribution for estimating reliable statistics [50, 76, 161] whereas in few other related researches, a sample size of at least 1000 pixels is suggested to estimate reliable statistics [15, 48].

Chapter 3

Methodology

3.1 Introduction

The research is a scientific investigation carried out in a systematic way for search of knowledge on a specific topic. Research in any specific domain or branch of knowledge should yields new facts by probing deeper and deeper for understanding the unknown. It comprises many crucial steps like defining and redefining the problem, formulation of possible solutions, collection, organization and evaluation of data, making deductions by careful observation, comparison and exhaustive experimentation and finally arriving at some conclusions.

Formulation of research objectives and the collection of image database are crucial for design of experimental work flow for a researcher working in the area of medical image processing. The research objectives are to be framed according to the needs of the radiologists based on the practical difficulties faced by them during their routine practice. Thus, the formulation of research objectives require detailed discussions and interactive sessions with the domain experts from medical fraternity. Collection of a comprehensive and representative image database is time consuming as it depends upon the frequency of patients with a particular disease visiting the hospital.

For the researchers working specifically in the area of analysis and classification of liver ultrasound (US) images, collection of a comprehensive database representative of all the image subclasses is an absolute pre-requisite. Furthermore, due to non-availability of the standard reference image database, there is absolutely no means of reliable and direct quantitative comparison of results reported by other research studies in this area. As a result, most of the research groups working in the area of classification of liver ultrasound images have to depend upon image databases acquired by them.

The development of a comprehensive database of B-Mode liver US images, with representative images from all the subclasses requires the consent, cooperation and time involvement of the radiologists. Thus, a Memorandum of Understanding (MoU) was signed, between Indian Institute of Technology, Roorkee (IITR) and Post Graduate Institute of Medical Education and Research (PGIMER), Chandigarh, to support each other in this research work.

The medical images are directly related to the patients; therefore it is important to obtain ethical clearance as well as the informed consent of the patients before image acquisition. It is also necessary to maintain their confidentiality, dignity and anonymity. In order to carry out

the research work, an experimental work flow was designed and a comprehensive image database of B-Mode liver US images with representative cases from all the image subclasses was developed during the time period from March 2010 to March 2012.

This Chapter gives brief outline of the proposed interactive system for diagnosis of liver diseases by using B-Mode liver US images. The description of the dataset used in the present research work is given in detail. The protocols followed for data collection, extraction of ROIs and selection of ROI size for the present research work are also described.

3.2 Proposed Interactive System for Diagnosis of Liver Diseases

The block diagram of the proposed interactive system for diagnosis of liver diseases (earlier shown as Fig.1 in Abstract), is revisited here in Fig. 3.1.

The proposed interactive system for diagnosis of liver diseases consists of two modules. The *Module 1* is designed to assist or provide second opinion to the radiologist in cases where the radiologist has confusion within normal, cirrhosis, HCC or MET liver image classes. Since cirrhosis is considered as a pre-cursor to development of HCC and it is considerably difficult to diagnose small HCCs developed on already nodular cirrhotic liver parenchyma. The diagnosis as to whether the parenchymal changes are cirrhotic or indicative of the development of HCC is absolutely necessary. Furthermore since there is considerable overlap between the sonographic appearances of HCC and MET lesions, the characterization of liver malignancies as HCC or MET lesions is absolutely essential for effective treatment of liver malignancies. Accordingly, the *Module 1* incorporates three different CAD systems, i.e., CAD System-I for binary classification between normal and cirrhotic liver tissue, CAD System-II for classification between normal, cirrhotic and HCC liver, and CAD System-III for binary classification between HCC and metastasis (MET) liver malignancies. The region of interest (ROI) extracted by the radiologist, is fed to CAD System-I for characterization between normal and cirrhotic liver tissue. Although the design of the proposed CAD System-I yields 100 % accuracy for the characterization between normal and cirrhotic liver tissue, but considering the fact that the sensitivity of US for detection of SHCCs developed on cirrhotic liver is severely limited, it is quite possible that the ROI belonging to cirrhotic liver class may actually represent a HCC. Therefore, the ROI which is predicted as cirrhotic by the CAD System-I is passed through CAD System-II for characterization between normal, cirrhotic and HCC liver tissue. If the prediction of the CAD System-II for a ROI is cirrhosis it gives greater confidence to the radiologist that the liver tissue is cirrhotic. However, if for a particular ROI the decision of the

34

CAD System-II is HCC, it is advised to investigate whether the ROI belongs to a HCC lesion or a MET lesion, because of their significant overlapping sonographic appearances. Although, both HCC and MET lesions represents malignant liver lesions but differential diagnosis between HCC and MET lesion is absolutely necessary for better management of the disease and adequate scheduling of treatment options. Therefore, if the ROI is predicted as HCC by CAD System-II, it is fed to CAD System-III for binary classification between HCC and MET liver tissue. If it is predicted as HCC, it gives greater confidence to the radiologist that the ROI represents HCC, or else if the ROI is predicted as MET, it is recommended to pass the ROI through CAD System-IV of *Module 2* of the proposed interactive system for its differential diagnosis with other FLLs.
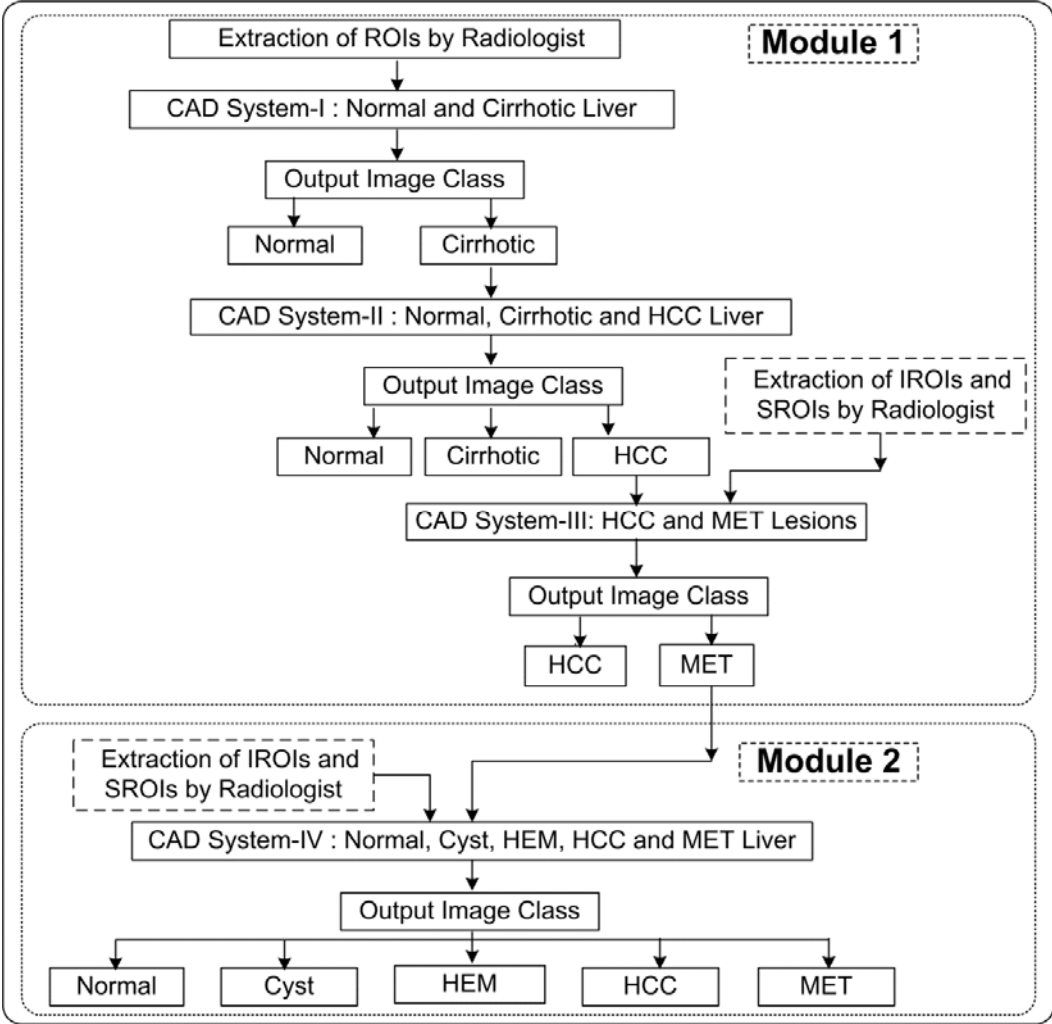
Fig. 3.1 Block diagram of the proposed interactive system for diagnosis of liver diseases.
Note: IROIs: Inside lesion regions of interest; SROIs: Surrounding lesion regions of interest.

Exhaustive experimentation was carried out for the design of efficient classifiers for CAD system-I, CAD System-II, CAD System-III and CAD System-IV. The radiologists observe the

texture patterns of the IROIs (inside regions of interest, i.e. regions of interest extracted from region inside the lesion boundary) as well as the texture patterns of the SROIs (surrounding regions of interest, i.e., regions of interest extracted from liver parenchyma surrounding the lesion and approximately at the same depth as that of the centre of the lesion) for making differential diagnosis between HCC and MET lesions using B-Mode US images. Accordingly, texture feature extraction from IROIs and SROIs were carried out for design of CAD System-III for classification between HCC and MET lesion. Therefore, if the prediction of CAD System-II is HCC, the radiologist is required to mark IROI as well as SROI for feature extraction. The results obtained from exhaustive experiments carried out in the present work indicate that texture feature extraction from both IROIs and SROIs enhances the efficiency of the CAD System-III for classification between HCC and MET lesions.

The *Module 2* of the proposed interactive system for diagnosis of liver diseases is designed for differential diagnosis between FLLs by using B-Mode liver US images. Accordingly, the *Module 2* incorporates a CAD System-IV for classification between Normal, Cyst, HEM, HCC and MET liver image classes. In the present work, rigorous experimentation was carried out for the design of a stand-alone multiclass classifier for characterization of FLLs.

In case of atypical cases of different FLLs the differential diagnosis is carried out not only by looking at the texture patterns of the regions inside the lesion but also by looking at the texture of the background liver parenchyma on which the lesion has evolved. Texture feature extraction from IROIs as well as SROIs was considered for the design of the proposed CAD system. Thus ROIs extracted from within the inside lesion boundary (IROIs) and a single SROI extracted from the region surrounding the lesion and approximately at the same depth as that of the centre of the lesion are inputted to the *Module 2* for classification into NOR, Cyst, HEM, HCC or MET liver image classes.

3.3 Data Acquisition Protocols

3.3.1   Medical Ethics and Ethical Clearance

The medical ethics are basically the moral values which must be followed during clinical practice and medical imaging research. Ethical guidelines indicate the binding principles on researchers, radiologists as well as the patients/subjects involved in the research activity. The reputed institutions and hospitals across the world have an Institutional Review Board (IRB) to review the submitted research proposals in terms of the ethical issues involved in undertaking a research activity. The IRB generally consists of health care professionals and the philosophers

which ensure that the researcher has considered all the important ethical issues during formulation of research procedures, so that there is no ethical conflict by undertaking the research activity. The IRB after careful investigation of the submitted research proposal may at its discretion impose certain additional guidelines to ensure the safety and rights of the patients/ subjects. The careful review of research proposals by the IRB protects the researcher as well as the organization against possible legal actions of ignoring to address important ethical issues concerning patients/subjects.

The aim of the present research work is to do value addition in the diagnostic performance obtained by most commonly available conventional gray scale B-Mode US imaging modality for diagnosis of liver diseases. The present research work is related to human healthcare and the collection of comprehensive database of B-Mode liver US images with representative images of different subclasses from various patients is absolutely necessary. Therefore for the present research work the author was required to obtain the ethical clearance from the medical ethics committee of the associated medical education and research institute, i.e., Post Graduate Institute of Medical Education and Research (PGIMER), Chandigarh. The medical ethics committee of PGIMER approved the research proposal submitted by the author after examining the research problem, and imposed the following research ethics for the researcher to follow:

(*i*)   The researcher will not involve in any procedure which may infringe or interfere with the medical ethics.

(*ii*)   The researcher will not provide any input to the participating radiologists, as it may bias their opinion regarding the medical management.

(*iii*) The researcher would be required to obtain written consent from the patients before collecting the data.

(*iv*)   There should be no disclosure of personal information of the patients in any of the publication by the researcher.

(*v*)   The data collected by the researcher would be used for academic purposes only.

3.3.2   Image Assessment Protocols

Experienced participating radiologists with more than 13 years of experience in radiology ensured that all the images are of diagnostic quality (i.e., free from artifacts), and confirmed the representativeness of each image class, i.e., normal liver, cirrhotic liver, typical and atypical cases of Cyst, HEM, MET lesions, and SHHC as well as LHCC cases, using liver image assessment criteria including (*a*) visualization of sonographic appearances of normal liver,

cirrhotic liver and FFLs lesions based on their knowledge. (*b*) follow-up of clinical history of the patient and associated findings, and (*c*) imaging appearance on dynamic helical CT/ magnetic resonance imaging (MRI)/pathological examinations and biopsy, which is an invasive procedure.

3.4 Dataset Description

To develop a comprehensive image database with representative cases form each image class, i.e., normal liver, cirrhotic liver, typical and atypical cases of Cyst, HEM and MET lesions and small and large HCC lesions. For the present research work total 124 conventional gray scale B-Mode US images (consisting of 21 NOR, 16 CIRR, 12 Cyst, 15 HEM, 28 HCC and 32 MET) were acquired from the patients who underwent US examination at the Department of Radiodiagnosis and Imaging, PGIMER, Chandigarh, India during the period from March 2010 to March 2012. The Philips ATL HDI 5000 US scanner equipped with transducer of 2-5 MHz range was used for recording of images. The images were digitized to 800×564 pixels with gray scale consisting of 256 tones. The horizontal and vertical resolution of the recorded images is 96 dpi. The bifurcation of the image database consisting of total 124 conventional gray scale B-Mode US images into different liver image classes is shown in Fig. 3.2.
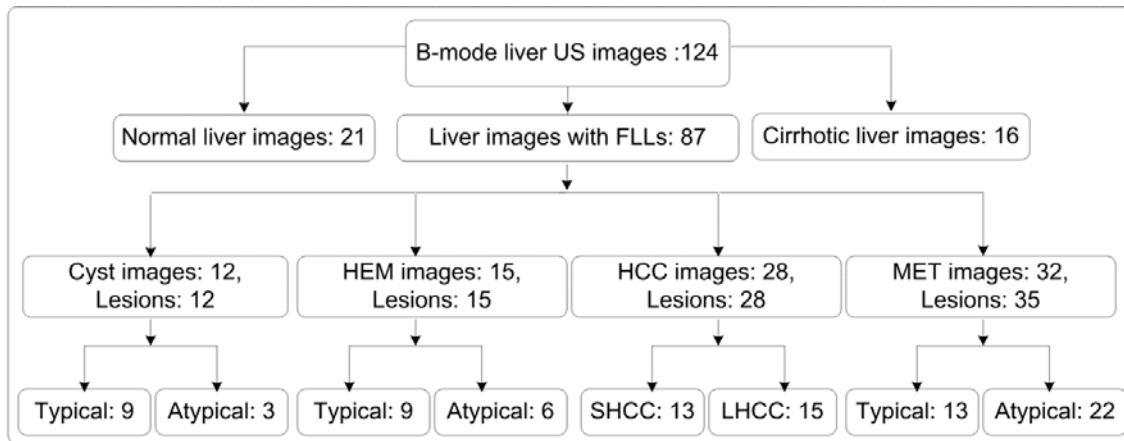
Fig. 3.2 The distribution of acquired image database into various liver image classes.

To design a robust classification system, it is ensured that the constituent HCC images in the dataset offer a high degree of variability in terms of size and sonographic features. The size of SHCC varied from 1.5 to 1.9 cm and the size of LHCC varied from 2.1 to 5.6 cm.

To ensure generality, the training data for designing the classifier was chosen carefully in consultation with experienced participating radiologists, so as to include all the typical and

atypical image classes for Cyst, HCC, HEM and MET lesions as well as small and large HCC lesions for designing a robust classifier with representative cases for all image subclasses. Two sets of images were created for each image class, ROIs from one set of images were used for training and ROIs from the other set were used for testing to avoid any biasing.

3.4.1   Data Collection Protocols

The following protocols were followed for data collection:

(*i*)   Before recording the image for a patient suffering from liver cirrhosis it was ensured that the patient is not suffering from any other hepatopathy.

(*ii*)   Only HCC lesions developed on cirrhotic liver were included as the existence of HCC on normal liver is very rare.

(*iii*)   Labeling of HCC lesions as SHCC (< 2 cm) or LHCC was done by observing the size of the lesion in transverse and longitudinal views.

(i*v*)   Labeling of HCC as SHCC or LHCC and Cyst, HEM and MET as typical or atypical lesion was carried out during data collection in order to ensure that the training dataset used for classifier design should consist of representative cases from all image subclasses.

3.4.2   ROI Extraction Protocols

The protocols followed for selection of ROIs in different experiments carried out in the present research work, as well as the protocols followed for selection of ROI size are discussed in this section.

3.4.2.1 Selection of ROIs

The following protocols were followed for cropping the regions of interest (ROIs) from the image database:

(*i*)   The ROIs were cropped by an experienced participating radiologist by using a graphic user interface (GUI) based ROI manager software developed in Biomedical Instrumentation Laboratory, Indian Institute of Technology, Roorkee. The ROI manager software provided the radiologist the flexibility to load the image, choose the ROI size and shape, move the ROI to any desired location over the image, freeze the ROI at any location and crop the ROIs together after the position of all the ROIs for an image is frozen.

(*ii*) For the design of *CAD system for characterization of normal and cirrhotic liver tissue* maximum non-overlapping ROIs were cropped from right lobe of the liver such that the ROIs contain only liver parenchyma without any inhomogeneous structures like hepatic ducts, blood vessels, etc.

(*iii*) For the design of *CAD system for characterization of normal, cirrhotic and HCC liver tissue:* (*a*) from normal and cirrhotic images, maximum non-overlapping ROIs were cropped from right lobe of the liver such that the ROIs contain only liver parenchyma without any inhomogeneous structures like hepatic ducts, blood vessels, etc., and (*b*) from HCC images maximum non-overlapping ROIs were cropped from well inside the boundary of the lesion.

(*iv*) For the design of *CAD system for characterization of HCC and MET liver tissue:* (*a*) two type of ROIs (i.e., IROIs and SROIs) were extracted, (*b*) maximum non-overlapping IROIs were cropped from well inside the boundary of the lesion, (*c*) the necrotic areas inside the lesions were avoided while cropping IROIs (*d*) for each lesion a single SROI was cropped from region surrounding the lesion approximately at the same depth as that of the centre of the lesion, (*e*) due care was taken while cropping SROI such that the SROI contain only liver parenchyma without any inhomogeneous structures like hepatic ducts, blood vessels, etc.

(*v*) For the design of *CAD system for characterization of focal liver lesions* : (*a*) two type of ROIs (i.e., IROIs and SROIs) were extracted, (*b*) maximum non-overlapping IROIs were cropped from well inside the boundary of the lesion, (*c*) the necrotic areas inside the lesions were avoided while cropping IROIs (*d*) for each lesion a single SROI was cropped from region surrounding the lesion approximately at the same depth as that of the centre of the lesion, (*e*) due care was taken while cropping SROI such that the SROI contain only liver parenchyma without any inhomogeneous structures like hepatic ducts, blood vessels, etc., and (*f*) for each NOR image, maximum ROIs were cropped at the same depth and a single extreme ROI is considered as SROI and all other ROIs at the same depth are considered as IROIs.

3.4.2.2 Selection of ROI Size

The selection of ROI size plays important role as texture measurements are sensitive to ROI size. In other studies, it has been demonstrated that ROI size must be at least 800 pixels to provide good sampling distribution for estimating reliable statistics [50, 76, 161] whereas in

few other related researches, a sample size of at least 1000 pixels is suggested to estimate reliable statistics [15, 48]. However for characterization of diffuse liver diseases different ROI sizes ranging from 32×32 pixels [95, 133, 200], 40×40 pixels [183, 185] to 64×64 pixels [27, 118] have been considered.

Similarly, for characterization of FLLs, the study reported in [114] used ROI size of 25×25 pixels for computing texture features, and in studies [138, 167] the use of ROI size of 10×10 pixels is reported. The use of 10×10 pixels and even 25×25 pixels as ROI size yields smaller number of pixels in comparison to minimum 800 pixels required to estimate reliable statistics [14, 50, 76, 189, 191]. The study reported in [209] used 64×64 pixels as ROI size extracted from high-resolution scanned images instead of real US images. It is otherwise difficult to select such a large ROI size keeping in view the size of small lesions and resolution of images obtained from US machines.

After interaction with the participating radiologists, ROI size of 32×32 pixels was considered appropriate for the present study considering the facts such as:

(*i*)   There is sufficient evidence in the literature that ROI size must be at least 800 pixels to provide good sampling distribution for estimating reliable statistics [14, 50]; as ROI size of 32×32 gives 1024 pixels, it can be assumed that the computed texture parameters are reliable estimates.

(*ii*) During initial discussions with the participating radiologists, an attempt was made to mark larger ROI sizes, but few practical difficulties were faced. Certain lesions had necrotic area; radiologists opined that the necrotic area inside lesions must be avoided while extracting IROIs, and it was not possible to consider large ROI size for these lesions. Also, participating radiologists were of the view that SROI for each lesion, and ROIs for each normal and cirrhotic liver image, must be selected by avoiding the inhomogeneous structures like hepatic ducts, blood vessels, etc., which was practically difficult by considering larger ROI size.

(*iii*) For real-time implementation, small ROI size is always favourable as time taken for feature extraction and classification is obviously less in comparison to large ROI size. Also, with small ROI size, more number of samples are available for classifier design.

The entire image database was stored in a personal computer with Pentium Core-2-Duo, 2.67 GHz processor and 1.97 GB RAM.

3.5 Brief Description of Experiments Carried out in the Present Work

The brief description of experiments carried out in the present work is given below:

3.5.1 Design of CAD System for Characterization of Normal and Cirrhotic Liver Tissue

The experiments carried out for the design of an efficient CAD system to characterize normal and cirrhotic liver in the present research work have been carried using total 120 ROIs, (60 normal and 60 cirrhotic ROIs) extracted from 31 clinically acquired B-Mode liver ultrasound images, i.e., 15 normal and 16 cirrhotic liver images.

(i)   *Experiment* 1: In this study, a CAD system to characterize normal and cirrhotic liver by multi-resolution texture features is proposed. Mean and standard deviation multiresolution texture features derived by using 2D-Discrete wavelet transform (2D-DWT), 2D-Wavelet packet transform (2D-WPT) and 2D-Gabor wavelet transform (2D-GWT) are considered for analysis and exhaustive search with J3 criterion of class seperability is used for feature selection. The performance of subset of five most discriminative texture descriptors obtained from 2D-DWT, 2D-WPT and 2D-GWT is compared by using a support vector machine (SVM) classifier. It is observed that only five mean multiresolution texture descriptors obtained from 2D-GWT at selective scale and orientations yield highest classification accuracy of 98.3 % and sensitivity of 100 % by using a SVM classifier.

(ii)   *Experiment* 2: In this experiment, initially the performance of GLCM-Mean and GLCM-Range texture features (computed by varying the inter-pixel distance d from 1 to 4) is compared by using SVM classifier. It is observed that the highest classification accuracy and sensitivity value of 100 % is obtained by using GLCM-Mean features computed for $d = 2$, GLCM-Range features computed for $d = 2$ and also with GLCM-Range features computed for $d = 4$. Further, three scalar feature ranking methods based on fisher discriminant ratio (FDR), divergence (Div.) and Bhattacharyya distance (B-dist) as class seperability measures and two feature subset selection methods, i.e., sequential forward selection (SFS) and sequential backward selection (SBS) based on divergence as a class seperability measure are used to find the subset of optimal GLCM-Range features computed at $d = 2$, which are significant to account for textural variations exhibited by normal and cirrhotic liver. It is observed that the subset consisting of four features (i.e., contrast, sum of squares: variance, inverse difference moment and information measures of correlation-1) selected by SBS feature subset selection method yield the highest

classification accuracy and sensitivity value of 100 % for characterization between normal and cirrhotic liver.

(*iii*) *Experiment* 3: In this experiment, the potential of singular value mean features derived from singular value decomposition (SVD) of GLCM for characterization of normal and cirrhotic liver is tested by using SVM classifiers. It is observed that the highest classification accuracy and sensitivity value of 100 % is obtained by using first four singular mean features obtained by SVD of GLCM.

3.5.2 Design of CAD System for Characterization of Normal, Cirrhotic and HCC Liver Tissue

The experiment carried out for the design of an efficient CAD system to characterize normal and cirrhotic liver in the present research work have been carried out using total 180 ROIs (60 ROIs from each image class) extracted from 56 clinically acquired B-Mode liver ultrasound images, i.e., 15 normal, 16 cirrhotic and 25 HCC liver images.

A system to characterize normal liver, cirrhotic liver and hepatocellular carcinoma (HCC) evolved on cirrhotic liver is proposed in this study. The multiresolution wavelet packet texture descriptors, i.e. mean, standard deviation and energy features, are computed from all 180 ROIs by using various compact support wavelet filters including Haar, Daubechies (db4 and db6), biorthogonal (bior3.1, bior3.3 and bior4.4), symlets (sym3 and sym5) and coiflets (coif1 and coif2). It is observed that a combined texture feature vector (TFV) of length 48 consisting of 16 mean, 16 standard deviation and 16 energy features estimated from all 16 sub-band feature images (wavelet packets) obtained by second-level decomposition with 2D-WPT by using Haar wavelet filter gives the best characterization performance of 86.6 %. Feature selection by genetic algorithm–support vector machine (GA–SVM) method increased the classification accuracy to 88.8 % with sensitivity of 90 % for detecting normal and cirrhotic cases and sensitivity of 86.6 % for HCC cases. Considering limited sensitivity of B-Mode ultrasound for detecting HCCs evolved on cirrhotic liver, the sensitivity of 86.6 % for HCC lesions obtained by the proposed CAD system is quite promising and suggests that the proposed system can be used in a clinical environment to support radiologists in lesion interpretation.

3.5.3 Design of CAD System for Characterization of Primary and Secondary Focal Liver Lesions

For the design of an efficient CAD system for differential diagnosis between HCC and MET lesions, total 174 ROIs (i.e., 120 IROIs, 60 HCC+ 60 MET IROIs and 54 SROIs, i.e., 27

HCC+ 27 MET SROIs) are extracted 51 real ultrasound liver images with 54 malignant lesions, i.e., 27 HCC images with 27 solitary HCCs lesions and 24 MET images with 27 MET lesions.

The differential diagnosis of HCCs from METs is often carried out by observing the texture of regions inside the lesion and the texture of background liver on which the lesion has evolved. The present study investigates the contribution made by texture patterns of regions inside (IROIs) and regions surrounding (SROIs) the lesions for binary classification of HCC and MET lesions. A total of 120 IROIs and 54 SROIs are cropped from 54 lesions. Subsequently, 112 texture features (56 texture features and 56 texture ratio features) are computed by statistical, spectral, and spatial filtering based texture features extraction methods. A two-step methodology is used for feature set optimization, i.e., feature pruning by removal of nondiscriminatory features followed by feature selection by GA–SVM approach. The SVM classifier is used for classifier design based on optimum features. The proposed CAD system yields the classification accuracy of 91.6 % with sensitivity of 90 % and 93.3 % for HCCs and METs, respectively. The promising results obtained by the proposed CAD system indicate its usefulness to assist radiologists in diagnosing liver malignancies.

3.5.4   Design of CAD System for Focal Liver Lesions

For the design of an efficient CAD system for differential diagnosis between FLLs, total 491 ROIs (380 IROIs i.e., 75 NOR+55 Cyst+70 HEM+ 90 HCC + 95 MET, IROIs and 111 SROIs, i.e., 21 NOR+12 Cyst+15 HEM+28 HCC+35 MET SROIs) are extracted from 108 B-Mode liver US images comprising 21 NOR images, 12 Cyst images with 12 Cystic lesions (8 typical cases and 4 atypical cases), 15 HEM images with 15 HEM lesions (8 typical cases and 7 atypical cases), 28 HCC images with 28 HCC lesions (13 SHCC cases and 15 LHCC cases) and 32 MET images with 35 MET lesions (12 typical cases and 23 atypical cases).

(*i*)   *Experiment* 1: A comparative study of four CAD systems designed for characterization of most commonly occurring FLLs, such as Cyst, HEM, HCC and MET lesions along with NOR liver tissue is carried out in the present work. In order to develop an efficient CAD system, a comprehensive and representative dataset consisting of B-Mode ultrasound images with (*a*) typical and atypical cases of Cyst, HEM and MET lesions, (*b*) SHCC as well as LHCC lesions, and (*c*) NOR liver cases, have been used for designing *k*-Nearest Neighbor (*k*NN), Probabilistic Neural Network (PNN), Neural Network (NN), and Support Vector Machine (SVM) classifiers. For differential diagnosis between atypical FLLs, expert radiologists often visualize the textural characteristics of regions inside and outside the lesion. Accordingly in the present work, texture features and texture ratio

features are computed from regions inside and outside the lesions. The texture features extracted by using first order statistics, second order statistics (GLCM method, i.e., gray level co-occurrence matrix method), higher order statistics (GLRLM method, i.e., gray level run length matrix method), spectral features (GWT based multiresolution features and FPS based features), and spatial filtering based Laws' texture features are used in the present study. Feature set consisting of 208 texture features (i.e., 104 texture features and 104 texture ratio features) is subjected to principal component analysis (PCA) for feature space dimensionality reduction; it is observed that maximum classification accuracy of 87.7 % is obtained for PCA-NN based CAD system in comparision to 85 %, 86.1 %, and 87.2 % as obtained by PCA-kNN, PCA-PNN, and PCA-SVM based CAD systems. Keeping in view the comprehensive and representative dataset used for designing the classifier the results obtained by the proposed PCA-NN based CAD system are quite encouraging and indicate its usefulness to assist experienced radiologists for interpretation and diagnosis of FLLs.

(*ii*) *Experiment* 2: The study proposes a hybrid-hierarchical computer-aided diagnostic (Hy–HCAD) system for FLLs, designed using texture features computed for regions inside and outside the lesions. The Hy–HCAD system consists of four binary classifiers which are arranged in a hierarchical framework. The first classifier classifies into normal (NOR) or Abnormal (ABNOR) cases. The ABNOR cases are classified by second classifier as Cyst or 'Other Lesion' (OL) cases. The third classifier classifies 'OL' cases into Primary Benign Lesion (PBL) or Malignant Lesion (ML) cases. Finally, fourth classifier classifies 'ML' cases into Primary Malignant Lesion (PML) or Secondary Malignant Lesion (SML) cases. Feature space dimensionality reduction using PCA is carried out for designing each classifier. Initially SVM, NN, PNN and k-NN classifiers are used for design of four hierarchical CAD systems. The Hy–HCAD system is designed using four best binary classifiers. The proposed Hy–HCAD system yields highest classification accuracy of 92.7 % for characterization of FLLs using B-Mode US images.

(*iii*) *Experiment* 3: A neural network ensemble (NNE) based CAD system to assist radiologists in differential diagnosis between FLLs, including (*a*) typical and atypical cases of Cyst, HEM and MET lesions, (*b*) SHCC as well as LHCC lesions along with, (*c*) normal (NOR) liver cases, is proposed in the present work. Expert radiologists visualize the textural characteristics of regions inside and outside the lesions to differentiate between different FLLs, accordingly texture features computed from inside lesion regions

of interest (IROIs) and texture ratio features computed from IROIs and surrounding lesion regions of interests (SROIs) are taken as input. PCA is used for reducing the dimensionality of the feature space before classifier design. The first step of classification module consists of a five class PCA-NN based primary classifier which yields probability outputs for five liver image classes. The second step of classification module consists of ten binary PCA-NN based secondary classifiers for NOR/Cyst, NOR/HEM, NOR/HCC, NOR/MET, Cyst/HEM, Cyst/HCC, Cyst/MET, HEM/HCC, HEM/MET and HCC/MET classes. The probability outputs of five class PCA-NN based primary classifier is used to determine the first two most probable classes for a test instance, based on which it is directed to the corresponding binary PCA-NN based secondary classifier for crisp classification between two classes. By including the second step of the classification module, the classification accuracy increases from 88.7 % to 95 %. The promising results obtained by the proposed CAD system indicate its usefulness to assist radiologists in differential diagnosis of FLLs.

3.6 Concluding Remarks

The methodology adopted to accomplish the research objectives of the present work on *Analysis and Classification of B-Mode Liver US Images* is presented in this Chapter. The design of the proposed interactive system for diagnosis of liver diseases, the criterion followed for assessment of liver images, the description of protocols followed for collection of image database, the description of protocols followed for cropping of ROIs from images and preparation of datasets for each experiment. The main steps involved in the design of a CAD system are illustrated in Fig. 3.3.
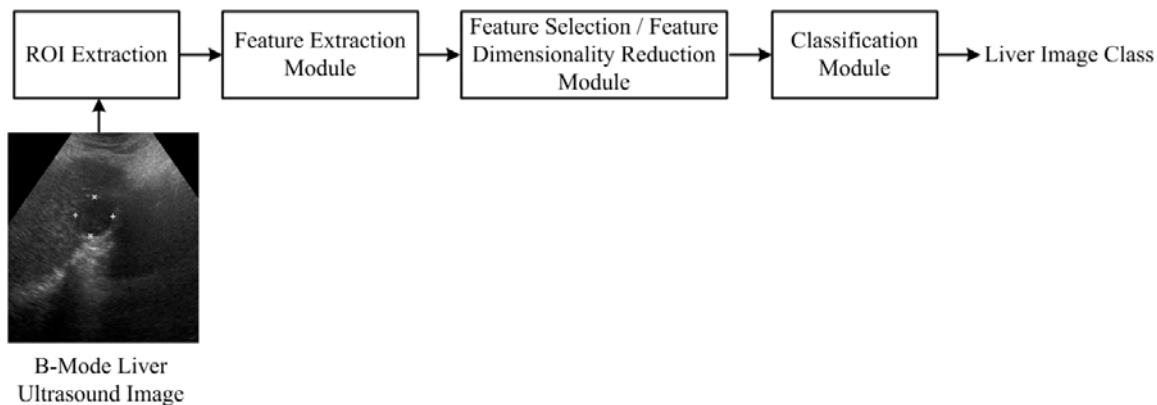
Fig 3.3 Generalized block diagram of a computer-aided diagnostic system

The ROIs extracted from the acquired image database are used as texture samples for feature extraction. The texture features computed from ROIs are subjected to feature selection and the reduced optimal set of features is used for classifier design. The details of feature extraction, feature selection or feature space dimensionality reduction and classification methods used in the experiments carried out in the present research work, are discussed in detail in the subsequent Chapters.

Prediction of Liver Cirrhosis

4.1 Introduction

Among diffuse liver diseases, the liver cirrhosis is considered more serious as it is the end stage of chronic diffuse liver disease which is characterized by replacement of normal liver tissue by fibrosis, scar tissue and regenerative nodules. Liver fibrosis refers to the formation of fibrous scar tissue in the liver as a result of injury to heptocytes (functional liver cells) because of infection with virus or due to heavy alcohol consumption. Thus, alcoholism, chronic viral hepatitis and fatty liver disease are considered most common causes for the occurrence of liver cirrhosis.

Cirrhosis is a diffuse process, which converts normal liver architecture into structurally abnormal nodules. This process can be micronodular in which the size of the regenerating nodules is less than 3 mm in diameter or macronodular with regenerative nodules of size 3 mm and above. Micronodular cirrhosis, which generally gives a coarse echotexture, results from consumption of alcohol whereas chronic viral hepatitis is considered as the most frequent cause of macronodular form. The cirrhotic liver is initially enlarged but it tends to shrink as the disease progresses; however in certain cases the liver tissue remains normal in size due to disproportionate changes in different lobes. Cirrhosis causes scarring of the liver, which in-turn slows down the blood flow through the liver, leading to back up of blood in portal vein (portal hypertension). This back up causes high blood pressure in the portal vein which may lead to variceal rupture.

Early diagnosis of liver cirrhosis is absolutely essential as (*i*) most of the cirrhotic patients are asymptomatic, (*ii*) biochemical tests like elevated liver enzyme detect cirrhosis at an advanced stage, (*iii*) patients with cirrhosis are at high risk of developing hepatocellular carcinoma, and (*iv*) it is the most common cause of portal hypertension.

Further, since cirrhosis is generally irreversible the treatment options generally focus on preventing progression and related complications.

The conventional grayscale B-Mode ultrasound (US) is commonly used as initial examination for diagnosis of diffuse liver diseases because of its nonradioactive, noninvasive and inexpensive nature. Experienced radiologists differentiate normal liver from cirrhotic liver by observing the echotexture which is mostly homogeneous with medium echogenicity

(i.e., same or slightly increased echogenicity in comparison to right kidney) in case of normal liver and coarse with diffused uneven nodularity in case of cirrhotic liver.

Although, currently liver biopsy is considered a 'gold standard' for determining the extent of the liver disease; there is no need of biopsy if clinical, laboratory and radiologic findings suggest cirrhosis [14, 15]. Since the biochemical tests are able to detect cirrhosis at an advanced stage when the liver is already infected with its associated complications therefore there has been a significant clinical interest in the ability to detect cirrhosis using conventional gray scale US images.

Zohu *et al.* used features extracted from M-Mode (amplitude and standard deviation of the motion curve) and B-Mode (FOS and GLRLM features) liver US images along with sequential forward selection (SFS) algorithm for feature selection and linear discriminant analysis (LDA) for classification between normal and cirrhotic liver [213]. Lu *et al.* used comparision of echotexture of normal and cirrhotic liver with the echotexture of accompanying spleen for classification of normal and cirrhotic liver [101]. Huang *et al.* used GLCM features extracted from B-Mode US images processed by wavelet packet denoising method for classification between normal and cirrhotic liver [67]. Wan and Zhou used mean and energy, multiresolution texture features computed from 2D-DWT and 2D-WPT sub-band images resulting by use of db4 wavelet filter along with SVM classifier for classification between normal and cirrhotic liver [192]. Few other related researches in the literature attempted classification between normal liver and different grades of cirrhosis. Sun *et al.* used LL sub-band images obtained by processing ROIs of size 16×16 by 2D-DWT along with BPNN and PNN classifiers for classification between normal liver, mild, moderate and severe cirrhosis [168]. Wu *et al.* used pre-processed images filtered by using Gaussian filter for extraction of GLCM features along with ensemble of SVM classifiers for classification between normal liver , mild, moderate and severe cirrhosis [202]. Jeong *et al.* used relative degree of coarseness of liver parenchyma with accompanying spleen by computing FOS, GLCM, GLRLM, SFM, Edge density, and fractal dimension features for classification between normal liver and different grades of cirrhosis [75].

In the present work, exhaustive experiments have been carried out to develop an efficient computer-aided diagnostic (CAD) system for prediction of liver cirrhosis using B-Mode US images.

4.2 Dataset Description – CAD System for Prediction of Liver Cirrhosis

The design of CAD system for characterization of normal and cirrhotic liver tissue was carried out with 31 B-Mode liver US images, i.e., 15 normal images and 16 Cirrhotic images. The protocols followed for collection of dataset, selection of ROIs and selection of ROI size are described in Section 3.4.1 of Chapter 3. The normal and cirrhotic liver variants from the acquired image database with ROIs marked are shown in Fig. 4.1(a) and Fig. 4.1(b), respectively.
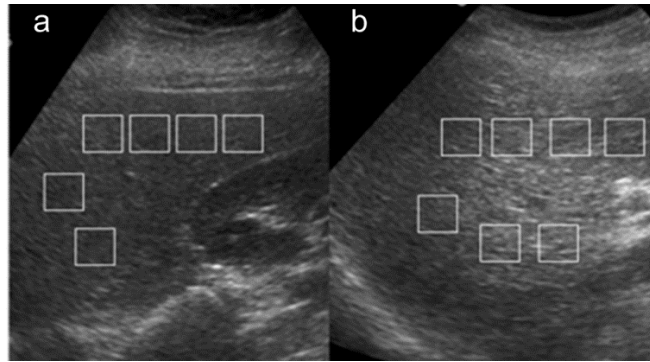
Fig. 4.1 (a) Normal liver image with ROIs marked; **(b)** Cirrhotic liver image with ROIs marked.

The description of the dataset used in this study, and its bifurcation into training dataset and testing dataset is shown in Fig. 4.2.
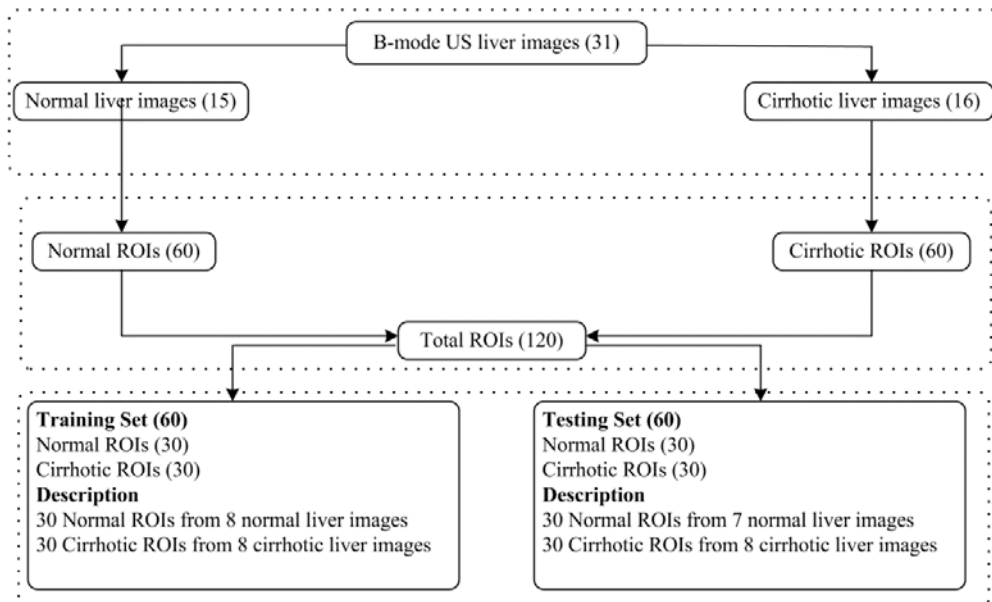
Fig. 4.2 Dataset description – CAD system for characterization of normal and cirrhotic liver.

4.3 Experimental Work Flow – Prediction of Liver Cirrhosis

In the present work, exhaustive experimentation have been carried out with multiresolution texture features, GLCM-Mean and GLCM-Range texture features as well as with features derived by singular value decomposition (SVD) of GLCM in order to design an efficient CAD system for characterization between normal and cirrhotic liver tissue. In all the experiments, SVM classifier has been used extensively for the classification task.

The brief description of the experiments carried out in the present work is given below.

Experiment 1: In this experiment, an investigation is made to realize the potential of 2D-DWT, 2D-WPT and 2D-GWT based multiresolution texture features for characterization of normal and cirrhotic liver tissue. Exhaustive search procedure combined with *J3* criterion of class seperability is used in order to obtain optimal reduced texture feature vector (TFV) for the classification task. The classification is carried out by using SVM classifiers.

Experiment 2: In this experiment, the efficacy of TFV consisting of 13 GLCM-Mean and TFV consisting of 13 GLCM-Range features (computed at inter-pixel distance d varying from 1 to 4) for characterization of normal and cirrhotic liver is tested by using SVM classifiers. Further, different feature selection techniques are applied to texture feature set consisting of 13 GLCM-Range features computed at $d = 2$, in order to find out the prominent features which are significant to account for textural variations exhibited by normal and cirrhotic liver. Five feature selection methods, i.e., three scalar feature ranking methods based on fisher discriminant ratio (FDR), divergence (Div.) and Bhattacharyya distance (B-dist) as class seperability measures and two feature subset selection methods, i.e., sequential forward selection (SFS) and sequential backward selection (SBS) based on divergence as a class seperability measure are used in this experiment. The efficacy of the selected features is tested by using SVM classifiers.

Experiment 3: In this experiment, the potential of singular value mean features derived from singular value decomposition (SVD) of GLCM for characterization of normal and cirrhotic liver is tested by using SVM classifiers.

The block diagram depicting the experimental work flow of the present study for prediction of liver cirrhosis using B-Mode US images is shown in Fig. 4.3.
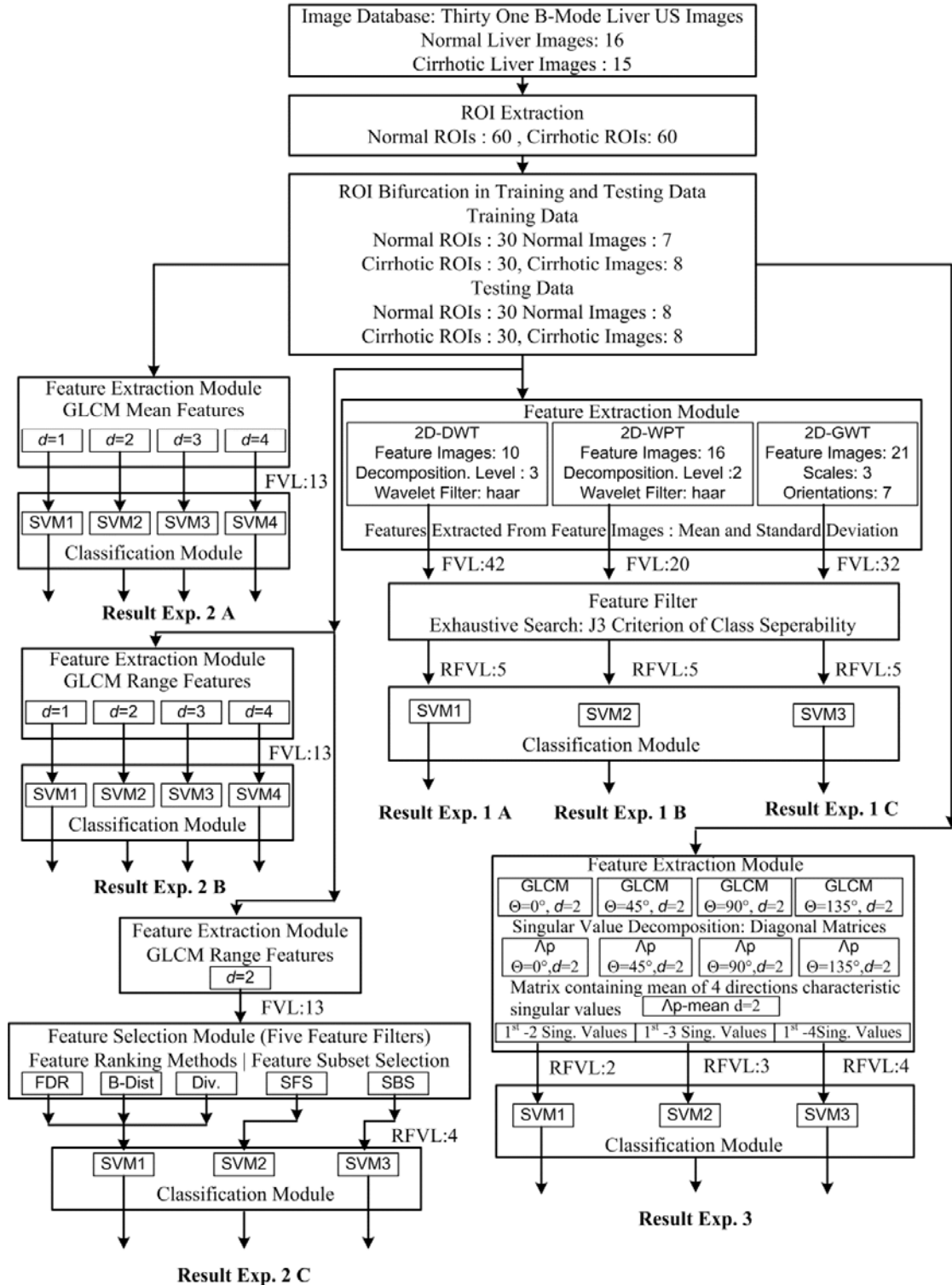
Fig. 4.3 Block Diagram – Experimental Work Flow (Prediction of Cirrhosis).
Note: FDR: Fisher discriminant ratio, B-Dist: Bhattacharya distance, Div.: Divergence, SFS: Sequential forward selection, SBS: Sequential backward selection, FVL: Feature vector length, RFVL: Reduced feature vector length, SVM: Support vector machine.

4.4 Experiment 1 – Design of CAD System for Prediction of Liver Cirrhosis using Multiresolution Texture Features

The block diagram indicating the experimental work flow for design of CAD system for prediction of liver cirrhosis using multiresolution texture features is shown in Fig. 4.4.

Dataset Description	
Normal Images: 15, Cirrhotic Images: 16	
Total ROIs: 120	
Training Data	Testing Data
NOR ROIs:30, Images:7 CIRR ROIs:30, Images:8	NOR ROIs:30, Images:8 CIRR ROIs:30, Images:8

Feature Extraction		
MRS (2D-DWT)	MRS (2D-WPT)	MRS (2D-GWT)
Feature Images: 10 Decomposition Level: 3 Wavelet Filter: haar	Feature Images: 16 Decomposition Level: 2 Wavelet Filter: haar	Feature Images: 21 Scales: 3 Oreintations: 7
Features Extracted: Mean and Standard Deviation		

FVL: 20   FVL: 32   FVL: 42

Feature Selection
Exhaustive search combined with J3 criterion of class seperability

RFVL: 5   RFVL: 5   RFVL: 5

Classification		
SVM 1	SVM 2	SVM 3
96.6	90	98.3

Fig. 4.4 Block diagram – Experimental work flow – Design of CAD system for prediction of liver cirrhosis using multiresolution texture features.
Note: MRS: Multiresolution Scheme, FVL: Feature vector length, RFVL: Reduced feature vector length, SVM: Support vector machine. Accuracy values are expressed in percentage.

The CAD system consist of feature extraction, feature selection and classification stages. In feature extraction stage, mean and standard deviation texture descriptors are extracted from sub-band feature images obtained by all the three multiresolution schemes, i.e., 2D-DWT, 2D-WPT and 2D-GWT. For feature selection, exhaustive search procedure combined with *J3* criterion of class seperability is used in order to obtain reduced TFVs of length 5

from initial TFVs of length 20, 32 and 42 in case of 2D-DWT, 2D-WPT and 2D-GWT, respectively. For classification, three different binary SVM classifiers are trained and tested with instances of reduced TFVs consisting of 5 most discriminative texture features selected by feature selection stage. These binary SVM classifiers are implemented using LibSVM library [31].

4.4.1　Feature Extraction − Experiment 1

Feature extraction can be carried on a single scale by considering the spatial interactions which exists over small neighborhoods, for example, by using gray level co-occurrence matrix (GLCM), gray level difference statistics (GLDS), neighborhood gray tone dependence matrix (NGTDM), statistical feature matrix (SFM) and gray level run length matrix (GLRL), etc [6, 36, 61]. Feature extraction in transform domain is carried out over various scales by using various multiresolution schemes such as discrete wavelet transform (DWT), wavelet packet transform (WPT) and Gabor wavelet transform (GWT). Computing texture features in transform domain is much more logical given the fact that human visual system (HVS) processes any image in a multiscale way and scale is a dominant aspect for analysis of texture. This multiscale processing by HVS provides motivation for multiresolution representations and multiscale texture analysis methods [43].

Extensive literature survey on texture classification in transform domain using multiresolution approaches like 2D-DWT, 2D-WPT and 2D-GWT reveals that mean and standard deviation features are frequently used not only for texture characterization of natural texture, i.e., Brodatz image database [12, 32, 120] but also for medical images [178, 192, 209]. In the present work mean and standard deviation texture descriptors evaluated from various sub-band feature images obtained by 2D-DWT, 2D-WPT and 2D-GWT are considered for characterization between normal and cirrhotic liver tissue.

4.4.1.1　Multiresolution Analysis

Texture characterization in transform domain using multiresolution features is affected by the choice of filter bank as the properties of the decomposition filters play important role in description of texture. The criteria like support width, shift invariance, orthogonality or biorthogonality and symmetry are important and must be considered for selecting an appropriate wavelet filter. Compact support means that the non-zero values exist only for a finite duration and support width indicates the length of the non-zero duration. A wavelet with small support width (compact support) is fast to compute and is therefore desired for

ease of implementation [205]. Orthogonality is another important property for conservation of energy at each decomposition level. Symmetry is required to avoid dephasing in processing images. It is a well known fact that only Haar wavelet has all the useful properties like compact support, orthogonality and symmetry. For the present work, Haar wavelet is considered for analysis with 2D-DWT and 2D-WPT multiresolution schemes. Mean and standard deviation texture descriptors are estimated from the sub-band feature images by using equations 4.1 and 4.2.

$$\text{Mean}_j = \frac{1}{M \times N} \sum_{X=1}^{M} \sum_{Y=1}^{N} \left| SI_j(X,Y) \right| \qquad 4.1$$

$$\text{Std}_j = \left(\frac{1}{M \times N} \sum_{X=1}^{M} \sum_{Y=1}^{N} \left| SI_j(X,Y) - \text{Mean}_j \right|^2 \right)^{1/2} \qquad 4.2$$

Here, SI_j are sub images of size $M \times N$ at level $j = 1, 2, \dots$

A. Two Dimensional - Discrete Wavelet Transform (2D-DWT)

The 2D-DWT tree up to third level of decomposition results in 10 sub-band feature images as shown in Fig. 4.5 [9, 10]. Mean and standard deviation texture descriptors estimated from all 10 sub-band feature images result in a TFV of length 20.
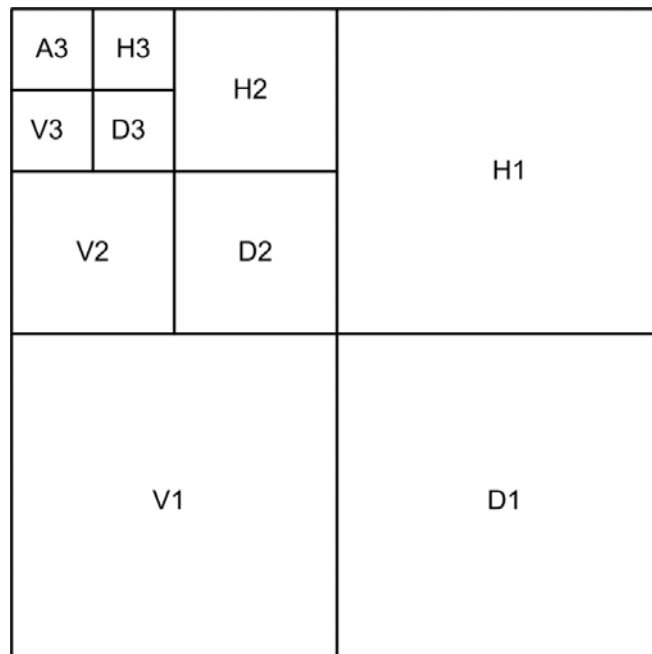
Fig. 4.5 2D-DWT tree up to 3rd level of decomposition. A3, H3, D3, V3, H2, D2, V2, H1, D1and V1 represent 10 sub-band feature images.

B.   Two Dimensional - Wavelet Packet Transform (2D-WPT):

The 2D-WPT tree up to second level of decomposition results in 16 sub-band feature images (wavelet packets) each representing a band in the frequency plane as shown in Fig. 4.6.
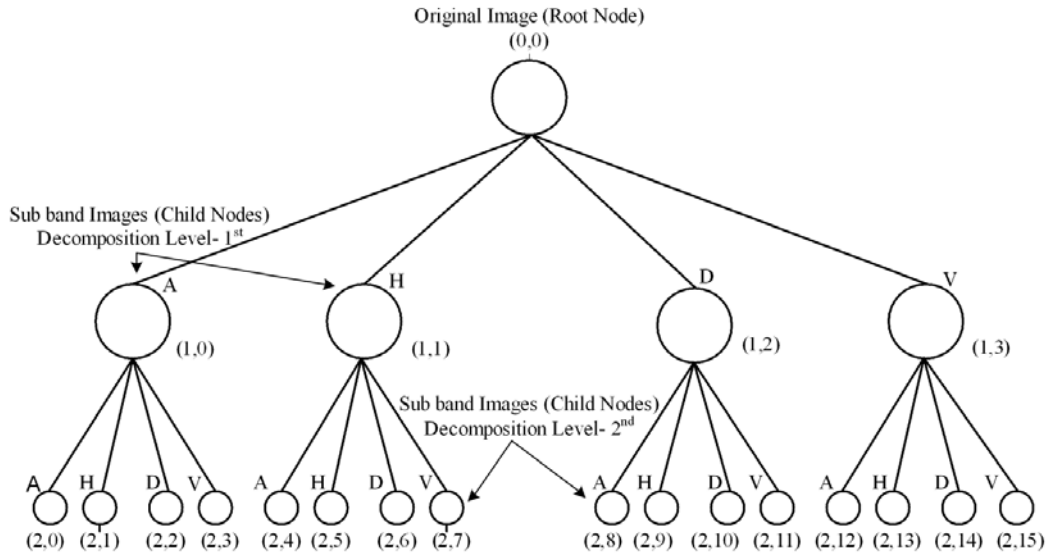
Fig. 4.6 2D-WPT tree up to 2nd level of decomposition [(2, 0) to (2, 15)] represents 16 sub-band feature images (wavelet packets).
Note: A: Approximate sub-band, H: Horizontal sub-band, D: Diagonal sub-band, V: Vertical sub-band.

Mean and standard deviation texture descriptors estimated from all 16 sub-band feature images result in a TFV of length 32.

C.   Two Dimensional - Gabor Wavelet Transform (2D-GWT)

Gabor wavelets are regarded as a set of frequency and orientation selective filters [9, 85, 124, 164]. 2D-GWT considering 3 scales (0, 1, 2) and 7 angles (22.5°, 45°, 67.5°, 90°, 112.5°, 135°, 157.5°) results in a group of 21 (7×3) wavelets with each wavelet capturing energy at a specific frequency and specific orientation. The real parts of Gabor filter family of 21 wavelets resulting from 13×13 convolution mask, 3 scales and 7 orientations are shown in Fig. 4.7.

When this group of Gabor filter family of 21 wavelets is convolved with a given ROI image a set of 21 filtered images (Gabor outputs or feature images) is obtained. Each filtered image represents the image information at a certain scale and orientation [90, 114].
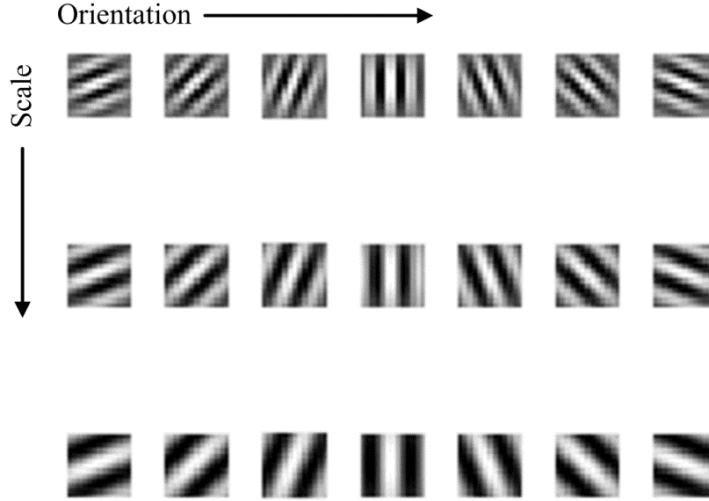
Fig. 4.7 Real parts of Gabor filter family of 21 wavelets.
Note: Orientation: 22.7°, 45°, 67.5°, 90°, 112.5°, 135° and 157.5° from left to right, Scale: 0, 1 and 2 from top to bottom.

The mean and standard deviation texture descriptors estimated from the 21 Gabor outputs or feature images results in a TFV of length 42.

4.4.2   Feature Selection — Experiment 1

In order to find the subset of five most discriminative texture features, exhaustive search procedure combined with *J3* criterion of class seperability based on within-class scatter matrix, between-class scatter matrix and mixture scatter matrix is used as a feature selection method [173]. The *J3* criterion is used to quantify the class seperability of instances of the TFVs in the reduced feature space based on the way these instances are scattered in the reduced feature space. The subset of 5 most discriminative texture features is obtained by looking for the maximum value of *J3* criterion by exhaustive search with all possible combinations of TFVs of length five. The *J3* criterion of class seperability is obtained by using equations 4.3 to 4.9.

4.4.2.1 Within-Class Scatter Matrix

$$S_w = \sum_{i=1}^{M} P_i \sum_i \qquad 4.3$$

Here, *M* represents the number of classes, for the present work *M* is 2 and $\sum_i$ represents the covariance matrix for class ω_i, such that

58

$$\sum_i = E\left[(x-\mu_i)(x-\mu_i)^T\right]$$

P_i represents priori probability of class ω_i, i.e., $P_i = n_i/N$, here, n_i represents number of training samples of class ω_i out of total N training samples. μ_i represents individual class mean, i.e., $\mu_i = E[x_i]$, where E is the expectation operator. The trace $\{S_w\}$ which is the sum of the diagonal elements of within-class scatter matrix S_w represents the average over all classes, variance of the features.

4.4.2.2 Between-Class Scatter Matrix

$$S_b = \sum_{i=1}^{M} P_i(\mu_i - \mu_0)(\mu_i - \mu_0)^T \tag{4.5}$$

Here, μ_0 represent global mean vector given by

$$\mu_0 = \sum_{i=1}^{M} P_i\mu_i \tag{4.6}$$

The trace $\{S_b\}$ represents distance of the mean of each individual class from their respective global mean value, averaged over all classes.

4.4.2.3 Mixture Scatter Matrix

S_m represents the covariance matrix of the feature vector with respect to the global mean μ_o, and is given as

$$S_m = E\left[(x-\mu_0)(x-\mu_0)^T\right] \tag{4.7}$$

Also, $$S_m = S_w + S_b \tag{4.8}$$

The trace $\{S_m\}$ represents the sum of variances of features around their respective global mean.

4.4.2.4 J3 Criterion

It is defined by the following relation and is used to find optimal features.

$$J3 = trace\{S_w^{-1} S_m\} \tag{4.9}$$

A large value of *J3* indicates that training samples are well clustered around their respective class means and the clusters of different classes are well separated, i.e., small within-class variance and large between-class distances.

4.4.3   Classification — Experiment 1

It is well known that classifier designs which use regularization like SVM are less prone to over fitting and obtain good generalization performance to a certain extent even without feature space dimensionality reduction [25]. For the present work SVM classifier is chosen for classification between normal and cirrhotic liver tissue.

4.4.3.1 SVM Classifier

The SVM classifier attempts to construct an optimum hyper plane in the higher dimensional feature space to separate the training data with minimum expected risk [27]. Nonlinear mapping of the training data from input space to higher dimensional feature space is carried out by kernel functions which satisfy Mercer's theorem. In the present work, the performance of Gaussian radial basis function (GRBF) kernel is considered as it provides better results in most situations.

Crucial step for obtaining good generalization performance is correct choice of the regularization parameter C and kernel parameter γ. The regularization parameter C attempts to maximize the margin while keeping low value for training error. In the present study, extensive search is carried out in the parameter space for the values of $C \in \{2^{-4}, 2^{-3},\ldots\ldots, 2^{15}\}$ and $\gamma \in \{2^{-12}, 2^{-11},\ldots\ldots, 2^{5}\}$ using 10 fold cross validation to obtain optimal values of C and γ for training the SVM model. The SVM classifier trained with this C and γ is subsequently used for classification of unseen testing dataset.

Out of total 120 ROIs (60 Normal and 60 cirrhotic ROIs), the training dataset and testing dataset have 60 ROIs each, with 30 normal ROIs and 30 cirrhotic ROIs. i.e., 50 % of the data from each class is hold out as testing dataset for evaluating the performance of the classifier. To avoid the bias caused by unbalanced feature values the extracted features were normalized in the range [0, 1] by using min-max normalization procedure.

4.4.4   Results — Experiment 1

4.4.4.1 Feature Selection Results

In case of 2D-DWT the mean and standard deviation texture descriptors, estimated from 10 sub-band feature images, result in a TFV of length 20. Five most discriminative texture descriptors (3 mean and 2 standard deviation texture descriptors), estimated from four sub-band feature images (shaded in gray in Fig. 4.8), are selected by exhaustive search procedure on the basis of *J3* criterion of class seperability. Note that both mean and standard deviation

texture descriptors obtained from horizontal detail coefficients at 1st level of decomposition are discriminative.
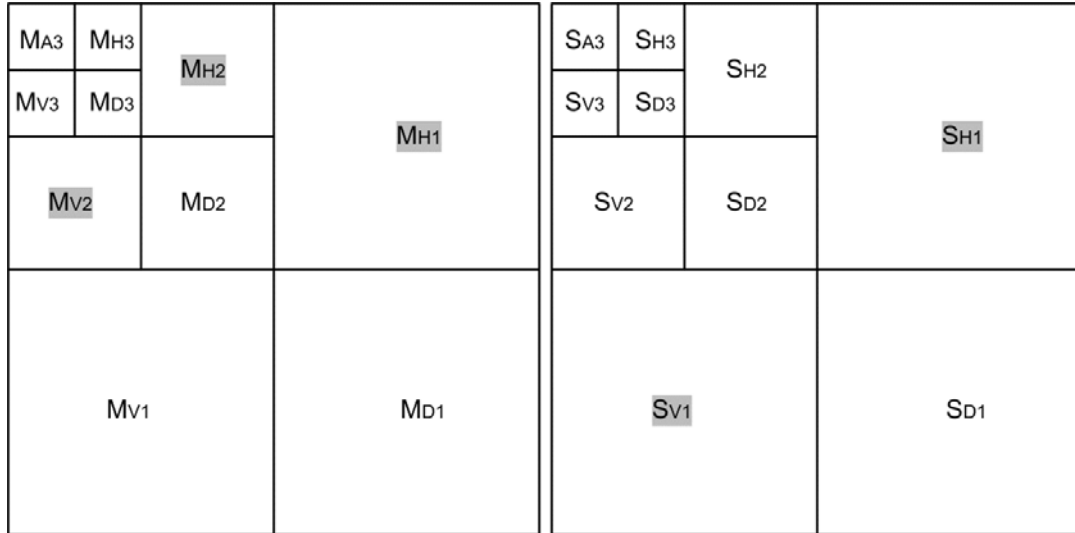
Fig 4.8 2D-DWT tree up to 3rd level of decomposition.
Note: M: Mean, S: Standard deviation, Five most discriminative texture features (shaded in gray).

In case of 2D-WPT the mean and standard deviation texture descriptors, estimated from 16 sub-band feature images, result in a TFV of length 32. Five most discriminative texture descriptors (2 mean and 3 standard deviation texture descriptors), estimated from five sub-band feature images selected by exhaustive search procedure on the basis of *J3* criteria of class seperability are shaded in gray in Fig. 4.9 and Fig. 4.10.

M$_{AA}$ (2,0)	M$_{AH}$ (2,1)	M$_{HA}$ (2,4)	M$_{HH}$ (2,5)	S$_{AA}$ (2,0)	S$_{AH}$ (2,1)	S$_{HA}$ (2,4)	S$_{HH}$ (2,5)
M$_{AV}$ (2,3)	M$_{AD}$ (2,2)	M$_{HV}$ (2,7)	M$_{HD}$ (2,6)	S$_{AV}$ (2,3)	S$_{AD}$ (2,2)	S$_{HV}$ (2,7)	S$_{HD}$ (2,6)
M$_{VA}$ (2,12)	M$_{VH}$ (2,13)	M$_{DA}$ (2,8)	M$_{DH}$ (2,9)	S$_{VA}$ (2,12)	S$_{VH}$ (2,13)	S$_{DA}$ (2,8)	S$_{DH}$ (2,9)
M$_{VV}$ (2,15)	M$_{VD}$ (2,14)	M$_{DV}$ (2,11)	M$_{DD}$ (2,10)	S$_{VV}$ (2,15)	S$_{VD}$ (2,14)	S$_{DV}$ (2,11)	S$_{DD}$ (2,10)

Fig. 4.9 2D-WPT decomposition at 2nd level.
Note: M: Mean, S: Standard deviation. Five most discriminative texture features are shaded in gray.

61
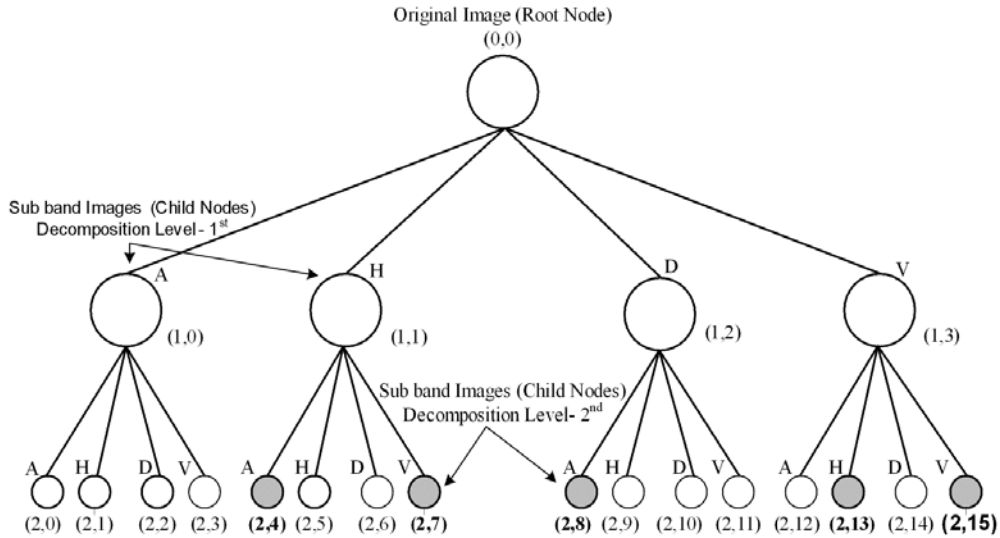
Fig. 4.10 2D-WPT tree at 2nd level of decomposition (2, 0), (2, 1),……..,(2,15) represent 16 sub-band feature images (wavelet packets).
Note: M: Mean, S: Standard deviation. Five most discriminative texture features are shaded in gray.

In case of 2D-GWT considering three scales (0, 1, 2) and seven angles (22.5°, 45°, 67.5°, 90°, 112.5°, 135°, 157.5°) results in a group of 21 (7×3) wavelets with each wavelet capturing energy at a specific frequency and specific orientation. When the real parts of Gabor filter family of 21 wavelets (as shown in Fig. 4.7) are convolved with a given ROI image, a set of 21 filtered images (Gabor outputs or feature images) is obtained. The mean and standard deviation texture descriptors, estimated from the 21 Gabor outputs or feature images, results in a TFV of length 42. Five most discriminative texture descriptors (5 mean texture descriptors), estimated from selected scale and orientation sensitive Gabor output feature images selected by exhaustive search procedure on the basis of *J3* criterion of class seperability are shaded in gray as shown in Fig. 4.11.

M$_{(0,22.5°)}$ S$_{(0,22.5°)}$	M$_{(0,45°)}$ S$_{(0,45°)}$	M$_{(0,67.5°)}$ S$_{(0,67.5°)}$	M$_{(0,90°)}$ S$_{(0,90°)}$	M$_{(0,112.5°)}$ S$_{(0,112.5°)}$	M$_{(0,135.5°)}$ S$_{(0,135.5°)}$	M$_{(0,157.5°)}$ S$_{(0,157.5°)}$
M$_{(1,22.5°)}$ S$_{(1,22.5°)}$	M$_{(1,45°)}$ S$_{(1,45°)}$	M$_{(1,67.5°)}$ S$_{(1,67.5°)}$	M$_{(1,90°)}$ S$_{(1,90°)}$	M$_{(1,112.5°)}$ S$_{(1,112.5°)}$	M$_{(1,135.5°)}$ S$_{(1,135.5°)}$	M$_{(1,157.5°)}$ S$_{(1,157.5°)}$
M$_{(2,22.5°)}$ S$_{(2,22.5°)}$	M$_{(2,45°)}$ S$_{(2,45°)}$	M$_{(2,67.5°)}$ S$_{(2,67.5°)}$	M$_{(2,90°)}$ S$_{(2,90°)}$	M$_{(2,112.5°)}$ S$_{(2,112.5°)}$	M$_{(2,135.5°)}$ S$_{(2,135.5°)}$	M$_{(2,157.5°)}$ S$_{(2,157.5°)}$

Fig 4.11 Twenty one Gabor outputs or feature images.
Note: M: Mean, S: Standard deviation. Five most discriminative features are shaded in gray.

The study carried out by [90] studied the classification of liver diseases from CT (computed tomograpgy) images by using scale and orientation sensitive Gabor features along with SVM classifer. Their study highligted the Gabor outputs for various classes for visualisation purposes. The real parts of Gabor outputs for a normal and cirrhotic ROI selected randomly from the image database are shown in Fig. 4.12(a) and Fig. 4.12(b) for visualization. It is observed that mean texture descriptors obtained from five Gabor output images encircled in Fig. 4.12(a) and Fig. 4.12(b) provide adequate descrimination between normal and cirrhotic ROIs.
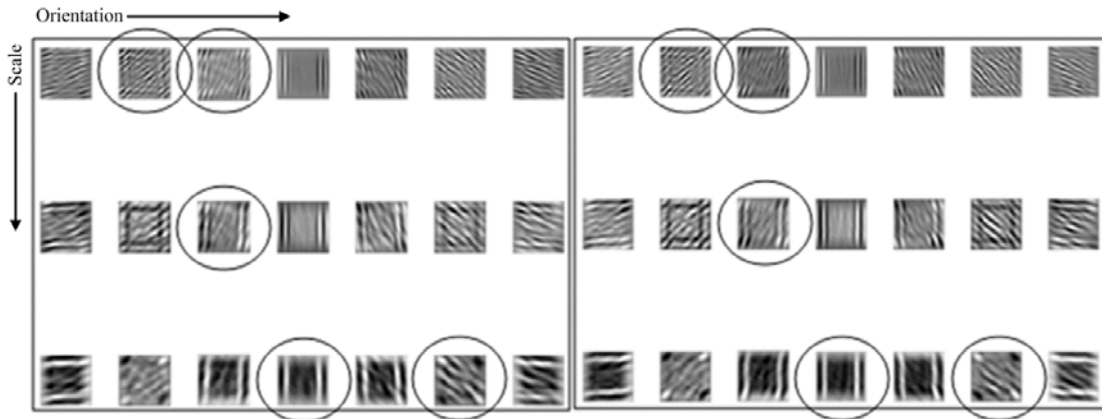
Fig. 4.12 (a) Real part of Gabor outputs (Normal ROI); **(b)** Real part of Gabor outputs (Cirrhotic ROI). **Note:** Mean texture descriptors computed from 5 encircled Gabor outputs provide adequate discrimination between normal and cirrhotic ROIs.

4.4.4.2 Classification Results

The performance of the CAD system without feature selection is depicted in Table 4.1.

Table 4.1 *Comparison of classification performance of SVM for 2D-DWT, 2D-WPT and 2D-GWT Multiresolution resolution schemes (MRS) with mean and standard deviation texture descriptors (TDs).*

Classification Performance: SVM						
MRS (*TDs*)(*FVL*)		*CM*		*Acc.* (*%*)	*Sen.* (*%*)	*Spec.* (*%*)
		C	N			
2D-DWT (μ, σ) (20)	C	26	4	93.3	86.6	100
	N	0	30			
		C	N			
2D-WPT (μ, σ) (32)	C	29	1	98.3	96.6	100
	N	0	30			
		C	N			
2D-GWT (μ, σ) (42)	C	30	0	98.3	100	96.6
	N	1	29			

Note: MRS: Multiresolution scheme, TDs: Texture descriptors, FVL: Feature vector length, CM: Confusion matrix, Acc.: Accuracy, Sen.: Sensitivity, Spec.: Specificity, N: Normal and C: Cirrhotic. The maximum accuracy and sensitivity is obtained by 2D-GWT texture signatures (shaded in gray).

From Table 4.1, it can be observed that maximum classification accuracy of 98.3 % and sensitivity of 100 % is obtained with TFVs of length 42 consisting of mean and standard deviation texture descriptors estimated from 21 feature images (obtained by convolving the ROI with a family of 21 Gabor wavelets obtained for 3 scales and 7 orientations). The classification accuracy of 98.3 % but slightly reduced sensitivity of 96.6 % is achieved with TFVs of length 32 consisting of mean and standard deviation texture descriptors estimated from 16 sub-band feature images obtained by 2D-WPT by using Haar wavelet filter. In comparison it is observed that with TFVs of length 20 (consisting of mean and standard deviation texture descriptors estimated from 10 sub-band feature images) obtained by using 2D-DWT using Haar wavelet filter, the classification accuracy of 93.3 % and sensitivity of 86.6 % is obtained. It can be observed that the best performance is obtained by using 2D-GWT texture descriptors. The performance of the proposed CAD system with feature selection (i.e., with 5 most discriminative mean and standard deviation texture descriptors found by exhaustive search to maximize the *J3* criterion of class seperability) is depicted in Table 4.2. From Table 4.2, it can be observed that the maximum classification accuracy and sensitivity of 98.3 % and 100 % is obtained by using only five mean texture descriptors computed from Gabor outputs or feature images obtained at selected scale and orientations. In comparison, the reduced TFVs of length five in case of 2D-DWT and 2D-WPT yielded the classification accuracies of 96.6 % and 95 % with sensitivity values of 93.3 % and 90 %, respectively.

Table 4.2 *Comparison of classification performance of SVM for 2D-DWT, 2D-WPT and 2D-GWT Multiresolution resolution schemes (**MRS**) with five most discriminating mean and standard deviation texture descriptors (**TDs**).*

Classification Performance: SVM						
(MRS)(TDs)(RFVL)	*CM*			*Acc.(%)*	*Sen.(%)*	*Spec.(%)*
2D-DWT (μ, σ) (5)		C	N	96.6	93.3	100
	C	28	2			
	N	0	30			
2D-WPT (μ, σ) (5)		C	N	95.0	90.0	100
	C	27	3			
	N	0	30			
2D-GWT (μ) (5)		C	N	98.3	100	96.6
	C	30	0			
	N	1	29			

Note: MRS: Multiresolution scheme, TDs: Texture descriptors, RFVL: Reduced feature vector length, CM: Confusion matrix, Acc.: Accuracy, Sen.: Sensitivity, Spec.: Specificity, N: Normal and C: Cirrhotic. The maximum accuracy and sensitivity is obtained by 2D-GWT texture descriptors, (shaded in gray).

From Table 4.2, it can be observed that the maximum classification accuracy and sensitivity of 98.3 % and 100 % is obtained by using only five mean texture descriptors computed from Gabor outputs or feature images obtained at selected scale and orientations. In comparison, the reduced TFVs of length five in case of 2D-DWT and 2D-WPT yielded the classification accuracies of 96.6 % and 95 % with sensitivity values of 93.3 % and 90 %, respectively.

The highest classification accuracy of 98.3 % and sensitivity of 100 % is achieved by using a subset of five mean texture descriptors obtained from Gabor outputs feature images at selective scale and orientations, i.e., $M_{(0,22.5°)}$, $M_{(0,45°)}$, $M_{(1,45°)}$, $M_{(2,90°)}$ and $M_{(2,135°)}$ shown highlighted in Fig 4.11. These five scale and orientation selective mean texture features yield the sensitivity of 100 %.

The results of the study indicate that only a subset 5 mean texture descriptors, obtained from selected scale and orientation sensitive Gabor outputs, can significantly account for textural variations exhibited by normal and cirrhotic liver. Further experimentation were carried out to evaluate the performance of five most discriminative Gabor mean features by fine tuning the parameters of polynomial and sigmoid kernel with SVM classifier.

It is observed that maximum accuracy of 95 % is obtained with polynomial kernel, and maximum accuracy of 83.3 % is obtained with sigmoid kernel. In case of RBF kernel, maximum classification accuracy of 98.3 % is obtained. The results of the study indicate that the application of radial basis function (RBF) kernel outperformed the performance of polynomial and sigmoid kernel for the present classification task.

4.4.5 Conclusions – Experiment 1

The results of the study demonstrate that selective frequency and orientation properties of Gabor filters are extremely useful for providing multiscale texture description specifically in case of discrimination between normal and cirrhotic liver. Only mean texture descriptors obtained from five frequency, and orientation selective Gabor output feature images are sufficient to account for textural variations exhibited by normal and cirrhotic liver. In further experiments, the efficacy of GLCM features for characterization of normal and cirrhotic liver tissue is evaluated.

4.5 Experiment 2A and 2B — Design of CAD System for Prediction of Liver Cirrhosis using GLCM - Mean and GLCM - Range Texture Features

GLCM method [42, 45, 61] is most commonly used method for texture analysis. The four direction GLCMs obtained for both normal as well as cirrhotic ROI are shown in Fig. 4.13(a) and Fig. 4.13(b) respectively.

It can be seen that the GLCM elements are concentrated in case of normal ROI and relatively more dispersed in case of cirrhotic ROI. This fact was reported earlier in study [67],

In further experiments, an attempt is made to capture this difference in dispersion of GLCM elements by considering GLCM texture features for the classification task.
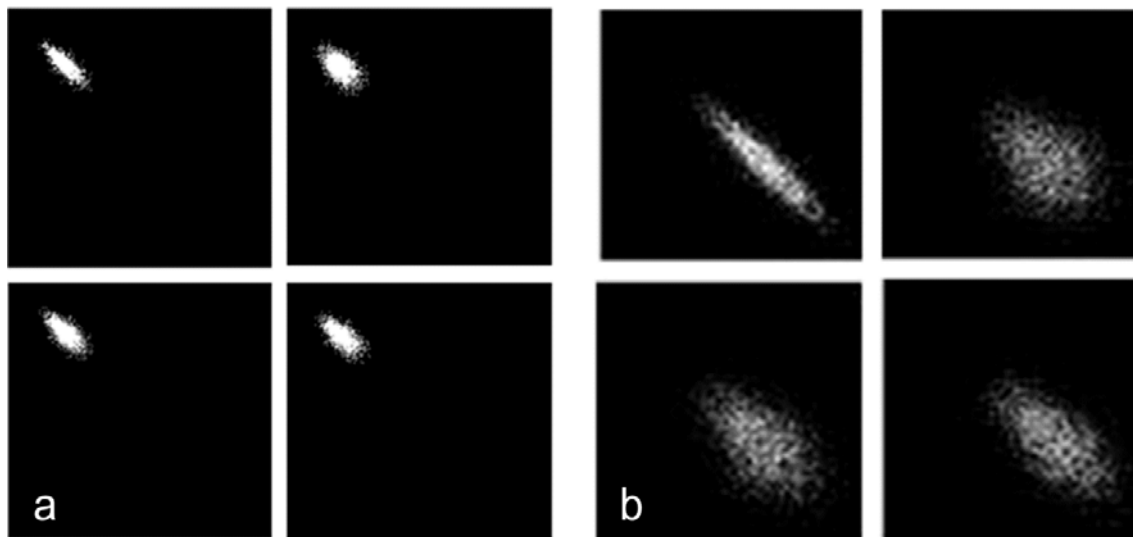
Fig. 4.13 (a) GLCMs for a normal ROI for 4 directions (0º, 45º, 90º and 135º); **(b)** GLCMs for a cirrhotic ROI for 4 directions (0º, 45º, 90º and 135º).

In the experiment 2-A and 2-B the efficacy of TFVs consisting of thirteen GLCM-Mean features (computed at inter-pixel distance d varying from 1 to 4) and the efficacy of TFVs consisting of thirteen GLCM-Range features (computed at inter-pixel distance d varying from 1 to 4) is tested for characterization of normal and cirrhotic liver by using SVM classifiers.

The block diagram indicating the experimental work flow for the design of CAD system for prediction of liver cirrhosis using GLCM features is depicted in Fig 4.14.

Fig. 4.14 Block Diagram – Experimental work flow – Design of CAD system for prediction of liver cirrhosis using GLCM-Mean and GLCM-Range features.
Note: FVL: Feature vector length, The maximum classification accuracy value of 100 % is obtained by TFV of length thirteen consisting of GLCM-Mean features computed at $d = 2$ and also with TFVs of length thirteen each with GLCM-Range features computed at $d = 2$ and $d = 4$ (shaded in gray).

4.5.1 Feature Extraction — Experiment 2A and 2B

The GLCM-Mean and GLCM-Range features estimated for inter-pixel $d = 1$ to 4 and are used as TFVs for the present study [67]. For example, GLCM-Mean feature, inverse difference moment (IDM) at inter-pixel distance $d = 1$ and GLCM-Range feature IDM at inter-pixel distance $d = 1$ are calculated by using equations 4.10 and 4.11.

$$GLCM - Mean_{IDM(d=1)} = \left(\frac{A + B + C + D}{4} \right) \qquad 4.10$$

$$GLCM - Range_{IDM(d=1)} = \max\left(A, B, C, D\right) - \min\left(A, B, C, D\right) \qquad 4.11$$

Here,

$A = GLCM_{IDM(\theta=0°, d=1)}$, $B = GLCM_{IDM(\theta=45°, d=1)}$, $C = GLCM_{IDM(\theta=90°, d=1)}$ and $D = GLCM_{IDM(\theta=135°, d=1)}$

67

In the same way, four TFVs consisting of thirteen GLCM-Mean features (F1 to F13 of Table 4.3) are computed at inter-pixel distance d varying from 1 to 4 and four TFVs consisting of thirteen GLCM-Range texture features (F14 to F26 of Table 4.3) are computed at inter-pixel distance d varying from 1 to 4. These features are tabulated in Table 4.3.

Table 4.3 *GLCM-Mean features (F1 to F13) and GLCM-Range features (F14 to F26)*

Feat. Id	Feature Name	Feat. Id	Feature Name
F1	Angular second moment-Mean	F14	Angular second moment-Range
F2	Contrast-Mean	F15	Contrast-Range
F3	Correlation-Mean	F16	Correlation-Range
F4	Sum of squares: variance-Mean	F17	Sum of squares: variance-Range
F5	IDM-Mean	F18	IDM-Range
F6	Sum average-Mean	F19	Sum average-Range
F7	Sum Variance-Mean	F20	Sum variance-Range
F8	Sum Entropy-Mean	F21	Sum entropy-Range
F9	Entropy-Mean	F22	Entropy-Range
F10	Difference variance-Mean	F23	Difference variance-Range
F11	Difference entropy-Mean	F24	Difference entropy-Range
F12	Inf. measures of corr.1-Mean	F25	Inf. measures of corr.1-Range
F13	Inf. measures of corr.2-Mean	F26	Inf. measures of corr.2-Range

4.5.2 Classification — Experiment 2A and 2B

In classification module, the TFVs consisting of GLCM-Mean texture features (F1 to F13) and TFVs consisting of GLCM-Range texture features (F14 to F26) computed for inter-pixel distance d varying from 1 to 4 are fed separately to eight binary SVM classifiers.

4.5.3 Results — Experiment 2A and 2B

The classification accuracy, sensitivity and specificity values obtained by using TFVs consisting of thirteen GLCM-Mean features (F1 to F13) computed at $d = 1$ to 4 and for TFVs consisting of GLCM-Range features (F14 to F26) computed for $d = 1$ to 4 along with SVM classifier are tabulated in Table 4.4.

Table 4.4 *The classification accuracies obtained for GLCM-Mean features (d = 1 to 4) and GLCM-Range features (d = 1 to 4) with SVM classifier.*

TFV	CM			Acc. (%)	Sen.(%)	Spec.(%)
Classification Performance: SVM						
GLCM-Mean F1 to F13 for *d* = 1		C	N	98.3	96.6	100
	C	29	1			
	N	0	30			
GLCM-Mean F1 to F13 for *d* = 2		C	N	100	100	100
	C	30	0			
	N	0	30			
GLCM-Mean F1 to F13 for *d* = 3		C	N	92.8	96.6	93.3
	C	29	1			
	N	2	28			
GLCM-Mean F1 to F13 for *d* = 4		C	N	98.3	100	96.6
	C	30	0			
	N	1	29			
GLCM-Range F14 to F26 for *d* = 1		C	N	98.3	100	96.6
	C	30	0			
	N	1	29			
GLCM-Range F14 to F26 for *d* = 2		C	N	100	100	100
	C	30	0			
	N	0	30			
GLCM-Range F14 to F26 for *d* = 3		C	N	98.3	100	96.6
	C	30	0			
	N	1	29			
GLCM-Range F14 to F26 for *d* = 4		C	N	100	100	100
	C	30	0			
	N	0	30			

Note: TFV: Texture feature vector, CM: Confusion matrix, Acc.: Accuracy, Sen.: Sensitivity, Spec.: Specificity, N: Normal and C: Cirrhotic. The maximum classification accuracy value of 100 % is obtained by GLCM-Mean features computed at *d* = 2 and GLCM-Range features computed at *d* = 2 and *d* = 4 (shaded in gray).

From Table 4.4, it can be observed that with TFV consisting of thirteen GLCM-Mean features estimated at inter-pixel distance *d* = 2 provide 100 % classification accuracy and sensitivity for characterization between normal and cirrhotic liver. It is also observed that the TFVs consisting of thirteen GLCM-Range features estimated at inter-pixel distances *d* = 2 and *d* = 3 also provide 100 % classification accuracy and sensitivity for characterization of normal and cirrhotic liver tissue.

4.5.4 Conclusions – Experiment 2A and 2B

It can be observed that TFV consisting of thirteen GLCM-Mean texture features computed at inter-pixel distance *d* = 2 as well as TFVs consisting of thirteen GLCM-Range features computed at inter-pixel distance *d* = 2 and at *d* = 4 provide effective discrimination

between normal and cirrhotic ROIs. Further, in order to find an optimal reduced TFV consisting of discriminative GLCM-Range texture features, the feature set consisting of TFVs of thirteen GLCM-Range features computed at inter-pixel distance $d = 2$ is subjected to various feature filter methods in experiment 2C.

4.6 Experiment 2C — Design of CAD System for Prediction of Liver Cirrhosis using Selected GLCM-Range Texture Features

The block diagram indicating the experimental work flow for the design of CAD system for prediction of liver cirrhosis using selected GLCM-Range features computed at inter-pixel distance $d = 2$ is depicted in Fig 4.15.

Image Database
Normal Images:15, Cirrhotic Images: 16

ROI Extraction
Total ROIs: 120

Training Data	Testing Data
NOR: ROIs:30, Images:7	NOR: ROIs:30, Images:8
CIRR: ROIs:30, Images:8	CIRR: ROIs:30, Images:8

Feature Extraction Module
GLCM(range) Features $d = 2$

FVL:13

Feature Selection Module
Five Feature Filters

Three Feature Ranking Methods	Two Feature Subset Selection Methods
FDR, B. Distance, Divergence [Feature Id. F2,F8,F11,F4]	SFS[Feature Id.F2,F4,F5,F12], SBS[Feature Id.F2,F4,F9,F12]

RFVL:4   RFVL:4   RFVL:4

Classification Module		
SVM1	SVM2	SVM3
96.6	90	100

Fig. 4.15 Block Diagram – Experimental work flow – Design of CAD system for prediction of liver cirrhosis using selected GLCM-Range features computed at inter-pixel distance $d = 2$.

4.6.1   Feature Extraction – Experiment 2C

From the results of experiment 2A and 2B, it is observed that thirteen GLCM-Range features computed at inter-pixel distances $d = 2$ provide 100 % classification accuracy and sensitivity for classification between normal and cirrhotic liver tissue. In this experiment, an investigation is made to determine the optimal GLCM-Range features computed at inter-pixel

distance $d = 2$, which could account for the textural variations within normal and cirrhotic liver tissue. In feature extraction module, thirteen GLCM-Range features (tabulated as F1 to F13 in Table 4.5) are computed at inter-pixel distance $d = 2$.

Table 4.5 *GLCM-Range Features for d = 2, (F1 to F13)*

Feature Id	Feature
F1	Angular second moment-Range
F2	Contrast-Range
F3	Correlation-Range
F4	Sum of squares: variance-Range
F5	Inverse difference moment-Range
F6	Sum average-Range
F7	Sum variance-Range
F8	Sum entropy-Range
F9	Entropy-Range
F10	Difference variance-Range
F11	Difference entropy-Range
F12	Information measures of correlation-1-Range
F13	Information measures of correlation-2-Range

4.6.2 Feature Selection — Experiment 2C

In feature selection module, five feature filers including three scalar feature ranking methods based on class seperability measures, i.e., Fisher discriminant ratio (FDR), divergence (Div.) and Bhattacharyya distance (B-dist) and two feature subset selection methods, i.e., sequential forward search (SFS) and sequential backward search (SBS) based on divergence as a measure of class seperability are implemented [85, 173]. For each feature filter only top four features were retained for the classification task.

In scalar feature ranking methods each feature is considered individually and ranked according to some class seperability criterion like:

(i) *Fisher's Discriminant Ratio (FDR)*: The ability of any individual feature to discriminate two classes can be quantified by estimating the FDR by using equation 4.12.

$$\text{FDR} = \frac{\left(\mu_1 - \mu_2\right)^2}{\left(\sigma_1^{2} + \sigma_2^{2}\right)} \qquad\qquad 4.12$$

Here, μ_1, μ_2 represent the mean values and σ_1^{2}, σ_2^{2} represent the variances of a single feature in two classes.

71

(ii) *Divergence*: The divergence ($Div._{1,2}$) between two classes in l dimensional space can be estimated by using equation 4.13.

$$\text{Div.}_{1,2} = \frac{1}{2} trace\left\{S_1^{-1}S_2 + S_2^{-1}S_1 - 2I\right\} + \frac{1}{2}(m_1 - m_2)^T(S_1^{-1} + S_2^{-1})(m_1 - m_2)$$

4.13

Here, S_i represents the covariance matrix, m_i represents mean vector of ith class and I represents $l \times l$ identity matrix.

(iii) *Bhattacharyya Distance* : The Bhattacharyya distance (B-$dist_{1,2}$) between two classes can be estimated by using equation 4.14.

$$B - dist_{1,2} = \frac{1}{8}(m_1 - m_2)^T\left(\frac{S_1 + S_2}{2}\right)^{-1}(m_1 - m_2) + \frac{1}{2}\ln\frac{0.5(|S_1 + S_2|)}{\sqrt{|S_1||S_2|}}$$

4.14

Here, S_i represents the covariance matrix, m_i represents mean vector of ith class and $|\ |$ represents matrix determinant.

In feature subset selection methods like SBS and SFS, best combination of predefined number of features is obtained by using some class seperability criterions like FDR, Div. and B-dist, etc. In the SFS procedure, firstly a single most discriminatory feature is selected from all the available features based on adopted class seperability criterion. This feature is permanently selected and its combination with all other remaining features is tested and the best pair is chosen again in terms of adopted class seperability criterion. The process continues until the desired number of features is reached [169].

In the SBS procedure, firstly a single feature is removed from the complete set of features. The feature which when removed, results in maximum separation between two classes in the remaining feature space is considered for exclusion. The process is continued and a single feature is removed with every iteration such that the adopted class seperability measure ensures maximum class seperability amongst the remaining feature space. The process is terminated when the desired numbers of features are remaining [127].

4.6.3   Classification – Experiment 2C

In classification module, the reduced TFVs of feature vector length (FVL) four resulting from corresponding feature filters are fed separately to three binary SVM classifiers.

4.6.4   Results — Experiment 2C

4.6.4.1 Feature Selection Results

In feature selection module, three scalar feature ranking methods based on class seperability measures including Fisher discriminant ratio (FDR), divergence and Bhattacharyya distance as well as two feature subset selection methods including sequential forward search (SFS) and sequential backward search (SBS) based on divergence as a measure of class seperability are implemented. For each feature filter only top four features are retained as reduced TFVs for the classification task. The initial TFVs of FVL thirteen, consisting of GLCM-Range texture features computed at inter-pixel distance $d = 2$ are fed to these five feature filters and reduced TFVs of FVL four are obtained. The top four most discriminatory GLCM-Range features selected by individual feature filters are tabulated in Table 4.6.

Table 4.6 *Top four ranked features listed in order of priority selected by scalar feature ranking methods based on class seperability criterion (S. No 1to 3). A subset consisting of four most discriminatory features, i.e., optimal reduced TFV selected by feature subset selection methods, SFS and SBS using divergence as class seperability measure (S. No. 4 and 5).*

S.No	Feature Filter	Ordered List of Feature Ids
1	Fisher discriminant ratio (FDR)	F2, F8, F11, F4
2	Divergence (Div.)	F2, F8, F11,F4
3	Bhattacharyya distance (B-Dist)	F2, F8, F11, F4
4	Sequential forward selection (SFS)	F2, F4, F9, F12
5	Sequential backward selection (SBS)	F2, F4, F5, F12

From Table 4.6, it can be observed that same four GLCM-Range features, i.e., feature ids (F2, F8, F11 and F4) representing (contrast, sum entropy, difference entropy and sum of squares: variance) are selected as top four discriminatory features by all the three scalar feature ranking algorithms (S. No 1to 3). The SFS feature subset selection method yielded the best combination of four features with feature ids, F2, F4, F9 and F12 (i.e., contrast, sum of squares: variance, entropy and information measures of correlation-1) as optimal reduced TFV and SBS feature subset selection method yielded the best combination of four features with feature ids F2, F4, F5 and F12 (i.e., contrast, sum of squares: variance, inverse difference moment and information measures of correlation-1) as optimal reduced TFV.

4.6.4.2 Classification Results

In classification module the top four GLCM-Range texture features obtained by different feature filters are fed separately to three binary SVM classifiers. The classification accuracy,

sensitivity and specificity values obtained by using selected GLCM-Range features are tabulated in Table 4.7.

Table 4.7 *The classification accuracy, sensitivity and specificity values obtained for selected GLCM-Range features computed for d = 2 with SVM classifiers.*

Features Filters [Feature Ids]	CM			Acc. (%)	Sen.(%)	Spec.(%)
Classification Performance: SVM						
FDR, Div. and B-Distance [F2,F8,F11,F4]		C	N	96.6	96.6	96.6
	C	29	1			
	N	1	29			
SFS [F2,F4,F9,F12]		C	N	90.0	86.6	93.3
	C	26	4			
	N	2	28			
SBS [F2,F4,F5,F12]		C	N	100	100	100
	C	30	0			
	N	0	30			

Note: CM: Confusion matrix, Acc.: Accuracy, Sen.: Sensitivity, Spec.: Specificity, N: Normal and C: Cirrhotic. The maximum accuracy of 100 % obtained for features selected by SBS feature selection procedure (shaded in gray).

From Table 4.7, it can be observed that four GLCM-Range features (i.e., feature ids, F2, F8, F11 and F4 representing contrast, sum entropy, difference entropy and sum of squares: variance selected as top four discriminatory features by three scalar feature ranking algorithms based on FDR, Div., and B-dist as measure of class seperability) yield the classification accuracy and sensitivity value of 96.6 %. It can also be observed the best combination of four features (i.e., feature ids F2, F4, F9 and F12 representing contrast, sum of squares: variance, entropy and information measures of correlation-1) selected by SFS feature subset selection method yield the classification accuracy and sensitivity values of 90 % and 86.6 % respectively.

Further, it is observed that the best combination of four features (i.e., feature ids, F2, F4, F5 and F12 representing contrast, sum of squares: variance, inverse difference moment and information measures of correlation-1) selected by SBS feature subset selection method yield the highest classification accuracy and sensitivity value of 100 % for characterization between normal and cirrhotic liver.

4.6.5   Conclusions – Experiment 2C

From the results of experiment 2C, it can be concluded that out of total thirteen GLCM-Range features computed for inter-pixel distance $d = 2$, considered initially in the experiment 2-B, only four GLCM-Range features (i.e., contrast, sum of squares: variance, inverse

difference moment and information measures of correlation-1) selected by SBS feature subset selection method based on Div. as a measure of class seperability are significant to account for textural variations exhibited by normal and cirrhotic liver.

4.7 Experiment 3 — Design of CAD System for Prediction of Liver Cirrhosis using Features derived by Singular Value Decomposition of GLCM

The block diagram indicating the experimental work flow for design of CAD system for prediction of liver cirrhosis using singular value mean features derived by SVD of GLCM is shown in Fig. 4.16.

Image Database		
Normal Images:15, Cirrhotic Images: 16		
ROI Extraction		
Total ROIs: 120		
Training Data		Testing Data
NOR: ROIs:30, Images:7 CIRR: ROIs:30, Images:8		NOR: ROIs:30, Images:8 CIRR: ROIs:30, Images:8

Feature Extraction Module			
Four Directions GLCMs for $d = 2$			
GLCM $\theta = 0°, d = 2$	GLCM $\theta = 45°, d = 2$	GLCM $\theta = 90°, d = 2$	GLCM $\theta = 135°, d = 2$
Singular Value Decomposition (Diagonal Matrices)			
Λp $\theta = 0°, d = 2$	Λp $\theta = 45°, d = 2$	Λp $\theta = 90°, d = 2$	Λp $\theta = 135°, d = 2$
Matrix containing mean of Four directions characteristic singular values			
Λp-mean ($d = 2$) matrix			
1st two singular values	1st three singular values		1st four singular values

RFVL:2   RFVL:3   RFVL:4

Classification Module		
SVM1	SVM2	SVM3
98.3	98.3	100

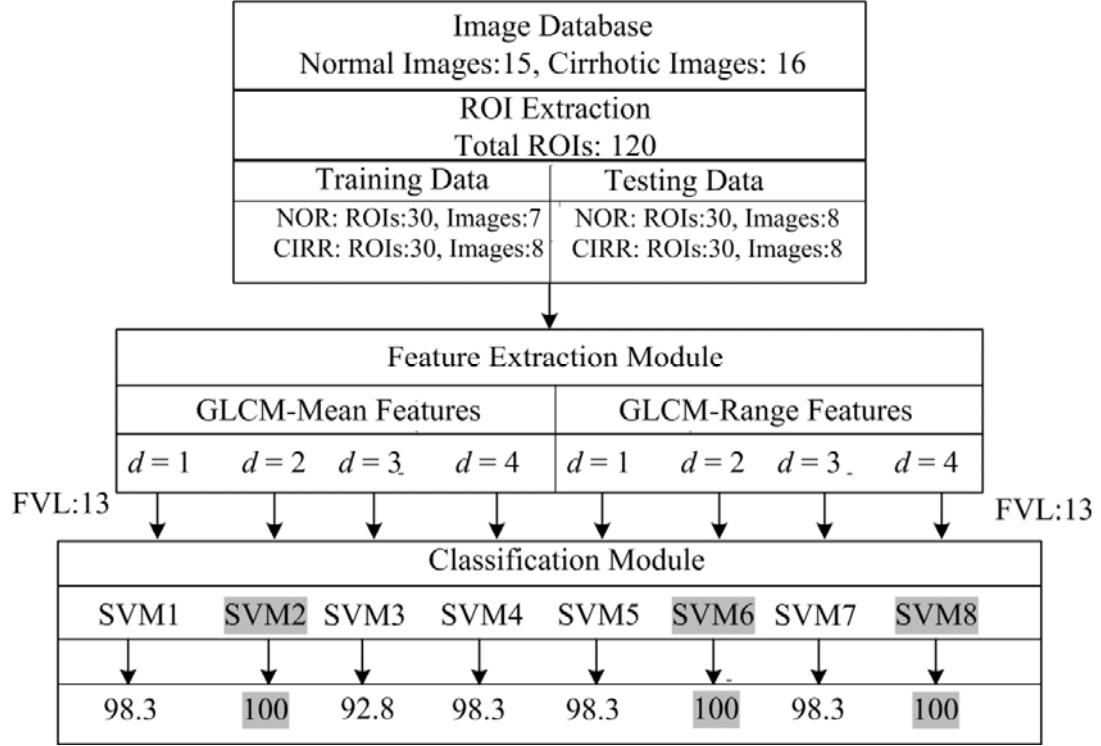**Fig. 4.16** Block Diagram – Experimental work flow – Design of CAD system for prediction of liver cirrhosis using singular value mean features.
Note: RFVL: Reduced feature vector length, (Classification accuracies are expressed in percentage). Maximum classification accuracy of 100 % is obtained from first four singular values obtained from SVD of GLCM (shaded in gray).

4.7.1 Feature Extraction — Experiment 3

Singular value features have been used extensively with SVM classifier for various classification tasks [63, 171, 175, 205]. In the present work, singular value mean features derived by SVD of GLCM are considered for classification between normal and cirrhotic liver.

In feature extraction module, four direction GLCMs (i.e., for $\theta = 0°$, 45°, 90° and 135°) with inter-pixel distance $d = 2$ are estimated. These four GLCMs are then decomposed by singular value decomposition (SVD) method. By SVD, any matrix is decomposed into its component matrices, which expose many useful properties of the original matrix [175, 205].

The GLCM of a ROI consists of $n \times n$ matrix A_p of real numbers such that $p = 1$ to L. The matrix A_p decomposed by SVD takes the following form:

$$A_P = U_P \Lambda_P V_P^T \tag{4.15}$$

Here, U_p and V_p are orthogonal and represent row vector and column vector, respectively and Λ_p is a diagonal matrix whose diagonal entities represent the singular values which are real and decreasing.

$$\sigma_p^1 \geq \sigma_p^2 \geq \sigma_p^3 \geq \sigma_p^4 ..... \geq \sigma_p^n \geq 0 \tag{4.16}$$

The diagonal matrix $\Lambda_p(d = 2, \theta = 0°)$ obtained by SVD of GLCM ($d = 2, \theta = 0°$) contain singular value-$1(0°)$, singular value-$2(0°)$ up to singular value-$n(0°)$ as diagonal entities. Similarly, diagonal matrices $\Lambda_p(d = 2, \theta = 45°)$, $\Lambda_p(d = 2, \theta = 90°)$ and $\Lambda_p(d = 2, \theta = 135°)$ obtained by SVD of corresponding GLCMs are obtained. Finally, Λ_p-mean ($d = 2$), i.e., a diagonal matrix consisting of mean of the four directions (0°, 45°, 90° and 135°) characteristic singular values is estimated. The matrix Λ_p-mean ($d = 2$) contains n singular values as its diagonal elements, i.e., σ_p^1(mean), σ_p^2(mean), σ_p^3(mean), σ_p^4(mean), σ_p^5(mean), ..., σ_p^n(mean) such that σ_p^1(mean) = $[\sigma_p^1(0°) + \sigma_p^1(45°) + \sigma_p^1(90°) + \sigma_p^1(135°)] / 4$. Similarly, the mean value for all the singular values is calculated [185]. The average values of the first 15 singular values-mean features, [i.e., average of sixty σ_p^1(mean) values up to average of sixty σ_p^{15}(mean) values corresponding to 60 normal ROIs and average of sixty σ_p^1(mean) values up to average of sixty σ_p^{15}(mean) values corresponding to 60 cirrhotic ROIs] are plotted in Fig. 4.17
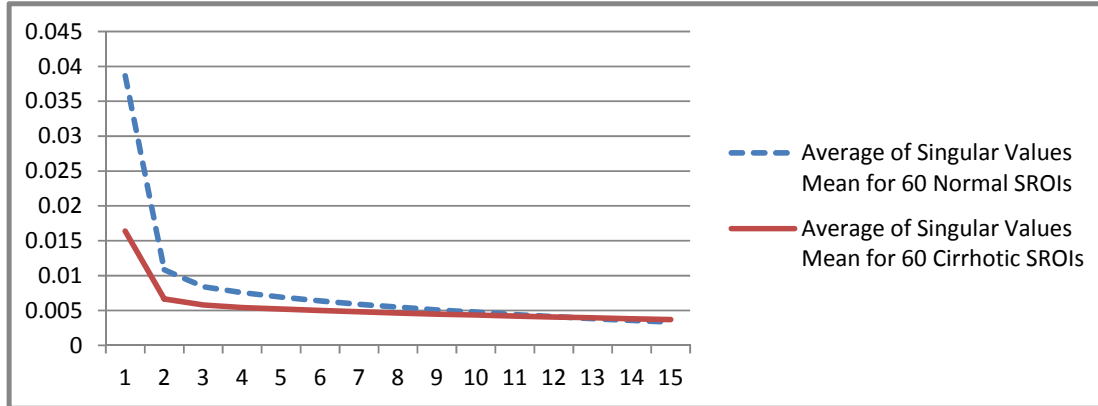
Fig. 4.17 First 15 singular value mean features (Average value for 60 normal liver ROIs and 60 cirrhotic liver ROIs.

From Fig. 4.17., it is observed that the average of first four singular value-mean features differ significantly in case of normal and cirrhotic liver ROIs and therefore these singular value mean features are considered for further analysis.

4.7.2 Classification – Experiment 3

In classification module the TFVs of FVL, two (i.e., first two singular value mean features), FVL, three (i.e., first three singular value mean features) and FVL, four (i.e., first four singular value mean features) are fed separately to three binary SVM classifiers.

4.7.3 Results – Experiment 3

The classification accuracy, sensitivity and specificity values obtained by using first two, three and four singular value mean features with SVM classifier are tabulated in Table 4.8.

Table 4.8 *The classification accuracies obtained for singular value mean features obtained by SVD of GLCM with SVM classifier.*

Classification Performance: SVM					
Features		*CM*	*Acc. (%)*	*Sen.(%)*	*Spec.(%)*
First two singular value mean features		C	N	98.3	96.6	100
	C	29	1			
	N	0	30			
First three singular value mean features		C	N	98.3	96.6	100
	C	29	1			
	N	0	30			
First four singular value mean features		C	N	100	100	100
	C	30	0			
	N	0	30			

Note: CM: Confusion matrix, Acc.: Accuracy, Sen.: Sensitivity, Spec.: Specificity, N: Normal and C: Cirrhotic. The maximum accuracy is obtained by using first four singular value mean features (shaded in gray)

Form Table 4.8, it is observed that a first four singular value mean features yield the highest classification accuracy, sensitivity and specificity value of 100 %.

4.7.4   Conclusions — Experiment 3

It can be concluded that first four singular value mean features estimated by SVD of GLCM contain most of the energy and texture information which is significant to account for textural variations exhibited by normal and cirrhotic liver.

4.8 Concluding Remarks

The comparison of the results, obtained by different experiments undertaken in the present work for prediction of liver cirrhosis using B-Mode ultrasound images are shown in the Table 4.9

Table 4.9 *Comparison of results (prediction of liver cirrhosis).*

Experiment	Features	Acc. (%)
Exp. 1A	Selected multi-resolution features [MRS: 2D-DWT, RFVL: 5]	96.6
Exp. 1B	Selected multi-resolution features [MRS: 2D-WPT, RFVL: 5]	90.0
Exp. 1C	Selected multi-resolution features [MRS: 2D-GWT, RFVL: 5]	98.3
Exp. 2A	GLCM-Mean features ($d = 2$) [FVL:13]	100
Exp. 2B	GLCM-Range features ($d = 2$) [FVL:13]	100
Exp. 2B	GLCM-Range features ($d = 4$) [FVL:13]	100
Exp. 2C	Selected GLCM-Range features ($d = 2$) [FDR, B-Dist and Div, RFVL:4]	96.6
Exp. 2C	Selected GLCM-Range features ($d = 2$) [SFS, RFVL:4]	90.0
Exp. 2C	Selected GLCM-Range features ($d = 2$) [SBS, RFVL:4]	100
Exp. 3	First two singular value mean features [RFVL:2]	95.0
Exp. 3	First three singular value mean features [RFVL:3]	95.0
Exp. 3	First four singular value mean features [RFVL:4]	100

Note: MRS: Multiresolution scheme, FVL: Feature vector length, RFVL: Reduced feature vector length, Acc. Accuracy, For experiment 2A and 2B, the results obtained by GLCM-Mean and GLCM-Range features yielding the maximum classification accuracy are reported.

It is observed that among the 2D-DWT, 2D-WPT and 2D-GWT multiresolution texture descriptors, the highest classification accuracy of 98.3 % is achieved by using only mean texture descriptors obtained from five frequency and orientation selective Gabor output feature images. The results of the study demonstrate that selective frequency and orientation properties of Gabor filters are extremely useful for providing multiscale texture description in case of discrimination between normal and cirrhotic liver.

Further, by plotting four direction GLCMs of a normal and cirrhotic ROI, it is observed that GLCM elements are concentrated for normal ROI and relatively dispersed for cirrhotic ROI, therefore in the present study characterization between normal and cirrhotic liver by using GLCM-Mean and GLCM-Range texture features computed at inter-pixel distance d varying from 1 to 4 is carried out. It is worth observing that TFV consisting of thirteen GLCM-Mean features computed at inter-pixel distance $d = 2$ yield the classification accuracy and sensitivity values of 100 %. Also, TFV consisting of thirteen GLCM-Range features computed at inter-pixel distance $d = 2$ and the TFV consisting of thirteen GLCM-Range features computed at inter-pixel distance $d = 4$ yield the classification accuracy and sensitivity value of 100 % for characterization between normal and cirrhotic liver tissue.

The feature set consisting of TFV of thirteen GLCM-Range features computed at inter-pixel distance $d = 2$ is subjected three feature ranking methods and two feature subset selection methods in order to obtain the optimal GLCM-Range texture features for characterization of normal and cirrhotic liver tissue. It is observed that a subset of four GLCM-Range computed at inter-pixel distance $d = 2$ selected by SBS feature subset selection method with divergence as a class seperability measure (consisting of features, contrast, sum of squares-variance, inverse difference moment and information measures of correlation-1) also yield the maximum classification accuracy and sensitivity value of 100 % for characterization between normal and cirrhotic liver tissue.

Since reduced TFV of FVL five consisting of scale and orientation selective multi-resolution Gabor mean texture features yield the classification accuracy of 98.3 % and reduced TFV of FVL four consisting of selected GLCM-Range texture features yield the classification accuracy of 100 %, another experiment based on singular value mean features derived by SVD of GLCM is carried out and it is observed that the first four singular value mean features obtained by SVD of GLCM yield the classification accuracy and sensitivity value of 100 % for discrimination of normal and cirrhotic ROIs.

Early diagnosis of liver cirrhosis is absolutely essential as cirrhosis is an irreversible liver disease and also patients with liver cirrhosis are at increased risk of development of hepatocellular carcinoma [71]. Early diagnosis always helps radiologist for better management of the disease and adequate scheduling of treatment options. The promising results obtained by the experiments carried out in this study indicate that while only mean

79

texture descriptors obtained from five frequency and orientation selective Gabor output images are sufficient to account for textural variations exhibited by normal and cirrhotic liver, the CAD system design using first four singular value mean features obtained by SVD of GLCM yields 100 % classification accuracy and sensitivity for characterization between normal and cirrhotic liver tissue. Thus, it can be concluded that the proposed CAD system design using singular value mean features derived by SVD of GLCM along with SVM classifier can be routinely used in a clinical environment to assist radiologists for diagnosis of liver cirrhosis.

In case of diffuse liver diseases the progression takes place from normal liver tissue towards different grades of fibrosis. The end stage of fibrosis is referred to as cirrhosis which is considered as a precursor to development of hepatocellular carcinoma [71]. Given the fact that diagnosis of small HCCs developed on already nodular cirrhotic liver parenchyma by B-Mode US images is a daunting challenge even for experienced radiologists, it is necessary to investigate the progression of cirrhosis towards HCC. Thus, it is clinically significant to investigate if the changes in the textural patterns of the liver correspond to cirrhosis or indicate development of HCC. Early detection of HCC is necessary for better management of liver malignancy by adequate scheduling of treatment options. Therefore the design of an efficient CAD system for characterization of normal, cirrhotic and HCC liver is taken up as the next objective and is discussed in Chapter 5.

Chapter 5

Characterization of Normal, Cirrhotic and HCC Liver

5.1 Introduction

Although biopsy is the "gold standard" for diagnosing liver diseases; ultrasonography is mostly preferred for screening, due to its noninvasive, nonradioactive and inexpensive nature. Echotexture of normal liver, as it appears on ultrasound (US), is homogeneous with medium echogenicity, i.e., it exhibits same or slightly increased echogenicity compared to the right kidney. Cirrhosis is considered to be the end stage of chronic hepatopathies which often leads to hepatocellular carcinoma (HCC). The diagnosis of cirrhosis is best achieved by looking at the granular structure of the liver parenchyma and the degree of nodularity present in the heterogeneous echotexture. HCC is viewed as most probable solid primary malignant liver lesion occurring on cirrhotic liver. Most small HCCs (SHHCs) are diagnosed with a follow-up procedure for patients with cirrhosis. In few cases, when HCC develops on normal liver parenchyma it can be easily diagnosed by its sonographic appearance as it appears as a well differentiated HCC or as fibrolamellar HCC (commonly appears with calcified areas). A lesion can be labeled as typical in appearance when its subjective diagnosis can be made with a good confidence level by looking at the US examination. The associated radiologists opined that no sonographic appearance is typical for HCCs as they exhibit a high degree of variability in terms of sonographic appearances even within SHCCs and large HCCs (LHCCs).

SHCCs frequently appear as hypoechoic nodule (solid tumor nodule without necrosis) or as hyperechoic nodule (solid tumor likely containing fat). In very few cases SHCCs can also be isoechoic, i.e., same echogenicity as surrounding parenchyma. The HCC lesion may also exhibit hyperechoic echotexture with a hypoechoic halo (rim like structure surrounding HCC lesion) or alternatively hypoechoic echotexture with hyperechoic halo sign. LHCCs appear much more complex and heterogeneous with mixed echogenicity (coarse irregular internal echoes) as a result of areas of necrosis, fibrosis as well as active growth areas [110].

It is always considered difficult to diagnose small focal liver lesions (FLLs < 2 cm) developed on already nodular and coarse textured cirrhotic liver parenchyma by using B-Mode liver US images. Also, since cirrhosis is a precursor to development of HCC it is necessary to monitor the progress of the disease from cirrhosis towards HCC. Thus, it is essential to investigate whether the textural changes in the liver parenchyma are cirrhotic changes or indicate the development of HCC. Therefore, it is clinically significant to design an efficient

CAD system for characterization of normal, cirrhotic and HCC liver. The study presented in this Chapter addresses this issue.

There are few related researches in literature for characterization of liver tissue as normal, cirrhotic or HCC. The study in [200] reports characterization between normal, cirrhotic and HCC liver by using combination of roughness and granularity texture descriptors computed at various resolutions along with Fourier power spectrum based texture features by using bayes classifier. In another related research [199], multi threshold dimension feature vector based on fractal geometry is proposed for classification between normal, cirrhotic and HCC liver. The study in [97] used fractal dimension of subimages obtained at various resolutions with M-band wavelet transform as fractal feature vector for classification between normal, cirrhotic and HCC liver. The study in [95] used the same fractal feature vector and developed a system to characterize normal, cirrhotic and HCC by fusion of classifiers. The study in [95, 97], reports the use of images scanned by high resolution scanner, (i.e., 32-pixel/cm and 8-bit/pixel resolution) with ROI size of 64×64 pixels, (i.e., 2 cm by 2 cm for the given image resolution); however, in case of SHCCs (< 2 cm), it is not possible to extract such a large ROI. The dataset description reported in studies [95, 97, 199, 200] doesn't clarify if only HCCs developed on cirrhotic liver are considered and also about the number of SHCCs and LHCCs considered for their CAD designs.

Keeping in view the research perspective in literature, the current study is different in the sense that only HCC lesions evolved on cirrhotic liver are considered and the representative dataset of HCC images consisting of both small HCC images (SHCCIs) and large HCC images (LHCCIs) is used for designing an efficient classifier.

Although detection of HCC in early stages has important clinical value, at the same time it is observed that in many cases HCCs are detected in advanced stages therefore the participating radiologists opined that isolation of a single case series, i.e., HCC lesions into incipient (small) and advanced (large) HCC for characterization is not adequate as a ROI from HCC lesion representing primary malignancy of liver should be predicted as HCC irrespective of the fact whether the ROI belongs to SHCC or LHCC.

It is worth mentioning that conventional gray scale B-Mode US offers limited sensitivity for detection of lesions developed on already nodular and coarse textured cirrhotic liver parenchyma as a result differentiating the texture patterns exhibited by HCCs developed on top of cirrhosis from its preceding stage of cirrhosis presents a daunting challenge even for experienced radiologists, therefore a US tissue characterization system capable of providing

adequate discrimination between normal liver, cirrhotic changes in the liver, and HCC developed on cirrhotic liver, is proposed in this study.

5.2 Dataset Description – CAD for Normal, Cirrhotic and HCC liver

The design of CAD system for characterization of normal, cirrhotic and HCC liver tissue was carried out with 56 B-Mode liver US images, i.e., 15 normal images, 16 cirrhotic images and 25 HCC images.

Experienced participating radiologists were of the view that the HCC image dataset used in the present work consists of representative images, offering a high degree of variability encountered during subjective analysis of these lesions in routine clinical practice. The size of SHCC varied from 1.5 to 1.9 cm and the size of LHCC varied from 2.1 to 5.6 cm, respectively. Fig. 5.1 and Fig. 5.2 represent 5 SHCCI variants and 5 LHCCI variants from the acquired image database.
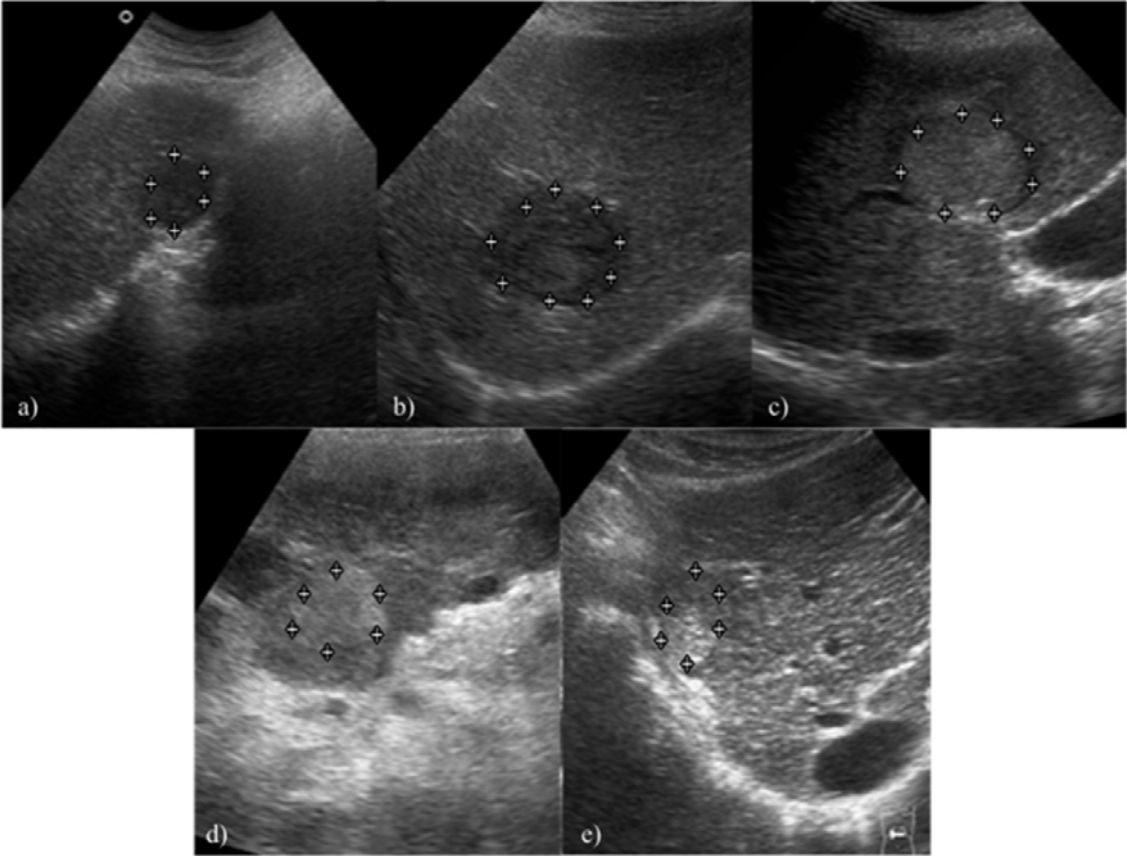
Fig. 5.1(a) Hypoechoic SHCCI; **(b)** Hypoechoic SHCCI; **(c)** Hyperechoic SHCCI with hypoechoic halo; **(d)** Homogeneously hyperechoic SHCCI without halo; **(e)** Variant of SHCCI with mixed echogenicity (coexistence of hyperechoic and isoechoic areas).
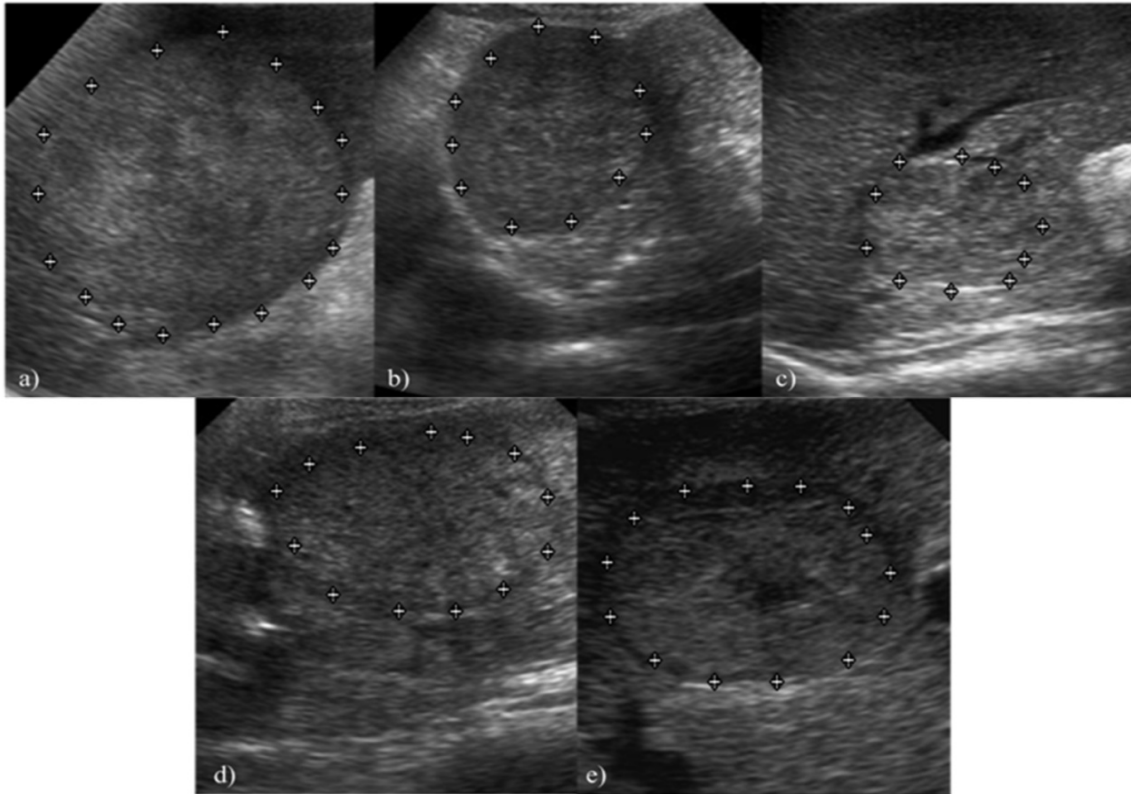
Fig. 5.2 Heterogeneous echotexture represents complex and chaotic structure exhibited by LHCCIs due to coexistence of areas of necrosis, fibrosis and active growth areas.
Note: Hypoechoic halo formation is visible in **(d)** and **(e)**. Necrotic area is visible in the centre of LHHCI shown in **(e).**

The protocols followed for collection of dataset, selection of ROIs and selection of ROI size are described in Section 3.4 of Chapter 3. The sample of normal, cirrhotic and HCC liver image from the acquired image database with ROIs marked are shown in Fig. 5.3.
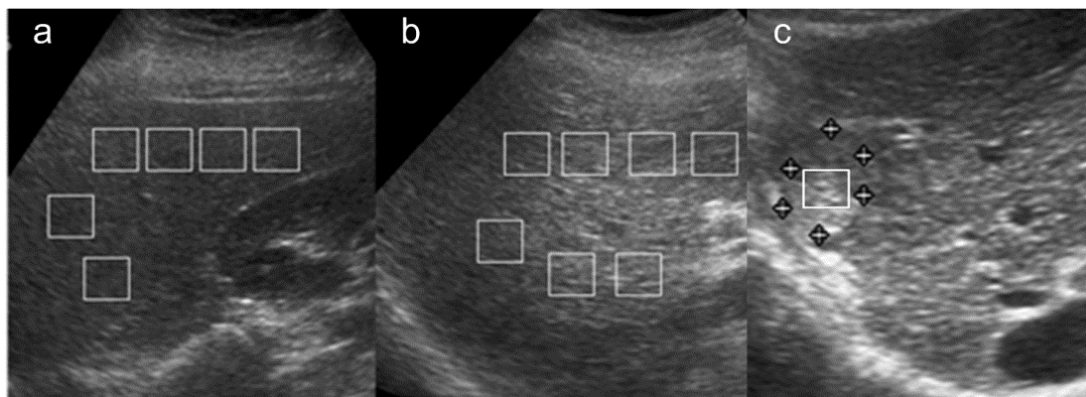
Fig. 5.3 Sample B-Mode US images with ROIs marked: **(a)** Normal liver image; **(b)** Cirrhotic liver image; **(c)** HCC on top of cirrhosis.

The detailed description of the dataset used in this study, and its bifurcation into training dataset and testing dataset is shown in Fig. 5.4.
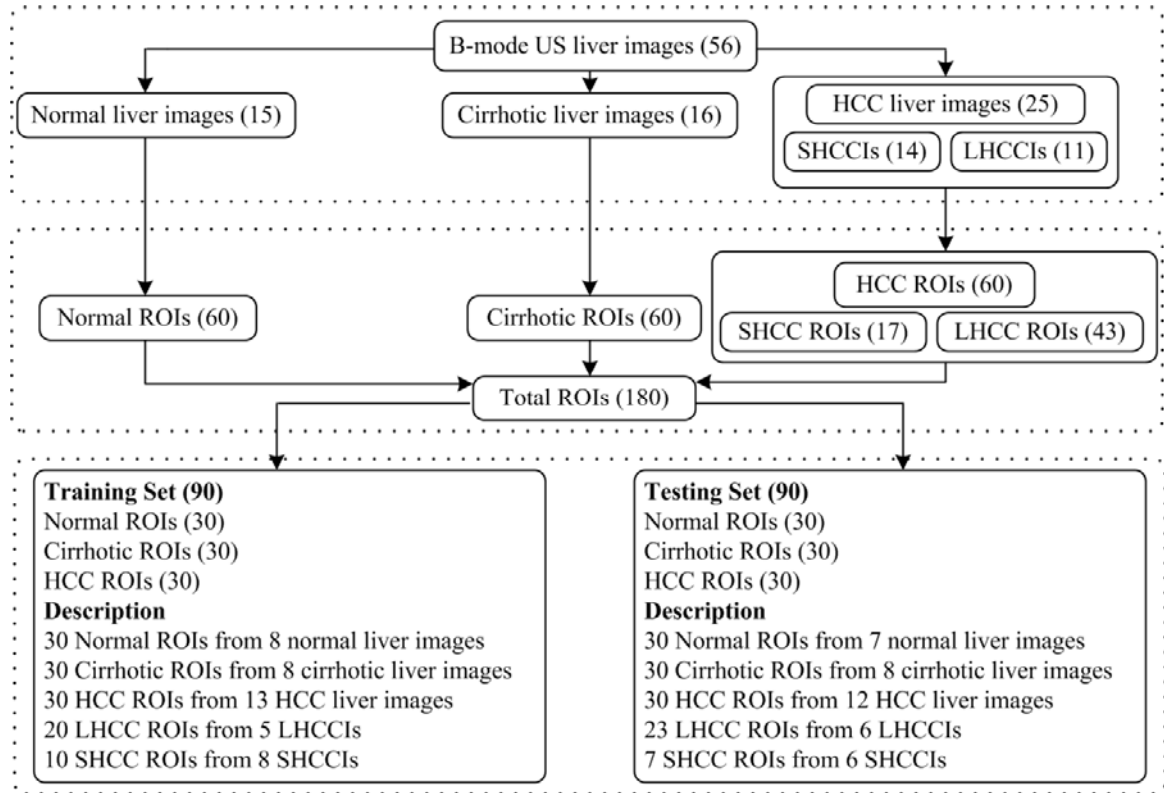
Fig. 5.4 Dataset description – CAD for normal, cirrhotic and HCC liver.
Note: LHCCIs: Large HCC images, SHCCIs: Small HCC images, LHCC: Large HCC, SHCC: Small HCC

5.3 Proposed CAD System for Normal, Cirrhotic and HCC Liver Tissue

For implementation of the proposed CAD system, database of 180 non-overlapping ROIs is created from 56 clinically acquired US images. The CAD system consisted of three modules: (*i*) feature extraction module, (*ii*) feature selection module, and (*iii*) classification module. The block diagram of the proposed CAD system for characterization of normal, cirrhotic and HCC liver using B-Mode US images is shown in Fig. 5.5.

In feature extraction module, each ROI in the database is decomposed up to 2nd level of decomposition by 2D-WPT, resulting in 16 sub-band feature images for each ROI. The texture feature vectors (TFVs) of length 48 are computed by estimating mean, standard deviation (Std) and energy features from all the 16 sub-band feature images for each ROI. In feature selection module, Genetic algorithm-support vector machine (GA–SVM) feature selection method is used to find the optimal reduced TFV, which can significantly account for the textural variations exhibited by normal, cirrhotic and HCC liver. The feature set consisting of instances of optimal reduced TFV outputted by the feature selection module is passed to the classification

module. In classification module, a multiclass SVM classifier is implemented using LibSVM library [31].
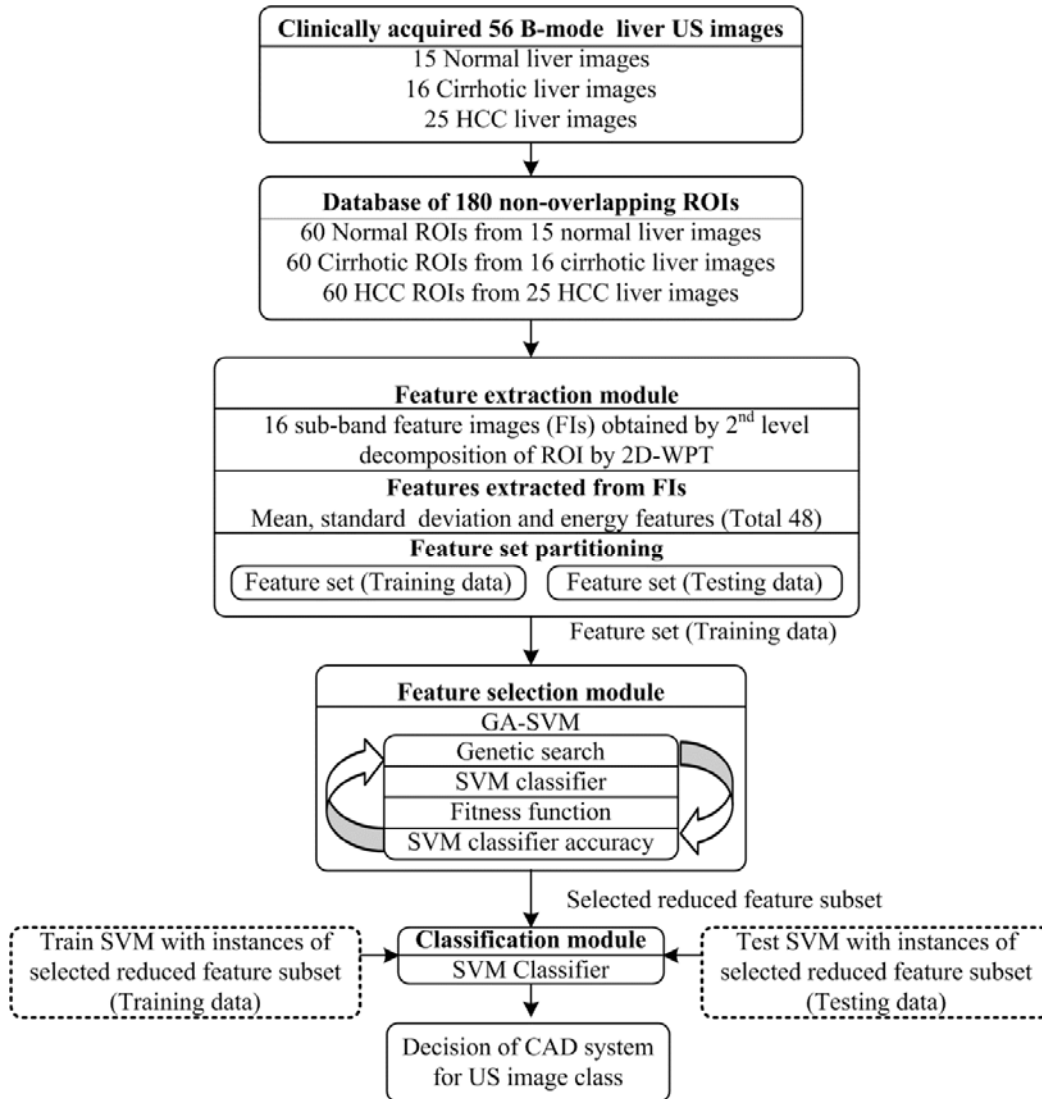
Fig. 5.5 Proposed CAD system for characterization of normal, cirrhotic and HCC liver.

5.3.1   Feature Extraction Module

A speckled image of liver tissue is produced on US [44]. It is a well known fact that speckle in US images carries useful information and therefore cannot be treated as a typical random noise [58, 65, 165, 193]. As speckle represents high frequency components of the US image, the 2D-WPT, which is considered as richer space-frequency multiresolution analysis scheme may offer appropriate texture descriptors for classification tasks. Other researches where multiresolution wavelet packet texture descriptors have shown remarkable performances are [192, 209]. For the present study, multiresolution texture descriptors obtained from 2D-WPT are considered for analysis.

5.3.1.1 Multiresolution Analysis

Feature extraction can be carried on a single scale by considering the spatial interactions which exists over small neighborhoods, for example, by using gray level co-occurrence matrix (GLCM), gray level run length matrix (GLRLM), gray level difference statistics (GLDS), neighborhood gray tone dependence matrix (NGTDM), statistical feature matrix (SFM), etc. Feature extraction in transform domain is carried out over various scales by using multiresolution schemes such as discrete wavelet transform (DWT), stationary wavelet transform (SWT), wavelet packet transform (WPT) and Gabor wavelet transform (GWT). Computing texture descriptors in transform domain is much more logical in the sense that human visual system (HVS), processes images in a multiscale way and scale is a dominant aspect for analysis of texture [43, 115]. In case of 2D-DWT as only the low frequency sub-image is recursively decomposed; it may not be efficient for texture characterization, as most significant texture information usually appears in the middle and high frequency channels [32].

5.3.1.2 Wavelet Packet Transform

As a result of 2D-WPT decomposition, complete frequency plane is sub-divided into equal size bands. The 2D-WPT tree up to second level of decomposition results in 16 sub-band feature images (wavelet packets) each representing a band in the frequency plane as depicted in Fig. 5.6.
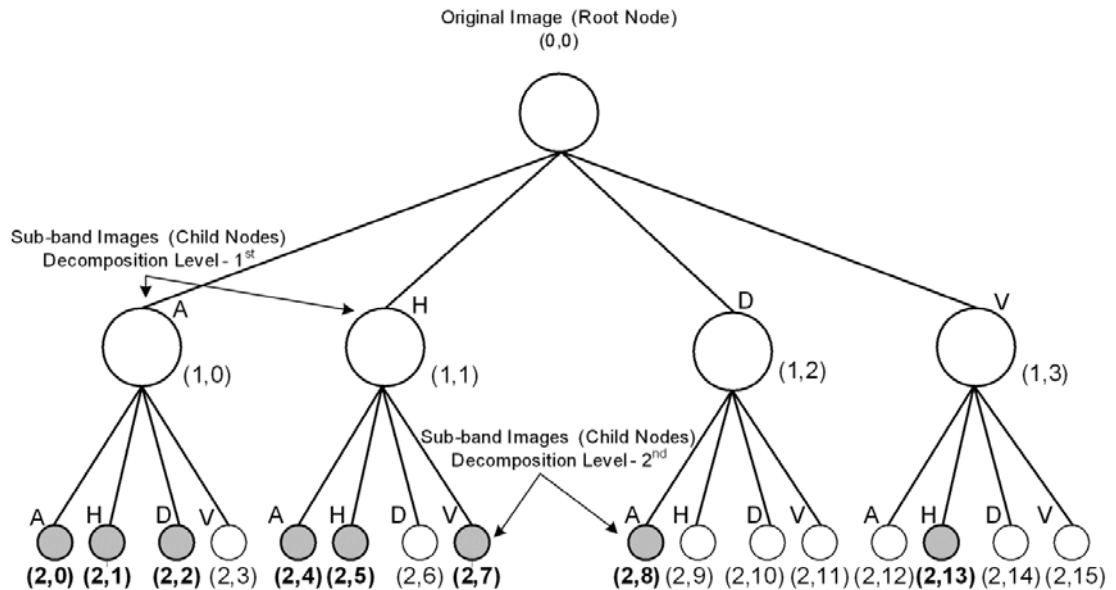
Fig. 5.6 2D-WPT tree up to 2nd level of decomposition represent 16 [(2,0) to (2,15)] sub-band feature images (wavelet packets). Eight sub-band feature images (wavelet packets) are shaded in gray; features from these eight images are selected by GA–SVM feature selection method.
Note: A: Approximate sub-band, H: Horizontal sub-band, D: Diagonal sub-band and V: Vertical sub-band.

Computing mean, standard deviation (Std), and energy features estimated from all 16 sub-band feature images result in a TFV of feature vector length (FVL) forty eight. Ten texture descriptors, (i.e., 3 mean features, 5 Std features and 2 energy features, shaded in gray in Fig. 5.7) computed from eight sub-band feature images (shaded in gray in Fig. 5.6) are selected by GA–SVM feature selection method as optimal features for the classification task.

M$_{AA}$ (2,0)	M$_{AH}$ (2,1)	M$_{HA}$ (2,4)	M$_{HH}$ (2,5)
M$_{AV}$ (2,3)	M$_{AD}$ (2,2)	M$_{HV}$ (2,7)	M$_{HD}$ (2,6)
M$_{VA}$ (2,12)	M$_{VH}$ (2,13)	M$_{DA}$ (2,8)	M$_{DH}$ (2,9)
M$_{VV}$ (2,15)	M$_{VD}$ (2,14)	M$_{DV}$ (2,11)	M$_{DD}$ (2,10)

S$_{AA}$ (2,0)	S$_{AH}$ (2,1)	S$_{HA}$ (2,4)	S$_{HH}$ (2,5)
S$_{AV}$ (2,3)	S$_{AD}$ (2,2)	S$_{HV}$ (2,7)	S$_{HD}$ (2,6)
S$_{VA}$ (2,12)	S$_{VH}$ (2,13)	S$_{DA}$ (2,8)	S$_{DH}$ (2,9)
S$_{VV}$ (2,15)	S$_{VD}$ (2,14)	S$_{DV}$ (2,11)	S$_{DD}$ (2,10)

E$_{AA}$ (2,0)	E$_{AH}$ (2,1)	E$_{HA}$ (2,4)	E$_{HH}$ (2,5)
E$_{AV}$ (2,3)	E$_{AD}$ (2,2)	E$_{HV}$ (2,7)	E$_{HD}$ (2,6)
E$_{VA}$ (2,12)	E$_{VH}$ (2,13)	E$_{DA}$ (2,8)	E$_{DH}$ (2,9)
E$_{VV}$ (2,15)	E$_{VD}$ (2,14)	E$_{DV}$ (2,11)	E$_{DD}$ (2,10)

Fig. 5.7 Features extracted from 2D-WPT tree at 2nd level of decomposition. Ten features shaded in gray are selected by GA–SVM feature selection method.
Note: M: Mean, S: Standard deviation and E: Energy features. 10 features (3 mean features, 5 standard deviation features and 2 energy features) estimated from eight sub-bands {(2,0), (2,1), (2,2), (2,4), (2,5), (2,7), (2,8) and (2,13)} feature images selected by GA–SVM feature selection method are shaded and indicated in bold.

5.3.1.3 Selection of Wavelet Filter

The review of literature for texture characterization in transform domain using multiresolution features indicates that the choice of wavelet filter is important as the properties of these decomposition filters play a significant role in description of texture; specifically with 2D-DWT and 2D-WPT schemes, the choice of an appropriate wavelet filter affects the characterization performance. Studies in literature [12, 52, 123, 147, 178, 192, 209] have shown empirical success by using different wavelet filters for specific classification tasks. The criteria like support width, shift invariance, orthogonality or biorthogonality, and symmetry are important and must be considered for selecting an appropriate wavelet filter. Usually compact support wavelet filters are desired for the ease of implementation. Orthogonality is another important property for conservation of energy at each decomposition level. Symmetry is required to avoid dephasing in processing the images [120, 178]. In the present work, ten compact support wavelet filters including Haar, Daubechies (db4 and db6), biorthogonal (bior3.1, bior3.3 and bior4.4), symlets (sym3 and sym5) and coiflets (coif1 and coif2) are considered for analysis with 2D-WPT. Comparison of important properties of wavelet filters used in the present study is summarized in Table 5.1.

Table 5.1 *Comparison of properties of wavelet filters used in the present study.*

Wavelet	*Biorthogonal*	*Orthogonal*	*Symmetry*	*Asymmetry*	*Near Symmetry*	*Compact Support*
Db	No	Yes	No	Yes	No	Yes
Haar	No	Yes	Yes	No	No	Yes
Bior	Yes	No	Yes	No	No	Yes
Coif	No	Yes	No	No	Yes	Yes
Sym	No	Yes	No	No	Yes	Yes

5.2.1.4 **Selection of Wavelet Packet Texture Descriptors**

Extensive literature survey on texture classification in transform domain using multiresolution approaches reveals that mean, standard deviation and energy features are frequently used for texture description [12, 32, 120, 178, 192, 204, 209]. For the present study, mean, standard deviation (Std) and energy features are computed for each sub-band feature image by using equations 5.1, 5.2 and 5.3.

$$\text{Mean}_j = \frac{1}{M \times N} \sum_{X=1}^{M} \sum_{Y=1}^{N} \left| \text{SI}_j (X,Y) \right| \qquad 5.1$$

$$\text{Std}_j = \left(\frac{1}{M \times N} \sum_{X=1}^{M} \sum_{Y=1}^{N} \left| \text{SI}_j (X,Y) - \text{Mean}_j \right|^2 \right)^{1/2} \qquad 5.2$$

$$\text{Energy}_j = \frac{1}{M \times N} \sum_{X=1}^{M} \sum_{Y=1}^{N} \left| \text{SI}_j (X,Y) \right|^2 \qquad 5.3$$

Here, SI_j are subimages of size $M \times N$ at level $j = 1, 2,...,5$. As the size of the ROI is 32 by 32 pixels, decomposition up to 5th level is possible.

The study in [178], determined the best level of decomposition for 2D-WPT with entropy criterion based best level algorithm according to which decomposition is carried out until the entropy of the sub-band is less than the sum of entropy of all its child sub-bands. However, in another study [142], it is reported that such a criterion for obtaining the best level of decomposition may not be suitable for texture classification tasks as small entropy value obtained from a particular sub-band may not necessarily indicate that the sub-band will separate the texture classes effectively. By 2nd level decomposition of a ROI with 2D-WPT, 16 sub-band images are obtained. Computing mean, standard deviation (Std), and energy features from these 16 sub-band images yields a TFV of FVL 48 (16×3). By subsequent 3rd, 4th and 5th level decomposition of ROI with 2D-WPT, 64, 256 and 1024 sub-band images are obtained.

Computing mean, Std, and energy features from these sub-band images results in large TFVs of FVLs, 192 (64×3), 768 (256×3) and 3072 (1024×3), respectively. These large TFVs are not considered for analysis due to computational efficiency constraints.

Wavelet packet decomposition tree up to 2nd level of decomposition yields 16 sub-band images (wavelet packets) as shown in Fig. 5.6. Only mean feature estimated from these 16 sub-band images results in mean TFV of FVL 16, similarly the standard deviation TFV and energy TFV of FVL 16 are obtained. The combined TFVs like, Mean+Std TFV consisting of mean and standard deviation features of FVL 32, Mean+Energy TFV and Std+Energy TFVs of FVLs 32 are obtained. The Mean+Std+Energy TFV, consisting of mean, standard deviation and energy features is of FVL 48.

5.3.2   Feature Selection Module

Designing CAD systems with smallest number of features is always desired as interference of irrelevant features can lead to reduced learning performance of the classifier which further increases the time taken to perform classification task and reduces the classification accuracy [160, 180]. GA–SVM feature selection method is used in this study to remove irrelevant features. For applying genetic algorithm (GA) to any problem two steps are extremely important, adequate representation and appropriate fitness function [66, 84, 127]. In the present study, binary representation is used for representing all possible feature subspaces of a given feature set and the training accuracy obtained by the SVM classifier is used as fitness function. The main steps of GA–SVM feature selection method are:

(*i*)   *Initialization*: An initial population of possible candidate solutions (individuals or chromosomes) is created randomly.

(*ii*)   *Representation*: Each chromosome is a 48-bit binary mask where each bit corresponds to a single feature, 0 at any location in the bit string indicates that the corresponding feature is excluded and 1 indicates that it is included.

(*iii*)   *Fitness Evaluation*: The performance of each individual or chromosome is gauged by appropriate fitness function.

(*iv*)   *Selection*: Roulette Wheel selection - The individuals or chromosomes which are deemed fit have high probability to enter the mating pool than those deemed unfit.

(*v*)   *Crossover*: The selected individuals in the mating pool are recombined with the probability P_c using crossover operator to produce next-generation offspring.

(*vi*) *Mutation*: A mutation operator is applied to these offspring with a low probability P_m to ensure that there is always a variability added to the pool of solutions.

(*vii*) *Fitness Check*: The offspring are then again evaluated using the fitness function and those which have higher fitness values then the earlier individuals are considered for forming a new population.

At the end of one iteration, the new population formed after selection, crossover, mutation and fitness check contains old individuals which are fitter than the new individuals and those which are comparatively fitter amongst the new individuals. In this way, in subsequent generations the chromosomes which are fittest mate more often and propagate their genetic material to the offspring which form potential candidate solutions thus biasing the search space towards promising candidate subspaces. The GA search procedure terminates when either there is no improvement in the fitness value after a fixed number of successive iterations or after a predefined number of generations.

In this study single point crossover is used and the other GA run parameters are set as crossover rate (P_c) equal to 0.6, mutation rate (P_m) equal to 0.033, and population size equal to 20 by manual optimization after a series of trails.

5.3.3   Classification Module

The generalization capability of the classifier is tested with instances of the TFVs which are not used in classifier design. The dataset used in the present work consists of total 180 ROIs (60 normal ROIs taken from 15 normal images, 60 cirrhotic ROIs taken from 16 cirrhotic images, and 60 HCC ROIs taken from 25 HCC images). The training dataset and testing dataset consists of 90 ROIs each, i.e., 30 ROIs from each image class. A complete description of dataset used in this study is summarized in Fig. 5.4.

5.3.3.1   SVM Classifier

It has been argued in [25, 59] that classifier designs which use regularization like SVM are less prone to over fitting and obtain good generalization performance to a certain extent even without feature space dimensionality reduction. For the present work, SVM classifier is chosen for the classification task. To avoid the bias caused by unbalanced feature values, all the extracted features were normalized in the range of [0, 1] by using min-max normalization procedure.

For multiclass classification, LibSVM library [31] uses one-against-one (OAO) technique by constructing M ($M-1$) / 2 binary sub-classifiers, where M is the number of classes. Each

binary sub-classifier is trained to separate a pair of classes and prediction is made by majority voting technique.

In present three class classification problem, the prediction of the class for an instance of TFV of the testing dataset is made by majority voting mechanism on the predictions of 3 binary sub-classifiers, i.e., SVM (normal/cirrhosis), SVM (normal/HCC) and SVM (cirrhosis/HCC).

Crucial step for obtaining good generalization performance with SVM classifier is the correct choice of the regularization parameter C and kernel parameter γ. The regularization parameter C attempts to maximize the margin while keeping low value for training error. In the present study, extensive search is carried out in the parameter space for the values of $C \in \{2^{-4}, 2^{-3}, \ldots, 2^{15}\}$ and $\gamma \in \{2^{-12}, 2^{-11}, \ldots, 2^{5}\}$ using 10 fold cross validation to obtain optimal values of C and γ for training the SVM model. The SVM classifier trained with this C and γ is subsequently used for classification of unseen testing dataset.

5.3.3.2 Classification performance

In addition to the overall classification accuracy (OCA) value, the individual class accuracy (ICA) values for each class are also estimated.

ICA for a particular class, say, for HCC ROIs abbreviated as ICA_{HCC} is the ratio of number of correctly classified HCC ROIs over the total number of actual HCC ROIs.

5.4 Results – CAD System for Normal, Cirrhotic and HCC Liver

Initially, all the seven TFVs, i.e., mean TFV, standard deviation TFV (Std TFV), energy TFV, Mean+Std TFV, Mean+Energy TFV, Std+Energy TFV and Mean+Std+Energy TFV estimated from all 16 sub-band feature images obtained from 2nd level decomposition of a ROI with 2D-WPT by using ten compact support wavelet filters including Haar, Daubechies (db4 and db6), biorthogonal (bior3.1,bior3.3 and bior4.4), symlets (sym3 and sym5) and coiflets (coif1 and coif2) are used for classification with SVM classifier to compare the capability of different wavelet filters to characterize textural variations exhibited by normal, cirrhotic and HCC liver.

The maximum and minimum classification accuracy values obtained by all the seven TFVs with the corresponding wavelet filters are reported in Table 5.2.

Table 5.2 *Comparison of maximum and minimum accuracy obtained by all seven TFVs with the corresponding wavelet filter.*

			Classification performance: SVM			
S.No	TFVs	l	Max. Acc. (%)	Wavelet filter	Min. Acc.(%)	Wavelet filter
1	Mean	16	84.4	Haar	73.3	sym3
2	Std	16	84.4	Haar	70.0	sym5
3	Energy	16	81.1	Haar	72.2	coif2,db6
4	Mean+Std	32	84.4	Haar	76.6	bior3.3
5	Mean+Energy	32	85.5	Haar	71.1	sym3
6	Std+Energy	32	84.4	Haar	74.4	coif1
7	Mean+Std+Energy	48	86.6	Haar	74.4	bior3.1

Note: TFVs: Texture feature vectors, *l*: Length of TFV.

From Table 5.2, it is interesting to note that for all seven TFVs maximum classification accuracy is obtained by using Haar wavelet filter. The highest accuracy of 86.6 % is obtained by using Haar wavelet filter with Mean+Std+Energy TFV (7th row of Table 5.2).

The classification results, i.e., OCA value and ICA values of each image class, obtained by all seven TFVs using Haar wavelet filter are reported in Table 5.3.

Table 5.3 *The classification results obtained by all seven TFVs using Haar wavelet filter.*

			Classification performance: SVM			
S.No	TFV	FVL	OCA (%)	ICA_{NOR} (%)	ICA_{CIRR} (%)	ICA_{HCC}(%)
1	Mean	16	84.4	93.3	76.6	83.3
2	Std	16	84.4	90.0	83.3	80.0
3	Energy	16	81.1	86.6	70.0	76.6
4	Mean+Std	32	84.4	93.3	80.0	80.0
5	Mean+Energy	32	85.5	93.3	80.0	83.3
6	Std+Energy	32	84.4	90.0	80.0	83.3
7	Mean+Std+Energy	48	86.6	93.3	83.3	83.3

Note: TFV: Texture feature vector, FVL: Feature vector length, OCA: Overall classification accuracy, ICA_{NOR}: Individual class accuracy for normal, ICA_{CIRR}: Individual class accuracy for cirrhosis, ICA_{HCC}: Individual class accuracy for HCC.

From Table 5.3, it can be visualized that the second highest OCA of 85.5 % is obtained by using Mean+Energy TFV (5th row of Table 5.3). By including standard deviation features with mean and energy features the ICA for cirrhosis has increased from 80.0 % to 83.3 % (compare 5th and 7th rows of Table 5.3).

It can be concluded that mean, standard deviation and energy features all contribute to capture the textural variations of normal, cirrhotic and HCC ROIs with highest OCA of 86.6 % obtained by Mean+Std+Energy TFV.

The classification results obtained by using Mean+Std+Energy TFVs with all ten wavelet filters are reported in Table 5.4.

Table 5.4 *The classification results obtained by using Mean+Std+Energy TFVs with all 10 compact support wavelet filters.*

		Classification performance: SVM			
S.No.	Wavelet filter	OCA (%)	ICA_{NOR} (%)	ICA_{CIRR} (%)	ICA_{HCC} (%)
1	bior3.1	74.4	93.3	73.3	56.6
2	bior3.3	77.7	100.0	66.6	66.6
3	bior4.4	76.6	83.3	70.0	76.6
4	Haar	86.6	93.3	83.3	83.3
5	db4	80.0	86.6	80.0	73.3
6	db6	80.0	93.3	76.6	70.0
7	sym3	78.8	90.0	73.3	73.3
8	sym5	76.6	83.3	73.3	73.3
9	coif1	81.1	90.0	83.3	70.0
10	coif2	78.8	86.6	73.3	76.6

Note: OCA: Overall classification accuracy, ICA_{NOR}: Individual class accuracy for normal, ICA_{CIRR}: Individual class accuracy for cirrhosis, ICA_{HCC}: Individual class accuracy for HCC.

It can be observed that the highest OCA of 86.6 % is obtained by Mean+Std+Energy TFV with Haar wavelet filter (4th row of Table 5.4). It can also be noted that the highest ICA value of 83.3 % for cirrhosis and HCC cases is obtained in this case.

It can be concluded that compactly supported, orthogonal and symmetric Haar wavelet filter is suitable for use with 2D-WPT multiresolution scheme along with SVM classifier for characterizing the normal, cirrhotic and HCC liver.

However, since the FVL of Mean+Std+Energy TFV (16 mean, 16 standard deviation and 16 energy features) is 48 and the total number of training instances are 90; feature selection with GA as search procedure and classification accuracy of the SVM classifier as fitness function is used for removing noisy, non-informative and redundant features.

The GA–SVM feature selection method selected a subset of 10 features, i.e., 3 mean, 5 standard deviation and 2 energy features (highlighted in Fig. 5.7) out of total 48 features, i.e., 16 mean, 16 standard deviation and 16 energy features (shown in Fig. 5.7).

It can also be noted that the 10 features of optimal reduced TFV (highlighted in Fig. 5.7) are estimated from eight sub-band feature images (highlighted in Fig. 5.6).

The classification results obtained by using Mean+Std+Energy TFV with Haar wavelet filter and optimal reduced TFV selected by GA–SVM method by using SVM classifier are reported in Table 5.5.

Table 5.5 *The classification results obtained by using Mean+Std+Energy TFV with Haar wavelet filter and optimal reduced TFV selected by GA−SVM method.*

TFV	FVL	Confusion Matrix			ICA (%)	OCA (%)
Classification performance: SVM						
Mean+Std+Energy TFV	48		NOR	CIRR	HCC		
		NOR	28	0	2	93.3	86.6
		CIRR	0	25	5	83.3	
		HCC	1	4	25	83.3	
Optimal reduced TFV	10		NOR	CIRR	HCC		
		NOR	27	0	3	90.0	88.8
		CIRR	0	27	3	90.0	
		HCC	2	2	26	86.6	

Note: TFV: Texture feature vector, FVL: Feature vector length, NOR: Normal, CIRR: Cirrhosis, OCA: Overall classification accuracy, ICA: Individual class accuracy, Mean+Std+Energy Features: 16 mean features, 16 standard deviation features and 16 energy features, optimal reduced TFV: 3 mean, 5 standard deviation and 2 energy features selected by GA−SVM method.

It can be observed that optimal reduced TFV of FVL 10 selected by GA−SVM feature selection method yields the OCA value of 88.8 %. However, the OCA achieved by using Mean+Std+Energy TFV of FVL 48 is 86.6 %. The other interesting fact is that by use of optimal reduced TFV the ICA for detecting abnormal cases, i.e., cirrhotic as well as HCC cases has increased. The ICA value for HCC cases has increased from 83.3 % to 86.6 % and sensitivity for cirrhosis cases has increased from 83.3 % to 90.0 %. The results obtained are promising as the sensitivity of conventional gray scale B-Mode US for detecting HCC lesions evolved on cirrhotic liver is limited and it is reported that contrast-enhanced US improves the sensitivity to around 85 % [62].

The sensitivity of the proposed CAD system for detecting HCCs is 86.6 % with conventional B-Mode US images. The results of the study indicate that optimal reduced TFV consisting of 10 features (3 mean and 5 standard deviation and 2 energy features) estimated from 8 sub-band feature images (wavelet packets) obtained by 2D-WPT using Haar wavelet filter can significantly account for textural variations exhibited by a variety of HCCs evolved on cirrhotic liver as well as cirrhotic and normal liver.

5.4.1   Misclassification Analysis

The 12 HCC images of the testing dataset were reviewed by an experienced participating radiologist and the remarks are summarized in Table 5.6.

Table 5.6 *Review remarks from experienced radiologist for 12 HCC images of the testing dataset.*

Image No. in Test Data	LHCCI/ SHCCI	ROI Identification No.	Prediction of Proposed CAD	Remarks
1	SHCCI	1	Predicted as HCC	Correct
2	SHCCI	2	Predicted as HCC	Correct
3	LHCCI	**3***,4,5,6	**3* misclassified as Normal**	Incorrect*
			Remaining 4,5,6 Predicted as HCC	Correct
4	SHCCI	7	Predicted as HCC	Correct
5	SHCCI	8	Predicted as HCC	Correct
6	SHCCI	9	Predicted as HCC	Correct
7	SHCCI	**10,11**	**10,11 both misclassified as Cirrhotic**	Incorrect
8	LHCCI	12,13,14	All predicted as HCC	Correct
9	LHCCI	15,16,17	All predicted as HCC	Correct
10	LHCCI	18,19,20	All predicted as HCC	Correct
11	LHCCI	21,22,23,24,25,26,27,28	All predicted as HCC	Correct
12	LHCCI	**29**,30	**29 misclassified as Normal**	Incorrect
			30 predicted as HCC	Correct

From Table 5.6, it is observed that HCC ROIs predicted as normal belong to two different LHCC images (Image No. 3 and Image No. 12 in Table 5.6) and remaining 2 misclassified HCC ROIs predicted as cirrhotic belong to a single SHCC Image (Image No. 7 in Table 5.6). Experienced participating radiologists opined that ROI with identification number 3* might have been misclassified due to close proximity with the halo although it is confirmed that the ROIs with identification numbers 3, 10, 11 and 29 are actual misclassifications of the proposed CAD system.

ROIs with identification numbers 3 and 29 are patches inside HCC lesion which are predicted as normal by the proposed CAD system. As US is commonly used to facilitate liver lesion biopsy, the participating radiologist were of the view that any ROI inside the HCC lesion if predicted as normal should be avoided for taking the sample for biopsy.

5.5 Summary

Brief description of CAD systems proposed in literature for characterization of normal, cirrhotic and HCC liver from B-Mode US images (earlier shown as Table 2.1 of Chapter 2 is revisited here as Table 5.7 for comparision with the present study).

Table 5.7 *Brief description of CAD systems proposed in literature for characterization of normal, cirrhotic and HCC liver*

	Dataset Description				Classification Performance: SVM			
Author's (year)	Patients	Images/ class	No. of ROIs	ROI Size	$ICA_{NOR}(\%)$	$ICA_{CIRR}(\%)$	$ICA_{HCC}(\%)$	$OCA(\%)$
Wu et al. [200]	45	Normal-15 Cirrhotic-15 HCC-15	90	32×32	86.6	100	83.3	90.0
Wu et al. [199]	-	-	90	30×30	80.0	90.0	93.3	87.8
Le et al. [97]	-	-	150	64×64	92.0	100	96.0	96.0
Le et al. [95]	-	-	432	64×64	100	91.5	94.5	95.3
Virmani et al. [191]	56	Normal-15 Cirrhotic-16 HCC-25*	180	32×32	90.0	90.0	86.7	88.8

Note: ICA: Individual class accuracy, OCA: Overall classification accuracy. *25 HCC images consisting of 25 solitary HCC lesions (14 small HCC lesions and 11 large HCC lesions) developed on top of cirrhotic liver are used in this study.

From the data description reported in studies [95, 97, 199, 200], it is not clear whether or not, only HCCs developed on cirrhotic liver are considered, further the bifurcation of number of HCCs into SHCC and LHCC is also not specified. The direct comparison of the present study with other related researches is not possible because image databases and image acquisition methods are different. However, it can be stated that the proposed approach for characterization between normal, cirrhotic and HCC liver yields comparable results with use of comprehensive and representative training data for classifier design.

5.6 Concluding Remarks

In the present study, a CAD system for characterizing normal, cirrhotic and HCC liver is proposed by multiresolution texture analysis of B-Mode liver US images. The proposed CAD system achieved OCA of 88.8 % with the ICA values of 90.0 % for normal and cirrhotic liver and 86.6 % for HCC liver with optimal reduced TFV obtained by GA–SVM feature selection method and SVM classifier. Considering limited sensitivity of conventional B-Mode gray-scale US for detecting HCCs evolved on cirrhotic liver, the sensitivity of 86.6 % for HCC lesions obtained by the proposed CAD system is quite promising and suggests that the proposed system can be used in a clinical environment to support radiologists in lesion interpretation thereby improving diagnostic accuracy which can avoid unnecessary biopsies.

Since the development of HCC is most often associated with liver cirrhosis, in radiology practice cirrhosis is considered to be the precursor for development of HCC. In very rare cases when a HCC occur on normal liver, it can be easily diagnosed by radiologists but the diagnosis

of these lesions on coarse and nodular cirrhotic liver parenchyma pose a diagnostic challenge for radiologists in routine practice. The HCC (primary malignant lesion) is the second most common liver malignancy only after metastasis (secondary malignant lesion). Due to highly overlapping sonographic appearances between HCC and MET lesions, the differential diagnosis between these lesions using conventional gray-scale B-Mode US images is considerably difficult. However, the differential diagnosis between these malignant lesions is clinically significant for proper management of liver malignancies. Therefore, an efficient CAD design for achieving binary classification between primary and secondary malignant focal liver lesions by using B-Mode liver US images is taken as the next objective of the present research work and is discussed in Chapter 6.

Chapter 6

Characterization of Primary and Secondary Malignant Liver Lesions

6.1 Introduction

The sensitivity of contrast-enhanced US, contrast-enhanced spiral computed tomography and magnetic resonance imaging modalities for detection and characterization of FLLs is higher than that of conventional gray-scale US, but these modalities are not widely available, are expensive and pose greater operational inconvenience [4, 16, 20, 62, 73, 130, 135, 150, 162]. On the other hand, the real-time imaging capabilities offered by widely available ultrasound (US) imaging modality along with its inexpensive, nonradioactive and noninvasive nature makes it a first-line examination for screening of focal liver lesions (FLLs) [20,107, 151, 170, 184]. However, there are certain distinct disadvantages associated with the use of conventional gray-scale US for characterization of malignant FLLs; (*i*) Limited sensitivity for detection of small FLLs (< 2 cm) developed on cirrhotic liver which is already nodular and coarse-textured [16, 62, 162]. (*ii*) Sonographic appearance of hepatocellular carcinoma (HCC), primary malignant solid FLL and metastatic carcinoma (MET), secondary malignant solid FLL are highly overlapping [16, 20, 62, 73, 162].

An early and accurate characterization of malignant FLLs is extremely important, because treatment options like curative surgical resection or successful percutaneous ablation are only possible if these malignancies are detected early [4, 62, 162]. However, the practical problem faced by the radiologists during routine practice is highly overlapping sonographic appearances of HCC (small and large HCCs on top of cirrhosis) and MET lesions (atypical METs) [16, 20, 62]. Therefore a computer aided diagnostic (CAD) system for accurate characterization of primary and secondary malignant FLLs based on conventional gray-scale US is highly desired to facilitate radiologists in clinical environment.

Among malignant FLLs the present study is focused on characterization between HCC (most common primary malignant FLL) and MET (most common secondary malignant FLL).

In 85 % of cases, HCC occurs in patients with cirrhosis. In fact in radiology practice, the condition of cirrhosis is seen as a precursor to the development of HCC [16, 20, 62, 73, 162]. The only feature that favours the possibility of HCC in differential diagnosis between HCC and other FLLs is that HCC is most commonly associated with cirrhosis [4, 20]. The sonographic appearances of small HCCs (< 2 cm) vary from hypoechoic to hyperechoic. Large HCCs

appear frequently with mixed echogenicity [16, 62]. A lesion can be labeled as typical in appearance when its subjective diagnosis can be made with a good confidence level by looking at the US examination. Experienced participating radiologists opined that the HCC case series should not be isolated as having typical or atypical sonographic appearance because of wide variability of sonographic appearances even within small and large HCCs, therefore no sonographic appearance is typical for HCC, however a representative dataset for designing the classifier should contain both small and large HCCs.

The occurrence rate of MET is twenty times more than that of HCC, because liver is the most common site for metastatic disease [62, 73]. Metastatic deposits may appear as single solitary mass or multiple masses of varying sizes. The sonographic appearance of MET lesions is extremely variable ranging from anechoic, hypoechoic, isoechoic, hyperechoic and even with mixed echogenicity [16, 20, 62, 73, 162]. However, the typical sonographic appearance of MET lesion is the 'target' or bull's-eye appearance, i.e., hypoechoic centre surrounded by a hyperechoic rim [20, 114, 152]. Diagnosis of these typical MET lesions can be made easily by an experienced radiologist from B-Mode US but differentiating atypical metastasis from HCCs lesions is considerably difficult.

The sonographic characterization between HCC and MET lesions is often carried out not only by observing the textural characteristics of regions inside the lesion but also by the texture of the background liver on which the lesion has evolved [20, 97]. The experienced participating radiologists opined that the textural feature computation from regions surrounding the lesion should effectively contribute for differential diagnosis between HCC and MET lesions. Accordingly, in the present work exhaustive experimentation have been carried out to investigate the contribution made by the texture information from the surrounding liver parenchyma, for characterization between HCC and MET liver malignancies.

The related researches in literature for characterization of FLLs are few. The details of these studies [114, 138, 167, 209] are summarized in Table 2.2 of Chapter 2.

The study in [167] reported classification between normal liver, benign and malignant FLLs with statistical texture analysis methods by using linear discriminant analysis (LDA) and neural network (NN) classifier. The study in [209] reported classification between normal liver, Cyst, HEM and FLLs with manually selected optimal statistical and spectral texture features by using NN classifier. A CAD system for five-class classification between normal liver, Cyst, HEM, HCC and MET is proposed in [114]. However, their proposed CAD system is developed using a large feature vector consisting of 208 features extracted with statistical, spectral and

spatial filtering based methods and NN classifiers. The researches in [167, 209] experimented characterization by considering malignant lesions as single class; however the characterization of malignant lesions as HCC or MET lesions is clinically significant for effective treatment and management of liver malignancies [62, 162]. The study in [114] used the ROI size of 25×25 pixels for computing texture features, however in [138, 167] the use of ROI size of 10×10 pixels is reported. The use of 10×10 pixels and even 25×25 pixels as ROI size yields smaller number of pixels in comparison to minimum 800 pixels required to estimate reliable statistics [14, 50, 76].

The related research, reported in [209] used wavelet packet texture descriptors with NN classifier for binary classification tasks, i.e., HEM vs. HCC, HEM vs. MET and HCC vs. MET. Among these the lowest characterization performance for HCC vs. MET is reported on their data. Their study reports the use of 64×64 pixels as ROI size, possibly because they used high resolution scanned images instead of real US images. It is otherwise difficult to select such a large ROI size keeping in view the size of small lesions and resolution of images obtained from US machines.

All the researches in literature for characterization of FLLs have considered only the texture patterns of regions inside the lesions and a CAD system for characterization between HCC and MET lesions has not been experimented as yet. The present study investigates the contribution made by texture patterns of inside lesion regions of interest (IROIs) and surrounding lesion regions of interest (SROIs) for binary classification between HCC and MET lesions.

6.2 Dataset Description – CAD for Primary and Secondary Malignant Liver Lesions

The design of CAD system for characterization of HCC and MET lesions was carried out with 51 B-Mode liver US images, i.e., 27 HCC images and 24 MET images.

Experienced participating radiologists were of the view that the HCC and MET image dataset used in this study is a complete representative data offering a high degree of variability encountered during subjective analysis of these lesions in routine practice. The size of SHCC varied from 1.5 to 1.9 cm and size of LHCC varied from 2.1 to 5.6 cm.

The sample images of SHCC, LHCC, typical MET and atypical MET lesions from the acquired database are shown in Fig. 6.1(a), (b), (c) and (d), respectively.
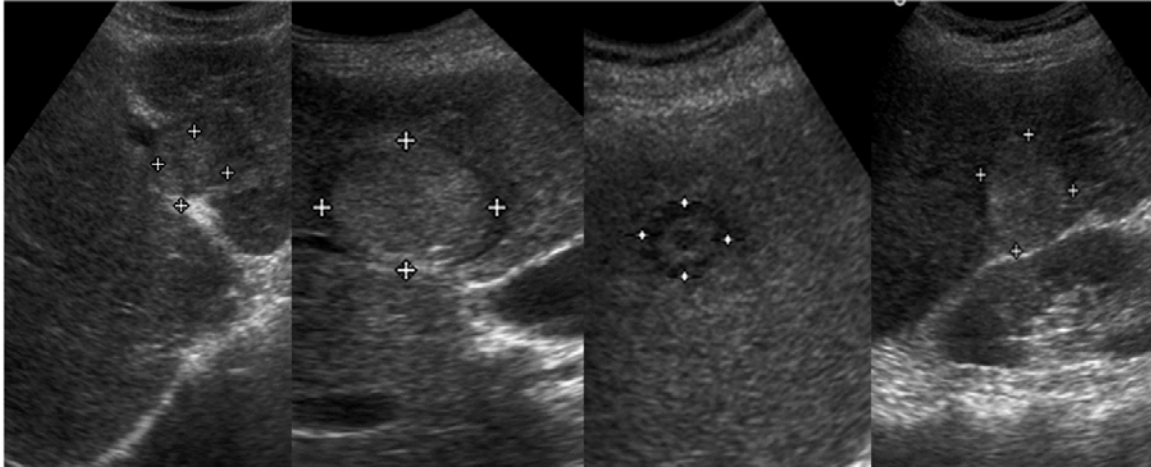
Fig. 6.1 Ultrasound liver images with **(a)** SHCC image; **(b)** LHCC image; **(c)** typical MET image; **(d)** atypical MET image.
Note: In **(c)** typical bull's-eye appearance of MET lesion alternating layers of hyper and hypoechoic tissue is clearly visible.

The protocols followed for collection of dataset, selection of ROIs and selection of ROI size are described in Section 3.4.1 of Chapter 3. The sample of HCC and MET liver images with IROIs and SROI marked is shown in Fig 6.2.
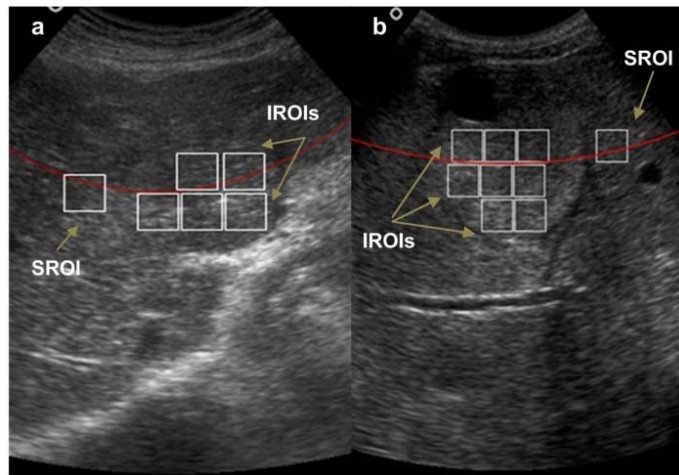
Fig. 6.2 Sample images with IROIs and SROI marked: **(a)** HCC liver image with 5 IROIs and a corresponding SROI; **(b)** MET liver image with 8 IROIs and a corresponding SROI.
Note: IROIs: Inside lesion ROIs; SROI: Surrounding lesion ROI. As shown in **(b)**, necrotic area within the MET lesion is avoided while extracting IROIs.

In the present work, two types of features are considered for analysis, i.e., texture features computed from IROIs and texture ratio features computed by taking the ratio of texture feature computed from IROI and texture feature computed from corresponding SROI. It can be noted that HCC lesion in Fig. 6.2(a) contains five IROIs and a corresponding SROI, Thus five instances of a single texture feature can be obtained with these five IROIs and five instances of

texture ratio feature can be obtained by dividing the texture feature value obtained for each IROI with the texture feature value obtained for corresponding SROI.

The detailed description of the dataset used in this study, and its bifurcation into training dataset and testing dataset is shown in Fig. 6.3.
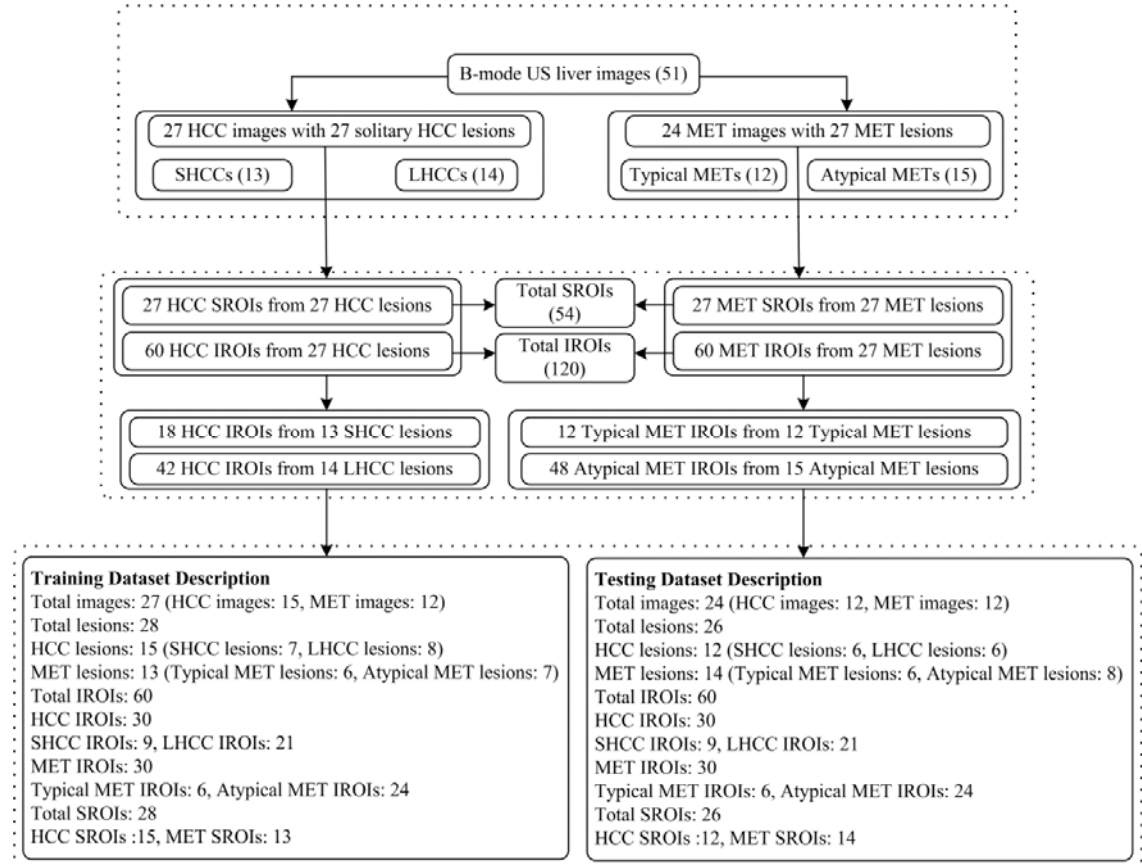
Fig. 6.3 Dataset description for design of CAD system for characterization of HCC and MET lesions. **Note:** IROIs: Inside lesion ROIs; SROIs: Surrounding lesion ROIs; SHCC: Small HCC; LHCC: Large HCC; Only HCC lesions evolved on cirrhotic liver are considered. The size of SHCC lesion varied from 1.5 to 1.9 cm and size of LHCC lesion varied from 2.1 to 5.6 cm.

To ensure generality, the training dataset for designing the classifier was chosen carefully in consultation with experienced participating radiologists, so as to include, typical and atypical cases of MET lesions as well as cases of SHCC and LHCC lesions, for designing a robust classifier with representative cases for all image subclasses. Two sets of images were created for each image class, ROIs from one set of images were used for training and ROIs from the other set were used for testing to avoid any biasing.

The final data set consisting of total 120 IROIs and 54 SROIs was stored in a PC (Pentium Core-2-Duo, 2.67 GHz with 1.97 GB RAM).

6.3 Proposed CAD System for Primary and Secondary Malignant FLLs using B-Mode Ultrasound Images

The block diagram of the proposed CAD system is depicted in Fig. 6.4.

| Clinically Acquired Image Database | | |
| 51 Real B-Mode Ultrasound Images 27 HCC Images and 24 MET Images | | |

Feature Extraction Module Total Features :112		
Method	No. of WLROI Features	No. of Ratio Features
GLCM	13	13
GLRLM	11	11
FPS	2	2
Laws' TEM	30	30
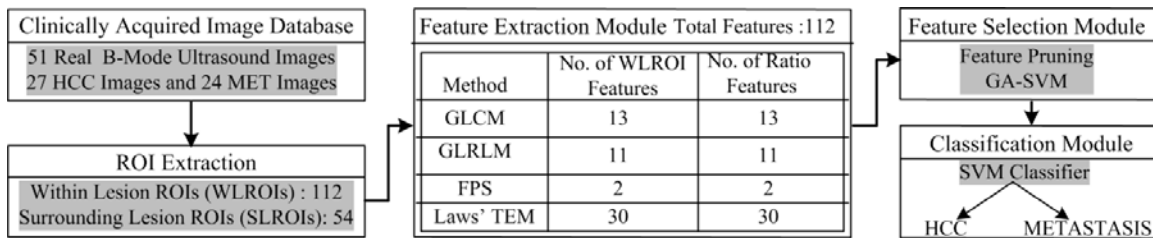
Fig. 6.4 CAD system for characterization of malignant FLLs.

For implementation of the proposed CAD system, the database of 120 non-overlapping IROIs and 54 SROIs is created from 51 clinically acquired US images. The CAD system consisted of feature extraction, feature selection and classification module. In feature extraction module, texture features are computed from IROIs as well as SROIs by gray level co-occurrence matrix GLCM [61], gray level run length matrix (GLRLM) [28, 36, 40, 51], Fourier power spectrum (FPS) [196] and Laws' texture feature [89] extraction methods. In feature selection module, initially feature pruning is carried out by removal of non-discriminatory feature vectors followed by feature selection by Genetic algorithm–Support vector machine (GA–SVM) approach. The GA–SVM procedure results in optimal reduced set of features. In classification module, a support vector machine (SVM) classifier is designed with the selected optimal features. The SVM classifier is implemented using LibSVM library [31].

6.3.1 Feature Extraction

Texture features are important attributes which are used to describe images in computer vision and image processing [13]. The general idea of feature extraction is to convert both visually extractable and visually non-extractable sonographic features into mathematical descriptors [106]. These mathematical descriptors are either morphological (based on shape or contour of the lesion) or textural features (based on intensity distribution) [82]. Both these morphological as well as textural features are significant for developing CAD systems for breast lesions using B-Mode US images [5, 8, 46, 68, 117, 127]. Experienced participating radiologists opined that morphological sonographic features of FLLs doesn't give any significant information for their characterization as also evident from other related researches the proposed CAD systems for characterization of FLLs using B-Mode US images have relied on textural features only [114, 138, 167, 209].

Initially a wide variety of visual and non-visual echotexture features are extracted by using statistical, spectral and spatial filtering based feature extraction methods. These features are then applied in the present classification system with a tedious task of combining the most relevant and effective features while discarding the non-performing features.

The statistical texture features are defined by the spatial distribution of gray level intensity values in the image. Local features are computed at each point in the image and a set of statistics are derived from the distribution of these local features.

Statistical methods are classified as first order statistics, second order statistics or higher order statistics depending upon the number of pixels used in defining a local feature [114, 163].

The spectral features computed by FPS method such as radial sum and angular sum of the discrete Fourier transform are used to describe texture [32].

The spatial filtering based texture descriptors, i.e., Laws' texture features determine texture properties by performing local averaging, edge detection, spot detection, wave detection and ripple detection in texture [89].

Law's texture features are computed by using special 1-D filters of length 3, 5, 7 and 9. Different filter lengths correspond to different resolutions for extraction of texture features from a ROI.

In the present work, 1-D filters of length 7, i.e., L7 = [1, 6, 15, 20, 15, 6, 1], E7 = [−1, −4, −5, 0, 5, 4, 1], S7 = [−1, −2, 1, 4, 1, −2, −1] are used.

Special 2-D filters called Laws' masks are derived by outer vector product of these 1-D kernels with themselves or with each other as shown in Fig. 6.5.

L7L7	E7L7	S7L7
L7E7	E7E7	S7E7
L7S7	E7S7	S7S7

Fig. 6.5 Nine 2-D Laws Masks

The texture images (TIs) are obtained by convolving the ROI of size M × N with these 2D Laws' masks, for example

$$TI_{E7E7} = ROI \otimes E7E7 \qquad\qquad 6.1$$

The output TIs are processed by texture energy measurement (TEM) filters. The TEM filter performs moving average non-linear filtering operation as depicted by

$$TEI = TEM[TI(x, y)] = \sum_{i=-7}^{7} \sum_{j=-7}^{7} |TI(x+i, y+j)| \qquad\qquad 6.2$$

Here, 15×15 descriptor windows are used to obtain nine texture energy images (TEIs). Texture energy images obtained by a pair of identical filters for example, TEI_{E7L7} and TEI_{L7E7} are combined to obtain rotational invariant image (TR) [183].

$$TR_{E7L7} = \frac{TEI_{E7L7} + TEI_{L7E7}}{2} \qquad\qquad 6.3$$

Statistics derived from these TR images provide significant texture information of ROI. Five statistics, i.e., mean, standard deviation, skewness, kurtosis and energy are extracted from each TR image [141, 183]. Thus, thirty Laws' texture features (6 TR images × 5 statistical parameters) are computed for each ROI.

In the present work, statistical methods, i.e., GLCM and GLRLM methods, spectral method, i.e., FPS method and spatial filtering based method, i.e., Laws' texture feature extraction method are selected for the classification task.

The selection of these methods for the classification task is based on other related researches with US images [14, 76, 183, 185] and few other studies for diagnosis of FLLs with US images [114, 138, 167, 209].

For extraction of efficient diagnostic features for characterization of liver malignancies, initially 112 features (56 features computed from IROIs + 56 texture ratio features) are computed using GLCM, GLRLM, FPS and Laws' texture feature extraction methods as tabulated in Table 6.1.

Table 6.1 *Description of 112 texture features extracted for characterizing HCC and MET FLLs.*

Statistical Methods		Spectral Method	Spatial Filtering Method	
GLCM features (13)	*GLRLM features* (11)	*FPS features* (2)	*Laws' texture features* (30)	
F1: Angular second moment	F14: Short run emphasis	F25: Angular sum	F27:LLmean	F45:LLkurt
F2: Contrast	F15: Long run emphasis	F26: Radial sum	F28:EEmean	F46:EEkurt
F3: Correlation	F16: Low gray level run emphasis		F29:SSmean	F47:SSkurt
F4: Sum of squares: variance	F17: High gray level run emphasis		F30:LEmean	F48:LEkurt
F5: Inverse difference moment	F18: Short run low gray level emphasis		F31:LSmean	F49:LSkurt
F6: Sum average	F19: Short run high gray level run emphasis		F32:ESmean	F50:ESkurt
F7: Sum variance	F20: Long run low gray level emphasis		F33: LLstd	F51:LLenergy
F8: Sum entropy	F21: Long run high gray level emphasis		F34: EEstd	F52:EEenergy
F9: Entropy	F22: Gray level non uniformity		F35: SSstd	F53:SSenergy
F10: Difference variance	F23: Run length non uniformity		F36: LEstd	F54:LEenergy
F11: Difference entropy	F24: Run percentage		F37: LSstd	F55:LSenergy
F12: Information measures of Correlation-1			F38: ESstd	F56:ESenergy
F13:Information measures of Correlation-2			F39: LLskew	
			F40: EEskew	
			F41: SSskew	
			F42: LEskew	
			F43: LSskew	
			F44: ESskew	

F57 to F112: 56 Texture ratio features corresponding to above features (F1 to F56).
Note: Above 56 features (F1 to F56) are computed for each IROI and SROI so as to compute another 56 texture ratio features (F57 to F112) corresponding to the above features.

F57 to F69 GLCM ratio features (13)	F70 to F80 GLRLM ratio features (11)	F81 to F82 FPS ratio features (2)	F83 to F112 Laws' ratio features (30)

For computation of Laws' texture features, different 1-D filters of length 5, 7 and 9 were experimented as shown in Table 6.2.

Table 6.2 *Description of various 1-D filters used for computation of Laws' texture features.*

Length of 1-D filter	1-D filter coefficients	No. of 2-D Laws' masks (X)	TRs obtained from identical filters pairs (Y)	Total TRs (X-Y)
5	L5 = [1, 4, 6, 4, 1] E5 = [−1, −2, 0, 2, 1] S5 = [−1, 0, 2, 0, −1] W5 = [−1, 2, 0, −2, 1] R5 = [1, −4, 6, −4, 1]	25	10	15
7	L7 = [1, 6, 15, 20, 15, 6, 1] E7 = [−1, −4, −5, 0, 5, 4, 1] S7 = [−1, −2, 1, 4, 1, −2, −1]	9	3	6
9	L9 = [1, 8, 28, 56, 70, 56, 28, 8, 1] E9 = [1, 4, 4, −4, −10, −4, 4, 4, 1] S9 = [1, 0, −4, 0, 6, 0, −4, 0, 1] W9 = [1, −4, 4, 4, −10, 4, 4, −4, 1] R9 = [1, −8, 28, −56, 70, −56, 28,−8, 1]	25	10	15

Note: TRs: Rotation invariant texture images.

Statistics derived from TRs are used as texture feature vectors (TFVs). In the present work, five features, i.e., mean, standard deviation, skewness (skew), kurtosis (kurt) and energy are computed from TRs. Thus, TFVs of lengths 70, 30 and 70, are obtained with 1-D filter of length 5, 7 and 9, respectively. It is observed that the classification accuracy obtained by SVM classifier by TFV of length 30 obtained for filter length 7 is higher in comparison with TFVs of length 70 obtained for filter lengths 5 and 9. Thus, 30 Laws' texture features computed for filter length 7 are considered for further analysis.

6.3.2   Feature Selection

Feature selection is used to eliminate the interference of irrelevant features which often increases the time taken to perform classification task and also reduces the classification accuracy [41]. In the present work, a two step methodology is followed for feature selection. In the first step, initial feature pruning is carried out by removal of non-discriminatory individual texture feature vectors (TFVs). The discrimination ability of a TFV is measured by the classification accuracy obtained by SVM classifier. Feature pruning yields a pruned TFV consisting of best performing individual TFVs.

In second step, GA–SVM feature selection is applied on pruned TFV; here binary genetic algorithm (GA) is used to evolve subsets of pruned TFV and the training accuracy obtained by the SVM classifier is used as a fitness function. The GA–SVM feature selection procedure removes irrelevant features from pruned TFV to yield an optimal subset of discriminatory features. The main steps for implementation of binary GA [127] algorithm are already explained in Section 5.3.2 of Chapter 5.

In the present work, single point cross over is used and the other run parameters are set as crossover rate (P_c) equal to 0.7, mutation rate (P_m) equal to 0.05, and population size equal to 20 by manual optimization after a series of trials.

6.3.3   Classification

In the present work, SVM classifier has been chosen for the classification task. Literature survey on texture classification reveal that SVM has shown remarkable performance for the classification of biomedical signals and images [68, 70, 79, 90 – 92, 98, 108, 117, 128, 145, 177, 192].

6.3.3.1 **SVM Classifier**

The SVM classifier attempts to construct an optimum hyper plane in the higher dimensional feature space to separate the training data with minimum expected risk. Kernel

functions that are used for nonlinear mapping of the training data from input space to higher dimensional feature space [25, 59, 99]. In the present study, the performance of Gaussian radial basis function (GRBF) kernel is investigated. Extensive search is carried out in the parameter space for obtaining the values of $C \in \{2^{-4}, 2^{-3}... 2^{15}\}$, $\gamma \in \{2^{-12}, 2^{-11}... 2^{4}\}$ using 10 fold cross validation on training data. To avoid the bias caused by unbalanced feature values, extracted features were normalized in the range [0, 1] by using min-max normalization procedure. The SVM classifier is implemented using LibSVM library [31]. The generalization capability of the SVM classifier is tested with instances of the TFVs which are not used in classifier design. The dataset used in the present work consists of total 120 ROIs (60 HCC ROIs taken from 27 HCC images, 60 MET ROIs taken from 24 MET images). The training dataset and testing dataset consists of 60 ROIs each, i.e., 30 ROIs from each image class. A complete description of dataset used in this study is summarized in Fig. 6.3.

6.4 Results

Rigorous experimentation has been carried out to identify potential TFVs of texture features and TFVs of texture ratio features for characterization of HCC and MET FLLs. In all the experiments the discrimination ability of TFVs has been evaluated by using a SVM classifier.

(*i*)   *Experiment 1*: In experiment 1, the discrimination ability of total 112 texture features, i.e., total eight TFVs (four TFVs corresponding to texture features and four TFVs corresponding to texture ratio features) obtained by GLCM, GLRLM, FPS and Laws' feature extraction methods is investigated. By comparing the results obtained by all the eight individual TFVs, the non-performing TFVs are removed to obtain a pruned TFV for the classification task.

(*ii*)   *Experiment 2*: In this experiment the discrimination ability of combined TFV (i.e., TFV consisting of all texture features) is investigated.

(*iii*)   *Experiment 3*: In this experiment the discrimination ability of combined TFV (i.e., TFV consisting of all texture ratio features) is investigated.

(*iv*)   *Experiment 4*: The discrimination ability of pruned TFV obtained from experiment 1 is investigated in this experiment.

(*v*)   *Experiment 5*: In this experiment 5, the discrimination ability of optimal reduced TFV, (obtained by applying GA–SVM method to pruned TFV) is investigated.

6.4.1 Results – Experiment 1– CAD System for Characterization of Primary and Secondary Malignant FLLs

This experiment compares the performance of SVM classifiers for all the eight individual TFVs. The results obtained are reported in Table 6.3.

Table 6.3 *Comparison of performance of SVM classifiers for individual TFVs.*

TFV (*l*)	CM			OCA (%)	ICA$_{HCC}$ (%)	ICA$_{MET}$ (%)
Classification performance: SVM						
GLCM features - IROIs (13)		HCC	MET	58.3	53.3	63.3
	HCC	16	14			
	MET	11	19			
GLCM ratio features (13)		HCC	MET	70.0	66.6	73.3
	HCC	20	10			
	MET	8	22			
GLRLM features - IROIs (11)		HCC	MET	56.6	66.6	46.6
	HCC	20	10			
	MET	16	14			
GLRLM ratio features (11)		HCC	MET	71.6	73.3	70.0
	HCC	22	8			
	MET	9	21			
FPS features - IROIs (2)		HCC	MET	68.3	53.3	83.3
	HCC	16	14			
	MET	5	25			
FPS ratio features (2)		HCC	MET	53.3	56.6	50.0
	HCC	17	13			
	MET	15	15			
Laws' features - IROIs (30)		HCC	MET	70.0	86.6	53.3
	HCC	26	4			
	MET	14	16			
Laws' ratio features (30)		HCC	MET	56.6	66.6	46.6
	HCC	20	10			
	MET	16	14			

Note: TFV: Texture Feature Vectors, *l*: length of TFV, CM: Confusion matrix, OCA: Overall classification accuracy, ICA$_{HCC}$: Individual class accuracy for HCC cases, ICA $_{MET}$: Individual class accuracy for MET cases. IROIs: Inside lesion ROIs.
Note: Best performing individual TFVs are shaded in gray. Here, Individual class accuracy of class A denoted as ICA$_A$ refers to (Number of cases correctly classified as class A / Total number of cases in class A).

It can be observed from Table 6.3, that GLRLM texture ratio features provide highest OCA value of 71.6 %. Both Laws' texture features computed from IROIs and GLCM texture ratio features provide second highest OCA value of 70 %. It can also be observed that GLCM

texture ratio features and GLRLM texture ratio features show better characterization performance than corresponding IROI texture features. Further, it can be noted that FPS texture features computed from IROIs and Laws' texture features computed from IROIs show better characterization performance in comparison to corresponding texture ratio features.

6.4.2   Results – Experiment 2 – CAD System for Characterization of Primary and Secondary Malignant FLLs

This experiment evaluates the performance of SVM classifier for combined TFV of all 56 IROI texture features. The results obtained are reported in Table 6.4.

Table 6.4 *Performance of SVM classifier for combined TFV of all 56 IROI texture features.*

Classification performance: SVM					
TFV (l)	*CM*		*OCA (%)*	*ICA*$_{HCC}$ *(%)*	*ICA*$_{MET}$ *(%)*
GLCM , GLRLM, FPS and Laws' IROI texture features (56)		HCC	MET		
	HCC	18	12	61.6	60.0	63.3
	MET	11	19			

Note: TFV: Texture Feature Vector, *l*: length of TFV, CM: Confusion matrix, OCA: Overall classification accuracy, ICA$_{HCC}$: Individual class accuracy for HCC cases, ICA $_{MET}$: Individual class accuracy for MET cases

It can be seen from Table 6.4 that the combined TFV of all 56 IROI texture features yields OCA value of 61.6 % for characterization of HCC and MET FLLs.

6.4.3   Results – Experiment 3 – CAD System for Characterization of Primary and Secondary Malignant FLLs

This experiment evaluates the performance of SVM classifier for combined TFV of all 56 texture ratio features. The results obtained are reported in Table 6.5.

Table 6.5 *Performance of SVM classifier for combined TFV of all 56 texture ratio features.*

Classification performance: SVM					
TFV (l)	*CM*		*OCA (%)*	*ICA*$_{HCC}$ *(%)*	*ICA*$_{MET}$ *(%)*
GLCM, GLRLM, FPS and Laws' texture ratio features (56)		HCC	MET		
	HCC	21	9	78.3	70.0	86.6
	MET	4	26			

Note: TFV: Texture Feature Vector, *l*: Length of TFV, CM: Confusion matrix, OCA: Overall classification accuracy, ICA$_{HCC}$: Individual class accuracy for HCC cases, ICA $_{MET}$: Individual class accuracy for MET cases

It can be seen from Table 6.5, that combined TFV of all texture ratio features yields OCA value of 78.3 %. For further experimentation, feature pruning is carried out on the basis of OCA value obtained by SVM classifier for eight individual TFVs shown in Table 6.3. The non-performing individual TFVs are removed and the best performing individual TFVs (highlighted

in Table 6.3) are combined to form a pruned TFV for adequate discrimination of HCC and MET FLLs.

6.4.4 Results – Experiment 4 – CAD for Characterization of Primary and Secondary Malignant FLLs

This experiment evaluates the performance of SVM classifier for pruned TFV of length 56 consisting of best performing individual TFVs. The results obtained are reported in Table 6.6.

Table 6.6 *Performance of SVM classifier for pruned TFV.*

TFV (*l*)	CM			OCA (%)	ICA_{HCC} (%)	ICA_{MET} (%)
Classification performance: SVM						
GLCM , GLRLM Texture ratio features and FPS, Laws' features - IROIs (56)		HCC	MET	80.0	76.6	83.3
	HCC	23	7			
	MET	5	25			

Note: TFV: Texture Feature Vector, *l*: Length of feature vector, CM: Confusion matrix, OCA: Overall classification accuracy, ICA_{HCC}: Individual class accuracy for HCC cases, ICA_{MET} : Individual class accuracy for MET cases.

From Table 6.6, it can be seen that pruned TFV yields the OCA value of 80 %. For further experimentation, this pruned TFV is subjected to GA–SVM feature selection procedure which iteratively removes the irrelevant and interfering features from the pruned TFV and returns an optimal reduced TFV of length 9. Nine texture features, i.e., four GLCM ratio features (angular second moment, sum average, difference entropy and inverse difference moment), three GLRLM ratio features (long run emphasis, gray level non-uniformity and long run high gray level emphasis), one FPS IROI feature (radial sum) and one Laws' IROI feature (LLmean) are selected by GA–SVM procedure.

6.4.5 Results – Experiment 5 – CAD for Characterization of Primary and Secondary Malignant FLLs

This experiment evaluates the performance of SVM classifier for optimal reduced TFV of length 9 consisting of features selected by GA–SVM procedure by using SVM classifier. The results obtained are reported in Table 6.7.

Table 6.7 *Performance of SVM classifier for optimal reduced TFV.*

TFV (*l*)	CM			OCA (%)	ICA_{HCC} (%)	ICA_{MET} (%)
Classification performance: SVM						
Texture ratio features and texture features - IROIs selected by GA–SVM method (9)		HCC	MET	91.6	90.0	93.3
	HCC	27	3			
	MET	2	28			

TFV: Texture Feature Vector, *l*: Length of TFV, CM: Confusion matrix, H: HCC, M: MET, ICA_{HCC} :Individual class accuracy for HCC cases, ICA_{MET} : Individual class accuracy for MET cases

From Table 6.7, it can be observed that optimal reduced TFV consisting of 9 features selected by GA–SVM procedure yields the OCA value of 91.6 % and ICA values of 90 % and 93.3 % for HCC and MET lesions respectively.

6.4.5.1 Misclassification Analysis

The analysis of 5 misclassified cases out of 60 cases in the testing dataset is reported in Table 6.8.

Table 6.8 *Misclassification analysis of 60 cases of testing dataset.*

Misclassification analysis for HCC cases	Misclassification analysis for MET cases
Total HCC cases: 30	Total MET cases: 30
Small HCC cases:9 , Large HCC cases:21	Typical MET cases:6 , Atypical MET cases: 24
Correctly classified: 27, Misclassified: 3	Correctly classified: 28, Misclassified: 2
ICA $_{HCC}$: 90.0 %	ICA $_{MET:}$ 93.3 %
1 out of 9 small HCC cases is misclassified	All six typical MET cases are correctly classified
2 out of 21 large HCC cases are misclassified	2 out of 24 atypical MET cases are misclassified
ICA $_{SHCC}$: 88.8 %	ICA $_{Typical\ MET}$: 100 %,
ICA $_{LHCC}$: 90.4 %	ICA $_{Atypical\ MET}$: 91.6 %

Note: ICA$_{SHCC}$: Individual class accuracy for small HCC cases, ICA$_{LHCC}$: Individual class accuracy for large HCC cases, ICA$_{Typical\ MET}$: Individual class accuracy for typical MET cases, ICA$_{Atypical\ MET}$: Individual class accuracy for atypical MET cases.

It can be observed from Table 6.8 that the proposed CAD system yields ICA values of 88.8 % and 90.4 %, for SHCC cases and LHCC cases, and the ICA values of 100 % and 91.6 % for typical and atypical MET cases, respectively.

However, it can be observed from Table 6.7, that the accuracy of the proposed CAD system is 91.6 % with ICA of 90 % for HCC cases and ICA of 93.3 % for MET cases. Given the fact that the sonographic appearances of HCC and MET overlap sufficiently, and the sensitivity of conventional B-Mode US is limited, the results obtained by the proposed CAD system are quite promising specifically in the presence of a comprehensive and representative dataset consisting of SHHCs, LHCCs and typical as well as atypical MET cases.

6.5 Concluding Remarks

The texture ratio features are more discriminatory than IROI texture features for characterization of HCC and MET FLLs. Only nine texture features (seven texture ratio features and two IROI texture features) are significant to account for textural variations exhibited by HCC and MET lesions. It can be concluded that the texture of the background liver on which the lesion has evolved, effectively contributes towards characterization of

primary and secondary malignant FLLs from B-Mode US images. The proposed CAD system yields the OCA value of 91.6 % with ICA values of 90 % and 93.3 % for HCC and MET cases, respectively. The results obtained by the proposed CAD are up to the satisfaction of experienced participating radiologists. The promising results of the study indicate that the proposed CAD system can be routinely used in a clinical environment to assist radiologists in diagnosing liver malignancies and thereby facilitate in providing better disease management.

Liver Cyst and HEM are the other commonly occurring FLLs apart from HCC and MET lesions. The subjective differential diagnosis between different FLLs from B-Mode US images in the presence of SHCCs and LHCCs as well as typical and atypical cases of Cyst, HEM and MET lesions is considerably difficult keeping few the important facts such as follows:

(*i*)   There is considerable sonographic overlap between atypical MET, atypical HEM and HCC lesions.

(*ii*)   The sonographic appearance of cystic MET and atypical cyst overlaps considerably.

(*iii*) It is difficult to diagnose certain isoechoic lesions having very slim difference in contrast from the surrounding liver parenchyma.

Thus, it is very much desired to reduce these limitations and design a robust CAD system for FLLs using B-Mode US images. Accordingly, the design of CAD system for FLLs using B-Mode US images is taken up as the next research objective of the present work and is discussed in Chapter 7.

CAD Systems for Focal Liver Lesions

7.1 Introduction

The differential diagnosis between focal liver lesions (FLLs) from B-Mode ultrasound (US) images is a difficult and confusing task for radiologists due to existence of wide variety of sonographic appearances even with-in individual classes of FLLs [16, 20, 62, 69, 73, 126, 162]. Even then, B-Mode US is considered as a primary choice for characterization of FLLs mainly due to its nonionising, noninvasive, inexpensive nature and real time imaging capabilities [20, 162].

The brief description of sonographic appearances of different liver image classes considered in the present study reported earlier in Chapter 1 is revisited here in Table 7.1 as ready reference for the readers.

Table 7.1 *Brief description of sonographic appearances of different liver image classes*

Image class	Sonographic Appearance (typical)	Sonographic Appearance (Atypical)
Normal	Appear homogeneous with slightly increased echogenicity as compared to the right kidney [108, 184, 186, 187, 191].	No atypical appearance
Cyst	Appear as round, anechoic lesion with posterior acoustic enhancement and well defined thin imperceptible wall [20, 62, 73, 114, 189]	Appear with internal echoes and thickened irregular walls
HEM	Appear as well circumscribed uniformly hyperechoic lesion [20, 62, 73, 114, 134, 189]	May appear as isoechoic or even hypoechoic mimicking the sonographic appearance of certain atypical MET and HCC lesions [20, 21, 104, 114, 179].
MET	Appear with 'target' or 'bull's-eye' appearance, i.e., hypoechoic centre surrounded by a hyperechoic rim [20, 114, 152, 174, 189, 209].	Appear with extremely variable sonographic appearances ranging from anechoic, hypoechoic, isoechoic, hyperechoic and even with mixed echogenicity [16, 20, 62, 73, 152, 189].
HCC	Sonographic appearance for HCC cannot be classified as typical or atypical. The sonographic appearances of SHCC vary from hypoechoic to hyperechoic. LHCC appear frequently with mixed echogenicity [62, 73, 189, 191].	

The disadvantages associated with use of conventional gray scale US for characterization of FLLs include (*i*) limited sensitivity for detection of small FLLs (< 2 cm) developed on cirrhotic liver which is already nodular and coarse-textured [16, 20, 62, 73, 191], (*ii*) sonographic appearance of HCC and MET lesions which are highly overlapping [16, 20, 62, 73, 152, 189], (*iii*) sonographic appearances of cystic metastasis and atypical cyst which is often overlapping [16, 62], (*iv*) sonographic appearances of atypical HEM, sometimes mimic

with atypical MET and HCC, [21, 73, 114, 179, 189, 209], and (*v*) difficulty to characterize isoechoic lesions with very slim difference in contrast between region inside the lesion and the surrounding liver parenchyma in some cases [114, 189].

It is very much desirable to reduce these limitations and to build an efficient CAD system for characterization of FLLs using B-Mode US images.

Typical FLLs can be easily diagnosed, even by an inexperienced radiologist, from their classic sonographic appearances. But differential diagnosis between atypical FLLs and HCC lesions developed on cirrhotic liver from B-Mode US images is considered a difficult task for radiologists in routine practice [62, 83, 104, 114, 152, 153, 174, 179, 189, 191, 209].

The experienced participating radiologists opined that the textural characteristics of the liver parenchyma surrounding the lesion should contribute for effective characterization of FLLs. The present work investigates the contribution of texture information extracted from inside lesion ROIs (IROIs) and surrounding lesion ROIs (SROIs) in characterization of FLLs using conventional gray scale B-Mode US images. The participating radiologists were of the view that the training dataset used in the present study is a comprehensive and diversified set consisting of representative images from various subclasses.

It is worth mentioning that till date, the research in the area of liver disease diagnosis using conventional B-Mode liver US images have been carried out using individual databases collected by the efforts of individual research groups due to non-availability of benchmark image database. Consequently, there are very few studies reported in literature in the area of developing CAD system for characterization of FLLs using B-Mode US images, the brief detail of these studies [114, 138, 167, 189, 209] is depicted in Table 2.2 of Chapter 2.

The study in [20], used statistical features based on first order statistics (FOS), second order statistics i.e. gray level co-occurrence matrix (GLCM), higher order statistics i.e. gray level run length matrix (GLRLM), spectral features, i.e. Gabor wavelet transform (GWT) based features and Laws' texture features for classification of NOR, Cyst, HEM, HCC and MET liver classes. The study in [25], reported classification between NOR, benign, malignant liver classes by using FOS and GLRLM statistical features with linear discriminant analysis and neural network (NN) classifier. The study in [26] used GLCM, autocorrelation, Laws' and edge frequency based texture features and a NN classifier for classification of NOR, cyst, HEM and malignant liver classes. In researches [25, 26] malignant lesions are considered as a single class; however diagnosis of malignant lesion as HCC or MET is clinically significant for

effective treatment and management of liver malignancies [2, 3, 19]. The recent study carried out by the authors of the present work, [19] reported the effect of texture analysis of region surrounding the lesions for designing an exclusive computer-aided diagnostic (CAD) system for diagnosis of HCC and MET liver malignancies using GLCM, GLRLM, FPS (Fourier power spectrum) and Laws' texture features along with SVM classifier. In another related study [21], multiscale wavelet packet texture descriptors are used with NN classifier for binary classification tasks i.e. HEM vs. HCC, HEM vs. MET and HCC vs. MET.

As per the best of the author's knowledge, only one study reported in literature, experimented classification between five liver image classes i.e. Cyst, HEM, HCC,MET and NOR liver [20] by using a large feature vector consisting of 208 texture features extracted by using FOS, GLCM, GLRLM, GWT and Laws' feature extraction methods. Their proposed CAD system design consisted of two stage classification system with total 11 NNs (i.e. a five class NN in the first stage and 10 binary NNs for the second stage). Their proposed CAD system design obtains good classification accuracy of 86.4 % with US images enhanced with modified anisotropic diffusion method [20]. One of the limitations of the proposed CAD system in [20], is that their design doesn't use any feature selection or feature dimensionality reduction methodology to get rid of superfluous and redundant features in a large feature set consisting of 208 texture features.

In present work, the CAD system designs implemented are different in the sense: (*i*) feature space dimensionality reduction using PCA has been applied to get rid of redundant features, (*ii*) the texture features computed from IROIs and SROIs have been used for the classification task, (*iii*) the raw conventional B-Mode gray scale US images have been used, without any sort of pre-processing, and (*iv*) a comprehensive and diversified image database consisting of representative images of (*a*) typical and atypical cases of Cysts, HEM and MET image classes, (*b*) SHCC and LHCC image classes, along with (*c*) normal liver tissue, have been used.

7.2 Dataset Description – CAD System for FLLs

The design of CAD system for characterization of FLLs was carried out with 108 B-Mode liver US images, i.e., 21 NOR, 12 Cyst, 15 HEM, 28 HCC and 32 MET images.

The participating radiologists opined that no sonographic appearance can be considered typical for HCC as there is wide variability of sonographic appearances even within SHCCs and LHCCs. However, the associated radiologists were of the view that a comprehensive and

117

representative dataset for designing the classifier should contain both SHCCs and LHCCs. The size of SHCCs and LHCCs in the acquired image database varied from 1.5 to 1.9 cm and 2.1 to 5.6 cm, respectively.

The experienced participating radiologists were of the view that the dataset used in this study is a comprehensive and representative dataset offering a high degree of variability encountered during subjective analysis of (*i*) typical and atypical cases of Cyst, HEM and MET lesions, (*ii*) SHCC and LHCC lesions, and (*iii*) NOR liver cases.

The sample images for (a) NOR liver tissue, (b) typical case of Cyst, HEM and MET lesions and (c) SHCC and LHCC lesions are shown in Fig. 7.1.
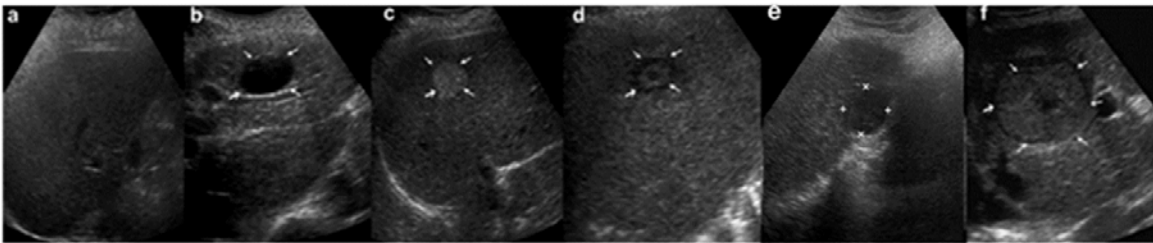
Fig. 7.1 B-Mode ultrasound liver images with appearance of: **(a)** Normal liver (homogeneous echotexture with medium echogenicity); **(b)** Typical cyst (thin walled anechoic lesion with posterior acoustic enhancement); **(c)** Typical HEM (well circumscribed uniformly hyperechoic appearance) ; **(d)** Typical MET ('target' or 'bull's-eye' appearance i.e., hypoechoic center surrounded by a hyperechoic rim); **(e)** Hypoechoic SHCC; **(f)** Heterogeneous echotexture represents complex and chaotic structure exhibited by LHCC due to coexistence of areas of necrosis, fibrosis and active growth areas.

The sample images for atypical case of Cyst, HEM and MET lesion shown earlier in Fig. 1.4 is revisited here in Fig. 7.2.
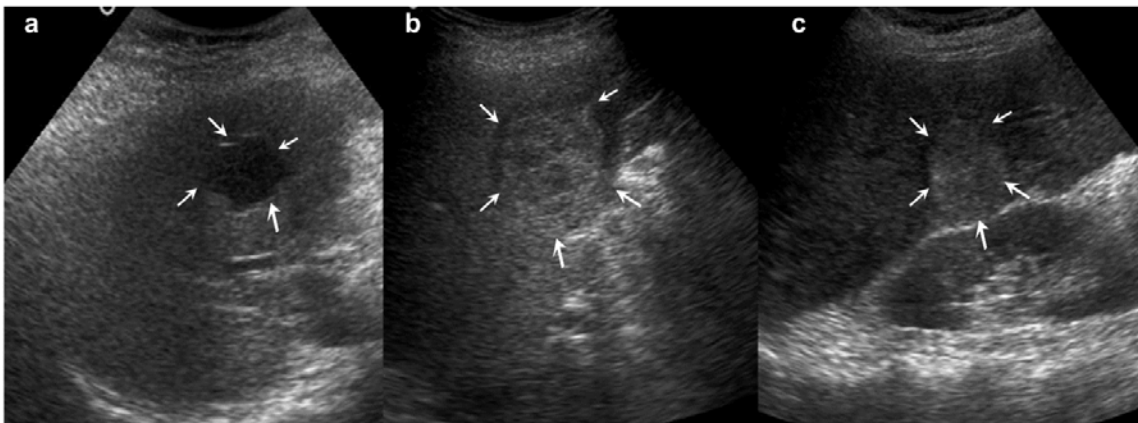
Fig. 7.1 Sample image variants of atypical cases: **(a)** Atypical cyst with internal echoes and irregular walls; **(b)** Atypical HEM with heterogeneous echotexture; **(c)** Hyperechoic atypical MET with heterogeneous echotexture.

The protocols followed for collection of dataset, selection of ROIs and selection of ROI size are described in Section 3.4.1 of Chapter 3. The sample images of NOR, Cyst, HEM, HCC and MET cases from the acquired image database with ROIs marked are shown in Fig. 7.3 (a) to (e).
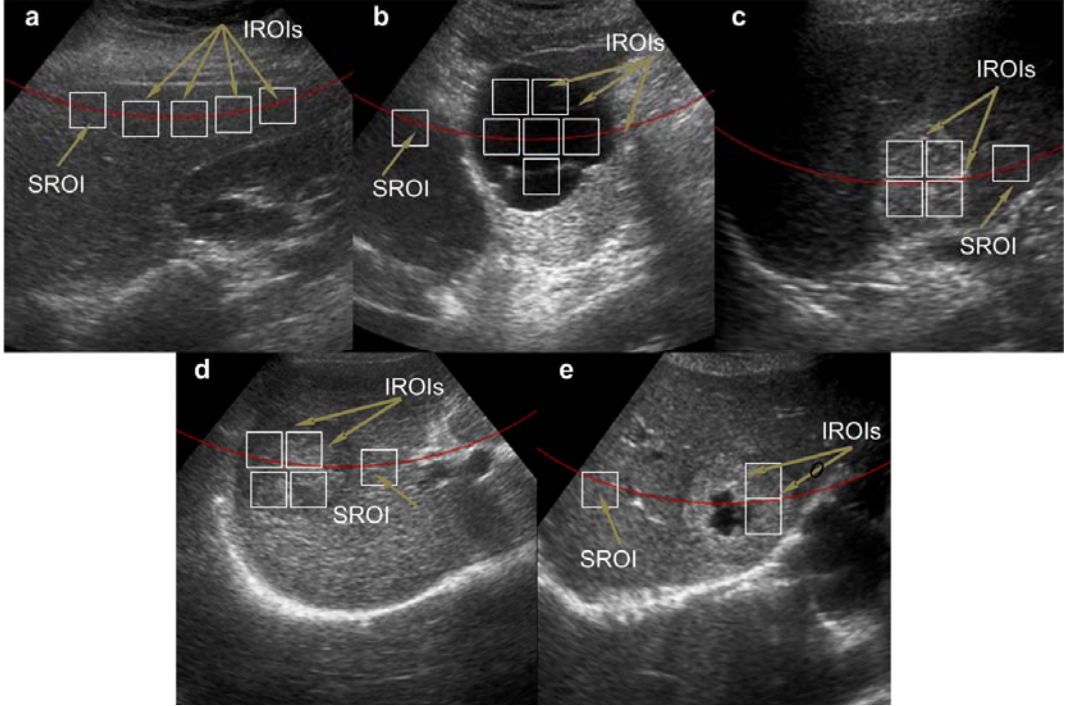
Fig. 7.3 (a) to **(e)** NOR, Cyst, HEM, HCC and MET image with IROIs and SROI marked.
Note: As shown in **(e)** necrotic area within the lesions is avoided while cropping IROIs. For NOR image, all the IROIs and SROI are taken at same depth and a single extreme ROI is considered as SROI as shown in **(a)**. For liver images with lesions, maximum non-overlapping IROIs are taken from well within the boundary of each lesion and a single SROI is extracted from liver parenchyma surrounding the lesion approximately at the same depth as that of centre of the lesion by avoiding inhomogeneous areas like blood vessels, hepatic ducts, etc., as shown in **(b)** to **(e)**.

In the present work, two types of features are considered for analysis, i.e., texture features computed from IROIs and texture ratio features computed by taking the ratio of texture feature computed from IROI and texture feature computed from corresponding SROI.

It can be noted that NOR liver image in Fig. 7.3(a) contains 4 IROIs and a corresponding SROI. Thus, 4 instances of texture feature set and 4 instances of texture ratio feature set are obtained. Similarly, from Cyst, HEM, HCC and MET lesions shown in Fig. 7.3(b-e), 6, 4, 4 and 2 instances of texture feature set and 6, 4, 4 and 2 instances of texture ratio feature set are obtained.

The distribution of clinically acquired database of 108 B-Mode liver US images (including NOR, Cyst, HCC, HEM and MET images) among various liver image subclasses is shown in Fig. 7.4.
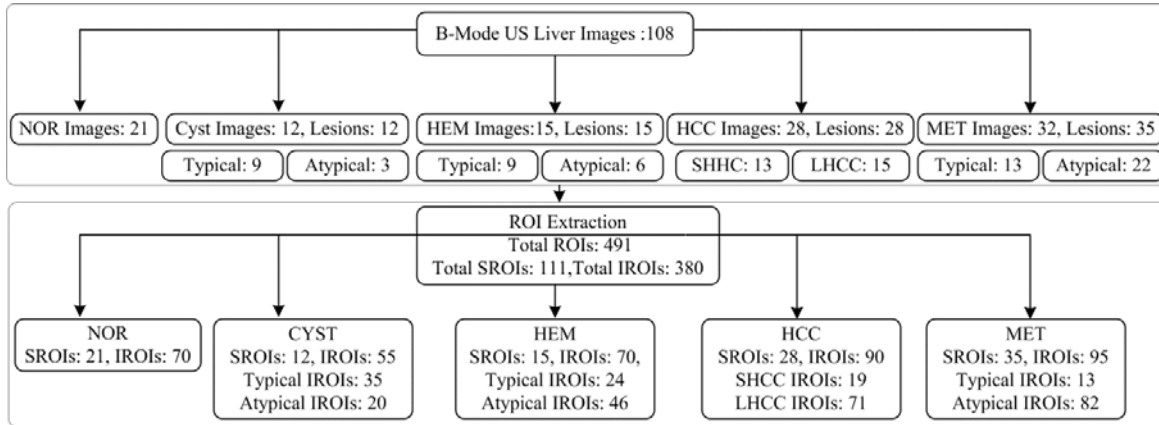
Fig.7.4 Dataset description – CAD system for FLLs

The bifurcation of total FLLs, among typical, atypical, SHCC and LHCC lesions and bifurcation of total ROIs, among IROIs and SROIs belonging to typical, atypical, SHCC and LHCC lesions is shown in Fig. 7.5.
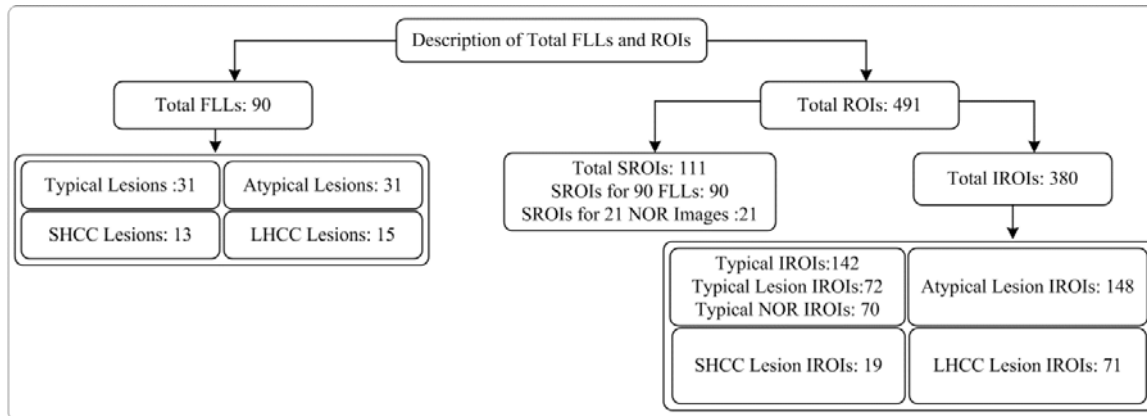
Fig.7.5 Description of total FLLs and ROIs

The bifurcation of acquired dataset into training dataset and testing dataset is shown in Fig. 7.6. To ensure generality, the training data was chosen carefully in consultation with experienced participating radiologists, so as to include typical and atypical cases of Cyst, HEM and MET lesions as well as cases of SHCC and LHCC lesions for designing a robust classifier with representative cases for all image sub-classes. Two sets of images were created for each image class, ROIs from one set of images were used for training and ROIs from the other set were used for testing to avoid any biasing.

Fig. 7.6 Description of training dataset and testing dataset
Note: The size of SHCC lesion varied from 1.5 to 1.9 cm and size of LHCC lesion varied from 2.1 to 5.6 cm.

The final dataset consisting of total 380 IROIs and 111 SROIs was stored in a PC (Pentium Core-2-Duo, 2.67 GHz with 1.97 GB RAM).

7.3 Experimental Work Flow — Proposed CAD Systems for FLLs using B-Mode Ultrasound Images

In present study, exhaustive experiments, (listed in Table 7.2), have been carried out for designing an efficient CAD system for characterization of FLLs using B-Mode US images.

Table 7.2 *Experiments carried out for the design of CAD system for characterization of FLLs using B-Mode US images.*

Experiment 1:	To design and evaluate the performance of CAD systems for characterization of FLLs using multi-class classifier based designs (Discussed in this Chapter).
Experiment 2:	To design and evaluate the performance of CAD systems for characterization of FLLs using hierarchical classifier based designs (Discussed in Chapter 8).
Experiment 3:	To design and evaluate the performance of CAD system for characterization of FLLs using an neural network ensemble based classifier design (Discussed in Chapter 9).

The experimental work flow for design of proposed CAD systems for characterization of FLLs using B-Mode US images is shown in Fig. 7.7.

121
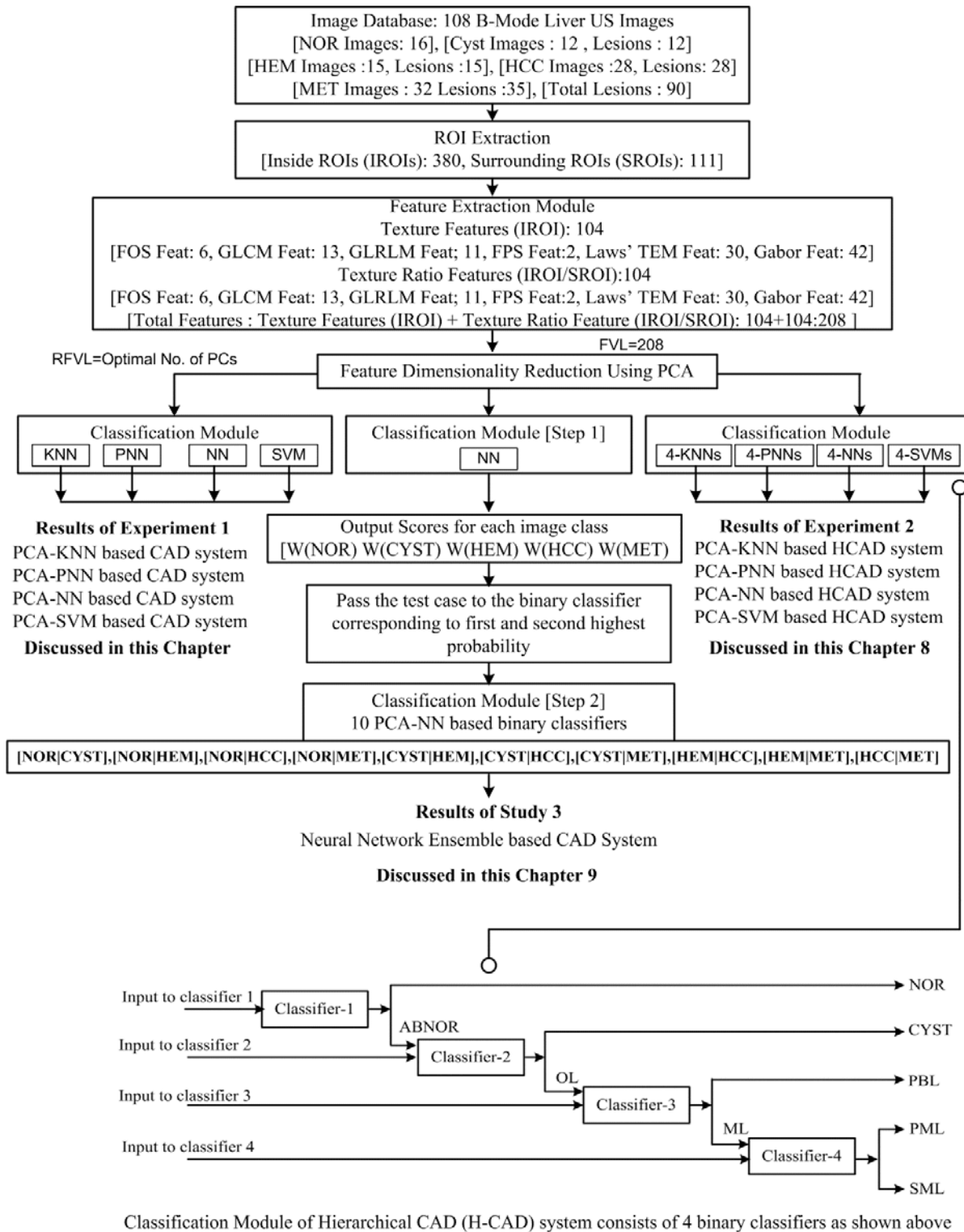
Fig. 7.7 Experimental work flow – Design of CAD systems for FLLs using B-Mode US images.
Note: The size of SHCC lesion varied from 1.5 to 1.9 cm and size of LHCC lesion varied from 2.1 to 5.6 cm.

7.4 CAD Systems for Characterization of FLLs using Multi-Class Classifier Designs

The block diagram of the experimental work flow followed for the design of CAD systems for characterization of FLLs using multi-class classifier designs is shown in Fig. 7.8.
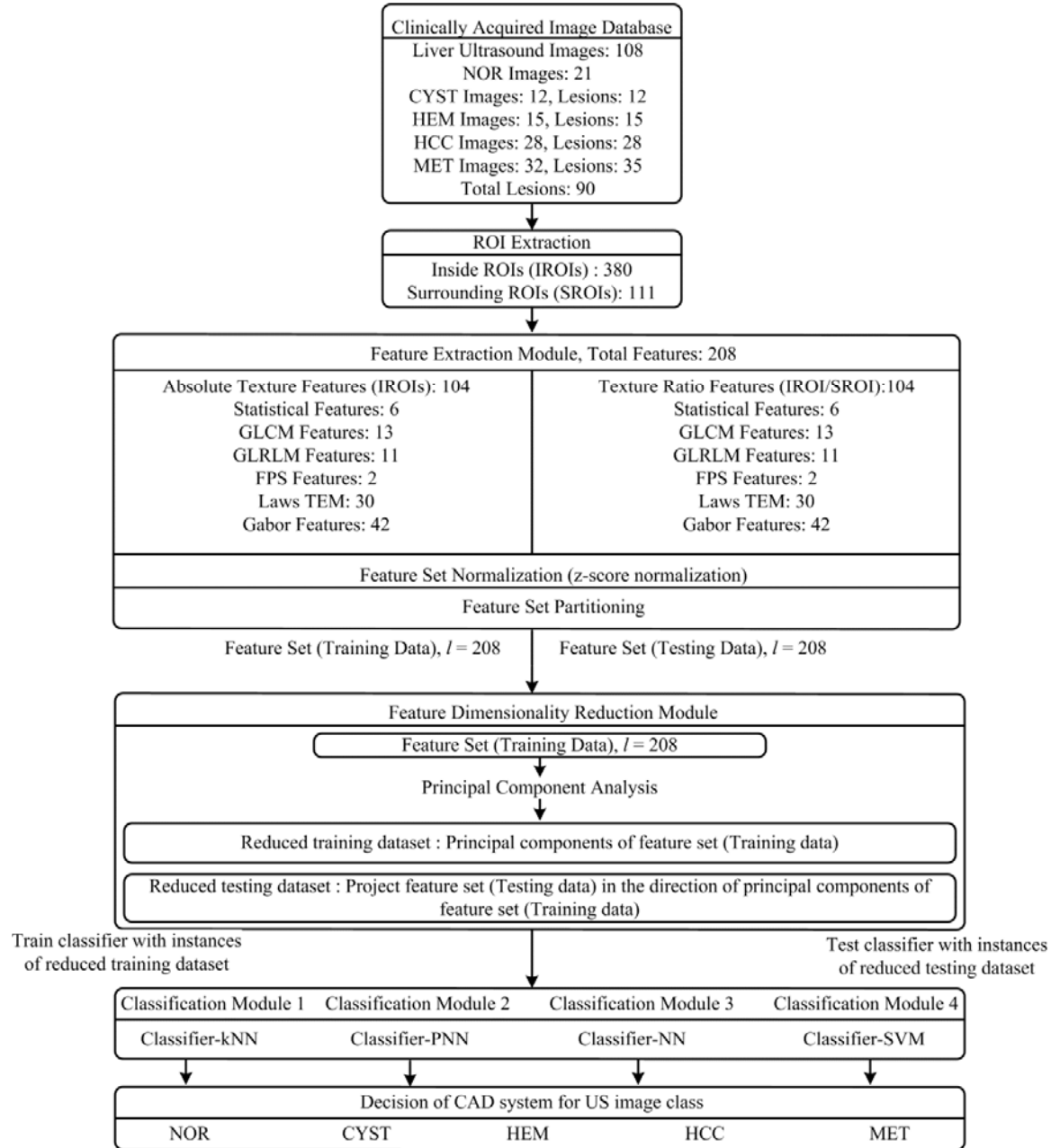
Fig. 7.8 Experimental work flow – CAD systems for FLLs using multi-class classifier based designs.

For the design of CAD systems a database of 380 non-overlapping IROIs and 111 SROIs was created from 108 clinically acquired B-Mode US liver images. The CAD systems consisted of feature extraction, feature dimensionality reduction and classification module. In feature

extraction module, statistical texture features based on first order statistics, second order statistics, (i.e., GLCM features [61, 128, 185, 189]), higher order statistics, (i.e., GLRLM features [36, 40, 51, 189]), spectral features, (i.e., FPS features [189, 197] and GWT features [90, 114]) as well as spatial filtering based Laws' texture features [89, 141, 183, 189], are computed from all 380 IROIs and 111 SROIs. Both texture features and texture ratio features are considered for analysis. The feature set of 208 texture features (104 texture features + 104 texture ratio features) is normalized using z-score normalization. The normalized feature set is partitioned into training data feature set and testing data feature set. The bifurcation of instances of individual classes in training data feature set and testing data feature set is described in Fig. 7.6.

In dimensionality reduction module, PCA is carried out on training data feature set and reduced training dataset of PCA derived principal components (PCs) is obtained. The reduced testing dataset is obtained by projecting the data points of testing data feature set in the direction of PCs of training data feature set.

In classification module, four different classifiers, i.e., kNN, PNN, NN and SVM are trained and tested with reduced feature sets obtained after applying PCA.

7.4.1 Feature Extraction Module

The general idea of feature extraction is to obtain mathematical descriptors for both visually extractable and visually non-extractable sonographic features of FLLs. These mathematical descriptors are either morphological (based on shape or contour of the lesion) or textural features (based on intensity distribution) [82]. Both these morphological as well as textural features are significant for developing CAD systems for breast lesions from B-Mode US images [46, 70, 117, 127]. Experienced participating radiologists opined that morphological features of FLLs do not give any significant information about their characterization as is also evident from other related researches, the proposed CAD systems for characterization of FLLs from B-Mode US have relied on textural features only [114, 138, 167, 189, 209]. In the present work initially, a wide variety of visual and non visual echotexture features are extracted by using statistical, spectral and spatial filtering based feature extraction methods.

7.4.1.1 *FOS Features*

Total six FOS texture features, i.e., average gray level, standard deviation, smoothness, third moment, uniformity and entropy$_{FOS}$ are computed for each ROI [55].

7.4.1.2 GLCM Features

Total thirteen GLCM mean texture features, i.e., angular second moment, contrast, correlation, variance, inverse difference moment, sum average, sum variance, sum entropy, entropy$_{GLCM}$, difference variance, difference entropy, information measures of correlation-1, and information measures of correlation-2 are computed for each ROI [61, 189].

7.4.1.3 GLRLM Features

Total eleven GLRLM texture features, i.e., short run emphasis, long run emphasis, low gray level run emphasis, high gray level run emphasis, short run low gray level emphasis, short run high gray level emphasis, long run low gray level emphasis, long run high gray level emphasis, gray level non uniformity, run length non uniformity and run percentage are computed for each ROI [36, 40, 51, 189].

7.4.1.4 FPS Features

Two spectral features, i.e., radial sum and angular sum of the discrete Fourier transform are computed for each ROI [189, 197].

7.4.1.5 GWT Features

Multiscale features estimated at various frequency and orientations of Gabor filters provide useful description of texture [23, 37, 90, 114, 131]. Two statistical features mean and standard deviation are computed by using a set of Gabor wavelets at 3 scales and 7 orientations resulting in a set of ($2{\times}3{\times}7 = 42$) texture features for each ROI.

7.4.1.6 Laws' Features

Spatial filtering based Laws' texture features determine texture properties by performing local averaging, edge detection, spot detection, wave detection and ripple detection in texture [89]. Law's texture features can be computed by using special 1-D filters of length 3, 5, 7 and 9 [114, 189]. Different filter lengths correspond to different resolutions for extraction of texture features from a ROI. In the present work, 1-D filters of length five, i.e., L5 = [1, 4, 6, 4, 1], E5 = [−1, −2, 0, 2, 1], S5 = [−1, 0, 2, 0, −1], W5 = [−1, 2, 0, −2, 1] and R5 = [1, −4, 6, −4, 1] are used. A total of twenty five 2-D filters are generated by combining these 1-D filters. These 2-D filters are convolved with the ROI images. A 15×15 square window is applied to the resulting convolved images in order to compute texture energy images. Out of twenty five 2-D filters, ten filters are identical to each other if they are rotated by 90°. Texture energy images computed from these pairs of identical filters can be combined to obtain rotation invariant image. Thus, total fifteen rotational invariant texture energy images are obtained for each ROI.

Two statistics, i.e., mean and standard deviation, computed from each rotational invariant texture energy image results in ($15 \times 2 = 30$) texture features for each ROI.

For detection and characterization of FLLs initially, three texture feature vectors (TFVs) are computed using FOS, GLCM, GLRLM, FPS, GWT and Laws' texture feature extraction methods. The brief description of these TFVs is tabulated in Table 7.3.

Table 7.3 *Description of TFVs*

TFV	Description	(l)
*TFV*1:	TFV consisting of 104 texture features (6 FOS, 13 GLCM, 11 GLRLM, 2 FPS, 42 Gabor and 30 Laws' features) computed from IROIs.	104
*TFV*2:	TFV consisting of 104 texture ratio features (6 FOS, 13 GLCM, 11 GLRLM, 2 FPS, 42 Gabor and 30 Laws' features) computed by taking the ratio of texture feature computed from IROI and the corresponding SROI.	104
*TFV*3:	Combined TFV consisting of 104 texture features (TFV1) and 104 texture ratio features (TFV2)	208

Note: TFV: Texture feature vector, *l*: Length of TFV.

7.4.2   Feature Space Dimensionality Reduction Module

The combined TFV of length 208 computed for the present classification task, i.e., TFV3 may contain redundant and correlated features. If these are used for classifier design, the performance of CAD systems in terms of accuracy and reliability can be degraded. PCA reduces the dimensionality of the feature space by retaining most of the original variability in the data. PCA is widely used for finding essential attributes / variables, i.e., PCs needed for the classification task [1, 47, 77, 148].

In the present work, PCA is used as preprocessing step for reducing the dimensionality of the feature space before classification. The main steps in PCA algorithm are (*i*) standardization of the values of all the features in the dataset to zero mean and unit variance, (*ii*) obtaining the covariance matrix form the training dataset, (*iii*) obtaining the Eigen values and Eigen vectors from the covariance matrix (Eigen vectors are the directions of the PCs), and (*iv*) projecting the data points in the testing dataset in the direction of PCs of the training dataset [47, 49, 166].

As the computed PCs are uncorrelated to each other and are arranged in decreasing order of variance explained by each PC, it is reasonable to step through first few PCs for building the classification model [47, 77, 148]. In the present work, the optimal number of PCs to be retained for classification task is determined empirically by repeated experimentations carried out by stepping through first 15 PCs to build the classification models, (i.e., by first considering only first PC and then first 2 PCs, first 3 PCs and so on up to first 15 PCs and verifying the performance of resulting classification models). The number of PCs yielding the maximum classification accuracy are used as features of reduced TFV as described in Table 7.4.

Table 7.4 *Description of reduced TFV.*

Reduced texture feature vector (*RTFV*)
TFV4: Reduced TFV consisting of first few PCs obtained by subjecting combined TFV (TFV3) to PCA

Note: RTFV: Reduced texture feature vector. The length of RTFV, i.e., length of TFV4 implies optimal number of PCs retained for the classification task, obtained by repeated experimentations carried out by stepping through first 15 PCs to build the classification models.

7.4.3   Classification module

7.4.3.1 *k-Nearest Neighbor (kNN) Classifier*

The *k*NN classifier attempts to cluster instances of feature vectors into disjoint classes assuming that the instances of the feature vector which lie close to each other in feature space represent instances of the same class. The algorithm stores all the instances of the feature vectors in the training data along with their class labels [7]. The class of an unknown instance of feature vector in the testing dataset is selected to be the class of majority of instances amongst its *k* nearest neighbors in the training dataset [121]. The optimum values for parameter *k* and the number of PCs to be retained in order to design a *k*NN model is determined empirically by repeated experimentation for values of $k \in \{1,2,\ldots,9,10\}$ and number of PCs $\in \{1,2,\ldots,14,15\}$. In the present work, Euclidean metric is used to calculate the distance between neighboring instances. In case of a tie, i.e., if the same classification accuracy is obtained for more than one value of *k*, the smallest value of *k* is used to obtain the classification results.

7.4.3.2 *PNN classifier*

The PNN classifier operates as a neural network implementation of kernel discriminant analysis; it constructs a classification function with the instances of features vectors in the training dataset. The PNN classification algorithm defines a probability density function for each class based on the training dataset and the optimized kernel width parameter. The spread parameter S_p determines the width of the radial basis kernel function that covers the space of the input features [57, 121, 154]. The optimum values for spread parameter S_p and the number of PCs to be retained in order to design a PNN model is determined empirically by repeated experimentation for values of $S_p \in \{1,2,\ldots,9,10\}$ and number of PCs $\in \{1,2,\ldots,14,15\}$. The PCA-PNN model for the present classification task consist of 5 neurons in the input layer (corresponding to first 5 PCs), 200 neurons in the pattern layer (each neuron corresponds to one instance of feature vector of the training dataset) and 5 neurons in the category layer (corresponding to NOR, Cyst, HEM, HCC and MET classes).

7.4.3.3 *NN classifier*

The NN architecture consists of an input layer, hidden layer and output layer. The optimum values for number of hidden layer neurons and the number of PCs to be retained in order to design a NN model is determined empirically by repeated experimentation for number of hidden layer neurons $\in \{4,5,\ldots,9,10\}$ and number of PCs $\in \{1,2,\ldots,14,15\}$. The PCA-NN model for the present classification task consist of 6 neurons (corresponding to first 6 PCs), one hidden layer with 10 neurons and one output layer with 5 neurons (corresponding to NOR, Cyst, HEM, HCC and MET classes). The output of the neuron corresponding to the labeled class is set to 1 and the output of other neurons is set to 0. The learning of the network is supervised and back-propagation algorithm with adaptive learning rate and momentum is used to obtain the desired input-output relationship [35, 39, 114].

7.4.3.4 *SVM Classifier*

SVM classifier is implemented using LibSVM library [31]. In kernel based classifiers such as SVM, kernel functions are used for nonlinear mapping of training data from input space to higher dimensional feature space. The performance of Gaussian radial basis function kernel is investigated for the present classification task. A crucial step for obtaining good generalization performance is correct choice of the regularization parameter C and kernel parameter γ. The optimal values of C and γ are obtained by extensive search, carried out in the parameter space for the values of $C \in \{2^{-4}, 2^{-3} \ldots 2^{15}\}$, $\gamma \in \{2^{-12}, 2^{-11} \ldots 2^{4}\}$ using 10 fold cross validation on training data.

7.5 Results

Rigorous experimentation has been carried out for performance analysis of proposed CAD systems for characterization of FLLs. Initial experiments were carried out using original features vectors (TFV1, TFV2 and TFV3) primarily, for the validation of the fact that texture information from the surrounding liver parenchyma significantly contributes towards classification of FLLs. It was observed that the combined TFV, i.e., TFV3 (consisting of both texture features and texture ratio features) yielded better classification performance in comparison with TFV1 (consisting of texture features computed from IROIs) and TFV2 (consisting of texture ratio features computed from IROIs and corresponding SROI).

These results indicate that texture information from inside lesion ROIs (IROIs) and surrounding lesion ROIs (SROIs) collectively yield significant improvement in classification accuracy. Thus, only combined TFV, i.e., TFV3 was considered for dimensionality reduction

through PCA, resulting in a reduced TFV, i.e., TFV4. The flow chart indicating the experimental work flow for design and comparative evaluation of the proposed CAD systems is depicted in Fig. 7.9.
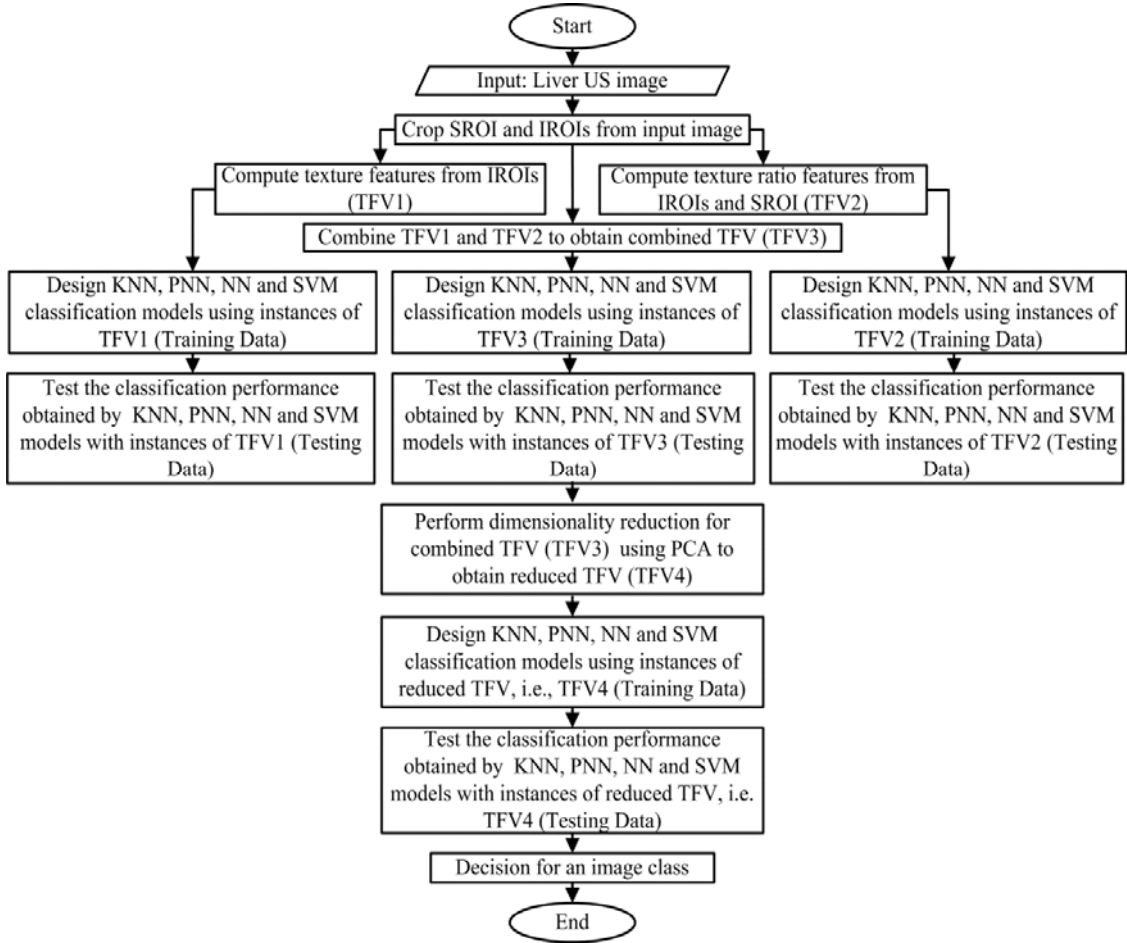
Fig. 7.9 Flow chart ─ Experimental work flow for design and comparative evaluation of the proposed CAD systems.
Note: Only combined TFV, i.e., TFV3 is considered for feature space dimensionality reduction using PCA as it yields the highest classification accuracy in comparison to TFV1 and TFV2.

7.5.1   Results – CAD Designs based on Five-Class PCA-*k*NN Classification Models

The classification performance of feature set consisting of instances of TFV1, TFV2, TFV3 and TFV4 is tested by using five-class *k*NN classification models. The results obtained are reported in Table 7.5.

Table 7.5 *Classification performance – CAD design based on five-class kNN classification models with TFV1, TFV2, TFV3 and TFV4.*

TFV (*l*)		*Classification performance: five-class kNN classification models*					*OCA (%)*	*ICA$_{CLASS}$: (%)*
		CM						
		NOR	CYST	HEM	HCC	MET		
TFV1 (104)	NOR	32	0	1	2	5	69.4	ICA$_{NOR}$: 80.0
	CYST	0	22	0	1	2		ICA$_{CYST}$: 88.0
	HEM	0	0	28	2	0		ICA$_{HEM}$: 93.3
	HCC	1	1	9	15	14		ICA$_{HCC}$: 37.5
	MET	0	1	4	12	28		ICA$_{MET}$: 62.2
		NOR	CYST	HEM	HCC	MET		
TFV2 (104)	NOR	32	0	0	5	3	74.4	ICA$_{NOR}$: 80.0
	CYST	0	23	0	1	1		ICA$_{CYST}$: 92.0
	HEM	0	0	26	0	4		ICA$_{HEM}$: 86.6
	HCC	2	6	0	27	5		ICA$_{HCC}$: 67.5
	MET	4	0	9	6	26		ICA$_{MET}$: 57.7
		NOR	CYST	HEM	HCC	MET		
TFV3 (208)	NOR	36	0	0	0	4	85.0	ICA$_{NOR}$: 90.0
	CYST	0	24	0	0	1		ICA$_{CYST}$: 96.0
	HEM	0	0	28	0	2		ICA$_{HEM}$: 93.3
	HCC	1	3	0	34	2		ICA$_{HCC}$: 85.0
	MET	4	0	10	0	31		ICA$_{MET}$: 68.8
		NOR	CYST	HEM	HCC	MET		
TFV4 (5)	NOR	36	0	0	1	3	85.0	ICA$_{NOR}$: 90.0
	CYST	0	24	0	0	1		ICA$_{CYST}$: 96.0
	HEM	0	0	30	0	0		ICA$_{HEM}$: 100
	HCC	3	3	1	32	1		ICA$_{HCC}$: 80.0
	MET	5	0	8	1	31		ICA$_{MET}$: 68.8

Note: TFV: Texture feature vector, *l*: Length of TFV, CM: Confusion matrix, OCA: Overall classification accuracy, ICA: Individual class accuracy, Here, ICA of class A, denoted as ICA (A) refers to (Number of cases correctly classified as class A / Total number of cases in class A).

It can be observed from Table 7.5, that TFV1 (consisting of texture features computed from IROIs), TFV2 (consisting of texture ratio features computed from IROIs and corresponding SROI) and combined TFV, i.e., TFV3 (consisting of texture features and texture ratio features) yield maximum OCA value of 69.4 %, 74.4 % and 85 % with values of *k* equal to 6, 1 and 8, respectively by using *k*NN classifier.

It can be noted that maximum OCA value of 85 % is achieved by using TFV3, i.e., combined TFV consisting of 104 texture features and 104 texture ratio features. Thus, TFV3 is considered for feature space dimensionality reduction by using PCA to design an efficient CAD system using *k*NN classifier. It can be observed that reduced TFV, i.e., TFV4 consisting of first five PCs obtained by subjecting combined TFV, i.e., TFV3 to PCA yield the same OCA value of 85 % with *k* equal to 9 by using *k*NN classification model.

From Table 7.5, it can be observed that texture features computed from IROIs yield OCA value of 69.4 % with the ICA values of 80 %, 88 %, 93.3 %, 37.5 % and 62.2 % for NOR, Cyst, HEM, HCC and MET classes, respectively.

The texture ratio features yield the OCA value of 74.4 % with the ICA values of 80 %, 92 %, 86.6 %, 67.5 % and 57.7 % for NOR, Cyst, HEM, HCC and MET classes, respectively.

Thus, it can be concluded that texture ratio features have more discrimination ability than texture features for classification of FLLs from B-Mode US.

It can be observed that combined TFV, i.e., TFV3 (consisting of texture features and texture ratio features) yields the OCA value of 85 % with the ICA values of 90 %, 96 %, 93.3 %, 85 % and 68.8 % for NOR, Cyst, HEM, HCC and MET classes, respectively.

In comparison to ICA values obtained by using texture ratio features only, the values obtained by using texture features and texture ratio features collectively show improvement by 10 %, 4 %, 6.7 % , 17.5 % and 11.1 %, for NOR, Cyst, HEM, HCC and MET classes, respectively.

These results indicate that both texture features and texture ratio features contribute towards effective classification of FLLs from B-Mode US. The results are in agreement with the premise that radiologists visualize the textural characteristics of regions inside and outside the lesions for differential diagnosis between FLLs.

Finally, it is observed that optimal reduced TFV with first six PCs also yields the maximum OCA value of 85 % with the ICA values of 90 %, 96 %, 100 %, 80 % and 68.8 % for NOR, Cyst, HEM, HCC and MET classes, respectively.

7.5.2 Results – CAD Designs based on Five-Class PCA-PNN Classification Models

The classification performance of feature set consisting of instances of TFV1, TFV2, TFV3 and TFV4 is tested by using five-class PNN classification models. The results obtained are reported in Table 7.6.

Table 7.6 *Classification performance – CAD design based on five-class PNN classification model with TFV1, TFV2, TFV3 and TFV4.*

Classification performance: five-class PNN classification models							
TFV (l)	*CM*					*OCA (%)*	*ICA$_{CLASS}$: (%)*
		NOR	CYST	HEM	HCC	MET		

TFV (l)		NOR	CYST	HEM	HCC	MET	*OCA (%)*	*ICA$_{CLASS}$: (%)*
TFV1 (104)	NOR	26	0	0	11	3	68.3	ICA$_{NOR}$: 65.0
	CYST	0	21	0	2	2		ICA$_{CYST}$: 84.0
	HEM	0	0	27	0	3		ICA$_{HEM}$: 90.0
	HCC	2	6	1	25	6		ICA$_{HCC}$: 62.5
	MET	4	0	13	4	24		ICA$_{MET}$: 53.3
TFV2 (104)	NOR	34	0	0	3	3	73.8	ICA$_{NOR}$: 85.0
	CYST	0	23	0	1	1		ICA$_{CYST}$: 92.0
	HEM	0	0	26	0	4		ICA$_{HEM}$: 86.6
	HCC	2	6	0	27	5		ICA$_{HCC}$: 67.5
	MET	5	0	10	7	23		ICA$_{MET}$: 51.1
TFV3 (208)	NOR	37	0	0	0	3	86.1	ICA$_{NOR}$: 92.5
	CYST	0	23	0	0	2		ICA$_{CYST}$: 92.0
	HEM	0	0	28	0	2		ICA$_{HEM}$: 93.3
	HCC	1	4	0	35	0		ICA$_{HCC}$: 87.5
	MET	5	0	8	0	32		ICA$_{MET}$: 71.1
TFV4 (6)	NOR	36	0	0	0	4	86.1	ICA$_{NOR}$: 90.0
	CYST	0	24	0	0	1		ICA$_{CYST}$: 96.0
	HEM	0	0	30	0	0		ICA$_{HEM}$: 100
	HCC	3	3	0	32	2		ICA$_{HCC}$: 80.0
	MET	6	0	6	0	33		ICA$_{MET}$: 73.3

Note: TFV: Texture feature vector, l: Length of TFV, CM: Confusion matrix, OCA: Overall classification accuracy, ICA: Individual class accuracy, Here, ICA of class A, denoted as ICA (A) refers to (Number of cases correctly classified as class A / Total number of cases in class A).

It can be observed from Table 7.6, that TFV1 (consisting of texture features computed from IROIs), TFV2 (consisting of texture ratio features computed from IROIs and corresponding SROI) and combined TFV, i.e., TFV3 (consisting of texture features and texture ratio features) yield maximum OCA value of 68.3 %, 73.8 % and 86.1 % with values of spread parameter S_p equal to 3, 1 and 6, respectively by using PNN classification models.

It can be noted that maximum OCA value of 86.1 % is achieved by using TFV3, i.e., combined TFV consisting of 104 texture features and 104 texture ratio features. Thus, TFV3 is considered for feature space dimensionality reduction by using PCA to design an efficient CAD system using PNN classifier. It can be observed that reduced TFV, i.e., TFV4 consisting of first

six PCs obtained by subjecting combined TFV, i.e., TFV3 to PCA yield the same OCA value of 86.1 % with spread parameter S_p equal to 3 by using PNN classification model.

From Table 7.6, it can be observed that texture features computed from IROIs yield OCA value of 68.3 % with the ICA values of 65 %, 84 %, 90 %, 62.5 % and 53.3 % for NOR, Cyst, HEM, HCC and MET classes, respectively. The texture ratio features yield the OCA value of 73.8 % with the ICA values of 85 %, 92 %, 86.6 %, 67.5 % and 51.1 % for NOR, Cyst, HEM, HCC and MET classes, respectively.

It can be concluded that texture ratio features have more discrimination ability than texture features for classification of FLLs from B-Mode US. It can be observed that combined TFV, i.e., TFV3 (consisting of texture features and texture ratio features) yields the OCA value of 86.1 % with the ICA values of 92.5 %, 92 %, 93.3 %, 87.5 % and 71.1 % for NOR, Cyst, HEM, HCC and MET classes, respectively. In comparison to ICA values obtained by using texture ratio features only, the values obtained by using texture features and texture ratio features collectively show improvement by 7.5 %, 0 %, 6.7 % , 20 % and 20 %, for NOR, Cyst, HEM, HCC and MET classes, respectively.

These results indicate that both texture features and texture ratio features contribute towards effective classification of FLLs from B-Mode US. The results are in agreement with the premise that radiologists visualize the textural characteristics of regions inside and outside the lesions for differential diagnosis between FLLs.

Finally, it is observed that optimal reduced TFV with first six PCs yields the maximum OCA value of 86.1 % with the ICA values of 90 %, 96 %, 100 %, 80 % and 73.3 % for NOR, Cyst, HEM, HCC and MET classes, respectively.

7.5.3   Results- CAD Design based on Five-Class PCA-NN classification models

The classification performance of feature set consisting of instances of TFV1, TFV2, TFV3 and TFV4 is tested by using five-class NN classification models. The results obtained are reported in Table 7.7.

Table 7.7 *Classification performance –CAD design based on five-class NN classification models with TFV1, TFV2, TFV3 and TFV4.*

TFV (l)		*Classification performance: five-class NN classification models*					OCA (%)	ICA$_{CLASS}$: (%)
TFV (l)		*CM*					*OCA (%)*	*ICA$_{CLASS}$: (%)*
		NOR	CYST	HEM	HCC	MET		
TFV1 (104)	NOR	31	0	0	5	4	66.1	ICA$_{NOR}$: 77.5
	CYST	0	23	2	0	0		ICA$_{CYST}$: 92.0
	HEM	0	0	15	10	5		ICA$_{HEM}$: 50.0
	HCC	0	1	8	15	16		ICA$_{HCC}$: 37.5
	MET	1	0	2	7	35		ICA$_{MET}$: 77.7
		NOR	CYST	HEM	HCC	MET		
TFV2 (104)	NOR	35	0	0	2	3	75.0	ICA$_{NOR}$: 87.5
	CYST	1	19	5	0	0		ICA$_{CYST}$: 76.0
	HEM	0	0	23	0	7		ICA$_{HEM}$: 76.6
	HCC	7	1	0	24	8		ICA$_{HCC}$: 60.0
	MET	1	0	8	2	34		ICA$_{MET}$: 75.5
		NOR	CYST	HEM	HCC	MET		
TFV3 (208)	NOR	34	0	0	4	2	82.7	ICA$_{NOR}$: 85.0
	CYST	0	23	2	0	0		ICA$_{CYST}$: 92.0
	HEM	0	0	25	1	4		ICA$_{HEM}$: 83.3
	HCC	1	0	0	35	4		ICA$_{HCC}$: 87.5
	MET	3	0	6	4	32		ICA$_{MET}$: 71.1
		NOR	CYST	HEM	HCC	MET		
TFV4 (6)	NOR	33	0	2	4	1	87.7	ICA$_{NOR}$: 82.5
	CYST	0	24	0	0	1		ICA$_{CYST}$: 96.0
	HEM	1	0	28	0	1		ICA$_{HEM}$: 93.3
	HCC	1	2	0	36	1		ICA$_{HCC}$: 90.0
	MET	1	0	4	3	37		ICA$_{MET}$: 82.2

Note: TFV: Texture feature vector, *l*: Length of TFV, CM: Confusion matrix, OCA: Overall classification accuracy, ICA: Individual class accuracy, Here, ICA of class A, denoted as ICA (A) refers to (Number of cases correctly classified as class A / Total number of cases in class A).

It can be observed from Table 7.7, that TFV1 (consisting of texture features computed from IROIs) yield maximum OCA value of 66.1 % with NN classification model consisting of input layer (104 neurons), one hidden layer (10 neurons) and output layer (5 neurons). TFV2 (consisting of texture ratio features computed from IROIs and corresponding SROI) yield maximum OCA value of 75 % with NN classification model consisting of input layer (104 neurons), one hidden layer (10 neurons) and output layer (5 neurons). Combined TFV, i.e., TFV3 (consisting of texture features and texture ratio features) yield maximum OCA value of 82.7 % with NN classification model consisting of input layer (208 neurons), one hidden layer (10 neurons) and output layer (5 neurons).

It can be noted that maximum OCA value of 82.7 % is achieved by using TFV3, i.e., combined TFV, consisting of 104 texture features and 104 texture ratio features. Thus, TFV3 is

considered for feature space dimensionality reduction by using PCA to design an efficient CAD system using NN classifier. It can be observed that reduced TFV, i.e., TFV4 consisting of first six PCs yield maximum OCA value of 87.7 % with NN classification model consisting of input layer (6 neurons), one hidden layer (10 neurons) and output layer (5 neurons).

From Table 7.7, it can be observed that texture features computed from IROIs yield OCA value of 66.1 % with the ICA values of 77.5 %, 92 %, 50 %, 37.5 % and 77.7 % for NOR, Cyst, HEM, HCC and MET classes, respectively. The texture ratio features yield OCA value of 75 % with the ICA values of 87.5 %, 76 %, 76.6 %, 60 % and 75.5 % for NOR, Cyst, HEM, HCC and MET classes, respectively. It can be concluded that texture ratio features have more discrimination ability than texture features for classification of FLLs from B-Mode US. It can be observed that combined TFV, i.e., TFV3 (consisting of texture features and texture ratio features) yields the OCA value of 82.7 % with the ICA values of 85 %, 92 %, 83.3 %, 87.5 % and 71.1 % for NOR, Cyst, HEM, HCC and MET classes, respectively.

In comparison to ICA values obtained by using texture ratio features only, the values obtained by using texture features and texture ratio features collectively show improvement by 16 %, 6.7 %, and 27.5 %, for Cyst, HEM and HCC classes, respectively. However, there is little fall in the ICA values for NOR and MET cases by 2.5% and 4.4%, respectively. These results indicate that both texture features and texture ratio features contribute towards effective classification of FLLs from B-Mode US.

The results are in agreement with the premise that radiologists visualize the textural characteristics of regions inside and outside the lesions for differential diagnosis between FLLs. Finally, it is observed that optimal reduced TFV with first six PCs yields the maximum OCA value of 87.2 % with the ICA values of 82.5 %, 96 %, 93.3 %, 90 % and 82.2 % for NOR, Cyst, HEM, HCC and MET classes, respectively.

7.5.4   Results – CAD Design based on Five-Class PCA-SVM Classification Models

The classification performance of feature set consisting of instances of TFV1, TFV2, TFV3 and TFV4 is tested by using five-class SVM classification models. The results obtained are reported in Table 7.8.

Table 7.8 *Classification performance – CAD design based on five-class SVM classification models with TFV1, TFV2, TFV3 and TFV4.*

TFV (*l*)	CM						OCA (%)	ICA$_{CLASS}$: (%)
		NOR	CYST	HEM	HCC	MET		
TFV1 (104)	NOR	32	0	0	5	3	66.1	ICA$_{NOR}$: 80.0
	CYST	0	22	0	1	2		ICA$_{CYST}$: 88.0
	HEM	0	0	18	8	4		ICA$_{HEM}$: 60.0
	HCC	2	2	9	12	15		ICA$_{HCC}$: 30.0
	MET	0	0	5	5	35		ICA$_{MET}$: 77.7
		NOR	CYST	HEM	HCC	MET		
TFV2 (104)	NOR	32	0	0	4	4	70.0	ICA$_{NOR}$: 80.0
	CYST	0	21	0	0	4		ICA$_{CYST}$: 84.0
	HEM	0	0	22	0	8		ICA$_{HEM}$: 73.3
	HCC	3	1	1	24	11		ICA$_{HCC}$: 60.0
	MET	2	1	11	4	27		ICA$_{MET}$: 60.0
		NOR	CYST	HEM	HCC	MET		
TFV3 (208)	NOR	35	0	0	2	3	86.1	ICA$_{NOR}$: 87.5
	CYST	0	23	0	1	1		ICA$_{CYST}$: 92.0
	HEM	0	0	26	1	3		ICA$_{HEM}$: 86.6
	HCC	4	0	0	35	1		ICA$_{HCC}$: 87.5
	MET	0	0	9	0	36		ICA$_{MET}$: 80.0
		NOR	CYST	HEM	HCC	MET		
TFV4 (6)	NOR	34	0	1	3	2	87.2	ICA$_{NOR}$: 85.0
	CYST	0	24	0	0	1		ICA$_{CYST}$: 96.0
	HEM	0	0	27	0	3		ICA$_{HEM}$: 90.0
	HCC	1	4	0	35	0		ICA$_{HCC}$: 87.5
	MET	1	0	5	2	37		ICA$_{MET}$: 82.2

Classification performance : five-class SVM classification models

Note: TFV: Texture feature vector, *l*: Length of TFV, CM: Confusion matrix, OCA: Overall classification accuracy, ICA: Individual class accuracy, Here, ICA of class A, denoted as ICA (A) refers to (Number of cases correctly classified as class A / Total number of cases in class A).

It can be observed from Table 7.8, that TFV1 (consisting of texture features computed from IROIs), TFV2 (consisting of texture ratio features computed from IROIs and corresponding SROI) and combined TFV, i.e., TFV3 (consisting of texture features and texture ratio features) yield maximum OCA values of 66.1 %, 70 % and 86.1 % with the values of (*C*, γ) equal to (32, 0.0038), (128, 4.8828×10^{-4}) and (8, 0.0078), respectively by using SVM classification models.

It can be noted that maximum OCA value of 86.1 % is achieved by using TFV3, i.e., combined TFV consisting of 104 texture features and 104 texture ratio features. Thus, TFV3 is considered for feature space dimensionality reduction by using PCA to design an efficient CAD system using SVM classifier. It can be observed that reduced TFV, i.e., TFV4 consisting of first six PCs obtained by subjecting combined TFV, i.e., TFV3 to PCA yield the same OCA

136

value of 86.1 % with the value of (C, γ) equal to (4, 0.0078) by using SVM classification model.

From Table 7.8, it can be observed that texture features computed from IROIs yield OCA value of 66.1 % with the ICA values of 80 %, 88 %, 60 %, 30 % and 77.7 % for NOR, Cyst, HEM, HCC and MET classes, respectively. The texture ratio features yield an OCA value of 70 % with the ICA values of 80 %, 84 %, 73.3 %, 60 % and 60 % for NOR, Cyst, HEM, HCC and MET classes, respectively.

It can be concluded that texture ratio features have more discrimination ability than texture features for classification of FLLs from B-Mode US. It can be observed that combined TFV, i.e., TFV3 (consisting of texture features and texture ratio features) yields the OCA value of 86.1 % with the ICA values of 87.5 %, 92 %, 86.6 %, 87.5 % and 80 % for NOR, Cyst, HEM, HCC and MET classes, respectively.

In comparison to ICA values obtained by using texture ratio features only, the values obtained by using texture features and texture ratio features collectively show improvement by 7.5 %, 8 %, 13.3 %, 27.5 % and 20 % for NOR, Cyst, HEM, HCC and MET classes, respectively. It can be concluded that both texture features and texture ratio features contribute towards effective classification of FLLs from B-Mode US.

The results are in agreement with the premise that radiologists visualize the textural characteristics of regions inside and outside the lesions for differential diagnosis between FLLs. Finally, it is observed that optimal reduced TFV with first six PCs yields the maximum OCA value of 87.2 % with the ICA values of 85 %, 96 %, 90 %, 87.5 % and 82.2 % for NOR, Cyst, HEM, HCC and MET classes, respectively.

7.5.5   Discussion on Misclassified Cases

The analysis of 27, 25 , 22 and 23 misclassified cases amongst 180 cases of the testing dataset as predicted by PCA-kNN, PCA-PNN ,PCA-NN and PCA-SVM based CAD systems is reported in Table 7.9.

It can be observed from Table 7.9, that PCA-kNN based CAD system yields highest ICA value of 90.6 % for detection of typical cases in comparison to 89.0 %, 85.9 % and 87.5 % as delivered by PCA-PNN, PCA-NN and PCA-SVM based CAD systems. Also, PCA-NN based CAD system yields highest ICA value of 88.1 % for detection of atypical cases in comparison

to 86.8 %, 82.8 % and 86.8 % as delivered by PCA-PNN, PCA-*k*NN and PCA-SVM based CAD systems.

Table 7.9 *Misclassification analysis.*

S.No.	PCA-kNN CAD System	PCA-PNN CAD System	PCA-NN CAD System	PCA-SVM CAD System
1.	NOR cases: 40	NOR cases: 40	NOR cases: 40	NOR cases: 40
	Misclassified: 4 ICA_{NOR}: 90.0	Misclassified: 4 ICA_{NOR}:90.0	Misclassified: 7 ICA_{NOR}: 82.5	Misclassified: 6 ICA_{NOR}: 85.0
2.	Typical Cyst cases: 13	Typical Cyst cases: 13	Typical Cyst cases: 13	Typical Cyst cases: 13
	Misclassified: Nil $ICA_{Typical\ CYST}$:100	Misclassified: Nil $ICA_{Typical\ CYST}$:100	Misclassified: Nil $ICA_{Typical\ CYST}$: 100	Misclassified: Nil $ICA_{Typical\ CYST}$: 100
3.	Atypical Cyst cases :12	Atypical Cyst cases: 12	Atypical Cyst cases: 12	Atypical Cyst cases: 12
	Misclassified:1 $ICA_{Atypical\ CYST}$:91.6	Misclassified:1 $ICA_{Atypical\ CYST}$:91.6	Misclassified:1 $ICA_{Atypical\ CYST}$: 91.6	Misclassified:1 $ICA_{Atypical\ CYST}$: 91.6
4.	Typical HEM cases: 6	Typical HEM cases: 6	Typical HEM cases: 6	Typical HEM cases: 6
	Misclassified: Nil $ICA_{Typical\ HEM}$:100	Misclassified: Nil $ICA_{Typical\ HEM}$:100	Misclassified: Nil $ICA_{Typical\ HEM}$: 100	Misclassified: 1 $ICA_{Typical\ HEM}$: 83.3
5.	Atypical HEM cases:24	Atypical HEM cases:24	Atypical HEM cases:24	Atypical HEM cases:24
	Misclassified: Nil $ICA_{Atypical\ HEM}$:100	Misclassified: Nil $ICA_{Atypical\ HEM}$:100	Misclassified:2 $ICA_{Atypical\ HEM}$:91.6	Misclassified:2 $ICA_{Atypical\ HEM}$:91.6
6.	Small HCC cases: 9	Small HCC cases: 9	Small HCC cases:9	Small HCC cases:9
	Misclassified:3 ICA_{SHCC}:66.6	Misclassified:3 ICA_{SHCC}:66.6	Misclassified: Nil ICA_{SHCC}: 100	Misclassified: 1 ICA_{SHCC}: 88.8
7.	Large HCC cases:31	Large HCC cases: 31	Large HCC cases: 31	Large HCC cases: 31
	Misclassified:5 ICA_{LHCC} :83.8	Misclassified:5 ICA_{LHCC} :83.8	Misclassified:4 ICA_{LHCC} : 87.0	Misclassified:4 ICA_{LHCC} : 87.0
8.	Typical MET cases:5	Typical MET cases:5	Typical MET cases:5	Typical MET cases:5
	Misclassified:2 $ICA_{Typical\ MET}$:60.0	Misclassified:3 $ICA_{Typical\ MET}$: 40.0	Misclassified:2 $ICA_{Typical\ MET}$: 60.0	Misclassified:1 $ICA_{Typical\ MET}$: 80.0
9.	Atypical MET cases:40	Atypical MET cases:40	Atypical MET cases: 40	Atypical MET cases: 40
	Misclassified:12 $ICA_{Atypical\ MET}$:70.0	Misclassified:9 $ICA_{Atypical\ MET}$:72.5	Misclassified:6 $ICA_{Atypical\ MET}$: 85.0	Misclassified:7 $ICA_{Atypical\ MET}$: 82.5
10.	*Total Typical cases:64	Total Typical cases: 64	Total Typical cases: 64	Total Typical cases: 64
	Misclassified: 6 $ICA_{Typical\ Cases}$:90.6	Misclassified: 7 $ICA_{Typical\ Cases}$:89.0	Misclassified: 9 $ICA_{Typical\ Cases}$: 85.9	Misclassified: 8 $ICA_{Typical\ Cases}$: 87.5
11.	*Total Atypical cases:76	Total Atypical cases:76	Total Atypical cases:76	Total Atypical cases:76
	Misclassified:13 $ICA_{Atypical\ Cases}$:82.8	Misclassified:10 $ICA_{Atypical\ Cases}$:86.8	Misclassified:9 $ICA_{Atypical\ Cases}$:88.1	Misclassified:10 $ICA_{Atypical\ Cases}$:86.8

Note: *Total typical cases in testing dataset = 40 NOR+13 Cyst + 6 HEM + 5 MET = 64; *Total atypical cases in testing dataset = 12 Cyst + 24 HEM + 40 MET = 76. ICA values are expressed in percentage. Here, ICA of class A, denoted as ICA_A refers to the ratio of Number of cases correctly classified as class A to Total number of cases in class A.

From the results of CAD systems with PCA-kNN, PCA-PNN, PCA-NN and PCA-SVM based five-class classifier designs implemented in the present work, it can be observed that PCA-NN based CAD system also yields maximum OCA value of 87.7 % for classification of FLLs in comparison to 86.1 % , 85 % and 87.2 % as delivered by PCA-PNN , PCA-kNN and PCA-SVM based CAD systems. Further, it can be noted from Table 7.8, that PCA-NN based CAD system yields ICA value of 100 % for SHHCs in comparison to 66.6 % as delivered by PCA-PNN as well as PCA-kNN based CAD systems and 88.8 % as delivered by PCA-SVM based CAD system.

Given the fact, that conventional gray scale B-Mode US has low sensitivity for atypical cases of FLLs and SHCCs developed on top cirrhotic liver, the experienced radiologists opined that the performance obtained by the proposed PCA-NN based CAD system is encouraging.

From the analysis of the results obtained by PCA-kNN, PCA-PNN, PCA-NN and PCA-SVM based CAD systems, it can be concluded that PCA-NN based CAD system clearly outperforms in comparison with PCA-PNN, PCA-kNN and PCA-SVM based CAD systems.

7.6 Summary

The brief performance comparison of PCA-kNN, PCA-NN, PCA-PNN and PCA-SVM based classifier designs for FLLs using B-Mode US images is given in Table 7.10.

Table 7.10 *Comparative analysis of PCA-kNN, PCA-NN, PCA-PNN and PCA-SVM based classifier designs.*

Classifier	ICA_{SHCC} (%)	ICA_{LHCC} (%)	$ICA_{Typical\ Cases}$ (%)	$ICA_{Atypical\ Cases}$ (%)	OCA (%)
PCA-kNN	66.6	83.8	90.6	82.8	85.0
PCA-NN	100	87.0	85.9	88.1	87.7
PCA-PNN	66.6	83.8	89.0	86.8	86.1
PCA-SVM	88.8	87.0	87.5	86.8	87.2

Note: ICA: Individual class accuracy, OCA: Overall classification accuracy. The maximum values for ICA in case of SHCCs and atypical cases is obtained by using PCA-NN based classifier design. The PCA-NN based classifier design also yield the maximum value for OCA, i.e., 87.7 % (shaded in gray).

Keeping in view the fact that the detection of SHCCs and differential diagnosis between HCCs and atypical FLLs is considerably difficult, the PCA-NN based classifier design outperforms in comparison to PCA-kNN, PCA-PNN and PCA-SVM based classifier designs.

The promising results obtained by proposed CAD system with PCA-NN based classifier design, indicate its usefulness to assist experienced radiologists for differential diagnosis between FLLs from B-mode US images. The proposed CAD system can also facilitate better

management of focal liver malignancies by providing second opinion in case of highly overlapping sonographic appearances of HCC and MET lesions.

7.7 Concluding Remarks

From experimentation carried out in the present study, it can be concluded that the texture information from IROIs and SROIs collectively yields significant improvement in classification accuracy. This indicates that the texture of the liver parenchyma surrounding the lesion significantly contribute towards differential diagnosis of FLLs from B-Mode US images. Further, it can also be concluded that by application of PCA to feature set consisting of 208 texture features (104 texture features and 104 texture ratio features), the information required for classification of FLLs was squeezed in first six PCs. This concludes that only first six PCs are significant to account for visually extractable and visually non-extractable textural variations exhibited by FLLs on conventional B-Mode gray scale US images. The proposed PCA-NN based CAD system obtained the OCA value of 87.7 % with ICA of 85.9 % and 88.1 % for typical and atypical cases, respectively. The ICA values for small and large HCC cases are 100 % and 87 %, respectively. The promising results obtained by the proposed PCA-NN based CAD system in the presence of a diversified, comprehensive and representative dataset used in the present study indicate its usefulness in a clinical environment to assist experienced radiologists in lesion interpretation and differential diagnosis of FLLs from conventional B-Mode gray scale US images.

In the present work, conventional gray scale B-Mode US images are considered for developing the CAD systems, primarily because the differential diagnosis between FLLs using US images is considered to a diagnostic challenge faced by radiologists in routine practice. The developed CAD system is an interactive system, radiologist can always freeze the image which is free from artifacts, and can carefully select the ROIs, the only prerequisite is the lesion should be imaged so that a SROI can be extracted from the surrounding liver parenchyma.

Keeping in view the fact that the CAD system designs with four hierarchically placed classifiers provide the possibility to go stepwise from the general classification problem, i.e., normal versus abnormal liver tissue to the more particular classification problem which is the identification of exact liver abnormality. Here, the first binary classifier identifies an unknown patch, (i.e., ROI) as normal (NOR) or abnormal (ABNOR). If the diagnosis is NOR the procedure is terminated, else the second binary classifier identifies the ROI belonging to ABNOR class as Cyst or 'other lesion' (OL) class. If the diagnosis is Cyst the procedure is

140

terminated, else the third binary classifier identifies a ROI belonging to OL class as primary benign lesion (PBL, i.e., HEM) or malignant lesion (ML). If the diagnosis is PBL the procedure is terminated, else the fourth binary classifier identifies the ROI belonging to ML class as primary malignant lesion (PML, i.e., HCC) or secondary malignant lesion (SML, i.e., MET).

It is worth observing that SVM multiclass classification using one-against-one (OAO) approach requires ten binary classifiers, (i.e., NOR/Cyst, NOR/HEM, NOR/HCC, NOR/MET, Cyst/HEM, Cyst/HCC, Cyst/MET, HEM/HCC, HEM/MET, and HCC/MET, respectively) at the same time four binary classifiers, (i.e., NOR/ABNOR, ABNOR/OL, PBL/ML, and PML/SML, respectively) are required for a hierarchical CAD (HCAD) design.

The design of an efficient HCAD system with texture features computed from IROIs and SROIs for characterization of FLLs using B-Mode US images is taken up as the next objective of the present research work and is discussed in Chapter 8.

Chapter 8

Hybrid Hierarchical CAD System for Focal Liver Lesions

8.1 Introduction

It has been demonstrated earlier that the radiologists diagnose typical focal liver lesions (FLLs) easily by their classic sonographic appearances; however, the differential diagnosis in the presence of atypical FLLs as well as small and large hepatocellular carcinoma (HCC) lesions using B-mode ultrasound (US) is considerably difficult due to existence of overlapping sonographic appearances even within individual classes of FLLs [16, 62, 73, 74, 114, 188, 189]. Thus, it is important to design of an efficient CAD system for characterization of FLLs using B-Mode US images. The results of the experimentation carried out for design of CAD systems using multi-class classifier designs (discussed in Chapter 7), demonstrate that an efficient CAD system for diagnosis of FLLs using B-Mode US images can be designed by using texture features computed extracted from IROIs and SROIs.

It is worth mentioning that the hierarchical CAD (HCAD) designs provide the possibility to go stepwise from the general classification problem, i.e., normal versus abnormal liver tissue, to the more particular classification problem which is the identification of exact liver abnormality with hierarchical framework of classifiers.

Further, the brief details of few studies reported in literature in the area of developing CAD system for characterization of FLLs using B-Mode US images are reported in Table 2.2 of Chapter 2. The design of HCAD system for diagnosis of FLLs using B-Mode US images has not been experimented as yet; however, the study in [54] reported design of HCAD system for FLLs using liver CT images. The HCAD system design in [54] used FOS and GLCM texture features with 3 binary NN classifiers arranged in a hierarchical framework for stepwise classification between NOR or abnormal (ABNOR), cyst or other lesion (OL) and HEM or HCC image classes.

In the present work, an efficient hybrid-hierarchical CAD (Hy-HCAD) system is designed with texture features computed from IROIs and SROIs by using a comprehensive and representative image database with (*i*) typical and atypical cases of liver Cyst, primary benign lesion (PBL, i.e., HEM) and secondary malignant lesion (SML, i.e., MET), (*ii*) small as well as large cases of primary malignant lesion (PML, i.e., HCC), and (*iii*) normal (NOR) liver tissue.

The sample images for (a) NOR liver tissue, (b) typical case of Cyst, PBL (i.e., HEM) and SML (i.e., MET) lesions and (c) small PML (i.e., SHCC) and large PML (i.e., LHCC) lesions

are shown earlier in Fig. 7.1 of Chapter 7. The sample images for atypical case of Cyst, PBL (i.e., HEM) and SML (i.e., MET) lesions are shown earlier in Fig. 7.2 of Chapter 7.

The protocols followed for collection of dataset, selection of ROIs and selection of ROI size are described in Section 3.4.1 of Chapter 3,

The sample images of NOR, Cyst, PBL, PML and SML liver image classes with ROIs marked are shown in Fig. 8.1.
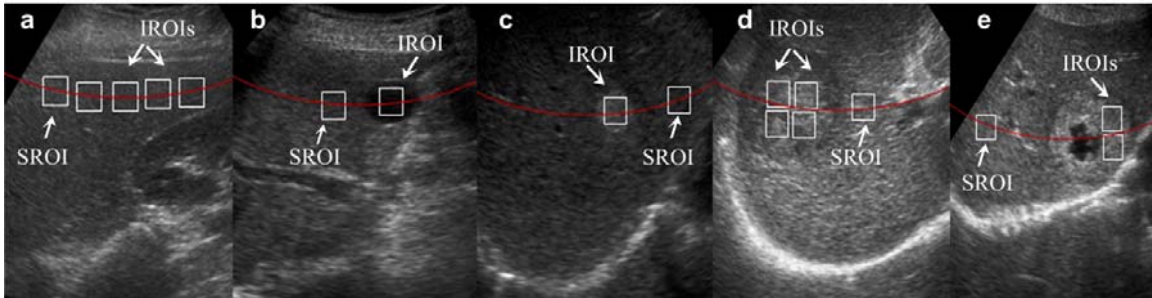
Fig. 8.1 (a) to **(e)** NOR, Cyst, PBL (i.e., HEM), PML (i.e., HCC) and SML (i.e., MET) image with IROIs and SROI marked.
Note: As shown in **(e)**, necrotic area within the lesion is avoided while extracting IROIs.

In the present study, two types of features are considered for analysis, i.e., texture features computed from IROIs and texture ratio features computed by taking the ratio of texture feature computed from IROI and texture feature computed from corresponding SROI.

NOR liver image in Fig. 8.1(a) has 4 IROIs and a corresponding SROI, thus 4 instances of texture feature set and 4 instances of texture ratio feature set are obtained.

Similarly, from Cyst, HEM, HCC and MET lesions shown in Fig. 8.1(b) to (e), 1, 1, 4 and 2 instances of texture feature set and 1, 1, 4 and 2 instances of texture ratio feature set are obtained.

8.2 CAD Systems for Characterization of FLLs using Hierarchical Classifier Designs

The proposed CAD systems for characterization of FLLs using hierarchical classifier designs consist of feature extraction, dimensionality reduction and classification module as shown in Fig. 8.2.
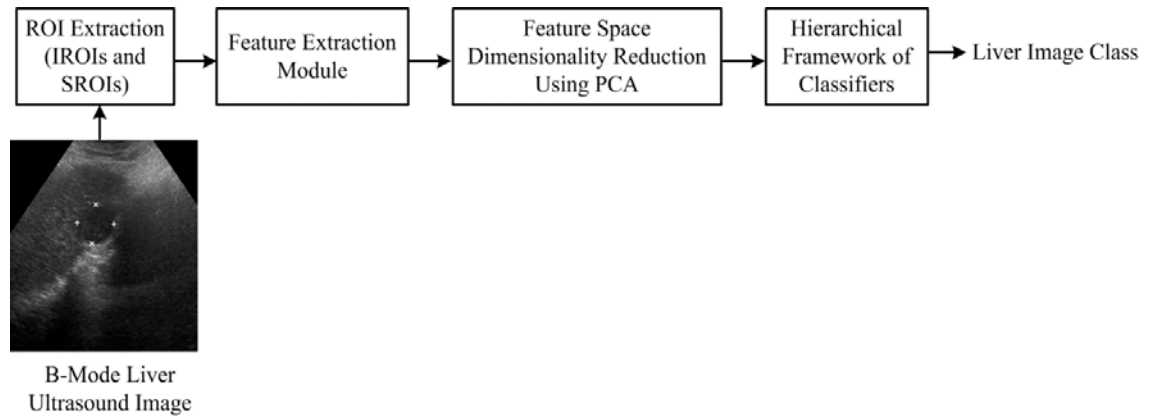
Fig. 8.2 Generalized block diagram of a hierarchical computer-aided diagnostic (HCAD) system.

8.2.1 Feature Extraction Module

In the present work, initially, a wide variety of texture features are extracted by using statistical, spectral and spatial filtering based feature extraction methods.

As described earlier in Section 7.4.1 of Chapter 7, a feature vector of 104 texture features, i.e., 6 FOS features, 13 GLCM features [61, 185, 189], 11 GLRLM features [36, 40, 51], 2 FPS features [189, 197], 42 Gabor features [90, 114] and 30 Laws' texture features [89, 183] is computed for each IROI. Similarly, a feature vector of 104 texture ratio features is computed for each IROI and a corresponding SROI. Finally, a combined feature set consisting of 208 features (104 texture features + 104 texture ratio features) is inputted to dimensionality reduction module.

8.2.2 Feature Space Dimensionality Reduction Module

In the present work, feature space dimensionality reduction has been carried out using principal component analysis (PCA). The optimal number of principal components (PCs) to be retained for classification task is determined empirically by repeated experiments carried out by stepping through first 15 PCs to build the classification model [77, 188]. The steps describing the implementation of PCA algorithm are discussed in Section 7.4.2 of Chapter 7.

8.2.3 Classification Module

The classification module consists of four binary classifiers arranged in a hierarchical framework. These four classifiers provide stepwise classification for the generalized five class classification problem. The first classifier is used to classify an unknown test case into normal (NOR) or abnormal (ABNOR) case. If the test case is predicted as abnormal (ABNOR), the second classifier is activated for classification into Cyst or 'Other Lesion' (OL) class. If the test

145

case is predicted as belonging to OL class, the third classifier is activated for classification into PBL or Malignant Lesion (ML) class. If the prediction of the third classifier is for ML class, the fourth classifier is activated for further classification into PML or SML classes. The block diagram of the classification module of the proposed HCAD systems is shown in Fig. 8.3.
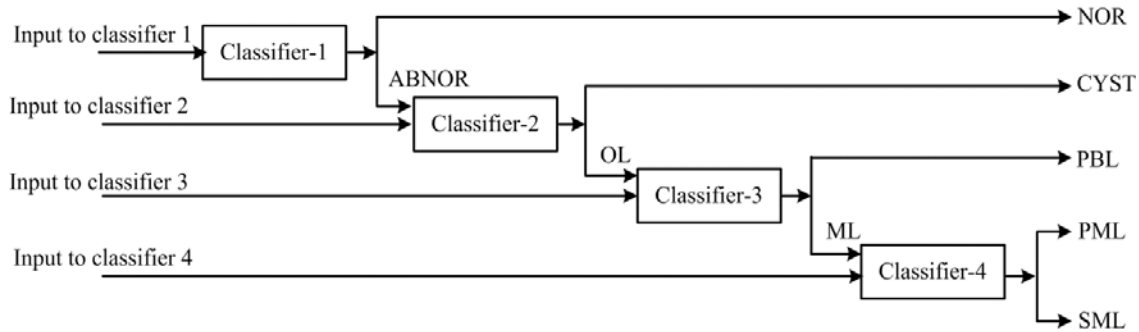
Fig. 8.3 Block diagram of the classification module of proposed HCAD systems.
Note: OL: Other lesion; ML: Malignant lesion; PBL: Primary benign lesion (HEM); PML: Primary malignant lesion (HCC); SML: Secondary malignant lesion (MET).

Feature space dimensionality reduction using PCA algorithm is applied individually before designing each binary classifier. Initially, four different HCAD systems are designed using four kNN classifiers (PCA-kNN based HCAD system, shown in Fig. 8.4), four PNN classifiers (PCA-PNN based HCAD system, shown in Fig. 8.5), four NN classifiers (PCA-NN based HCAD system, shown in Fig. 8.6), and four SVM classifiers (PCA-SVM based HCAD system, shown in Fig. 8.7). The performance of each binary classifier is evaluated at each stage and the best classifiers (yielding the maximum accuracy) are combined in a hierarchical framework for designing the Hy-HCAD system.

8.2.3.1 K-Nearest Neighbor (kNN) Classifier

The kNN classifier is an instance based classifier in which the class of an unknown instance in the testing dataset is selected to be the class of majority of instances amongst its k nearest neighbors in the training dataset [121, 188, 201]. Euclidean metric is used to calculate the distance between neighboring instances. The classification performance is affected by varying the parameter k. In the present work, the optimum value of k is obtained by repeated experimentation for classifier design by stepping through various values of k ranging from 1 to 10, and in case of a tie (i.e., if the same classification accuracy is obtained for more than one value of k), the smallest value of k is used to design the kNN classifier.

The classification module for PCA-kNN based HCAD system for classification of FLLs is shown in Fig. 8.4.
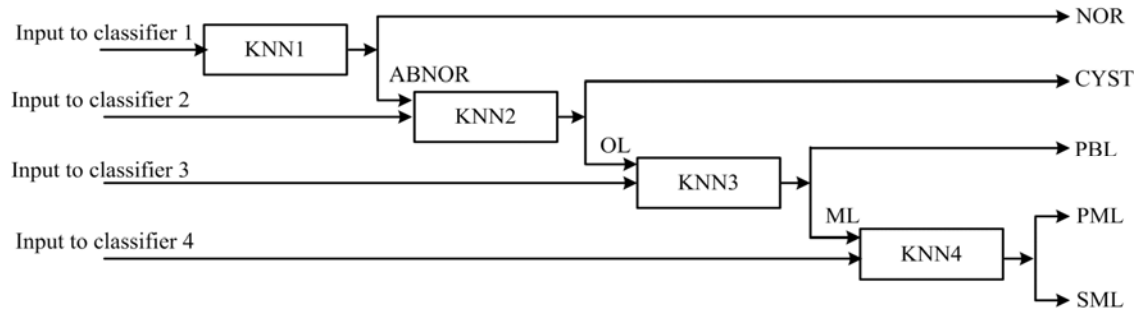
Fig. 8.4 Block diagram of classification module for PCA-*k*NN based HCAD system.
Note: NOR: Normal; ABNOR: Abnormal; OL: Other lesion; ML: Malignant Lesion; PML: Primary malignant lesion; SML: Secondary malignant lesion.

8.2.3.2 PNN Classifier

The architecture of PNN classifier consists of three layers, i.e., an input layer, pattern layer and category layer. Instances of feature vectors consisting of optimal number of PCs obtained for the binary classification tasks (i.e., NOR/ABNOR, CYST/OL, PBL/ML and PML/SML) are fed to the input layer of corresponding binary PNN classifiers.

PNN classifier constructs a classification function with instances of feature vectors in the training dataset. Thus, the pattern layer of each PNN consists of the number of instances of feature vectors in the corresponding training datasets.

The PNN classification algorithm defines a probability density function for each class based on the training dataset and the optimized kernel width parameter. The width of the radial basis kernel function that covers the space of the input features is determined by the spread parameter denoted as S_p [154, 188].

In the present work, the optimum value of the spread parameter S_p is obtained by repeated experimentation for classifier design by stepping through various values of S_p ranging from 1 to 10. The PNN classifier trained with the optimum value of S_p is then tested with testing dataset. The category layer of each PNN classifier has two neurons corresponding to the considered classes.

The block diagram of classification module for PCA-PNN based HCAD system for classification of FLLs is shown in Fig. 8.5.
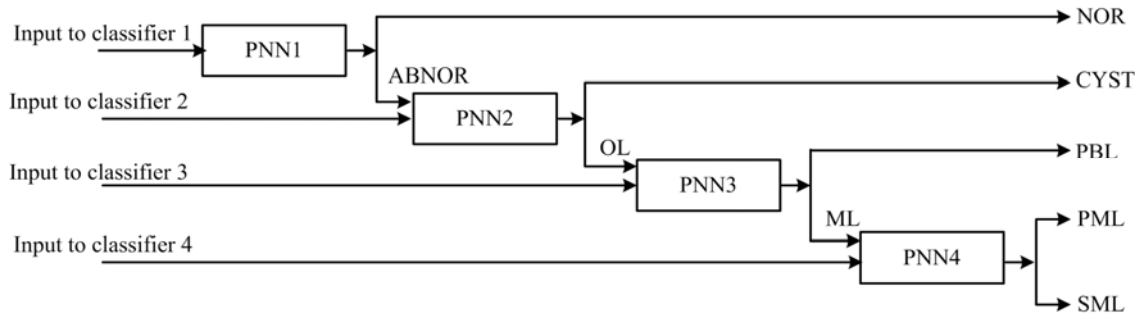
Fig. 8.5 Block diagram of classification module for PCA-PNN based HCAD system.
Note: NOR: Normal; ABNOR: Abnormal; OL: Other lesion; ML: Malignant Lesion; PML: Primary malignant lesion; SML: Secondary malignant lesion.

8.2.3.3 NN Classifier

The architecture of NN classifier consists of three layers (i.e., an input layer, hidden layer and output layer). Instances of feature vectors consisting of optimal number of PCs obtained for the binary classification tasks (i.e., NOR/ABNOR, CYST/OL, PBL/ML and PML/SML) are fed to the input layer of corresponding binary NN (BNN) classifiers. The number of neurons in the hidden layer is obtained by trial-and-error procedure. Experiments were carried out with different numbers of hidden neurons and it was observed that with 4 neurons in hidden layer, a reasonable tradeoff between accuracy and convergence is obtained. The output layer of each NN has two neurons corresponding to the considered classes. For designing each NN classifier, the output of the neuron corresponding to the labeled class is set to 1 and the output of other neuron is set to 0, i.e., the learning of each NN classifier is supervised and back-propagation algorithm with adaptive learning rate and momentum is used to obtain the desired input-output relationship [114, 188].

The block diagram of classification module for PCA-NN based HCAD system for classification of FLLs is shown in Fig. 8.6.
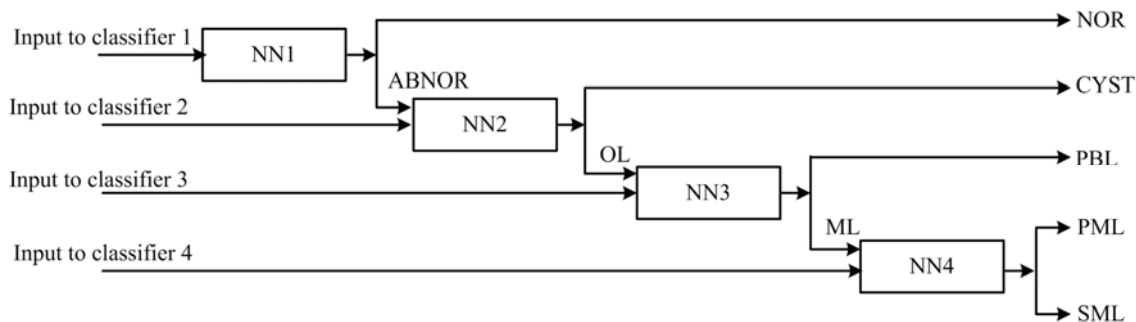
Fig. 8.6 Block diagram of classification module for PCA-NN based HCAD system.
Note: NOR: Normal; ABNOR: Abnormal; OL: Other lesion; ML: Malignant Lesion; PML: Primary malignant lesion; SML: Secondary malignant lesion.

8.2.3.4 SVM Classifier

All four binary SVM classifiers are implemented using LibSVM library [31]. In SVM algorithm, training data is mapped from lower dimensional input space to higher dimensional feature space.

In the present work, the Gaussian radial basis function kernel is used for classifier design. The optimal values for regularization parameter C and kernel parameter γ are obtained by extensive search, carried out in the parameter space for the values of $C \in \{2^{-4}, 2^{-3}, \ldots, 2^{15}\}$, $\gamma \in \{2^{-12}, 2^{-11}, \ldots, 2^{4}\}$ using 10 fold cross validation on training data [189].

The block diagram of classification module for PCA-SVM based HCAD system for classification of FLLs is shown in Fig. 8.7.
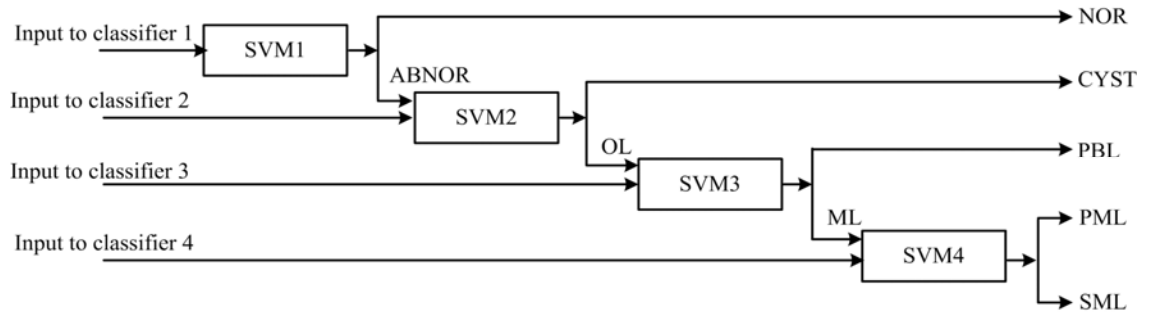
Fig. 8.7 Block diagram of classification module for PCA-SVM based HCAD system.
Note: NOR: Normal; ABNOR: Abnormal; OL: Other lesion; ML: Malignant lesion; PML: Primary malignant lesion; SML: Secondary malignant lesion.

8.3 Results

Four classification tasks were considered, corresponding to four classifiers arranged in a hierarchical framework. Each binary classifier was trained independently. The design of HCAD systems for characterization of FLLs was carried out with 108 B-Mode liver US images, i.e., 21 NOR, 12 Cyst, 15 PBL, 28 PML and 32 SML images.

The dataset description and the bifurcation of dataset into disjoint training and testing datasets for each binary classifier is shown in Table 8.1.

Table 8.1 *Dataset Description – HCAD systems for FLLs*

Dataset Description: 108 *B-Mode Liver US images*								
NOR Images : 21	Cyst Images : 12		PBL Images:15		PML Images: 28		SML Images: 32	
-	Cyst Lesions: 12		PBL lesions :15		PML lesions:28		SML lesions: 35	
-	typ. : 9	atyp.: 3	typ.:9	atyp.: 6	small:13	large:15	typ.:13	atyp.: 22
Description: 491 *ROIs* (*SROIs*: 111, *IROIs*: 380)								
Description: 111 *SROIs*								
NOR:21	Cyst:12		PBL:15		PML:28		SML:35	
Description: 380 IROIs								
NOR:70	Cyst:55		PBL:70		PML:90		SML:95	
typ.: 70	atyp.:Nil	typ.:35	atyp.:20	typ.:24	atyp.:46	small: 19	large:71	typ.:13	atyp.:82

Dataset Description – Binary Classifier NOR/ABNOR

Training Set Description	*Testing Set Description*
Images:57, SROIs:59, *IROIs*:200	Images:51, SROIs:52, *IROIs*:180
NOR: Images: 10, SROIs: 10, *IROIs*:30	NOR: Images: 11, SROIs: 11, *IROIs*:40
ABNOR: Images: 47, SROIs: 49, *IROIs*:170	ABNOR: Images: 40, SROIs: 41, *IROIs*:140
Cyst: Images: 4, Lesions: 4, typ.:3, atyp.: 1 SROIs: 4, *IROIs:* 30, typ. IROIs: 22, atyp. IROIs:8 PBL: Images: 9, Lesions: 9, typ.:6, atyp.: 3 SROIs: 9, *IROIs:* 40, typ. IROIs: 18, atyp. IROIs:22 PML: Images: 16, Lesions: 16, small :7, large: 9 SROIs: 16, *IROIs:* 50, small IROIs:10, large IROIs:40 SML: Images: 18, Lesions: 20, typ.:8, atyp.: 12 SROIs: 20, *IROIs:* 50, typ. IROIs: 8, atyp. IROIs:52	Cyst: Images: 8, Lesions: 8, typ.:6, atyp.: 2 SROIs: 8, *IROIs:* 25, typ. IROIs: 13, atyp. IROIs:12 PBL: Images: 6, Lesions:6, typ.:3, atyp.: 3 SROIs: 6, *IROIs:* 30, typ. IROIs: 6, atyp. IROIs:24 PML: Images: 18, Lesions: 20, small:8, large: 12 SROIs: 12, *IROIs:* 40, small IROIs:9, large IROIs:31 SML: Images: 14, Lesions: 15, typ.:5, atyp.: 10 SROIs: 15, *IROIs:* 45, typ. IROIs: 5, atyp. IROIs:40

Dataset Description – Binary Classifier CYST/OL

Training Set Description	*Testing Set Description*
Images:47, SROIs:49, *IROIs:*170	Images:40, SROIs:41, *IROIs:*140
Cyst: Images: 4, Lesions: 4, typ.:3, atyp.: 1 SROIs: 4, *IROIs:* 30, typ. IROIs: 22, atyp. IROIs:8	Cyst: Images: 8, Lesions: 8, typ.:6, atyp.: 2 SROIs: 8, *IROIs:* 25, typ. IROIs: 13, atyp. IROIs:12
OL*: Images: 43, SROIs:45, *IROIs:* 140	OL*: Images: 32, SROIs:33, *IROIs:* 115

Dataset Description – Binary Classifier PBL/ML

Training Set Description	*Testing Set Description*
Images:43, SROIs:45, *IROIs:140*	Images:32, SROIs:33, *IROIs:*115
PBL: Images: 9, Lesions: 9, typ.:6, atyp.: 3 SROIs: 9, *IROIs:* 40, typ. IROIs: 18, atyp. IROIs:22	PBL: Images: 6, Lesions:6, typ.:3, atyp.:3 SROIs: 6, *IROIs:* 30, typ. IROIs: 6, atyp. IROIs:24
ML*: Images: 34, SROIs:36, *IROIs:* 100	ML*: Images: 26, SROIs:27, *IROIs:* 85

Dataset Description – Binary Classifier PML/SML

Training Set Description	*Testing Set Description*
Images: 34, SROIs: 36, *IROIs:*100	Images:26, SROIs: 27, *IROIs:*85
PML: Images: 16, Lesions: 16, small.:7, large.: 9 SROIs: 16, *IROIs:50,* small IROIs: 10, large IROIs:40	PML: Images:12, Lesions:12, typ.:6, atyp.:6 SROIs: 12, *IROIs: 40*, small IROIs: 9, large IROIs:31
SML: Images: 18, Lesions: 20, typ.:8, atyp.: 12 SROIs: 20, *IROIs:* 50, typ. IROIs: 8, atyp. IROIs:42	SML: Images: 14, Lesions: 15, typ.:5, atyp.: 10 SROIs: 15, *IROIs:* 45, typ. IROIs: 5, atyp. IROIs:40

Note: typ.: Typical; atyp. : Atypical; OL: Other lesion (Further bifurcation of OL* class into PBL, PML and SML sub-classes in training and testing dataset is shown in dataset bifurcation for ABNOR image class); ML: Malignant lesion (Further bifurcation of ML* class into PML and SML sub-classes in training and testing dataset is shown in dataset bifurcation for ABNOR image class). The size of small PML lesion varied from 1.5 to 1.9 cm and size of large PML lesion varied from 2.1 to 5.6cm; **(a)** Total lesions = 90 [(typ. lesions (31) + atyp. lesions (31) + small PML lesions (13) + large PML lesions (15)]; **(b)** Total SROIs = 111 [90 SROIs corresponding to 90 lesions + 21 SROIs corresponding to 21 NOR images]; **(c)** Total typ. IROIs = 142 [typ. lesion IROIs (72) + typ. NOR IROIs (70)]; **(d)** Total atyp. IROIs = 148; **(e)** Total small PML lesion IROIs = 19; **(f)** Total large PML lesion IROIs = 71; **(g)** Total IROIs = **(c)** + **(d)** + **(e)** + **(f)** = 142 + 148 + 19 + 71 = 380.

The brief details of the experiments carried out with HCAD system designs for diagnosis of FLLs using B-Mode US images are depicted in Table 8.2.

Table 8.2 *Experiments carried out with HCAD system designs for diagnosis of FLLs using B-Mode US images.*

Experiment No	Experiment
Experiment 1	Design of PCA-kNN based HCAD system
Experiment 2	Design of PCA-PNN based HCAD system
Experiment 3	Design of PCA-NN based HCAD system
Experiment 4	Design of PCA-SVM based HCAD system
Experiment 5	Comparative evaluation of PCA-kNN, PCA-PNN, PCA-NN and PCA-SVM based HCAD systems
Experiment 6	Design of an efficient hybrid-HCAD (Hy-HCAD) system

These experiments have been carried out with a comprehensive and representative database consisting of (*i*) typical and atypical cases of liver Cyst, primary benign lesion (PBL, i.e., HEM) and secondary malignant lesion (SML, i.e., MET), (*ii*) small as well as large cases of primary malignant lesion (PML, i.e., HCC), and (*iii*) normal (NOR) liver tissue.

(*i*) *Experiment* 1: In this experiment the performance of binary classifiers of PCA-kNN based HCAD system is evaluated and the results obtained are given in Table 8.3.

Table 8.3 *Performance obtained by PCA-kNN based HCAD systems.*

Results - Experiment 1: PCA-kNN based HCAD system						
Classifier	PCs	CM		Acc_Bin_Class	OCA (%)	ICA (%)
PCA-kNN1	8		NOR	ABNOR	95.5 (172/180)		87.5 (35/40)
		NOR	35	5			
		ABNOR	3	137			97.8 (137/140)
PCA-kNN2	4		CYST	OL	97.1 (136/140)	90.5 (163/180)	88(22/25)
		CYST	22	3			
		OL	1	114			99.1(114/115)
PCA-kNN3	3		PBL	ML	96.5 (111/115)		93.3(28/30)
		PBL	28	2			
		ML	2	83			97.6(83/85)
PCA-kNN4	7		PML	SML	98.8 (84/85)		97.5(39/40)
		PML	39	1			
		SML	0	45			100(45/45)

Note: PCs: Optimal No. of principal components, CM: Confusion matrix, Acc_Bin_Class: Accuracy of binary classifier, OCA: Overall classification accuracy, ICA: Individual class accuracy, NOR: Normal liver, ABNOR: Abnormal liver, OL: Other lesion, PBL: Primary benign lesion, ML: Malignant lesion, PML: Primary malignant lesion, SML: Secondary malignant lesion, PCA: Principal component analysis, NN: Neural network, kNN: k-Nearest neighbour classifier.

(*ii*) *Experiment* 2: In this experiment the performance of binary classifiers of PCA-PNN based HCAD system is evaluated and the results obtained are given in Table 8.4.

Table 8.4 *Performance obtained by PCA-PNN based HCAD systems.*

Classifier	PCs	CM		Acc_Bin_Class	OCA (%)	ICA (%)
Results - Experiment 2: *PCA-PNN based HCAD system*						
PCA-PNN1	10	NOR	ABNOR	96.1 (173/180)		90 (36/40)
		NOR — 36	4			
		ABNOR — 3	137			97.8 (137/140)
PCA-PNN2	8	CYST	OL	97.1 (136/140)		96(24/25)
		CYST — 24	1			
		OL — 3	112		91.6 (165/180)	97.3(112/115)
PCA-PNN3	3	PBL	ML	97.3 (112/115)		96.6(28/30)
		PBL — 29	1			
		ML — 2	83			97.6(83/85)
PCA-PNN4	4	PML	SML	98.8 (84/85)		100(40/40)
		PML — 40	0			
		SML — 1	44			97.7(44/45)

Note: PCs: Optimal No. of principal components, CM: Confusion matrix, Acc_Bin_Class: Accuracy of binary classifier, OCA: Overall classification accuracy, ICA: Individual class accuracy, NOR: Normal liver, ABNOR: Abnormal liver, OL: Other lesion, PBL: Primary benign lesion, ML: Malignant lesion, PML: Primary malignant lesion, SML: Secondary malignant lesion, PCA: Principal component analysis, PNN: Probabilistic neural network.

(*iii*) *Experiment* 3: In this experiment the performance of binary classifiers of PCA-NN based HCAD system is evaluated and the results obtained are given in Table 8.5.

Table 8.5 *Performance obtained by PCA-NN based HCAD systems.*

Classifier	PCs	CM		Acc_Bin_Class	OCA (%)	ICA (%)
Results - Experiment 3: *PCA-NN based HCAD system*						
PCA-NN1	11	NOR	ABNOR	95.5 (172/180)		92.5 (37/40)
		NOR — 37	3			
		ABNOR — 5	135			96.4 (135/140)
PCA-NN2	15	CYST	OL	97.1 (136/140)		88(22/25)
		CYST — 22	3			
		OL — 1	114		88.3 (159/180)	99.1(114/115)
PCA-NN3	11	PBL	ML	93.0 (107/115)		100(30/30)
		PBL — 30	0			
		ML — 8	77			90.5(77/85)
PCA-NN4	3	PML	SML	98.8 (84/85)		100(40/40)
		PML — 40	0			
		SML — 1	44			97.7(44/45)

Note: PCs: Optimal No. of principal components, CM: Confusion matrix, Acc_Bin_Class: Accuracy of binary classifier, OCA: Overall classification accuracy, ICA: Individual class accuracy, NOR: Normal liver, ABNOR: Abnormal liver, OL: Other lesion, PBL: Primary benign lesion, ML: Malignant lesion, PML: Primary malignant lesion, SML: Secondary malignant lesion, PCA: Principal component analysis, NN: Neural Network.

(*iv*) *Experiment* 4: In this experiment the performance of binary classifiers of PCA-SVM based HCAD system is evaluated and the results obtained are given in Table 8.6.

Table 8.6 *Performance obtained by PCA-SVM based HCAD systems.*

Results - Experiment 4: PCA-SVM based HCAD system						
Classifier	*PC*	*CM*		*Acc_Bin_Class*	*OCA (%)*	*ICA (%)*
PCA-SVM1	11		NOR	ABNOR	96.6 (174/180)		87.5 (35/40)
		NOR	35	5			
		ABNOR	1	139			99.2 (139/140)
PCA-SVM2	15		CYST	OL	97.8 (137/140)		73.3(22/25)
		CYST	22	3		90.5 (163/180)	
		OL	0	115			100(115/115)
PCA-SVM3	11		PBL	ML	93.9 (108/115)		96.6(29/30)
		PBL	29	1			
		ML	6	79			92.9(79/85)
PCA-SVM4	4		PML	SML	98.8 (84/85)		100(40/40)
		PML	40	0			
		SML	1	44			97.7(44/45)

Note: PCs: Optimal No. of principal components, CM: Confusion matrix, Acc_Bin_Class: Accuracy of binary classifier, OCA: Overall classification accuracy, ICA: Individual class accuracy, NOR: Normal liver, ABNOR: Abnormal liver, OL: Other lesion, PBL: Primary benign lesion, ML: Malignant lesion, PML: Primary malignant lesion, SML: Secondary malignant lesion, PCA: Principal component analysis, SVM: Support vector machine.

The value of OCA is obtained by adding the number of misclassifications obtained at each stage of the HCAD system, e.g., PCA-SVM based HCAD system yield total 17 misclassifications (i.e., 6, 3, 7 and 1 misclassifications for PCA-SVM1, PCA-SVM2, PCA-SVM3 and PCA-SVM4 classifiers, respectively), therefore, OCA for PCA-SVM based HCAD system is {(180 – 17) / 180}×100 = {(163 / 180) ×100} = 90.5 %. It is observed that PCA-PNN based HCAD system yields the maximum OCA of 91.6 % with only 15 misclassifications out of 180 test cases.

By visualizing the performance of individual binary classifiers of PCA-*k*NN, PCA-PNN, PCA-NN, and PCA-SVM based HCAD systems (shown in Table 8.3, Table 8.4, Table 8.5 and Table 8.6), some interesting facts are observed:

(*a*)   For classification between NOR/ABNOR classes the maximum accuracy of 96.6 % is obtained by using PCA-SVM1 classifier in comparison with 95.5 %, 96.1 % and 95.5 % as obtained by using PCA-*k*NN1, PCA-PNN1 and PCA-NN1 classifiers.

(*b*)   For classification of ABNOR cases between CYST/OL classes the maximum accuracy of 97.8 % is obtained by using PCA-SVM2 classifier in comparison with 97.1 % as obtained by using PCA-NN2, PCA-PNN2 and PCA-*k*NN2 classifiers.

(*c*)   For classification of OL cases between PBL/ML classes the maximum accuracy of 97.3 % is obtained by using PCA-PNN3 classifier in comparison with 93.9 %, 93 % and 96.5 % as obtained by using PCA-SVM3, PCA-NN3 and PCA-*k*NN3 classifiers.

(*d*)   For classification of ML cases between PML/SML classes all the four classifiers (i.e., PCA-SVM4, PCA-NN4, PCA-PNN4 and PCA-*k*NN4) yield the same accuracy of 98.8 %. It may be noted that PCA-NN4 is considered as best classifier for PML/SML classes because it is designed with only 3 PCs (least number of PCs) for the classification task.

(v) *Experiment* 5: In this experiment the comparative performance analysis of proposed HCAD systems for characterization of FLLs has been carried out. The results obtained are reported in Table 8.7

Table 8.7 *Comparative performance analysis – Proposed HCAD systems.*

HCAD system	*Acc.$_{NOR/ABNOR}$ (%)*	*Acc.$_{CYST/OL}$ (%)*	*Acc.$_{PBL/ML}$ (%)*	*Acc.$_{PML/SML}$ (%)*	*OCA (%)*
PCA-*k*NN	95.5	97.1	96.6	98.8	90.5
PCA-PNN	96.1	97.1	97.3	98.8	91.6
PCA-NN	95.5	97.1	93.0	98.8	88.3
PCA-SVM	96.6	97.8	93.9	98.8	90.5

Table spanning title: *Results - Experiment 5: Comparative performance analysis of HCAD Systems*

Note: HCAD system: Hierarchical CAD system, Acc.: Accuracy of binary classifier, OCA: Overall classification accuracy

From Table 8.7, it can be observed that the PCA-PNN based HCAD outperforms in comparison with PCA-*k*NN, PCA-NN and PCA-SVM based HCADs. For classification between NOR/ABNOR and Cyst/OL, PCA-SVM1 and PCA-SVM2 are best. For classification between PBL/ML, PCA-PNN3 is the best and for classification between PML/SML all the four binary classifiers (i.e., PCA-*k*NN4, PCA-PNN-4, PCA-NN4 and PCA-SVM4) yield the same classification performance. However, PCA-NN4 is considered the best, because it uses only 3 PCs, in comparison with 7, 4 and 4 PCs used by PCA-*k*NN, PCA-PNN and PCA-NN based HCAD systems, respectively.

(*vi*) *Experiment* 6: In this experiment, the best performing individual classifiers are combined in a hierarchical framework to design an efficient Hy-HCAD system for classification of FLLs from B-Mode US images. The performance analysis of Hy-HCAD system is reported in Table 8.8.

Table 8.8: *Performance obtained by Hy-HCAD system.*

Classifier	PCs	CM			Acc_Bin_Class	OCA (%)	ICA (%)
			NOR	ABNOR			
PCA-SVM1	11	NOR	35	5	96.6 (174/180)		87.5 (35/40)
		ABNOR	1	139			99.2 (139/140)
			CYST	OL			
PCA-SVM2	15	CYST	22	3	97.8 (137/140)		73.3(22/25)
		OL	0	115		92.7 (167/180)	100(115/115)
			PBL	ML			
PCA-PNN3	3	PBL	29	1	97.3 (112/115)		96.6(29/30)
		ML	2	83			97.6(83/85)
			PML	SML			
PCA-NN4	3	PML	40	0	98.8 (84/85)		100(40/40)
		SML	1	44			97.7(44/45)

Note: PCs: Optimal No. of principal components, CM: Confusion matrix, Acc_Bin_Class: Accuracy of binary classifier, OCA: Overall classification accuracy, ICA: Individual class accuracy, NOR: Normal liver, ABNOR: Abnormal liver, OL: Other lesion, PBL: Primary benign lesion, ML: Malignant lesion, PML: Primary malignant lesion, SML: Secondary malignant lesion, PCA: Principal component analysis, SVM: Support vector machine, NN: Neural network, PNN: Probabilistic neural network.

From Table 8.8, it is observed that the proposed Hy-HCAD system yields the maximum OCA of 92.7 % with only 13 misclassifications out of 180 test cases. The proposed Hy-HCAD system outperforms in comparison PCA-*k*NN, PCA-PNN, PCA-NN and PCA-SVM based HCAD systems. The OCA obtained by Hy-HCAD system is 92.7 % in comparison with 90.5 %, 91.6 %, 83.3 %, 91.6 % as obtained by PCA-*k*NN, PCA-PNN, PCA-NN and PCA-SVM based HCAD systems, respectively.

The architecture of the classification module of the proposed Hy-HCAD system designed the best performing individual classifiers arranged in a hierarchical framework is shown in Fig. 8.8.
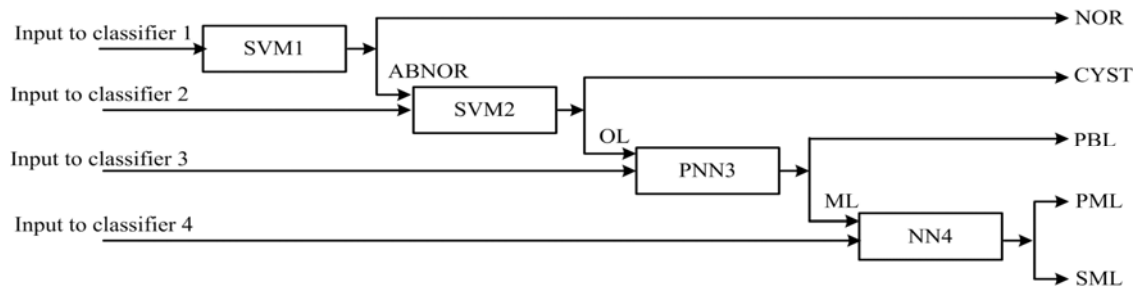
Fig. 8.8 Architecture of classification module of proposed Hy-HCAD system for classification of FLLs using B-Mode US images.
Note: NOR: Normal liver; ABNOR: Abnormal liver; OL: Other lesion; ML: Malignant lesion; PML: Primary malignant lesion; SML: Secondary malignant lesion.

8.4 Concluding Remarks

Among PCA-*k*NN, PCA-PNN, PCA-NN, and PCA-SVM based HCAD systems, the PCA-PNN based HCAD system yields maximum OCA of 91.6 % with 15 misclassifications out of total 180 test cases. However, it is observed that the Hy-HCAD system designed by using best binary classifiers yields OCA of 92.7 % with only 13 misclassifications out of total 180 test cases. Keeping in view the fact that conventional gray scale B-Mode US offers limited sensitivity for differential diagnosis between atypical cases of Cyst, PBL, SML lesions as well as small and large PML cases the results obtained by the proposed Hy-HCAD system are quite promising and indicate its usefulness to assist radiologist in a clinical environment.

In human society, many experts each specialized in a particular task meet to overcome a complicated problem and reach at a decision in a collective manner. This combined decision is expected to be a better solution than can be given by an individual expert. Therefore, in the area of medical decision making as well, CAD system designs based on ensemble methods, (i.e., methods based on combining decisions from various classifiers) are expected to yield better results in comparison to the results achieved by CAD system designs based on multi-class classifier.

The results of comparative evaluation of proposed CAD systems using multi-class classifier designs (reported in Table 7.10 of Chapter 7), it can be concluded that PCA-NN based CAD yields the maximum OCA value of 87.7 %, in comparison with 87.2 %, 86.1 % and 85 % as obtained with PCA-*k*NN, PCA-PNN and PCA-NN based CAD systems.

Accordingly, design of neural network ensemble (NNE) based CAD system for classification of FLLs using B-Mode US images is the next objective of the present research work as discussed in Chapter 9.

156

Chapter 9

Neural Network Ensemble based CAD System for Focal Liver Lesions

9.1 Introduction

It has been already demonstrated that the differential diagnosis in patients with focal liver lesions (FLLs) using B-Mode ultrasound (US) images is broad due to the existence of a wide variety of overlapping sonographic appearances even with-in individual classes of FLLs [20, 116, I56, 174, 195]. Therefore, an efficient computer-aided classification (CAD) system using ensemble of classifiers for classification of FLLs based on conventional gray scale B-Mode US is highly desired.

The motivation for experimenting with NNE based CAD design is that these designs based on ensemble methods (i.e., methods based on combining decisions from various classifiers) are expected to yield better results in comparison to the results achieved by CAD system designs based on multi-class classifier [60, 215].

By comparing the performance obtained by CAD systems based multi-class classifier designs from Table 7.10 of Chapter 7, it can be concluded that an efficient CAD system for characterization of FLLs using B-Mode US images can be designed by using texture features (computed from IROIs) and texture ratio features (computed from IROIs and SROIs) along with five-class PCA-NN based classifier.

It was observed that the PCA-NN based five-class classifier design yield the highest OCA value of 87.7 % in comparison to the OCA values of 85 %, 86.1 % and 87.2 %, obtained by using PCA-kNN, PCA-PNN and PCA-SVM, based five-class classifier designs, respectively. Therefore, it is desired to enhance the performance of the five-class PCA-NN based classifier design a using an ensemble of PCA-NN based classifiers.

In this chapter, the design of a neural network ensemble (NNE) based CAD system for characterization of commonly occurring FLLs such as Cyst, HEM, HCC, and MET along with normal (NOR) liver tissue is proposed.

9.2 Dataset Description – NNE based CAD System

The design of NNE based CAD system for characterization of FLLs was carried out with 108 B-Mode liver US images, (i.e., 21 NOR, 12 Cyst, 15 HEM, 28 HCC and 32 MET images) by using texture features computed from IROIs and SROIs.

The sample images for (a) NOR liver tissue, (b) typical case of Cyst, HEM and MET lesions and (c) SHCC as well as LHCC lesions are shown earlier in Fig. 7.1 of Chapter 7.

The sample images for atypical case of Cyst, HEM and MET lesions are shown earlier in Fig. 7.2 of Chapter 7. The protocols followed for collection of dataset, selection of ROIs and selection of ROI size are described earlier in Section 3.4 of Chapter 3.

The sample images of NOR, Cyst, HEM, HCC and MET cases from the acquired image database with ROIs marked are shown earlier in Fig. 7.3 (a) to Fig 7.3 (e) of Chapter 7.

The distribution of clinically acquired database of 108 B-Mode liver US images (including NOR, Cyst, HCC, HEM and MET images) among various liver image subclasses is shown earlier in Fig. 7.4 of Chapter 7.

The bifurcation of total FLLs, among typical, atypical, SHCC and LHCC lesions and bifurcation of total ROIs, among IROIs and SROIs belonging to typical, atypical, SHCC and LHCC lesions is shown earlier in Fig. 7.5 of Chapter 7.

The bifurcation of acquired dataset into training dataset and testing dataset is shown earlier in Fig. 7.6 of Chapter 7.

The final dataset consisting of total 111 SROIs and 380 IROIs was stored in a PC (Pentium Core-2-Duo, 2.67 GHz with 1.97 GB RAM).

9.3 CAD System for Characterization of FLLs using Ensemble of Neural Network Classifiers

The block diagram of proposed NNE based CAD system for characterization of FLLs is shown in Fig. 9.1.
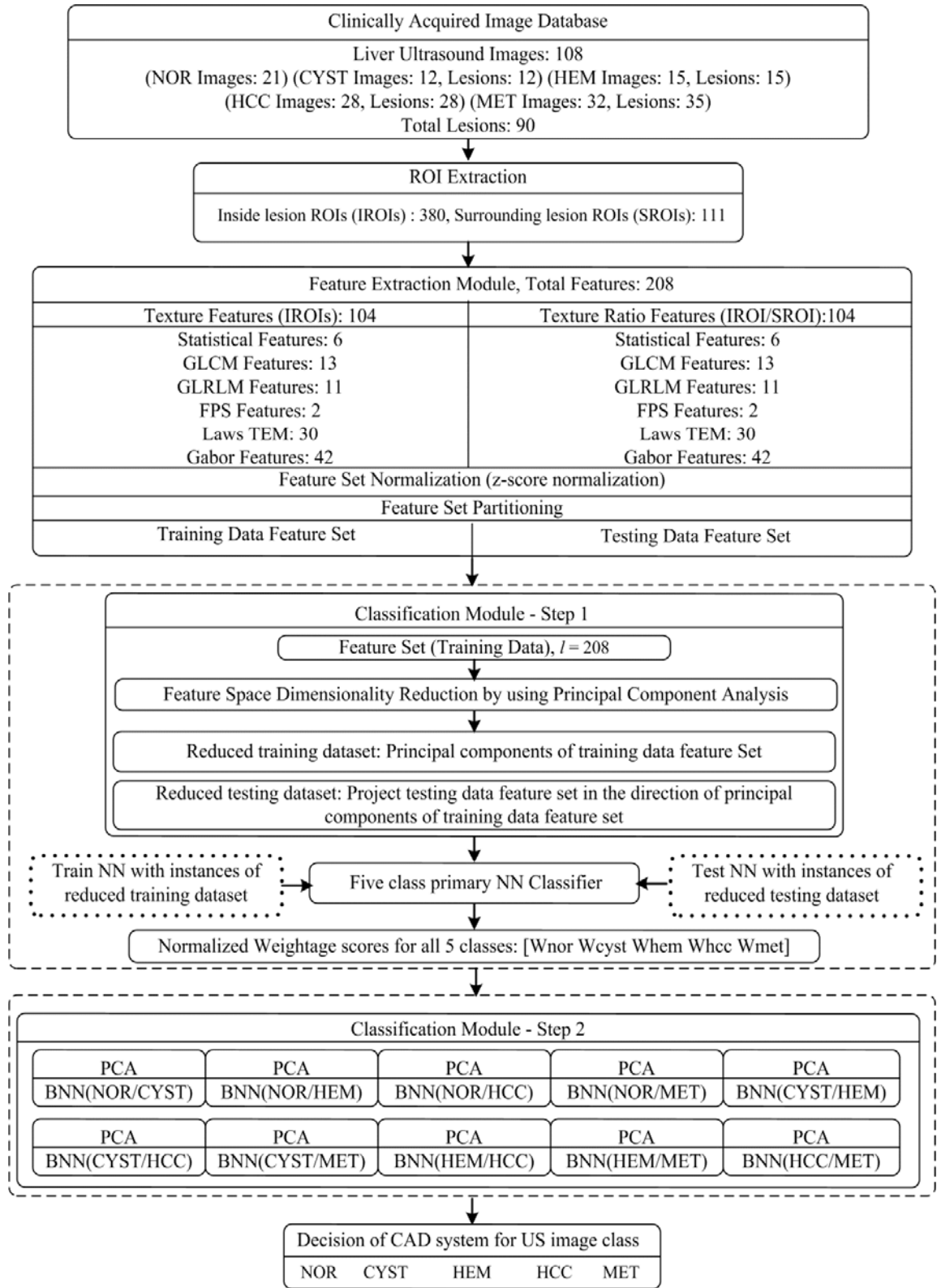
Fig. 9.1 Proposed NNE based CAD system for classification of FLLs from B-Mode US images.
Note: IROIs: Inside lesion ROIs: SROIs: Surrounding lesion ROIs; *l*: Length of feature vector; NN: Neural network; BNN: Binary neural network; PCA: Principal component analysis.

For implementation of the proposed NNE based CAD system, the database of 380 non-overlapping IROIs and 111 SROIs was created from 108 clinically acquired B-Mode US liver images. The NNE based CAD system consists of feature extraction module, and a two-step classification module. Feature dimensionality reduction by PCA is considered as an integral part of both the steps in classification module. In feature extraction module, 104 texture features and 104 texture ratio features are computed for all 380 IROIs, resulting in feature set consisting of 380 texture feature vectors (TFVs) of length 208. The feature set is normalized using z-score normalization. The normalized feature set is bifurcated into two disjoint feature sets, i.e., training data feature set and testing data feature set. PCA is carried out on the training data feature set and reduced training dataset of PCA derived principal components (PCs) is obtained. The reduced testing dataset is obtained by projecting the data points of the testing data feature set in the direction of PCs of training data feature set. Feature space dimensionality reduction by PCA is applied individually for the design of five-class NN primary classifier in Step 1 of the classification module and for the design of ten mutually independent binary neural network (BNN) secondary classifiers in Step 2 of the classification module in order to find out the number of PCs which could provide adequate discrimination capability in each case.

9.3.1 Feature Extraction Module

In feature extraction module, initially a wide variety of visual and nonvisual sonographic features are extracted by using statistical, spectral and spatial filtering based feature extraction methods as described earlier in Section 7.4.1 of Chapter 7.

For characterization of FLLs, initially three texture feature vectors (TFVs) are computed using FOS, GLCM, GLRLM, FPS, GWT and Laws' texture feature extraction methods. The brief description of these TFVs is given in Table 9.1.

Table 9.1 *Description of TFVs.*

Texture Feature Vectors (*TFVs*)	(*l*)
TFV1: TFV consisting of 104 texture features (6 FOS, 13 GLCM, 11 GLRLM, 2 FPS, 42 Gabor and 30 Laws features) computed from IROIs.	104
TFV2: TFV consisting of 104 texture ratio features (6 FOS, 13 GLCM, 11 GLRLM, 2 FPS, 42 Gabor and 30 Laws features) computed by taking the ratio of texture feature computed from IROI and the corresponding SROI.	104
TFV3: Combined TFV consisting of 104 texture features (TFV1) and 104 texture ratio features (TFV2).	208

Note: TFV: Texture feature vector; *l*: length of TFV; IROI: Inside lesion ROI; SROI: Surrounding lesion ROI; FOS: First order statistics; GLCM: Gray level co-occurrence matrix; GLRLM: Gray level run length matrix; FPS: Fourier power spectrum.

Initially, all the three feature sets, i.e., FS1, FS2 and FS3 consisting of instances of TFV1, TFV2 and TFV3, respectively, as described in Table 9.2, are used for classification of FLLs from B-Mode US images. The FS3 consisting of instances of combined TFV, i.e., TFV3 was considered for analysis, to investigate the effect of including texture information from SROIs in differential diagnosis between FLLs from B-Mode US. The classification experiments are carried out by using NN classifiers. The classification performance with respect to overall classification accuracy (OCA) values and the individual class accuracy (ICA) values obtained by five class primary NN classifier with FS1, FS2 and FS3 is summarized in Table 9.2.

Table 9.2 *Classification performance of five-class primary NN classifier with FS1, FS2 and FS3.*

	Classification Performance : *NN classifier*					
FS	*OCA* (%)	*ICA*$_{NOR}$ (%)	*ICA*$_{CYST}$ (%)	*ICA*$_{HEM}$ (%)	*ICA*$_{HCC}$(%)	*ICA*$_{MET}$ (%)
FS1	66.1	77.5	92.0	50.0	37.5	77.7
FS2	75.0	85.0	76.0	76.6	60.0	75.5
FS3	82.7	87.7	92.0	83.3	87.5	71.1

Note: FS: Feature set, OCA: Overall classification accuracy, ICA: Individual class accuracy

From Table 9.2, it can be observed that FS3 yield highest OCA value of 82.7 % in comparison to 66.1 % and 75 % as obtained by FS1 and FS2. The results justify the premise that both texture features and texture ratio features contribute for effective characterization of FLLs from B-Mode US. Thus FS3, consisting of combined TFVs is considered for all further analysis.

9.3.2 Classification Module

The proposed NNE based CAD system incorporates two steps in classification module. The Step 1 of the classification module consists of a five-class NN classifier and the Step 2 of the classification module consists of ten BNN (binary neural network) classifiers.

The FS3, consisting of instances of combined TFV of length 208 (i.e., TFV3), is used for the present classification task. This combined TFV may contain redundant and correlated features, which if used for classifier design can degrade its performance in terms of accuracy and reliability. Thus, PCA is used for feature space dimensionality reduction before classifier design in both the steps of classification module. The PCA algorithm ensures that the covariance of any of the components with any other component is zero. As it is quite possible that the PCs accounting for a lesser amount of variance in the data may be significant for the classification task, and also since the computed PCs are uncorrelated to each other, it is always reasonable to step through the first few PCs for building the classification model [47, 60]. In the present work, the optimal number of PCs to be retained for classification task is determined

empirically by repeated experiments carried out by stepping through first 15 PCs to build the classification models.

The flow chart showing the working of proposed NNE based CAD system for characterization of FLLs using B-Mode US images is shown in Fig. 9.2.
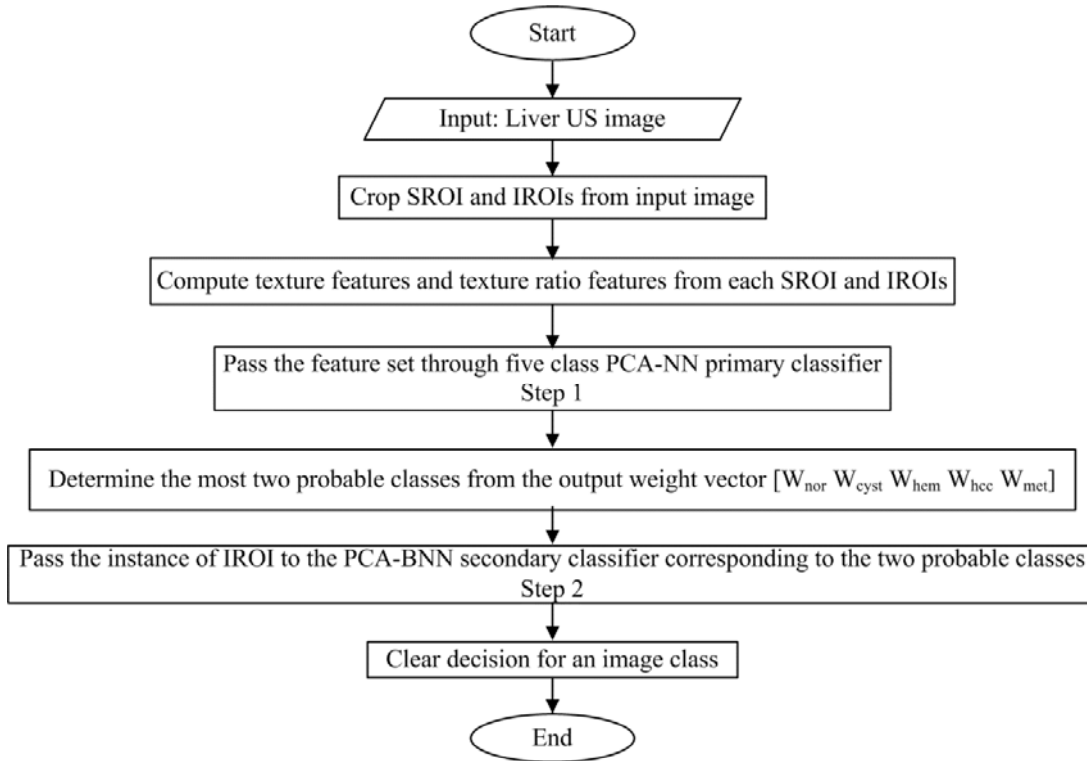
Fig. 9.2 Flowchart of the proposed NNE based CAD system for characterization of FLLs using B-Mode US images.

9.3.2.1 *Classification Module* (*Step* 1)

The Step 1 of classification module consists of a five-class PCA-NN based primary classifier. As shown in Table 9.2, the FS3, consisting of instances of combined TFV, (i.e., TFV3), yield higher OCA in comparison with FS2 and FS1. Thus, FS3 is subjected to feature space dimensionality reduction using PCA. The number of PCs yielding the maximum OCA are retained in reduced feature set (FS4) for classifier design. It is observed that the first six PCs yield maximum OCA of 87.7 %. Thus, reduced features set (i.e., FS4), consisting of instances of reduced TFVs of length 6 (Optimal number of PCs), is used for the design of the five-class PCA-NN based primary classifier. The classification performance obtained with FS4 is shown in Table 9.3.

Table 9.3 *Classification performance of five-class primary NN classifier with FS4 (Step 1).*

NN Arch: (I: H: O)	Optimal No. of PCs	OCA (%)
Five-class primary NN: (6:10:5) NOR/CYST/HEM/HCC/MET	6	87.7

Note: NN Arch: Neural network architecture; I: Input layer neurons; H: Hidden layer neurons; O: Output layer neurons.

For design of each PCA-NN based primary classifier, the optimal number of neurons in the hidden layer is obtained by trial-and-error procedure. Experiments were carried out with different numbers of hidden neurons and it was observed that for 10 neurons in hidden layer a reasonable tradeoff between accuracy and convergence is obtained [189].

The bifurcation of instances of individual classes in FS4 (training data) and FS4 (testing data) in case of five-class PCA-NN based primary classifier is shown is shown in Fig. 9.3.

Dataset Bifurcation for Five Class NN Primary Classifier

Training Set Description (SROIs: 59, IROIs: 200)	Testing Set Description (SROIs: 52, IROIs: 180)
NOR-Images:10, SROIs: 10, IROIs: 30	**NOR-**Images:11, SROIs: 11, IROIs: 40
CYST-Images: 4, Lesions: 4, Typical: 3, Atypical: 1 SROIs: 4, IROIs: 30,Typical IROIs: 22 , Atypical IROIs: 8	**CYST-**Images: 8, Lesions: 8, Typical: 6, Atypical: 2 SROIs: 8, IROIs: 25, Typical IROIs: 13 , Atypical IROIs: 12
HEM-Images: 9, Lesions: 9, Typical: 6, Atypical: 3 SROIs: 9, IROIs: 40, Typical IROIs: 18 , Atypical IROIs: 22	**HEM-**Images: 6, Lesions: 6, Typical: 3, Atypical: 3 SROIs: 6, IROIs: 30, Typical IROIs: 6 , Atypical IROIs: 24
HCC-Images: 16, Lesions: 16, SHCC: 7, LHCC: 9 SROIs: 16, IROIs: 50, SHCC IROIs: 10, LHCC IROIs: 40	**HCC-**Images: 12, Lesions: 12, SHCC: 6, LHCC: 6 SROIs: 12, IROIs: 40, SHCC IROIs: 9 LHCC IROIs: 31
MET-Images: 18, Lesions: 20, Typical: 8, Atypical: 12 SROIs: 20, IROIs: 50, Typical IROIs: 8, Atypical IROIs: 42	**MET-**Images: 14, Lesions: 15, Typical: 5, Atypical: 10 SROIs: 15, IROIs: 45, Typical IROIs: 5, Atypical IROIs: 40

Fig. 9.3 The bifurcation of instances of individual classes in FS3 (training data) and FS3 (testing data) for five-class NN primary classifier.

The five-class PCA-NN based primary classifier yield weightage scores for five liver image classes. Normalization of this five dimensional output weight vector makes it analogous to probability outputs for each class. The prediction of output weight vector [W_{nor} W_{cyst} W_{hem} W_{hcc} W_{met}] for all the 180 TFVs in the FS4 (testing data) is stored for analysis.

9.3.2.2 Classification Module (*Step* 2)

The Step 2 of classification module consists of ten mutually independent PCA-BNN based secondary classifiers for NOR/Cyst, NOR/HEM, NOR/HCC, NOR/MET, Cyst/HEM, Cyst/HCC, Cyst/MET, HEM/HCC, HEM/MET and HCC/MET classes, respectively. The output weight vector predicted by five-class PCA-NN based primary classifier for an unknown test instance in FS4 (testing data) is used to determine the first two most probable classes,

based on which it is directed to the corresponding binary PCA-NN based secondary classifier for crisp classification between two classes. The proposed approach can be understood as analogous to querying about the diagnosis of an unknown test case from a radiologist, with expertise of providing interpretation among all the five liver image classes, in the Step 1, and then based on his advice on first two most probable classes, again querying another radiologist, with expertise in interpretation of these two most probable classes only, in the Step 2. It is expected that the overall result will improve by including the Step 2.

The bifurcation of instances of individual classes in training data feature set and testing data feature set in the case of ten PCA-BNN secondary classifiers is shown is shown in Fig. 9.4. to Fig. 9.13. The bifurcation of instances of individual classes in training data feature set and testing data feature set in the case of PCA-BNN1 classier designed for classification between NOR/Cyst classes is shown is shown in Fig. 9.4.

Dataset Bifurcation PCA-BNN2 (NOR/CYST)

Training Set Description (SROIs: 14, IROIs: 60)	Testing Set Description (SROIs: 19, IROIs: 65)
NOR- Images:10, SROIs: 10, IROIs: 30	**NOR-**Images:11, SROIs: 11, IROIs: 40
CYST-Images: 4, Lesions: 4, Typical: 3, Atypical: 1 SROIs: 4, IROIs: 30 , Typical IROIs: 22 , Atypical IROIs: 8	**CYST-**Images: 8, Lesions: 8, Typical: 6, Atypical: 2 SROIs: 8, IROIs: 25,Typical IROIs: 13 , Atypical IROIs: 12

Fig. 9.4 Dataset bifurcation for PCA-BNN1 (NOR/CYST).

The bifurcation of instances of individual classes in training data feature set and testing data feature set in the case of PCA-BNN2 classier designed for classification between NOR/HEM classes is shown is shown in Fig. 9.5.

Dataset Bifurcation PCA-BNN2 (NOR/HEM)

Training Set Description (SROIs: 19, IROIs: 70)	Testing Set Description (SROIs: 17, IROIs: 70)
NOR-Images:10, SROIs: 10, IROIs: 30	**NOR-**Images:11, SROIs: 11, IROIs: 40
HEM-Images: 9, Lesions: 9, Typical: 6, Atypical: 3 SROIs: 9, IROIs: 40,Typical IROIs: 18 , Atypical IROIs: 22	**HEM-**Images: 6, Lesions: 6, Typical: 3, Atypical: 3 SROIs: 6, IROIs: 30,Typical IROIs: 6 , Atypical IROIs: 24

Fig. 9.5 Dataset bifurcation for PCA-BNN2 (NOR/HEM).

The bifurcation of instances of individual classes in training data feature set and testing data feature set in the case of PCA-BNN3 classier designed for classification between NOR/HCC classes is shown is shown in Fig. 9.6.

Dataset Bifurcation PCA-BNN3 (NOR/HCC)

Training Set Description (SROIs: 26, IROIs: 80)	Testing Set Description (SROIs: 23, IROIs: 80)
NOR-Images:10, SROIs: 10, IROIs: 30	**NOR-**Images:11, SROIs: 11, IROIs: 40
HCC-Images: 16, Lesions: 16, SHCC: 7, LHCC: 9 SROIs: 16, IROIs: 50, SHCC IROIs: 10, LHCC IROIs: 40	**HCC-**Images: 12, Lesions: 12, SHCC: 6, LHCC: 6 SROIs: 12, IROIs: 40, SHCC IROIs: 9 LHCC IROIs: 31

Fig. 9.6 Dataset bifurcation for PCA-BNN3 (NOR/HCC).

The bifurcation of instances of individual classes in training data feature set and testing data feature set in the case of PCA-BNN4 classier designed for classification between NOR/MET classes is shown is shown in Fig. 9.7.

Dataset Bifurcation PCA-BNN4 (NOR/MET)

Training Set Description (SROIs: 30, IROIs: 80)	Testing Set Description (SROIs: 26, IROIs: 95)
NOR-Images:10, SROIs: 10, IROIs: 30	**NOR-**Images:11, SROIs: 11, IROIs: 40
MET-Images: 18, Lesions: 20, Typical: 8, Atypical: 12 SROIs: 20, IROIs: 50,Typical IROIs: 8, Atypical IROIs: 42	**MET-**Images: 14, Lesions: 15, Typical: 5, Atypical: 10 SROIs: 15, IROIs: 45, Typical IROIs: 5, Atypical IROIs: 40

Fig. 9.7 Dataset bifurcation for PCA-BNN4 (NOR/MET).

The bifurcation of instances of individual classes in training data feature set and testing data feature set in the case of PCA-BNN5 classier designed for classification between CYST/HEM classes is shown is shown in Fig. 9.8.

Dataset Bifurcation PCA-BNN5 (CYST/HEM)

Training Set Description (SROIs: 11, IROIs: 70)	Testing Set Description (SROIs: 14, IROIs: 55)
CYST-Images: 4, Lesions: 4, Typical: 3, Atypical: 1 SROIs: 4, IROIs: 30 , Typical IROIs: 22 , Atypical IROIs: 8	**CYST-**Images: 8, Lesions: 8, Typical: 6, Atypical: 2 SROIs: 8, IROIs: 25,Typical IROIs: 13 , Atypical IROIs: 12
HEM-Images: 9, Lesions: 9, Typical: 6, Atypical: 3 SROIs: 9, IROIs: 40,Typical IROIs: 18 , Atypical IROIs: 22	**HEM-**Images: 6, Lesions: 6, Typical: 3, Atypical: 3 SROIs: 6, IROIs: 30,Typical IROIs: 6 , Atypical IROIs: 24

Fig. 9.8 Dataset bifurcation for PCA-BNN5 (CYST/HEM).

The bifurcation of instances of individual classes in training data feature set and testing data feature set in the case of PCA-BNN6 classier designed for classification between CYST/HCC classes is shown is shown in Fig. 9.9.

Dataset Bifurcation PCA-BNN6 (CYST/HCC)

Training Set Description (SROIs: 20, IROIs: 80)	Testing Set Description (SROIs: 18, IROIs: 65)
CYST-Images: 4, Lesions: 4, Typical: 3, Atypical: 1 SROIs: 4, IROIs: 30 , Typical IROIs: 22 , Atypical IROIs: 8	**CYST-**Images: 8, Lesions: 8, Typical: 6, Atypical: 2 SROIs: 8, IROIs: 25,Typical IROIs: 13 , Atypical IROIs: 12
HCC-Images: 16, Lesions: 16, SHCC: 7, LHCC: 9 SROIs: 16, IROIs: 50, SHCC IROIs: 10, LHCC IROIs: 40	**HCC-**Images: 12, Lesions: 12, SHCC: 6, LHCC: 6 SROIs: 12, IROIs: 40, SHCC IROIs: 9 LHCC IROIs: 31

Fig. 9.9 Dataset bifurcation for PCA-BNN6 (CYST/HCC).

The bifurcation of instances of individual classes in training data feature set and testing data feature set in the case of PCA-BNN7 classier designed for classification between CYST/MET classes is shown is shown in Fig. 9.10.

Dataset Bifurcation PCA-BNN7 (NOR/MET)

Training Set Description (SROIs: 24, IROIs: 80)	Testing Set Description (SROIs: 23, IROIs: 65)
CYST-Images: 4, Lesions: 4, Typical: 3, Atypical: 1 SROIs: 4, IROIs: 30 , Typical IROIs: 22 , Atypical IROIs: 8	**CYST**-Images: 8, Lesions: 8, Typical: 6, Atypical: 2 SROIs: 8, IROIs: 25,Typical IROIs: 13 , Atypical IROIs: 12
MET-Images: 18, Lesions: 20, Typical: 8, Atypical: 12 SROIs: 20, IROIs: 50,Typical IROIs: 8, Atypical IROIs: 42	**MET**-Images: 14, Lesions: 15, Typical: 5, Atypical: 10 SROIs: 15, IROIs: 45, Typical IROIs: 5, Atypical IROIs: 40

Fig. 9.10 Dataset bifurcation for PCA-BNN7 (CYST/MET).

The bifurcation of instances of individual classes in training data feature set and testing data feature set in the case of PCA-BNN8 classier designed for classification between CYST/MET classes is shown is shown in Fig. 9.11.

Dataset Bifurcation PCA-BNN8 (HEM/HCC)

Training Set Description (SROIs: 25, IROIs: 90)	Testing Set Description (SROIs: 18, IROIs: 70)
HEM-Images: 9, Lesions: 9, Typical: 6, Atypical: 3 SROIs: 9, IROIs: 40,Typical IROIs: 18 , Atypical IROIs: 22	**HEM**-Images: 6, Lesions: 6, Typical: 3, Atypical: 3 SROIs: 6, IROIs: 30,Typical IROIs: 6 , Atypical IROIs: 24
HCC-Images: 16, Lesions: 16, SHCC: 7, LHCC: 9 SROIs: 16, IROIs: 50, SHCC IROIs: 10, LHCC IROIs: 40	**HCC**-Images: 12, Lesions: 12, SHCC: 6, LHCC: 6 SROIs: 12, IROIs: 40, SHCC IROIs: 9 LHCC IROIs: 31

Fig. 9.11 Dataset bifurcation for PCA-BNN8 (HEM/HCC).

The bifurcation of instances of individual classes in training data feature set and testing data feature set in the case of PCA-BNN9 classier designed for classification between HEM/MET classes is shown is shown in Fig. 9.12.

Dataset Bifurcation PCA-BNN9 (HEM/MET)

Training Set Description (SROIs: 29, IROIs: 90)	Testing Set Description (SROIs: 21, IROIs: 85)
HEM-Images: 9, Lesions: 9, Typical: 6, Atypical: 3 SROIs: 9, IROIs: 40,Typical IROIs: 18 , Atypical IROIs: 22	**HEM**-Images: 6, Lesions: 6, Typical: 3, Atypical: 3 SROIs: 6, IROIs: 30,Typical IROIs: 6 , Atypical IROIs: 24
MET-Images: 18, Lesions: 20, Typical: 8, Atypical: 12 SROIs: 20, IROIs: 50,Typical IROIs: 8, Atypical IROIs: 42	**MET**-Images: 14, Lesions: 15, Typical: 5, Atypical: 10 SROIs: 15, IROIs: 45, Typical IROIs: 5, Atypical IROIs: 40

Fig. 9.12 Dataset bifurcation for PCA-BNN9 (HEM/MET).

The bifurcation of instances of individual classes in training data feature set and testing data feature set in the case of PCA-BNN10 classier designed for classification between HCC/MET classes is shown is shown in Fig. 9.13.

Dataset Bifurcation PCA-BNN10 (HCC/MET)

Training Set Description (SROIs: 36, IROIs: 100)	Testing Set Description (SROIs: 27, IROIs: 85)
HCC-Images: 16, Lesions: 16, SHCC: 7, LHCC: 9 SROIs: 16, IROIs: 50, SHCC IROIs: 10, LHCC IROIs: 40	**HCC-**Images: 12, Lesions: 12, SHCC: 6, LHCC: 6 SROIs: 12, IROIs: 40, SHCC IROIs: 9 LHCC IROIs: 31
MET-Images: 18, Lesions: 20, Typical: 8, Atypical: 12 SROIs: 20, IROIs: 50,Typical IROIs: 8, Atypical IROIs: 42	**MET-**Images: 14, Lesions: 15, Typical: 5, Atypical: 10 SROIs: 15, IROIs: 45, Typical IROIs: 5, Atypical IROIs: 40

Fig. 9.13 Dataset bifurcation for PCA-BNN10 (HCC/MET).

The optimal number of PCs and the resulting OCA for all ten PCA-BNN based secondary classifiers is reported in Table 9.4.

Table 9.4 *Classification performance of Ten PCA-BNN secondary classifiers*

NN: (*I*: *H*: *O*)	*Optimal No. of PCs*	*OCA (%)*
BNN1: (2:4:2) –[NOR/CYST]	2	100
BNN2: (2:4:2) – [NOR/HEM]	2	100
BNN3: (6:4:2) –[NOR/HCC]	6	98.7
BNN4: (5:4:2) – [NOR/MET]	5	96.4
BNN5: (2:4:2) – [CYST/HEM]	2	100
BNN6: (2:4:2) – [CYST/HCC]	2	98.4
BNN7: (2:4:2) – [CYST/MET]	2	95.7
BNN8: (2:4:2) – [HEM/HCC]	2	98.5
BNN9: (3:4:2) – [HEM/MET]	3	92.0
BNN10: (2:4:5) – [HCC/MET]	3	97.6

Note: NN: Neural network, BNN: Binary neural network, I: Input layer neurons, H: Hidden layer neurons, O: Output layer neurons; PCs: Principal components, OCA: Overall classification accuracy.

For designing each PCA-BNN secondary classifier, the optimal number of neurons in the hidden layer is obtained by trial-and-error procedure. After repeated experimentation with different numbers of hidden neurons, it was observed that with 4 neurons in hidden layer a reasonable tradeoff between accuracy and convergence is obtained. The output of the neuron corresponding to the labeled class is set to 1 and the output of other neurons is set to 0. The learning of the network is supervised and back-propagation algorithm with adaptive learning rate and momentum is used to obtain the desired input-output relationship [189].

The brief details of the experiments carried out in this study are reported in Table 9.5.

Table 9.5 *Brief details of experiments carried out in the present study.*

Experiment No 1:	To obtain classification performance of five-class PCA-NN based primary classifier, i.e., output of Step 1of the classification module.
Experiment No 2:	To obtain classification performance of Proposed NNE based CAD system, i.e., output of Step 2 of the classification module.

9.4 Results

9.4.1 Results – Experiment 1– Classification Performance Five-Class PCA-NN based Primary Classifier

The classification performance obtained by the five-class, PCA-NN based primary classifier (i.e., Step 1 of classification module), is reported in Table 9.6.

Table 9.6 *Classification performance obtained by five-class primary NN classifier (*Step* 1).*

NN Arch (I: H: O)	CM						OCA (%)	ICA_{CLASS}: (%)
		NOR	CYST	HEM	HCC	MET		
6:10:5	NOR	33	0	2	4	1	87.7(158/180)	ICA_{NOR}: 82.5(33/40)
	CYST	0	24	0	0	1		ICA_{CYST}: 96.0 (24/25)
	HEM	1	0	28	0	1		ICA_{HEM}: 93.3(28/35)
	HCC	1	2	0	36	1		ICA_{HCC}: 90.0 (36/40)
	MET	1	0	4	3	37		ICA_{MET}:82.2 (36/40)

Note: NN Arch: Neural network architecture, I: Input layer neurons, H: Hidden layer neurons, O: Output layer neurons, CM: Confusion matrix, NN Arch: Neural network architecture, OCA: Overall classification accuracy, $ICA_{CLASS-A}$: Individual classification accuracy for class A (Number of correctly classified instances of class A/ Total number of instances belonging to class A).

From Table 9.6, it can be visualized that out of total 180 testing instances, 22 instances are MIs and remaining 158 testing instances are correctly classified instances. Thus, Step 1 of the classification module yield the OCA of 87.7 % (158/180). It can be noted that, 158 out of 180 correctly classified instances, consist of 33 out of 40 correctly classified NOR instances, 24 out of 25 correctly classified cyst instances, 28 out of 30 correctly classified HEM instances, 36 out of 40 correctly classified HCC instances and 37 out of 45 correctly classified MET instances. Thus, the Step 1 of classification module yields ICA values of 82.5 % (33/40), 96 % (24/25), 93.3 % (28/30), 90 % (36/40) and 82.2 % (37/45) for NOR, Cyst, HEM, HCC and MET cases, respectively.

It can be observed that, 22 misclassified instances (MIs) out of total 180 instances in the testing data, consist of 7 NOR MIs out of 40 NOR instances, 1 Cyst MI out of 25 Cyst instances, 2 HEM MIs out of 30 HEM instances, 4 HCC MIs out of 45 HCC instances and 8 MET MIs out of 45 MET instances.

Further, it is observed that, out of total 22 MIs, 17 MIs have second highest probability for the correct class and the remaining 5 MIs have the third highest probability for the correct class.

These 17 out of 22 MIs, for which the second probability is for the correct class, consist of 7 out of 7 NOR MIs, 1 out 1 Cyst MI, 2 out of two HEM MIs, 3 out of 4 HCC MIs and 4 out of 8 MET MIs, respectively.

The remaining 5 out of 22 MIs, for which the third probability is for the correct class, consist of 1 out of 4 HCC MIs and 4 out of 8 MET MIs, respectively. These 5 MIs are *peculiar MIs*, as it is observed that for all these instances, there is a slim difference between the predicted probability values for all classes and even the highest probability value representing the predicted class is less than 0.4. This signifies that these *peculiar MIs* are confusing cases, as PCA-NN based primary classifier has assigned a low weightage for all the classes for these cases. Further, it is worth observing that these *peculiar MIs* are observed only for HCC and MET cases.

The prediction of five-class PCA-NN based primary classifier for first two most probable classes in 180 instances of testing data feature set is given in Table 9.7.

Table 9.7 *Prediction of first two most probable classes by five-class PCA-NN primary classifier for 180 testing instances (TIs) of the testing data feature set.*

Class pair	TIs	Class pair	TIs
NOR/CYST	7	CYST/HCC	22
NOR/HEM	12	CYST/MET	17
NOR/HCC	38	HEM/HCC	8
NOR/MET	20	HEM/MET	37
CYST/HEM	Nil	HCC/MET	19

Note: TIs: Testing Instances; TIs=7, for class pair NOR/CYST indicates that for (7/180) testing instances, the first highest and the second highest probability predictions of PCA-NN based primary classifier is among NOR or Cyst classes, therefore these 7 testing instances will be directed to PCA-BNN based secondary classifier for NOR/CYST cases.

From Table 9.7, it can be noticed that out of 180 instances in the testing data feature set, there is not even a single instance with Cyst and HEM among the first two most probable classes. This is in agreement with the fact that there is no overlap between sonographic appearances of Cyst and HEM image classes. Associated radiologists opined that while atypical Cyst can overlap significantly with Cystic metastasis cases, but there is no overlap even between atypical cases of Cyst and HEM image classes.

9.4.2 Results – Experiment 2– Classification Performance of Proposed NNE based CAD System

In experiment 2, the TFVs corresponding to testing instances (TIs) described in Table 9.7 are fed to corresponding PCA-BNN based secondary classifiers and the results obtained are reported in Table 9.8.

Table 9.8 *Description of misclassified instances (MIs) predicted by secondary PCA-BNN based classifiers for 180 testing instances (TIs) of the testing data feature set.*

BNN	No. of instances tested	Misclassified Instances (MIs)
NOR/CYST	7 (2 NOR, 5 CYST)	2NOR and 5Cyst correctly classified, MIs = 0
NOR/HEM	12(4NOR, 7HEM, 1MET*)	4NOR and 7HEM correctly classified, MIs = 1
		[One *peculiar case* of MET misclassified as NOR by Step 1 remains misclassified as NOR by Step 2]
NOR/HCC	38(21NOR, 16HCC, 1MET*)	21NOR and 16HCC correctly classified, MIs = 1
		[One *peculiar case* of MET misclassified as HCC by Step 1 is misclassified as NOR by Step 2]
NOR/MET	20(13NOR, 6MET, 1HCC*)	13NOR and 6MET correctly classified, MIs = 1
		[One *peculiar case* of HCC misclassified as NOR by Step 1 remains misclassified as NOR by Step 2]
CYST/HEM	Nil	Nil
CYST/HCC	22(14Cyst, 7HCC, 1MET*)	14CYST and7HCC correctly classified, MIs = 1
		[One *peculiar case* of MET misclassified as HCC by Step 1 remains misclassified as HCC by Step 2]
CYST/MET	17(6CYST, 11MET)	5CYST and 11 MET correctly classified, MIs = 1
		[One case of Cyst misclassified as MET by Step 1 remains misclassified as MET (atypical cyst resembling cystic metastasis]
HEM/HCC	8(1HEM, 6HCC, 1MET*)	1 HEM and 6 HCC predicted correctly, MIs = 1
		[One *peculiar case* of MET misclassified as HEM by Step 1 is misclassified as HCC by Step 2]
HEM/MET	37(22HEM, 15MET)	21HEM and 14MET correctly classified, MIs = 2
		[One case of MET misclassified as HEM by Step 1 remains misclassified as HEM by Step 2 (atypical cyst resembling cystic metastasis)]
		[1 HEM correctly classified as HEM by Step 1 is misclassified as MET by Step 2]**
HCC/MET	19(10HCC, 9MET)	9HCC and 9MET correctly classified, MIs = 1
		[One case of HCC misclassified as MET by Step 1 remains misclassified as MET by Step 2]

Note: BNN: Binary neural network, MIs: Misclassified instances.

From Table 9.8, it can be visualized that out of the total 180 testing instances, 9 instances are MIs and remaining 171 testing instances are correctly classified instances. Thus, Step 2 of the classification module yields the OCA of 95 % (171/180). It can be noted that, 171 out of 180 correctly classified instances, consist of 40 out of 40 correctly classified NOR cases, 24 out

of 25 correctly classified cyst cases, 29 out of 30 correctly classified HEM cases, 38 out of 40 correctly classified HCC cases and 40 out of 45 correctly classified MET cases. Thus, Step 2 of the classification module yields ICA values of 100 % (40/40), 96 % (24/25), 96.6 % (29/30), 95 % (38/40) and 88.8 % (40/45) for NOR, Cyst, HEM, HCC and MET cases, respectively.

It is interesting to note that the Step 1 of the classification module yielded 22 MIs out of 180 testing instances and by incorporating the Step 2 of the classification module the number of MIs have reduced to 9 out of 180 testing instances. Further, it is observed that 17 out of 22 MIs predicted by the Step 1 of classification module, for which the second highest probability was for the correct class, 14 out of these 17 MIs are correctly classified by the Step 2 of the classification module and remaining 3 out of 17 MIs remained misclassified. The 5 *peculiar MIs* out of 22 MIs, as predicted by the Step 1 of the classification module remained misclassified after Step 2 also. This is expected as for these cases the third highest probability prediction is for the correct class, so these cases were not directed to the correct BNNs in the Step 2 of classification module. It can be visualized 1HEM** correctly classified as HEM by Step 1 is misclassified as MET by Step 2. The classification performance obtained by the proposed NNE based CAD system is summarized in Table 9.9.

Table 9.9 *Classification performance of Proposed NNE based CAD system.*

Classification performance: NNE based CAD System						
CM					*OCA (%)*	*ICA$_{CLASS}$: (%)*
	NOR	CYST	HEM	HCC	MET	
NOR	40	0	0	0	0	ICA$_{NOR}$: 100 (40/40)
CYST	0	24	0	0	1	ICA$_{NOR}$: 96.0 (24/25)
HEM	0	0	29	0	1	95.0(171/180) ICA$_{HEM}$: 96.6 (29/30)
HCC	1	0	0	38	1	ICA$_{HCC}$: 97.5 (39/40)
MET	2	0	1	2	40	ICA$_{MET}$: 88.8 (40/45)

Note: CM: Confusion matrix, OCA: Overall classification accuracy, ICA: Individual classification accuracy; ICA$_{CLASS-A}$: Individual classification accuracy for class A (Number of correctly classified instances of class A/ Total number of instances belonging to class A).

It can be observed that by including the Step 2 in the classification module, the number of MIs has reduced from 22 MIs out of 180 testing instances to 9 MIs out of 180 testing instances, thus OCA has increased from 87.7 % to 95 %.

However, it is worth mentioning that as for (5/9) peculiar MIs, the PCA-NN based primary classifier (Step 1 of the classification module) has assigned a low weightage for all the classes (highest probability being 0.4). The developed CAD system is an interactive system which displays the weightage [W$_{nor}$ W$_{cyst}$ W$_{hem}$ W$_{hcc}$ W$_{met}$], i.e., probability outputs yielded by PCA-NN based primary classifier for each test instance. Therefore, for peculiar MIs having a low highest weightage and slim difference between all class weightages, it is expected that the

radiologist should consider an alternative approach for confirming the diagnosis, which may be taking a second opinion from another expert, patients history, other imaging modalities, biopsy, etc.

9.4.3   Analysis of Misclassified Instances (MIs)

The analysis of MIs predicted by the PCA-NN based primary classifier, i.e., after the Step 1 of the classification module and the analysis of MIs predicted by the proposed NNE based CAD system, i.e., after the Step 2 of the classification module, in terms of various sub-classes is reported is reported in Table 9.10.

Table 9.10 *Misclassification analysis of* **22 MIs out of** **180 test** *cases in classification Step* **1** *and* **9MIs out of** **180** *test cases in classification Step* **2.**

S.No.	PCA-NN based primary classifier (Step 1)	NNE based CAD System (Step 2)
1.	NOR cases: (40) Misclassified: 7 ICA_{NOR}: 82.5%	NOR cases: (40) Misclassified: Nil ICA_{NOR}: 100%
2.	Typical Cyst cases: (13) Misclassified: Nil $ICA_{TYPICAL\ CYST}$: 100%	Typical Cyst cases: (13) Misclassified: Nil $ICA_{TYPICAL\ CYST}$: 100%
3.	Atypical Cyst cases: (12) Misclassified:1 $ICA_{ATYPICAL\ CYST}$: 91.6%	Atypical Cyst cases: (12) Misclassified:1 $ICA_{ATYPICAL\ CYST}$: 91.6%
4.	Typical HEM cases: (6) Misclassified: Nil $ICA_{TYPICAL\ HEM}$: 100%	Typical HEM cases: (6) Misclassified: 1 $ICA_{TYPICAL\ HEM}$: 83.3%
5.	Atypical HEM cases: (24) Misclassified:2 $ICA_{ATYPICAL\ HEM}$: 91.6%	Atypical HEM cases: (24) Misclassified: Nil $ICA_{ATYPICAL\ HEM}$: 100%
6.	Small HCC cases: (9) Misclassified: Nil ICA_{SHCC}: 100%	Small HCC cases: (9) Misclassified: Nil ICA_{SHCC}: 100 %
7.	Large HCC cases: (31) Misclassified:4 ICA_{LHCC}: 87.0%	Large HCC cases: (31) Misclassified:2 ICA_{LHCC}: 93.5%
8.	Typical MET cases: (5) Misclassified:2 $ICA_{TYPICAL\ MET}$: 60.0%	Typical MET cases: (5) Misclassified:2 $ICA_{TYPICAL\ MET}$: 60.0%
9.	Atypical MET cases: (40) Misclassified:6 $ICA_{ATYPICAL\ MET}$: 85.0%	Atypical MET cases: (40) Misclassified:3 $ICA_{ATYPICAL\ MET}$: 92.5%
10.	Total Typical cases: (64) Misclassified: 9 $ICA_{TYPICAL\ CASES}$: 85.9%	Total Typical cases: (64) Misclassified: 3 $ICA_{TYPICAL\ CASES}$: 95.3%
11.	Total Atypical cases: (76) Misclassified:9 $ICA_{ATYPICAL\ CASES}$: 88.1%	Total Atypical cases: (76) Misclassified: 6 $ICA_{ATYPICAL\ CASES}$: 92.1%

Note: $ICA_{CLASS-A}$: Individual classification accuracy for class A (Number of correctly classified instances of class A/ Total number of instances belonging to class A).

From Table 9.10, it can be observed that by Step 2 of the classification module the ICA values for NOR, atypical HEM, Large HCC and atypical MET cases have increased from 82.5 %, 91.6 %, 87 % and 85 % to 100 %, 100 %, 93.5 % and 92.5 %, respectively. The ICA values for typical cyst, atypical cyst, small HCC and typical METs have remained the same, i.e., 100%, 91.6%, 100% and 60%, respectively. However, it can be visualized that ICA for typical HEM cases has decreased from 100 % to 83.3 %. It is expected that ICA for typical HEM cases should increase by adding more cases for classifier design. Overall, by incorporating the Step 2 of the proposed classification module the ICA values for typical and atypical cases has increased from 85.9 % and 88.1 % to 95.3 % and 92.1 %, respectively. Given the fact that conventional gray scale B-Mode US has limited sensitivity for detection and characterization of atypical cases of FLLs, the performance obtained by the proposed NNE based CAD system is encouraging.

From Table 9.6 and Table 9.9, it can be observed that the ICA values for HCC and MET cases have increased from 90 % and 82.2 % to 97.5 % and 88.8 %, respectively. These results indicate that the proposed NNE based CAD system can facilitate better management of focal liver malignancies by providing second opinion in case of highly overlapping sonographic appearances of HCC and MET lesions.

9.5 Concluding Remarks

From the experiments carried out in the present study, it is observed that significant improvement in classification performance is obtained by including the texture ratio features along with texture features computed from IROIs for characterization of FLLs from B-Mode US. Thus, it can be concluded that the texture analysis of the region surrounding the lesion significantly contribute towards the differential diagnosis of FLLs using B-Mode US images. Further, it is worth mentioning that by application of PCA to feature set consisting of 208 texture features (104 texture features and 104 texture ratio features); the information required for the classification of FLLs was squeezed in the first six PCs. It is concluded that by incorporating the Step 2 of classification module the OCA value increases from 87.7 % to 95 % and ICA values for typical and atypical cases increase from 85.9 % and 88.1 % to 95.3 % and 92.1 %, respectively. The promising results obtained by the proposed CAD with such a diversified, comprehensive and representative dataset used in the present study indicate that the proposed CAD system can be routinely used in clinical environment to assist radiologists in lesion interpretation and differential diagnosis of FLLs using conventional B-Mode gray scale US images.

Conclusions

10.1   Introduction

The main aim of the present study, "Analysis and Classification of B-Mode Liver Ultrasound Images" is to enhance the potential of commonly available conventional B-Mode US imaging modality for diagnosis of liver diseases. To achieve this, the design of an interactive system for diagnosis of liver diseases (block diagram shown earlier in Fig. 3.1 of Chapter 3 is revisited here in Fig. 10.1) has been proposed in this study.
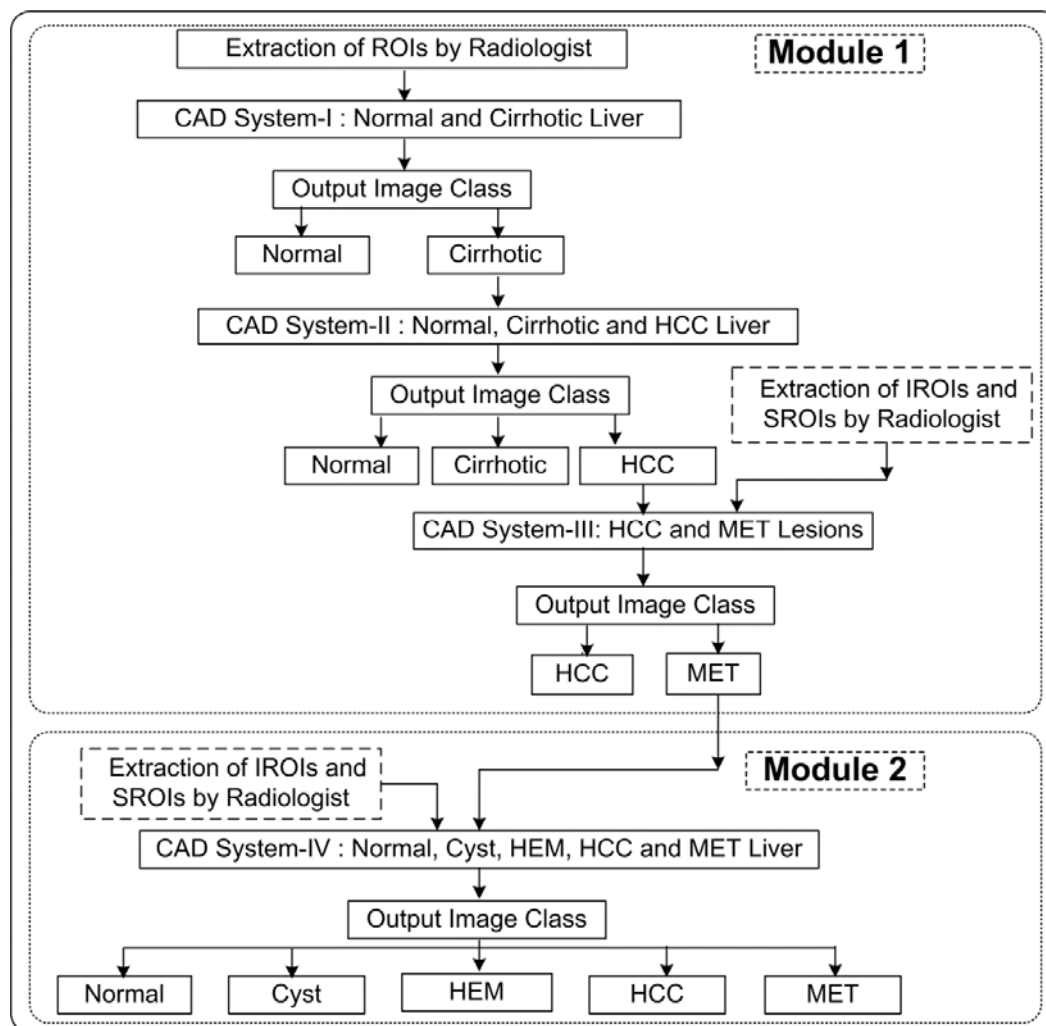

Fig. 10.1 Proposed interactive system for diagnosis of liver diseases.
Note: IROIs: Inside lesion regions of interest; SROIs: Surrounding lesion regions of interest.

Thus, efficient CAD system designs for characterization between: (*a*) normal and cirrhotic liver (i.e., CAD System-I) (*b*) normal, cirrhotic and HCC liver, i.e., (CAD-System-II) (*c*) HCC and MET lesions, i.e., CAD-System III and (*d*) focal liver lesions (Cyst, HEM, HCC and MET along with normal liver tissue), i.e., CAD System-IV are implemented in the present research work. The conclusions drawn from exhaustive experimentations carried out for design of CAD System-I, CAD System-II, CAD System-III and CAD System- IV are reported in this Chapter.

10.1.1 Conclusions – Design of an Efficient CAD System for Characterization of Normal and Cirrhotic Liver Tissue (CAD System-I of Module 1)

From the results of the studies undertaken in the present work, it can be concluded that:

(*i*)　The selective frequency and orientation properties of Gabor filters are extremely useful for providing multiscale texture description in case of discrimination between normal and cirrhotic liver with the highest classification accuracy of 98.3 % achieved by using only mean texture descriptors obtained from five frequency and orientation selective Gabor output feature images.

(*ii*)　The four direction GLCMs (plotted as an image) for normal and cirrhotic ROIs reveal that the distribution of GLCM elements are concentrated in case of normal liver and relatively more dispersed for a cirrhotic liver. This difference in dispersion of GLCM elements for normal and cirrhotic patches is captured by computing the GLCM-Mean and GLCM-Range texture features. It is observed that the GLCM-Mean texture features computed at $d = 2$ and GLCM-Range features computed at $d = 2$ and $d = 4$, yield 100 % classification accuracy for characterization between normal and cirrhotic liver.

(*iii*)　The four GLCM-Range features computed for $d = 2$, selected by sequential backward search with divergence as a measure of class seperability also yield 100 % classification accuracy for characterization between normal and cirrhotic liver.

(*iv*)　The difference in dispersion of GLCM elements for normal and cirrhotic patches captured using singular value decomposition of GLCM indicate that the first four singular value mean features also yield 100 % classification accuracy for characterization between normal and cirrhotic liver.

10.1.2 Conclusions – Design of an Efficient CAD System for Characterization of Normal, Cirrhotic and HCC Liver Tissue (CAD System-II of Module 1)

From the results of the study undertaken in the present work, for characterization of normal, cirrhotic and HCC liver tissue, it can be concluded that the optimal reduced texture

176

feature vector selected by GA–SVM approach (consisting of 10 features, i.e., 3 mean and 5 standard deviation and 2 energy features, estimated from sub-band feature images obtained by 2D-WPT using Haar wavelet filter) can significantly account for textural variations exhibited by normal, cirrhotic and HCC liver. The proposed CAD system yield individual class accuracy (ICA) value of 90 % for abnormal cases (i.e., for both cirrhotic and HCC cases) and ICA of 86.6 % for normal liver tissue, with overall classification accuracy of 88.8 %. From the analysis of misclassified cases, it is observed that certain HCC patches (ROIs belonging to large HCCs) are predicted as normal, the associated radiologists were of the view that these HCC ROIs should be avoided while taking the sample for biopsy.

As the sensitivity of conventional gray scale B-Mode US for detecting HCC lesions evolved on cirrhotic liver is limited (because cirrhotic liver exhibits diffused uneven nodularity so subjective differentiation between cirrhotic changes in the liver and development of HCC is difficult), the ICA value of 86.6 % for HCC cases obtained by the proposed CAD system is quite satisfactory. It can also be concluded that all the three multiresolution texture descriptors, i.e., mean, standard deviation and energy texture features are important to account for textural variations exhibited by normal, cirrhotic and HCC liver tissue. Finally, it can be concluded that the proposed CAD system can assist radiologist by providing second opinion for the diagnosis between cirrhotic changes in the liver parenchyma or development of HCC.

10.1.3 Conclusions – Design of an Efficient CAD System for Characterization of Primary and Secondary Malignant Liver Lesions (CAD System-III of Module 1)

It is worth mentioning that till date the CAD system designs proposed for characterization of focal liver lesions are based on texture features computed from IROIs only. The CAD system proposed in the present work investigates the contribution made by texture of the background liver for differential diagnosis between HCC and MET malignant liver lesions. The performance of texture features computed from IROIs and SROIs by statistical, spectral and spatial filtering based methods have been investigated for the classification task by using SVM classifier. The feature selection is carried out by first obtaining the pruned feature set by removing nonperforming features and then applying GA–SVM approach on pruned feature vector to obtain optimal reduced texture feature vector for the classification task. The CAD system based on optimal reduced features yield 91.6 % classification accuracy by using SVM classifier.

From the results of the study, it can be concluded that:

(*i*)   The ratio features are more discriminatory than features computed from IROIs.

177

(*ii*)   Nine features, i.e., four GLCM ratio features (ASM, sum average, difference entropy and IDM), three GLRLM ratio features (LRE, GLN and LRHGE), one FPS WLROI feature (radial sum) and one Laws' WLROI feature (LLmean) selected by GA–SVM procedure are significant to account for textural variations exhibited by HCC and MET lesions.

(*iii*)   The texture of the liver parenchyma surrounding the lesion contributes for differential diagnosis between HCC and MET liver malignancies.

(*iv*)   The proposed CAD system can be used as a second opinion tool for differential diagnosis between HCC and MET malignant neoplasms using B-Mode liver US images and thereby aid in proper management of liver malignancies.

10.1.4 Conclusions – Design of an Efficient CAD System for Characterization of Focal Liver Lesions (CAD System-IV of Module 2)

In the present research work, the proposed CAD systems for characterization of FLLs are based on multi-class classifier designs, four binary classifiers arranged in a hierarchical framework, and ensemble of neural network classifiers. In all the experiments, IROIs and SROIs are used for computing the texture features. The results obtained by these proposed CAD systems are summarized in Table 10.1

Table 10.1 *Performance***:** *CAD for characterization of FLLs using B-Mode US images.*

Experiment No.	CAD System Design	OCA (%)
1.	PCA-SVM based CAD system	87.2
2.	PCA-NN based CAD system	87.7
3.	PCA-PNN based CAD system	86.1
4.	PCA-*k*NN based CAD system	85.0
5.	PCA-SVM based Hierarchical CAD system	90.5
6.	PCA-NN based Hierarchical CAD system	88.3
7.	PCA-PNN based Hierarchical CAD system	91.6
8.	PCA-*k*NN based Hierarchical CAD system	90.5
9.	Hybrid Hierarchical CAD system	92.7
10.	Neural Network Ensemble based CAD system	95.0

Note: OCA: Overall classification accuracy, NN: Neural network, PNN: Probabilistic neural network, *k*NN: *k*-nearest neighbour classifier. SVM: Support vector machine.

By comparative evaluation of the proposed CAD systems, it can be concluded that the neural network ensemble based CAD system design is best for classification of FLLs using B-Mode US images.

The results obtained by the proposed NNE based CAD system in the presence of diversified and representative dataset demonstrates the usefulness of the proposed system to (*a*) facilitate better disease management by providing second opinion in case of highly overlapping

sonographic appearances of focal liver lesions, (*b*) assist radiology students as a training tool for interpretation of FLLs using B-mode US images, and (*c*) provide second opinion to radiologists to select patches inside malignant lesions for taking the sample for biopsy. (i.e., patches inside malignant lesions declared as normal should be avoided for taking the sample for biopsy).

The main conclusion of the present research work is that CAD system designs using texture features (computed from IROIs) and texture ratio features (computed from IROIs and corresponding SROI) collectively enhance the performance of the system for characterization of FLLs. **Thus, it can be concluded that the texture of the region surrounding the lesion contribute effectively for differential diagnosis between different FLLs.**

10.2   Limitations and Future Scope

Till date, no standard benchmark image database of liver ultrasound images has been created with an objective of pooling it for research purpose, Therefore it is not possible to compare similar studies on liver ultrasound due to lack of standard reference images.

The following are the recommendations for the future work:

(*i*)   There are certain focal liver lesions with very rare incidence for example, hepatoblastoma, cholangiocarcinoma and cystadenocarcinoma are rare malignant lesions and focal nodular hyperplasia, hepatic adenoma and abscess are rare benign lesions.   In future, image database for such rarely occurring focal liver lesions may be included; however, data collection may take a long span of time.

(*ii*)   In the CAD designs proposed in the present work, texture feature computation have been carried out on raw images (i.e., without any sort of preprocessing on the images). In future the effect of despeckling, the B-Mode US images by various methods on the performance of proposed CAD systems may be tested.

(*iii*) The exhaustive experiments carried out in the present research work indicate that texture feature computation from regions inside and outside of the lesions significantly enhances the performance of the CAD system for characterization of focal liver lesions. Thus, the concept of extracting SROI along with IROIs for computing texture ratio features, and using them for designing the classification system has been done in this study, can be extended to two dimensional images of focal hepatic lesions acquired from CT or MRI, as tumor aggression will show significant changes in surrounding liver parenchyma in CT

and MR images as well, the design and performance evaluation of such a CAD system can be taken up in future.

(*iv*) In the present work, ROIs are extracted manually. In future, texture based automatic segmentation algorithms can be developed to identify and extract ROIs automatically.

(*v*) Although the design of proposed CAD systems have been carried out by using a comprehensive image database with representative images from various liver image classes, but these images are acquired from a single US scanner (Philips ATL HDI 5000). Therefore, the generalization performance of the proposed system for images acquired from different US scanner remains to be tested.

(*vi*) The research in this important and clinically significant application domain "Analysis and Classification of B-Mode Liver Ultrasound Images" is lacking due to non availability of standard reference images as a result the research outputs are dependent on image databases collected by individual research groups. It is a dire necessity to collaborate with various medical institutes and research centers to create a bench mark dataset with labeled image classes acquired from different US scanners and pool it together for research purposes.

Publications from the Present Work

Referred Journal Publications

[1] Virmani, J., Kumar, V., Kalra, N. and Khandelwal, N., "SVM-Based characterization of liver ultrasound images using wavelet packet texture descriptors", *Journal of Digital Imaging,* Vol. 26, No.3, pp.530-543, 2013, DOI: 10.1007/s10278-012-9537-8

[2] Virmani, J., Kumar, V., Kalra, N. and Khandelwal, N., "Characterization of primary and secondary malignant liver lesions from B-mode ultrasound", *Journal of Digital Imaging,* 2013, Vol. 26, No.6, pp.1058-1070, 2013, DOI: 10.1007/s10278-013-9578-7.

[3] Virmani, J., Kumar, V., Kalra, N. and Khandelwal, N., "A comparative study of computer-aided classification systems for focal hepatic lesions from B-mode ultrasound", *Journal of Medical Engineering and Technology,* Vol. 37, No. 4, pp. 292-306, 2013, DOI:10.3109/030919 02.2013.794869.

[4] Virmani, J., Kumar, V., Kalra, N. and Khandelwal, N., "PCA-SVM based CAD System for Focal Liver Lesions from B-Mode Ultrasound", *Defence Science Journal*, Vol. 63, No.5, pp. 478-486, 2013.

[5] Virmani, J., Kumar, V., Kalra, N. and Khandelwal, N., "SVM-based characterization of liver cirrhosis by singular value decomposition of GLCM matrix", *International Journal of Artificial Intelligence and Soft Computing,* Vol. 3, No.3, pp. 276-296, 2013, DOI:10.1504/IJAI SC.2013.053407

[6] Virmani, J., Kumar, V., Kalra, N. and Khandelwal, N., "Prediction of liver cirrhosis based on multiresolution texture descriptors from B-mode ultrasound", *International Journal of Convergence Computing,* Vol. 1, No.1, pp. 19-37, 2013, DOI:0.1504/IJCONVC.2013. 054658.

[7] Virmani, J., Kumar, V., Kalra, N. and Khandelwal, N., 'Neural network ensemble based CAD system for focal liver lesions using B-mode ultrasound', *Journal of Digital Imaging,* [Accepted].

[8] Virmani, J., Kumar, V., Kalra, N. and Khandelwal, N., 'Hybrid hierarchical CAD system for focal hepatic lesions using B-mode ultrasound', *Biomedical Engineering: Applications Basis and Communications,* [under review].

Referred Conference Publications

[1] Virmani, J., Kumar, V., Kalra, N. and Khandelwal, N., "Prediction of cirrhosis from liver ultrasound B-mode images based on laws' masks analysis", In Proceedings of the IEEE International Conference on Image Information Processing, ICIIP-2011, Wakhnaghat, Shimla, India, pp. 1-5, 2011, DOI:10.1109/ICIIP.2011.6108894.

[2] Virmani J, Kumar V, Kalra N. and Khandelwal N., "A rapid approach for prediction of liver cirrhosis based on first order statistics", In Proceedings of the IEEE International Conference on Multimedia, Signal Processing and Communication Technologies, IMPACT-2011, pp. 212-215, 2011, DOI:10.1109/MSPCT.2011.6150477.

[3] Virmani, J., Kumar, V., Kalra, N. and Khandelwal, N., "Prediction of cirrhosis based on singular value decomposition of gray level co-occurence matrix and a neural network classifier", In Proceedings of the IEEE International Conference on Development in E-Systems Engineering, DeSe-2011, Dubai, pp. 146-151, 2011, DOI:10.1109/DeSE.2011.56.

References

[1]   Agarwal, R. K., Karmeshu, 'Perturbation scheme for online learning of features : Incremental principal component analysis', *Pattern Recognition*, Vol. 41, No. 5, pp. 1452 –1460, 2008.

[2]   Aggarwal, R., Karmeshu, 'Ultrasonic backscattering in tissue : characterization through nakagami-generalized inverse Gaussian distribution', *Computers in Biology and Medicine*, Vol. 37, No. 2, pp. 166 – 172, 2006.

[3]   Ahmad, A., Mostafa, A., Abolhassani , M.D., Alam, N.R., 'A method for texture classification of ultrasonic liver images based on Gabor wavelet', *In Proceedings : 27th Conference IEEE Engineering in Medicine and Biology*, Shanghai, China, pp. 1567 – 1570, 2005.

[4]   Albrecht, T., Hohmann, J., Oldenburg, A., Skrok, J., Wolf, K. J., 'Detection and characterization of liver metastasis', *European Radiology Supplements*, Vol. 14, No. 8, pp. 25 – 33, 2004.

[5]   Alto, H., Rangayyan, R.M., Paranjape, R.B., Desautels, J.E.L, Bryant, H., 'An indexed atlas of digital mammograms for computer-aided diagnosis of breast cancer', *Annals of Telecommunications*, Vol. 58, No. 5 – 6, pp. 820 – 835, 2003.

[6]   Amadasun, M., 'Texture features corresponding to textural properties', *IEEE Transactions on System, Man and Cybernetics*, Vol. 19, No.5, pp. 1264 – 1274, 1989.

[7]   Amendolia, S.R., Cossu, G., Ganadu, M.L., Masala, G.L., Mura, G.M., 'A comparative study of K-nearest neighbor, Support vector machine and multi layer perceptron for Thalassemia screening', *Chemometrics and Intelligent Laboratory Systems*, Vol. 69, No. 1 – 2, pp. 13 – 20, 2003.

[8]   André, T.C.S.S., Rangayyan, R.M., 'Classification of breast masses in mammograms using neural networks with shape, edge sharpness, and texture features', *Journal of Electronic Imaging*, Vol. 15, No. 1, pp. 1 – 10, 2006.

[9]   Arivazhagan, S., Ganesan, L., 'Texture classification using wavelet transform', *Pattern Recognition Letters*, Vol. 24, No. 9 – 10, pp. 1513 – 1521, 2003.

[10]   Arivazhagan, S., Ganesan, L., Priyal, S.P., 'Texture classification using gabor wavelets based rotation invariant features', *Pattern Recognition Letters*, Vol. 27, pp. 1976 – 1982, 2006.

[11] Assy, N., Nasser, G., Djibre, A., Beniashvili, Z., Elias, S., Zidan, J., 'Characteristics of common solid liver lesions and recommendations for diagnostic work up', *World Journal of Gastroenterology*, Vol. 15, No. 26, pp. 3217 – 3227, 2009.

[12] Avci, E., 'Comparison of wavelet families for texture classification by using wavelet packet entropy adaptive network based fuzzy inference system', *Applied Soft Computing*, Vol. 8, No. 1, pp. 225 – 231, 2008.

[13] Backes, A.R., Gonclaves, W.N., Martinez, A.S., Bruno, O.M., 'Texture analysis and classification using deterministic tourist walk', *Pattern Recognition*, Vol. 43, No.3, pp. 685 – 694, 2010.

[14] Badawi, A.M., Derbala, A.S., Youssef, A.B.M.,'Fuzzy logic algorithm for quantitative tissue characterization of diffuse liver diseases from ultrasound images', *International Journal of Medical Informatics*, Vol. 55, No. 2, pp.135 – 147, 1999.

[15] Badawi, A.M., Emara, S.M., Youssef, A.B.M., 'Ultrasound tissue characterization of diffuse liver diseases using fuzzy rules', *In Proceedings : International Congress of Ultrasonography*, Germany, pp. 288 – 298, 1996.

[16] Baert, A.L., Sartor, K., '*Focal liver lesions-dectection, characterization, ablation*', Springer Berlin Heidelberg, New York, pp. 167 – 77, 2005.

[17] Balasubramanian, D., Srinivasan, P., Gurupatham, R., 'Automatic classification of focal lesions in ultrasound liver images using principal component analysis and neural networks', *In Proceedings : 29th Annual IEEE EMBS International Conference*, Lyon, France, pp. 23 – 26, 2007.

[18] Bartolozzi, C., Lencioni, R., '*Liver Malignancies : Diagnostic and Interventional Radiology*', 1st Ed., Springer, 1999.

[19] Bass, T., Gravenhorst, F., Fischer, R., Khawaja, A., Dossel, O., 'Comparison of three t-wave delineation algorithms based on wavelet filter bank, correlation and PCA', *Computing in Cardiology*, Vol. 37, pp. 361 – 364, 2010.

[20] Bates, J., '*Abdominal Ultrasound How Why and When*' 2nd Ed., Churchill Livingstone, Oxford, pp. 80 – 107, 2004.

[21] Beussink, L.S., 'Atypical hepatic hemangioma', *Journal of Diagnostic Medical Sonography*, Vol. 25, No. 1, pp. 67 – 70, 2009.

[22] Bhandari, A., Khare, V., Trikha, M., Anand, S., 'Wavelet based novel technique for signal conditioning of elctro-oculogram signals', *In Proceedings* : *Annual IEEE India Conference*, pp. 1 – 6, 2006.

[23] Bianconi, F., Fernandez, A., 'Evaluation of the effects of Gabor filter parameters on texture classification', *Pattern Recognition*, Vol. 40, No. 12, pp. 3325 – 3335, 2007.

[24] Brazdeikis, A., Guzeldere, A.K., Padhye, N.S., Verklan, M.T., 'Evaluation of the performance of a QRS detector for extracting the heart interbeat RR time series from fetal magnetography recordings' *In Proceedings* : *Annual International Conference of the IEEE Engineering in Medicine and Biology*, pp. 369 – 372, 2004.

[25] Burges, C.J.C., 'A tutorial on support vector machines for pattern recognition', *Journal of Data Mining and Knowledge Discovery*, Vol. 2, No. 2, pp.1 – 43, 1998.

[26] Cao, G.T., Shi, P.F., Hu, B., 'Liver fibrosis identification based on ultrasound images captured under varied imaging protocols', *Journal of Zhejiang University Science*, Vol. 6B, No. 2, pp. 1107 – 1114, 2005.

[27] Cao, J., Shi, P., Hu, B., 'Texture classification based on the fractal performance of the moment feature images', LNCS, Springer, Vol. 3656, pp.762 – 769.

[28] Castellano, G., Bonilha, L., Li, L.M., Cendes, F., 'Texture analysis of medical images', *Clinical Radiology*, Vol. 59, No. 12, pp. 1061 – 1069, 2004.

[29] Cavouras, D., Prassopoulos, P., Karangellis, G., Raissaki, M., Kostaridou, L., Panayiotakis, G., 'Application of a neural network and four statistical classifiers in characterizing small focal liver lesions on CT', *In Proceedings* : *18th Annual International Conference of the IEEE Engineering in Medicine and Biology Society*, Amsterdam, pp. 1145 – 1146, 1996.

[30] Chaira, T., Anand S., 'A novel intuitionistic fuzzy approach for tumor/hemorrhage detection in medical images', *Journal of Scientific Industrial Research*, Vol. 70, No. 6, pp. 427 – 434, 2011.

[31] Chang, C.C., Lin, C.J.,'LIBSVM : a library of support vector machines', *ACM Transactions on Intelligent Systems and Technology*, Vol. 2, No. 3, pp.1–27, Software available at http ://www.csie.ntu.edu.tw/~cjlin/libsvm (Date last accessed :15 May 2013).

[32] Chang, T., Kuo, C.C.J.,'Texture analysis and classification with tree structured wavelet transform', *IEEE Transactions in Image Processing*, Vol. 2, No. 4, pp. 429 –441, 1993.

[33] Chen, E.L., Chung P.C., Chen C.L., Tsai, H.M., Chang C.I., 'An automatic diagnostic system for CT liver image classification', *IEEE Transactions on Biomedical Engineering*, Vol. 45, No. 6, pp. 783 – 794, 1998.

[34] Choi, B.L., Takayasu, K., Han, M.C., 'Small Hepatocellular carcinomas and associated nodular lesions of the liver : Pathology, Pathogenesis and imaging findings', *American Journal of Rongetenology*, Vol.160, No. 6, pp.1177 – 1187, 1993.

[35] Chong, C.C., Jia, J. C., Mital, D.P, 'Classification of multi-spectral images using BP neural networks classifiers- input coding assignment', *In Proceedings* : *IEEE Region 10's Ninth Annual International Conference on Frontiers of Computer Technology*, TENCON'94, Singapore, Vol. 2, pp. 867 – 871, 1994.

[36] Chu, A., Sehgal, C.M., Greenleaf, J.F., 'Use of gray value distribution of run lengths for texture analysis', *Pattern Recognition Letters*, Vol. 11, No. 6, pp. 415 – 420, 1990.

[37] Clausi, D.A., Jernigan, M.E., 'Designing Gabor filters for optimal texture seperability', *Pattern Recognition*, Vol. 33, No.11, pp. 1835 – 1849, 2000.

[38] Clayien, P.A., '*Malignant Liver Tumors* : *Current and Emerging Therapies*', Wiley-Blackwell, 3rd Ed., ISBN : 978-1-4051-7976-8, 2010.

[39] Daponte, J.S., Sherman, P., 'Classification of ultrasonic image texture by statistical discriminant analysis and neural networks', *Computerized Medical Imaging and Graphics*, Vol. 15, No.1, pp. 3 – 9, 1991.

[40] Dasarathy, B.V., Holder, E.B., 'Image characterizations based on joint gray level-run length distributions', *Pattern Recognition Letters*, Vol. 12, No. 8, pp. 497 – 502, 1991.

[41] Dash, M., Liu, h., 'Feature selection for classification', *Intelligent Data Analysis*, Vol. 1, No. 1– 4, pp. 131 – 156, 1997.

[42] Datta, A, Dutta, S., Surjya, K.P., Ranjan, S., Mukhopadhyay, S., 'Texture analysis of turned surface images using grey level co-occurrence technique', *Advanced Materials Research*, Vol. 365, pp 38 – 43, 2012.

[43] Daugman, J.G., 'An information-theoretic view of analog representation in striate cortex', in Schwartz, E. (Ed.) : *Computational Neuroscience*, pp. 403 – 423, MIT Press, Cambridge, MA, 1990.

[44] Deka, B., Bora, P.K., 'Despeckling of medical ultrasound images using sparse representation', *In Proceedings* : *International Conference on Signal Processing and Communications*, SPCOM'2010, pp.1 – 5, 2010.

[45] Dhawan, A.P., Chitre, U., Kaiser-Bonaso, C., 'Analysis of mammographic microcalcifications using gray-level image structure features', *IEEE Transactions in Medical Imaging*, Vol. 15, No. 3, pp. 246 – 259,1996.

[46] Diao, X.F., Zhang, X.Y., Wang, T.F., Chen, S.P., Yang, Y. Zhong, L., 'Highly sensitive computer aided diagnosis system for breast tumor based on color doppler flow images', *Journal of Medical Systems*, Vol. 35, No. 5, pp. 801 – 809, 2011.

[47] Du, C., Linker, R., Shaviv, A., 'Identification of agricultural mediterranean soils using mid-infrared photoacoustic spectroscopy', *Geoderma*, Vol. 143, No. 1, pp. 85 – 90, 2008.

[48] Emara, S.M., Badawi, A.M., Youssef, A.B.M., 'Fuzzy similarity measures for ultrasound tissue characterization', *In Proceedings* : *SPIE*, Vol. 2424, pp. 556-566, 1995.

[49] Frank, M.W., David, U. J.K., Stefan, B., Gunnar, S., Cristian, L., Dossel, O., 'Predicting tissue conductivity influences on body surface potentials - an efficient approach based on principal component analysis', *IEEE Transactions on Biomedical Engineering*, Vol. 58, No. 2, pp. 265 – 273, 2011.

[50] Fukunaga, K., '*Introduction to Statistical Pattern Recognition*', Academic Press, New York, USA, 1990.

[51] Galloway, R.M.M.,'Texture analysis using gray level run lengths', *Computerized Graphics and Image Processing*, Vol. 4, No. 2, pp. 172 –179, 1975.

[52] Gandhi, T.K., Panigrahi, B.K., Anand, S., 'A comparative study of wavelet families for EEG signal classification', *Neurocomputing*, Vol. 74, No. 17, pp. 3051 – 3057, 2011.

[53] Gangeh, M.J., Duin, R.P.W., Eswaran, C., Romeny, B.M.H., 'Scale space texture classification using combined classifiers with application to ultrasound tissue characterization', *In Proceedings* : *IFMBE, BIOMED'06*, pp. 287 – 290, 2006.

[54] Gletsos, M., Maogiakakou, S.G., Matsopoulos, G.K., Nikita K.S., Nikita A.S., Kelekis, D., 'A computer-aided diagnostic system to characterize CT focal liver lesions : design and optimization of a neural network classifier,' *IEEE Transactions on Information Technology in Biomedicine*, Vol. 7, No. 3, pp. 153 – 162, 2003.

[55] Golemati, S., Tegos, T.J., Sassano, A., Nikita, K.S., Nicolaides, A.N., 'Echogenicity of B-Mode sonographic images of the carotid artery : work in progress', *Journal of Ultrasound in Medicine*, Vol. 23, No. 5, pp. 659 – 669, 2004.

[56]   Gomaa, A.I., Khan, S.A., Toledano, M.B., Waked, I., Taylor, R. S. D., 'Hepatocellular carcinoma : epidemiology, risk factors, and pathogenesis', *World Journal of Gastroenterology*, Vol. 14, No. 27, pp. 4300 – 4308, 2008.

[57]   Gorunescu, M., Gorunescu, F., Ene, M. Darzi, E.E, 'A heuristic approach in hepatic cancer diagnosis using a probabilistic neural network based model', *In Proceedings* : *International Conference on Applied Stochastic Models and Data Analysis*, *ASMDA'2005*, Brest, France, pp. 1016 – 1025, 2005.

[58]   Gupta, A., Karmeshu, 'Statistical characterization of speckle in clinical echocardiographic images with pearson family of distributions', *Defence Science Journal*, Vol. 61, No. 5, pp. 473 – 478, 2011.

[59]   Guyon, I., Weston, J., Barnhill, S., Vapnik, V.,'Gene selection for cancer classification using support vector machines', *Journal of Machine Learning*, Vol. 46, No. 1 – 3, pp. 389 – 422, 2002.

[60]   Hansen, L. K., Salamon, P., 'Neural network ensembles- many could be better than all', *IEEE Transactions on Pattern Analysis and Machine Intelligence*, Vol. 12, No. 10, pp. 993 – 1001, 1990.

[61]   Haralick, R.M., Shanmugam, K. Dinstein, I., 'Textural features for image classification', *IEEE Transactions on Systems, Man and Cybernetics*, Vol. SMC-3, No. 6, pp. 610 – 621, 1973.

[62]   Harding, J., Callaway, M., 'Ultrasound of focal liver lesions', *RAD Magazine*, Vol. 36, No. 424, pp. 33 – 34, 2010.

[63]   Harikumar, R., Vijaykumar, T., Sreejith, J.,'Performance analysis of SVD and support vector machines for optimization of fuzzy outputs in classification of epilepsy risk level from EEG signals', *In Proceedings* : *IEEE Conference on Recent Advances in Intelligent Computational Systems*, *RAICS – 2011*, Kerala, India, pp. 718 – 723, 2011.

[64]   Hayat, M.A., '*Methods of Cancer Diagnosis, Therapy and Prognosis* : *Liver Cancer*', Springer, Vol. 5, ISBN : 978-1-4020-9803-1, 2009.

[65]   Hiremath, P. S., Akkasaligar, P.T., Badiger, S., 'Speckle reducing contourlet transform for medical ultrasound images', *International Journal of Computer and Information Engineering*, Vol. 4, No. 4, pp. 284 – 291, 2010.

[66]   Holland, J.H., '*Adaptation in Natural and Artificial Systems : An Introductory Analysis with Application to Biology, Control and Artificial Intelligence*', University of Michigan Press, 1st Ed., MIT Press, 1992.

[67] Huang, Y., Zhao, X., Zhang, Q., Wang, F., Zhao, Z., 'Texture analysis of ultrasonic image based on wavelet packet denoising and feature extraction', *In Proceedings : 3rd International Conference on Bioinformatics and Biomedical Engineering*, *ICBBE-2009*, pp.1 – 6, 2009.

[68] Huang, Y.L., Chen, D.R., Jiang, Y.R., Kuo, J., Wu, H.K., Moon, W.K., 'Computer-aided diagnosis using morphological features for classifying breast lesions on ultrasound', *Ultrasound in Obstetrics and Gynecology*, Vol. 32, No. 4, pp. 565 – 572, 2008.

[69] Huang, Y.L., Chen, J.H., Shen, W.C., 'Diagnosis of hepatic tumors with texture analysis in non-enhanced computed tomography images', *Academic Radiology*, Vol. 13, No. 6, pp. 713–720, 2006.

[70] Huang, Y.L., Wang K.L., Chen, D.R., 'Diagnosis of breast tumors with ultrasonic texture analysis using support vector machines', *Neural Computing and Applications*, Vol. 15, No. 2, pp. 164 – 169, 2006.

[71] Hui, L., Mei G. D., Xiang, L., "Cirrhosis classification based on MRI with duplicative-feature support vector machine (DFSVM)", *Biomedical Signal Processing and Control*, Vol. 8, No. 4, pp. 346 – 353, 2013.

[72] Jain, V., Sahambi, J.S., 'Neural network and wavelets in arrhythmia classification', *Lecture Notes in Computer Science*, Vol. 3285, pp. 92 – 99, 2004.

[73] Jeffery, R.B., Ralls, P.W. '*Sonography of Abdomen*', Raven, New York, 1995

[74] Jeon, J.H., Choi, J.Y., Lee, S., Yong, M.R., 'Multiple ROI selection based focal liver lesion classification in ultrasound images', *Expert Systems with Applications*, Vol. 40, No. 2, pp. 450 – 457, 2013.

[75] Jeong, J.W., Lee, S., Lee, J.W., Yoo, D.S., Kim, S.,'The echotextural characteristics for the diagnosis of liver cirrhosis using the sonographic images', *In Proceedings : 29th Annual International Conference of IEEE Engineering in Medicine and Biology Society*, France, pp. 1343 –1345, 2007.

[76] Kadah, Y.M., Farag, A.A., Zurada, J.M., Badawi, A.M., Youssef, A.M., 'Classification algorithms for quantitative tissue characterization of diffuse liver disease from ultrasound images', *IEEE Transactions in Medical Imaging*, Vol. 15, No. 4, pp. 466 – 478, 1996.

[77] Kadir, A., Nugroho, L.E., Susanto, A., Santosa, P.I., 'Performance improvement of leaf identification system using principal component analysis', *International Journal of Advanced Science and Technology*, Vol. 44, pp. 113 – 124, 2012.

[78] Karmeshu, Aggarwal, R., 'Study of ultrasonic echo envelope based on Nakagami-inverse Gaussian distribution', *Ultrasound in Medicine and Biology*, Vol. 32, No.3, pp. 371 – 376, 2006.

[79] Khadtare, M.S., Sahambi, J.S., 'ECG Arrhythmia analysis by multicategory support vector machine', *Lecture Notes in Computer Science*, Vol. 3285, pp. 100 – 107, 2004.

[80] Khare, V., Bhandari, A., Trikha, M., Anand, S., 'Wavelet based novel techniques for signal conditioning of electro-oculogram signals', *In Proceedings*: *IEEE INDICON'06*, pp. 1 – 6, 2006.

[81] Khare, V., Santhosh, J., Anand, S., 'Classification of EEG signals based on neural network to discriminate five mental states', *In Proceedings* : *International Conference on SPIT-IEEE Colloquium'08*, pp. 24 – 26, 2008.

[82] Kim, S.H., Lee, J.M., Kim, K.G., Kim, J.H., Lee, J.Y., Han, J.K., Choi, B.I., 'Computer-aided image analysis of focal hepatic lesions in ultrasonography : preliminary results', *Abdominal Imaging*, Vol. 34, No. 2, pp. 183 – 91, 2009.

[83] Kimura, Y., Fukada, R., Katagiri, S., Matsuda, Y., 'Evaluation of hyperechoic liver tumors in MHTS, *Journal of Medical Systems*, Vol. 17, No. pp. 3 – 4, 1993.

[84] Krcmar, M., Dhawan, A.P., 'Application of genetic algorithm in graph matching, neural networks', *In Proceedings* : *IEEE World Congress on computational Intelligence*, Vol. 6, pp. 3872 – 3876, 1994.

[85] Kudo, M., Sklansky, J., 'Comparision of algorithms that select features for pattern classifiers', *Pattern Recognition*, Vol. 33, No. 1, pp. 25 – 41, 2000.

[86] Kumar, A., Kumar, B., Kumar, Y., 'A novel method to determine the impedance of membrane material', *Ultrasonics*, Vol. 35, No. 1, pp. 53 – 56, 1997.

[87] Kumar, B., Kumar, A., 'Evaluation of ultrasonic attenuation without invoking the diffraction correction separately', *Ultrasonics*, Vol. 34, No.8, pp. 847 – 853, 1996.

[88] Kyriacou, E., Pavlopoulos, S., Koutsoris, D., Zoumpoulis, P., Theotokas, I., 'Computer assisted characterization of liver tissue using image texture analysis techniques on B-scan images', *In Proceedings* : *19th IEEE EMBS International Conference*, Chicago, IL, pp. 806 – 809, 1997.

[89] Laws, K.I., 'Rapid texture identification', *In Proceedings* : *SPIE Image Processing for Missile Guidance*, Vol. 376, pp. 376 – 380, 1980.

[90]   Lee, C.C., Chen, S.H., 'Gabor wavelets and SVM classifier for liver diseases classification from CT images', *In Proceedings : IEEE International Conference on Systems, Man and Cybernetics*, Taipei, Taiwan, pp. 548 – 552, 2006.

[91]   Lee, C.C., Chen, S.H., Chiang, Y.C., 'Automatic liver disease diagnosis for CT images using kernel based classifiers', *In Proceedings : World Automation Congress*, WAC'06, Budapest, Hungary, pp. 1 – 5, 2006.

[92]   Lee, C.C., Chen, S.H., Tsai, H.M., Chung P.C., Chiang, S.H., 'Discrimination of liver disease from CT images based on Gabor filters', *In Proceedings : 19th IEEE International Symposium on Computer Based Medical Systems*, *CBMS'06*, Salt lake city, Utah, pp. 203 – 206, 2006.

[93]   Lee, J.S., Sun Y.N., Lin, X.Z., 'A new approach to ultrasonic liver image classification', *ICICE Transactions on Information and Systems*, Vol. E83–D, No. 6, pp. 1301 – 1308, 2000.

[94]   Lee, W. L., Chen, Y.C., Hsieh, K. S., 'Robust calculation of fractal dimension of images and its applications to classification of ultrasonic liver images and texture images,' *In Proceedings : 2002 IEEE International Symposium on Circuits and Systems*, Vol. 2, pp. 656 – 659, 2002.

[95]   Lee, W.L., Hsieh, K.S., 'Computer assisted characterization for ultrasonic liver tissue by fusion of classifiers', *In Proceedings : 2nd International Conference on Innovative Computing Information and Control*, *ICICIC'2007*, Kumamoto, pp.100 – 100, 2007.

[96]   Lee, W.L., Chen, Y.C., Hsieh, K.S., 'Ultrasonic liver tissue classification by fractal feature vector based on M-band Wavelet Transform', *In Proceedings : 2001 IEEE International Symposium on Circuits and Systems*, Vol. 2, pp. 1 – 4, 2001.

[97]   Lee, W.L., Hsieh, K.S., Chen, Y.C., 'A study of ultrasonic liver images classification with artificial neural networks based on fractal geometry and multiresolution analysis', *Biomedical Engineering - Application Basis and Communication*, Vol. 16, No. 2, pp. 59 – 67, 2004.

[98]   Lenis, G., Bass, T., Dossel, O., 'Automatic detection and classification of ectopic beats in the ECG using a support vector machine', *In Proceedings : 45th Jahrestagung der DGBMT im VDE. BMT' 2011,* 2011.

[99]   Li, S., Kwok, J.T., Zhu, H., Wang, Y, 'Texture classification using the support vector machines', *Pattern Recognition*, Vol. 36, No.12, pp. 2883 – 2893, 2003.

[100] Liu, H., Guo, D.M., Liu, X., "Cirrhosis classification based on MRI with duplicative feature support vector machine (DFSVM)", *Biomedical Signal Processing and Control*, Vol.8, No. 8, pp. 346 – 353, 2013.

[101] Lu, H.H.S., Chen, C.M., Huang, Y.M., Wu, J.S., 'Computer aided diagnosis of liver cirrhosis by simultaneous comparisons of the ultrasound images of liver and spleen', *Journal of Data Science*, Vol. 6, No. 3, pp. 429 – 448, 2008.

[102] Lutz, H., Petzoldt, R., 'Possibilities and limitations of ultrasonic diagnosis of space occupying lesions in internal medicine', *Ultrasonics*, Vol. 14, No. 4, pp. 156 – 160, 1976.

[103] Manjunath, B.S., MA, W.Y., 'Texture features for browsing and retrieval of image data', *IEEE Transactions on Pattern Analysis and Machine Intelligence*, Vol. 18, No. 8, pp. 837 – 842, 1996.

[104] Marsh, J.I., Gibney, R.G. and David, K.B., 'Hepatic hemangioma in the presence of fatty infiltration : an atypical sonographic appearance', *Gastrointestinal Radiology*, Vol. 14, No. 3, pp. 262 – 264, 1989.

[105] Martino, M.D., Filippis, G.D., Santis, A.D., Geiger, D., Monte, M.D., Lombardo, C.V., Rossi, M., Corradini, S.G., Mennini, G., Catalano, C., 'Hepatocellular carcinoma in cirrhotic patients : Prospective comparison of US, CT and MR imaging', *European Radiology*, Vol. 23, No. 4, pp. 887 – 896, 2013.

[106] Materka, A., Strzelecki, M., 'Texture Analysis Methods- A Review', COST B11 report, *Technical University of Lodz, Institute of Electronics*, Brussels, 1998.

[107] Mathieu, D., Luciani, A., 'Imaging update in metastatic liver disease', *Controversies and Consensus in Imaging and Intervention*, pp. 21 – 26, 2003.

[108] Minhas, F., Sabih, D., Hussain, M., 'Automated classification of liver disorders using ultrasound images', *Journal of Medical Systems*, Vol. 36, No. 5, pp. 3163 – 3172, 2012.

[109] Mitrea, D., Nedevschi, S., Fratila, B., Lupsor, M., "Texture-based methods in biomedical image recognition of diffuse liver diseases", *In Proceedings : International Conference on System Theory and Software Engineering*, pp. 629-634, 2005.

[110] Mitrea, D., Nedevschi, S., Lupsor, M., Badea, R., 'Exploring texture based parameters for non-invasive detection of diffuse liver diseases and liver cancer from ultrasound images', *In Proceedings : 8th WSEAS International Conference on Mathematical Methods and Computational Techniques in Electrical Engineering, MMACTEE'06*, Wisconsin, USA, pp. 259 – 265, 2006.

[111] Mitrea, D., Nedevschi, S., Lupsor, M., Badea, R., 'Textural models based on ultrasound images for the detection of hepatocellular carcinoma in early and advanced stages', *International Journal of Computers*, Vol. 2, No. 1, pp. 66 –73, 2008.

[112] Mitrea, D., Nedevschi, S., Lupsor, M., Socaciu, M., Badea, R., 'Experimenting various classification techniques for improving the automatic diagnosis of the malignant liver tumors based on ultrasound images', *In Proceedings* : *International Congress on Image and Signal Processing*, CISP – 2010,Yantai, China, pp 1853-1858, 2010.

[113] Mitrea, D., Nedevschi, S., Lupsor, M., Socaciu, M., Badea, R., 'Improving the textural model of the hepatocellular carcinoma using dimensionality reduction methods', *In Proceedings* : *International Congress on Image and Signal Processing*, CISP-2009, Tianjin, China, pp. 1 – 5, 2009.

[114] Mittal, D., Kumar, V., Saxena, S.C., Khandelwal, N. and Kalra, N., 'Neural network based focal liver lesion diagnosis using ultrasound images', *Computerized Medical Imaging and Graphics*, Vol. 35, No. 4, pp. 315 – 323, 2011.

[115] Mittal, N, Mital, D.P., Chan, K.L, 'Features for texture segmentation using Gabor Filters', *In Proceedings* : *7th IEEE International Conference on Image Processing and its Applications*, Singapore, pp. 353 – 357, 1999.

[116] Mittelstaedt, C.A., 'Ultrasound as a useful imaging modality for tumor detection and staging', *American Association for Cancer Research*, Vol. 40, pp. 3072 – 3078, 1980.

[117] Moayedi, F., Azimifar, Z., Boostani, R., Katebi, S., 'Contourlet based mammography mass classification', *In Proceedings* : *ICIAR*, LNCS 4633, pp. 923 – 934, 2007.

[118] Mojsilovic, A., Popovic, M., Sevic, D., 'Classification of the ultrasound liver images with the 2N×l-D wavelet transform', *In Proceedings* : *IEEE International Conference on Image Processing*, Lausanne, Switzerland, pp. 367 – 370, 1996.

[119] Mojsilovic, A., Popovic, M., Markovic, S., Krstic, M., 'Characterization of visually similar diffuse liver diseases from B-scan liver images using non-separable wavelet transform', *IEEE Transactions on Medical Imaging*, Vol. 17, No. 4, pp. 541 – 549, 1998.

[120] Mojsilovic, A., Popovic, M.V., Rackov, D.M., 'On the selection of an optimal wavelet basis for texture characterization', *IEEE Transactions in Image Processing*, Vol. 9, No. 12, pp. 2043 – 2050, 2000.

[121] Mougiakakou, S.G., Valavanis, I.K., Nikita, A., Nikita, K.S., 'Differential diagnosis of CT focal liver lesions using texture features, feature selection and ensemble driven classifiers', *Artificial Intelligence in Medicine*, Vol. 41, No. 1, pp. 25 – 37, 2007.

[122] Moustakidis, S.P., Valavanis I.K, Nikita, K.S., Nikita, A., Kelekis, D., 'Characterization of CT liver lesions based on texture features and a multiple neural network classification scheme', *In Proceedings* : 25th *International Conference IEEE EMBS*, Cancun, Mexico, pp. 1287 – 1290, 2003.

[123] Mukherjee, A., Paul, R.R., Chaudhuri, K., Chatterjee, J., Pal, M., Banerjee, P., Mukherjee, K., Banerjee, S., Dutta, P.K., 'Performance analysis of different wavelet feature vectors in quantification of oral precancerous condition', *Oral Oncology*, Vol. 32, No. 9, pp. 914 – 928, 2006.

[124] Mukhopadhyay, S., Kumar J.D. Gupta, R.D., 'Content-based texture image retrieval using fuzzy class membership', *Pattern Recognition Letters*, Vol. 34, No. 6, pp. 646 – 654, 2013.

[125] Mukkavilli R. K., Sahambi, J. S., Bora, P. K., 'Modified homomorphic wavelet based despeckling of medical ultrasound images', *In Proceedings* : *Canadian Conference on Electrical and Computer Engineering*, *CCECE'08*, pp. 887 – 890, 2008.

[126] Namasivayam, S., Salman, K., Mittal, P.K., Martin, D. Small W.C., 'Hypervascular hepatic focal lesions : spectrum of imaging features', *Current Problems in Diagnostic Radiology*, Vol. 36, No. 3, pp. 107 – 123, 2007.

[127] Nandi, R.J., Nandi, A.K., Rangayyan, R.M., Scutt, D., 'Classification of breast masses in mammograms using genetic programming and feature selection', *Medical and Biological Engineering and Computing*, Vol. 44, No. 8, pp. 683 – 94, 2006.

[128] Nawaz, S., Dar, A.H., 'Hepatic lesions classification by ensemble of SVMs using statistical features based on co-occurrence matrix', *In Proceedings* : *4th IEEE International Conference on Emerging Technologies*, *ICET' 2008*, pp. 21 – 26, 2008.

[129] Ngo, T., Young Lin, T., 'Clustering high dimensional data using SVM', *In Proceedings* : *11th International Conference on Rough Sets, Fuzzy Sets, Data Mining and Granular Computing*, LNCS, Vol. 4482, pp. 256 – 262, 2007.

[130] Nielsen, M.B., Bang, N., 'Contrast enhanced ultrasound in liver imaging', *European Journal of Radiology*, Vol. 51, Supplement June 2004, pp. S3 – S8, 2004.

[131] Padhye, N.S., Brazdeikis, A., Verklan, M.T., 'Monitoring fetal development with magnetocardiography', *In Proceedings* : *IEEE Engineering in Medicine and Biology Society*, Vol. 26, pp. 3609 – 3610, 2004.

[132] Patwardhan, S.V., Dhawan, A.P., Relue, P.A., 'Classification of melanoma using tree structured wavelet transforms', *Computer Methods and Programs in Biomedicine*, Vol. 72, No. 3, pp. 223 – 239, 2003.

[133] Pavlopoulos, S., Kyriakou, E., Koutsouris, D., Blekas, K., Stafylopatis, A., Zoumpoulis, P.,'Fuzzy neural network based texture analysis of ultrasonic images', *IEEE Engineering in Medicine and Biology Magazine*, Vol. 19, No. 1, pp. 39 – 47, 2000.

[134] Pen, J.H., Pelckmans, P.A., Maercke, Y.M.V., Degryse, H.R., Schepper, A.M.D., 'Clinical significance of focal echogenic liver lesions', *Gastrointestinal Radiology*, Vol. 11, No. 1, pp. 61 – 66, 1986.

[135] Pompili, M., Riccardi, L., Semeraro, S., Orefice, R., Elia, F., Barbaro, B., Covino, M., Grieco, A., Gasbarrini, G., Rapaccini, G.L., 'Contrast-enhanced ultrasound assessment of arterial vascularization of small nodules arising in the cirrhotic liver', *Digestive and Liver Disease*, Vol. 40, No. 3, pp. 206 – 215, 2008.

[136] Pons, F., Llovet J.M., 'Approaching focal liver lesions', *Revista Espanola de Enfermedades Digestivas*, Vol. 96, No. 8, pp. 567 – 573, 2004.

[137] Poonguzhali, S., Ravindran, G., 'Automatic classification of focal lesions in ultrasound liver images using combined texture features', *Information Technology Journal*, Vol. 7, No. 1, pp. 205 – 209, 2008.

[138] Poonguzhali, S., Deepalakshmi, B., Ravindran, G., 'Optimal feature selection and automatic classification of abnormal masses in ultrasound liver images', *In proceedings* : *IEEE International Conference*, *ICSCN'07*, Chennai, India, pp. 503 –506, 2007.

[139] Prasad, G.K., Sahambi J.S., 'Classification of ECG arrhythmias using multiresolution analysis and neural networks', *In Proceedings* : *Conference on Convergent Technologies for Asia-Pacific Region, TENCON'2003*, Vol.1, pp. 227 – 231, 2003.

[140] Quala, E., Callada, F., Bertolotto, M., Rossl, S., Garloni, L., Pozzl-Mucelli, R., 'Characterization of focal liver lesions with contrast-specific US modes and a sulphur hexafluoride-filled microbubble contrast agent : diagnostic performance and confidence', *Radiology*, Vol. 232, No. 2, pp. 420 – 430, 2004.

[141] Rachidi, M., Marchadier, A., Gadois, C., Lespessailles, E., Chappard, C., Benhamou, C.L., 'Laws' masks descriptors applied to bone texture analysis : an innovative and discriminant tool in osteoporosis', *Skeletal Radiology*, Vol. 37, No. 6, pp. 541 – 548, 2008.

[142] Rajpoot, N., 'Local discriminant wavelet packet basis for texture classification', *In Proceedings : SPIE Wavelets X. SPIE*, San Diego, California, USA, 5207, pp. 774 –783, 2003.

[143] Rakebrandt, F., Crawford, D.C., Harvard, D., Coleman, D., Woodcock J.P., 'Relationship between ultrasound texture classification images and histology of atherosclerotic plaque', *Ultrasound in Medicine and Biology*, Vol. 26, No. 9, pp. 1393 – 1402, 2000.

[144] Rangayyan, R.M., Thanh, M.N., 'Pattern classification of breast masses via fractal analysis of their own contours', *In Proceedings : 19th International Congress and Exhibition, International Congress Series of Computer Assisted Radiology and Surgery, CARS'05*, Vol. 1281, pp. 1041 – 1046, 2005.

[145] Reddy, T.K., Kumaravel, N., 'A comparison of wavelet, curvelet and contourlet based texture classification algorithms for characterization of bone quality in dental CT', *In Proceedings : International Conference on Environmental, Biomedical and Biotechnology, IPCBEE'2011*, Vol. 16, pp. 60 – 65, 2011.

[146] Rinki, R., Mital D.P., Haque, S., Srinivasan, S., 'Prediction of hepatitis C by artificial neural networks', *In Proceedings : 7th International Conference on Control, Automation, Robotics and Vision, ICARCV'02*, Singapore, pp. 1545 – 1550, 2002.

[147] Rydgren, E., Thomas, E.A., Amiel, F., Rossant, F., Amara, A., 'Iris features extraction using wavelet packets'. *In Proceedings : 1International Conference on Image Processing, ICIP-04*, Vol. 2, pp. 861 – 864, 2004.

[148] Sachdeva, J., Kumar, V., Gupta, I. Khandelwal, N., 'A dual neural network ensemble approach for multiclass brain', *International Journal for Numerical Methods in Biomedical Engineering*, Vol. 28, No. 11, pp. 1107 – 1120, 2012.

[149] Sandulescu, L., Saftoiu, A., Dumitrescu, D., Ciurea, T., 'Real time contrast enhanced and real time virtual Sonography in the assessment of benign liver lesions', *Journal of Gastrointestinal and Liver Disorders*, Vol. 17, No. 4, pp. 475 – 478, 2007.

[150] Sandulescu, L., Saftoiu, A., Dumitrescu, D., Ciurea, T., 'The Role of Real time contrast enhanced and real time virtual Sonography in the assessment of malignant liver lesions', *Journal of Gastrointestinal and Liver Disorders*, Vol. 18, No. 1, pp. 103 – 108, 2008.

[151] Sarawadekar, K., Bera, D., Indana, H.B., Banerjee, S. 'VLSI-DSP based real time solution of DSC-SRI for an ultrasound system', *Microprocessors and Microsystems*, Vol. 36, No. 1, pp. 1 – 12, 2012.

[152] Scheible, W., Gosink, B.B., Leopold, G.R., 'Gray scale echographic patterns of hepatic metastatic disease', *American Journal of Roentgenology*, Vol. 129, No. 6,   pp. 983 – 987, 1977.

[153] Sekiguchi, R., Kuwajima, A., Nagamoto, M., Ohno, H., Tamura, M., 'Hepatocellular carcionoma : the diagnostic difficulties of ultrasonography and analysis of risk factors in MHTS', *Journal of Medical Systems*, Vol. 17, No. 3 – 4, pp. 133 –137, 1993.

[154] Shan, Y., Zhao, R., Xu, G., Liebich, H.M. Zhang, Y., 'Application of probabilistic neural network in the clinical diagnosis of cancers based on clinical chemistry data', *Analytica Chimica Acta*, Vol. 471, No. 1, pp. 77 – 86 , 2002.

[155] Sharma, M., Markou, M., Singh, S., Evaluation of texture methods for image analysis, *In Proceedings : 7thAustralian and New Zealand Intelligent Information Systems Conference*, pp. 117 – 121, 2001

[156] Sharma, L. N., Dandapat, S. Mahanta, A. 'Multiscale principal component analysis to denoise multichannel ECG Signals, *In Proceedings : 5th International Biomedical Engineering Conference*, Cairo, Egypt, pp. 17 – 20, 2010.

[157] Sharma, L. N., Dandapat, S., Mahanta, A., 'Multichannel ECG data compression based on multiscale principal component analysis', *IEEE Transactions on Information Technology in Biomedicine*, Vol. 16, No. 4, pp. 730 – 736, 2012.

[158] Sherman, M., 'Approaches to the diagnosis of hepatocellular carcinoma', *Current Gastroenterology Reports*, Vol. 7, No. 1, pp. 11 – 18, 2005.

[159] Shiraishi, J., Sujimoto, K., Moriyasu, F., Kamiyama, N. Doi, K., 'Computer-aided diagnosis of for the classification of focal liver lesions by use of contrast-enhanced ultrasonography', *Medical Physics*, Vol. 35, No. 5, pp. 1734 – 1746, 2008.

[160] Siedlecki, W., Sklansky, J., 'A note on genetic algorithms for large –scale feature selection', *Pattern Recognition Letters*, Vol. 10, No. 5, pp. 335 – 347, 1989.

[161] Singh, M., Singh, S. Gupta, S., 'A new measure of echogenicity of ultrasound images for liver classification', *In Proceedings : 24th IEEE Canadian Conference on Electrical and Computer Engineering, CCECE' 11*, pp. 317 – 320, 2011.

[162] Soye, J.A., Mullan, C.P., Porter, S., Beattie, H., Barltrop, A.H. Nelson, W.M., 'The use of contrast-enhanced ultrasound in the characterization of focal liver lesions', *Ulster Medical Journal*, Vol. 76, No. 1, pp. 22 – 25, 2007.

[163] Srinivasan, G.N., Shobha, G., 'Statistical texture analysis', *In Proceedings : World Academy of Science Engineering and Technology*, Vol. 36, pp. 264 – 1269, 2008.

[164] Sriram, N., Roopa, J., Aranya, M., Dhanalakshmi, M., 'Performance evaluation of computer aided diagnostic tool (CAD) for detection of ultrasonic liver disease', *Journal of Medical Systems*, Vol. 33, No. 4, pp. 267 – 274, 2009.

[165] Sudha, S., Suresh, G.R., Sukanesh, R., 'Speckle noise reduction in ultrasound images using context-based adaptive wavelet thresholding', *IETE Journal of Research*, Vol. 55, No. 3, pp. 135 – 143, 2009.

[166] Suganthy, M., Ramamoorthy, P., 'Principal component analysis based feature extraction, morphological edge detection and localization for fast iris recognition', *Journal of Computer Science*, Vol. 8, No. 9, pp. 1428 – 1433, 2012.

[167] Sujana, S., Swarnamani, S., Suresh, S., 'Application of artificial neural networks for the classification of liver lesions by image texture parameters', *Ultrasound in Medicine and Biology*, Vol. 22, No. 9, pp. 1177 – 1181, 1996.

[168] Sun, Y., Lu, J., Yahagi, T., 'Ultrasonographic classification of cirrhosis based on pyramid neural network', *In Proceedings : Canadian Conference on Electrical and Computer Engineering, CCECE'05*, Saskatoon, pp. 1678 – 1681, 2005.

[169] Sun, Y.N., Horng, M.H., Lid, X.Z., Wang I.Y., 'Ultrasonic image analysis for liver diagnosis', *In Proceedings : International conference of IEEE Engineering in Medicine and Biology*, pp. 93 – 101, 1996.

[170] Talukdar, A. K., Deka, B., Bora, P.K., 'Wavelet based adaptive Bayesian despeckling for medical ultrasound images', *In Proceedings : IEEE Region 10 Conference, TENCON'09*, pp. 1 – 6, 2009.

[171] Tao, X.M., Liu, F., Zhou, T., 'A novel approach to intrusion detection based on SVD and SVM', *In Proceedings*: 30th *Annual Conference of IEEE Industrial Electronics Society*, Vol. 3, pp. 2028 – 2033, 2004.

[172] Tchelepi, H., Ralls, P.W., Radin, R., Grant, E., 'Sonography of diffuse liver disease', *Journal of Ultrasound in Medicine*, Vol. 21, No. 9, pp. 1023 – 1032, 2002.

[173] Theodoridis, S., Koutroumbas, K., '*Pattern Recognition*', 4th Ed., Academic Press, Elsevier Inc., USA, 2008.

[174] Tiferes, D.A., Ippolito, G.D., 'Liver neoplasms : imaging characterization', *Radiologia Brasileira*, Vol. 41, No. 2, pp. 119 – 127, 2008.

[175] Tomczak, K., Mosorov, V., 'Singular value decomposition for texture defect detection in visual inspection systems', *In Proceedings : 2nd International Conference on Perspective Technologies and Methods in MEMS Design, MEMSTECH'06,* pp. 131 – 133, 2006.

[176] Tourassi, G.D., 'Journey toward computer-aided diagnosis : role of image texture analysis,' *Radiology*, Vol. 213, No. 2, pp. 317 – 320, 1999.

[177] Tsiaparas, N., Golemati, S., Andreadis, I., Stoitsis, J., 'Multiscale geometric texture analysis of ultrasound images of carotid atherosclerosis', *In Proceedings : 10th IEEE International Conference on Information Technology and Applications in Biomedicine, ITAB'10*, pp. 1 – 4, 2010.

[178] Tsiaparas, N., Golemati, S., Andreadis, I., Stoitsis, J.S., Valavanis, I., Nikita, K.S., 'Comparison of multiresolution features for texture classification of carotid Atherosclerosis from B mode ultrasound', *IEEE Transactions on Information Technology in Biomedicine*, Vol. 15, No. 1, pp. 130 – 137, 2011.

[179] Tsurusaki, M., Kawasaki, R, Yamaguchi, M., Sugimoto, K., Fukumoto, T., Ku, Y., Sugimura, K. 'Atypical hemangioma mimicking hepatocellular carcinoma with a special note on radiological and pathological findings', *Japanese Journal of Radiology*, Vol. 27, No. 3, pp. 156 – 160, 2009.

[180] Vafaie, H., DeJong, K., 'Robust Feature selection algorithms', *In Proceedings : International Conference on Tools with AI*, Boston, pp. 356 – 364, 1993.

[181] Valavanis I.K., Maugiakakou, S.G., Nikita A., Nikita K.S., 'Evaluation of texture features in hepatic tissue characterization from non-enhanced CT images,' *In Proceedings : 29th International Conference IEEE EMBS*, Lyon, France, pp. 3741 – 3744, 2007.

[182] Vilgrain, V., Boulos, L., Vullierme, M.P., 'Imaging of atypical hemangiomas of the liver with pathological correlation', *Radiographics*, Vol. 20, No. 2, pp. 379 – 397, 2000.

[183] Virmani, J., Kumar, V., Kalra, N., Khandelwal, N., 'Prediction of cirrhosis from liver ultrasound B-mode images based on laws' masks analysis', *In Proceedings : IEEE International Conference on Image Information Processing, ICIIP-2011*, Wakhnaghat, Shimla, India, pp. 1 – 5, 2011.

[184] Virmani J, Kumar V, Kalra N., Khandelwal N., 'A rapid approach for prediction of liver cirrhosis based on first order statistics', *In Proceedings* : *IEEE International Conference on Multimedia, Signal Processing and Communication Technologies, IMPACT-2011*, pp. 212 – 215, 2011.

[185] Virmani, J., Kumar, V., Kalra, N., Khandelwal, N., 'Prediction of cirrhosis based on SVD decomposition of GLCM matrix and a neural network classifier', *In Proceedings* : *IEEE International Conference on Developments in E-systems Engineering*, *DeSe'11*, Dubai, pp. 146 – 151, 2011.

[186] Virmani, J., Kumar, V., Kalra, N., Khandelwal, N., 'Prediction of liver cirrhosis based on multiresolution texture descriptors from B-mode ultrasound', *International Journal of Convergence Computing,* Vol. 1, No.1, pp. 19 – 37, 2013.

[187] Virmani, J., Kumar, V., Kalra, N., Khandelwal, N., SVM-based characterization of liver cirrhosis by singular value decomposition of GLCM matrix, *International Journal of Artificial Intelligence and Soft Computing,* Vol. 3, No. 3, pp. 276 – 296, 2013.

[188] Virmani, J., Kumar, V., Kalra, N., Khandelwal, N., 'A comparative study of computer-aided classification systems for focal hepatic lesions from B-mode ultrasound', *Journal of Medical Engineering and Technology,* Vol. 37, No. 4, pp. 292 – 306, 2013.

[189] Virmani, J., Kumar, V., Kalra, N., Khandelwal, N., 'Characterization of primary and secondary malignant liver lesions from B-mode ultrasound', *Journal of Digital Imaging,* Vol. 26, No. 6, pp. 1058 – 1070, 2013.

[190] Virmani, J., Kumar, V., Kalra, N., Khandelwal, N., 'PCA-SVM based CAD System for Focal Liver Lesions from B-Mode Ultrasound', *Defence Science Journal*, Vol. 63, No.5, pp. 478 – 486, 2013.

[191] Virmani, J., Kumar, V., Kalra, N., Khandelwal, N., 'SVM-Based characterization of liver ultrasound images using wavelet packet texture descriptors', *Journal of Digital Imaging,* Vol. 26, No.3, pp. 530 – 543, 2013.

[192] Wan, J., Zhou, S.,'Features extraction based on wavelet packet transform for B-mode ultrasound liver images', *In Proceedings* : *IEEE International Congress on Image and Signal Processing, CISP'10*,Yantai, Vol. 2, pp. 949 – 955, 2010.

[193] Wang, B., Liu, D.C., 'A novel edge enhancement method for ultrasound imaging', *In Proceedings* : *IEEE International Conference on Bioinformatics, Biomedical Engineering*, Shanghai, China, pp. 2414 – 2417, 2008.

[194] Wells, P.N.T., 'Current status and future technical advances of ultrasonic imaging', *IEEE Engineering in Medicine and Biology Magzine*, Vol. 19, No. 5, pp. 14-20, 2000.

[195] Wernecke, K., Vassallo, P., Bick, U., Diederich, S., Peters, P.E., 'Distinction between Benign and malignant liver tumors on sonography : value of hypoechoic halo', *American Journal of Roentgenology*, Vol. 159, No. 5, pp. 1005 – 1009, 1992.

[196] Weszka, J.S., Dyer, C.R., Rosenfeld, A., 'A comparative study of texture measures for terrain classification', *IEEE Transactions on Systems Man and Cybernetics*, Vol. SMC-6, No. 4, pp. 269 – 285, 1976.

[197] Weszka, J.S., Dyer, C.R., Rosenfeld, A., 'A comparative study of texture measures for terrain classification', *IEEE Transactions on Systems Man and Cybernetics*, Vol. SMC-6, No. 4, pp. 269 – 285, 1976.

[198] Wright, I.A., Gough, N.A., Rakebrandt, F., Wahab, M., Woodcock J.P., 'Neural network analysis of doppler ultrasound blood flow signals : a pilot study', *Ultrasound in Medicine and Biology*, Vol. 28, No. 5, pp. 683 – 690, 1997.

[199] Wu, C.M., Chen, Y.C., 'Multi-threshold dimension vector for texture analysis and its application to liver tissue classification', *Pattern Recognition*, Vol. 26, No. 1, pp. 37–144, 1993.

[200] Wu, C.M., Chen, Y.C., Hsiesh, K.S., 'Texture features for classification of ultrasonic liver images', *IEEE Transactions on Medical Imaging*, Vol. 11, No. 2, pp. 141– 152, 1992.

[201] Wu, Y., Ianakiev, K., Govindaraju, V., 'Improved k-nearest neighbour classification', *Pattern Recognition*, Vol. 35, No. 10, pp. 2311 – 2318, 2002.

[202] Wu, Y.H., Huang, J.Y., Cheng, S.C., Yang, C.K., Lin, C.L., 'Evolutionary feature construction for ultrasound image processing and its application to automatic liver disease diagnosis', *In Proceedings : IEEE International Conference on Complex, Intelligent and Software Intensive Systems, CISIS'11*, Seoul, pp. 565 – 570, 2011.

[203] Xian, G.M., 'An identification method of malignant and benign liver tumors from ultrasonography based on GLCM texture features and fuzzy SVM', *Expert Systems with Applications*, Vol. 37, No. 10, pp. 6737 – 6741, 2010.

[204] Xiaobin, L., Zheng, T., '*Neural Information Processing*', Springer Berlin Heidelberg, LNCS, Vol. 4233, pp. 474 – 480, 2006.

[205] Xie, Z., Liu, G., He, C., Wen, Y., 'Texture image retrieval based on gray level co-occurrence matrix and singular value decomposition', *In Proceedings : International Conference on Multimedia Technology, ICMT'10*, pp. 1 – 3, 2010.

[206] Xu, J.U., Suzuki, K., 'Computer-aided detection of hepatocellular carcinoma in hepatic CT : False positive reduction with feature selection' *In Proceedings* : *IEEE International Conference*, *ISBI'11*, pp. 1097 – 1100, 2011.

[207] Yang, J.D., Roberts, L.R., 'Epidemiology and management of hepatocellular carcinoma', *Infectious Disease Clinics of North America*, Vol. 24, No. 4, pp. 899–919, 2010.

[208] Yeh, W.C., Sheng, W.H., Pai, C.L., Liver fibrosis grade classification with B-Mode ultrasound, *Ultrasound in Medicine and Biology*, Vol. 29, No. 9, pp. 1229 – 1235, 2003.

[209] Yoshida, H., Casalino, D.D., Keserci, B., Coskun, A., Ozturk, O., Savranlar, A., 'Wavelet packet based texture analysis for differentiation between benign and malignant liver tumors in ultrasound images', *Physics in Medicine and Biology*, Vol. 48, No. 22, pp. 3735 – 3753, 2003.

[210] Zaid A.Z.S.A., Fakhr, M.W., Mohamed A.F.A, 'Automatic diagnosis of liver diseases from ultrasound images,' *In Proceedings* : *International Conference on Computer Engineering and Systems*, pp. 313 – 319, 2006.

[211] Zhang, X., Kanematsu, M., Fujita, H., Zhou, X., Hara, T., Yokoyama, R., Hoshi, H., 'Application of an artificial neural network to the computer-aided differentiation of focal liver disease in MR imaging', *Radiological Physics and Technology*, Vol. 2, No. 2, pp. 175 –182, 2009.

[212] Zhang, X., Fujita, H., Qin, T., Zhao, J., 'CAD on liver using CT and MRI', Medical Imaging and Informatics', *In Proceedings* : *Second International Conference MIMI 2007, LNCS 4987*, Beijing, China, pp. 367 – 376, 2008.

[213] Zhou, G., Wang, Y., Wang, W., Sun, Y., Chen, Y., 'Decision of cirrhosis using liver's ultrasonic images', *In Proceedings* : *27th Annual International Conference of the IEEE Engineering in Medicine and Biology Society*, Shanghai, pp. 3351 – 3354, 2006.

[214] Zhou, S., Wan, J., 'A survey of algorithms for the analysis of diffused liver disease from B-mode ultrasound images', *In Proceedings* : *9th International Conference on Electronic Measurement and Instruments*, *ICEMI'2009*, pp. 2576 – 2582, 2009.

[215] Zhou, Z.H., Wu, Z., Wei, T., 'Ensembling neural networks : many could be better than all', *Artificial Intelligence*, Vol. 137, No. 1–2, pp. 239 – 263, 2002.